Separation of Zr and Hf via fractional crystallization of $K_2Zr(Hf)F_6$:

A theoretical and experimental study

D.J. Branken

2009

Separation of Zr and Hf via fractional crystallization of $K_2Zr(Hf)F_6$:

A theoretical and experimental study

D.J. Branken

B.Sc (Industrial science)

Dissertation submitted in partial fulfilment of the requirements for the degree Master of Science in Chemistry at the Potchefstroom campus of the North-West University

Supervisor:	Prof. H.M. Krieg
Co-Supervisor:	Dr. G. Lachmann
Assistant Supervisor:	Prof. O.S.L. Bruinsma

May 2009

NORTH-WEST UNIVERSITY
YUNIBESITI YA BOKONE-BOPHIRIMA
NOORDWES-UNIVERSITEIT
POTCHEFSTROOM CAMPUS

Conference Contributions Resulting from this Research

Poster Presentation

Branken, D.J. Lachmann, G. Krieg, H.M., and Bruinsma, O.S.L. Separation of Zr and Hf via Fractional Crystallization of $K_2Zr(Hf)F_6$: A Theoretical Study on the Distribution Coefficient of the Hafnium Impurity. *BIWIC 2007 14th International Workshop on Industrial Crystallization.* 9 – 11 September 2007. University of Cape Town, Cape Town South Africa.

Oral Presentations

Branken, D.J. Lachmann, G. Krieg, H.M., and Bruinsma, O.S.L. A Theoretical and Experimental Study on the Separation of Zr and Hf via Fractional Crystallization of $K_2Zr(Hf)F_6$. *The South African Chemical Institute Young Chemists' Symposium.* 10 October 2007. University of South Africa, Pretoria, South Africa.

Branken, D.J. Lachmann, G. Krieg, H.M., and Bruinsma, O.S.L. Skeiding van Zr en Hf via Fraksionele Kristallisasie van $K_2Zr(Hf)F_6$: 'n Teoretiese en Eksperimentele Studie. *Die Suid-Afrikaanse Akademie vir Wetenskap en Kuns studentesimposium.* 2 November 2007. Tshwane University of Technology, Arcadia Campus Pretoria, South Africa.

Branken, D.J. Lachmann, G. Krieg, H.M., and Bruinsma, O.S.L. Separation of Zr and Hf via Fractional Crystallization of K_2ZrF_6 and K_2HfF_6. *Advanced Metals Initiative Seminar.* 14 November 2007. Department of Science and Technology Auditorium, Pretoria, South Africa.

Branken, D.J. Lachmann, G. Krieg, H.M., and Bruinsma, O.S.L. Fractional Crystallization of $K_2Zr(Hf)F_6$ for the Separation of Zr and Hf. *Advanced Metals Initiative Conference.* 18 - 19 November 2008. Oppenheimer conference centre, Gold Reef City Theme Park, Johannesburg, South Africa.

Acknowledgements

I herein express my sincerest gratitude towards:

- My heavenly father, God almighty, for bestowing me with the required cognitive abilities, and perseverance to complete this research.

- The New Metals Development Network (NMDN) of the Advanced Metals Initiative (AMI), funded by the South African Department of Science and Technology (DST), as coordinated by the South African Nuclear Energy Corporation Limited (Necsa), for their financial assistance.

- Dr. J.T. Nel and Dr. E. Snyders from Necsa, for their support and professional coordination of the various administrative facets of the NMDM branch of the AMI.

- Prof. H.M. Krieg for his continued scientific, and most appreciated, moral support throughout the duration of my research, as well as his conscientious contribution to the writing of my dissertation.

- Dr. G. Lachmann for his proficient advice and guidance with nearly every aspect of my research.

- Prof. O.S.L. Bruinsma for his valued suggestions, and assistance with the theoretical process evaluation, as well as his contribution to my dissertation, all of which is much appreciated.

- The Laboratory of Applied Molecular Modelling (LAMM), North-West University, for the use of their computational facilities. A special word of thanks to Prof. H.C.M. Vosloo, and Dr. C.G.C.E. van Sittert for their assistance in this regard.

- Dr. R.J. Kriek for taking the initiative in providing our Chemistry department with much needed ICP analytical facilities.

- Dr. L.R. Tiedt at the Laboratory for Electron Microscopy, North-West University for taking SEM images, and whose meticulous attention to detail is very much appreciated.

- Mr. J.H. Broodryk, Instrument-making, North-West University, who assembled the crystallization vessels used in this study with excellent craftsmanship.

- Mrs. B. Venter, at the XRD laboratory of the Geology department, North-West University, for performing the XRD analyses that was used in this study.

- Mrs. Linda Mey, for overseeing the administration regarding my bursary, and for processing orders for chemicals.

- My parents, Dawid, and Hermien Branken for providing me with the opportunity of tertiary education. I am also appreciative of the loving care and support I've always received from them as well as my grandmother.

- Hertzog Bissett, Derik van der Westhuizen, and Neels le Roux, for their valued friendship, and for lending a hand from time to time.

Abstract

Due to the low absorption cross section for thermal neutrons of zirconium (Zr) in contrast to hafnium (Hf), Zr-metal must essentially be Hf free (<100 ppm Hf) to be suitable for use in nuclear reactors. However, Zr and Hf always occur together in nature, and due to similar chemical and physical properties, their separation is complicated. Separation can be achieved by traditional liquid-liquid extraction or extractive distillation processes, using $Zr(Hf)Cl_4$ as feedstock. However, the production of $K_2Zr(Hf)F_6$ via the plasma dissociation route, developed by Necsa, could facilitate the development of an alternative separation process.

The fractional crystallization of $K_2Zr(Hf)F_6$ from solution was investigated as a possible alternative for the separation of Zr and Hf. Both molecular modelling and experimental techniques were used in this study in which molecular modelling was applied to determine whether any thermodynamic limitations exists in terms of solid solution formation of the pure salts that could hinder the separation efficiency of fractional crystallization. Using the calculated thermodynamic properties of mixing, the separation efficiency was theoretically evaluated using a thermodynamic model to calculate the relative distribution coefficients.

Crystallization was subsequently studied experimentally to investigate the validity of the separation efficiency predicted by the results obtained from molecular modelling. In addition, the influence of solvent composition and other physical parameters on the separation efficiency was investigated. A more efficient separation was obtained experimentally than predicted by the theoretical calculations; wherein the use of KF and HF as additives was found to influence the separation efficiency.

Despite the limited correlation between the molecular modelling and the experimental results, the relative ease of solid solution formation predicted by the modelling results, which is not surprising owing to the close similarities between Zr and Hf, might well restrict the separation efficiency by fractional crystallization. The disagreement between the experimental and the modelling results were attributed to different factors that could not be accounted for in the theoretical calculations. It was for example shown that the change in the vibrational entropy, which was initially neglected in the theoretical calculations, has a significant influence.

Opsomming

Sirkonium-metaal (Zr) is slegs geskik om as konstruksiemateriaal in kernreaktore gebruik te word indien dit van hafnium (Hf) gesuiwer is (< 100 dpm Hf), aangesien Zr, anders as Hf, oor 'n lae absorpsievermoë beskik teenoor termiese neutrone. Zr en Hf word egter gesamentlik in die natuur aangetref, en hul skeiding is moeisaam omdat hul chemiese en fisiese eienskappe baie soortgelyk is. Skeiding kan bewerkstellig word deur gebruik te maak van gevestigde tegnieke soos vloeistof-vloeistof-ekstraksie of ekstraktiewe distillasie met $Zr(Hf)Cl_4$ as voerstroom. Die produksie van $K_2Zr(Hf)F_6$ via die plasma-dissosiasie-roete, soos ontwikkel deur Necsa, kan moontlik aangewend word om 'n alternatiewe skeidingsproses daar te stel.

Die fraksionele kristallisasie van $K_2Zr(Hf)F_6$ uit waterige oplossings is daarom bestudeer as 'n moontlike alternatiewe skeidingsmetode, waar beide molekuul modellering en eksperimentele tegnieke in hierdie studie gebruik is. Molekuulmodellering is gebruik om te bepaal of die vorming van mengkristalle van die twee suiwer komponente termodinamies moontlik is, wat die skeidingseffektiwiteit kan benadeel. Die skeidingseffektiwiteit is teoreties bepaal deur gebruik te maak van berekende termodinamiese groothede t.o.v. die vorming van mengkristalle, waarmee die relatiewe verdelingskoëffisiënt met behulp van 'n termodinamiese model bereken is.

Kristallisasie is ook eksperimenteel bestudeer om die geloofwaardigheid van die teoretiese berekende skeidingseffektiwiteit, oftewel modelleringsresultate, te bepaal. Die invloed van die oplosmiddelsamestelling, en ander fisiese parameters, op die skeidingseffektiwiteit is ook tegelykertyd bestudeer. Beter skeidingseffektiwiteit is egter eksperimenteel, in vergelyking met die modelleringsresultate verkry, waar gewys is dat die gebruik van KF en HF as *bymiddels die skeidingseffektiwiteit* beïnvloed.

Ondanks die beperkte korrelasie tussen die modellerings- en eksperimentele resultate, is dit moontlik dat die relatiewe gemak waarmee mengkristalle vorm, soos voorspel deur die modelleringsresultate en in die lig van die klein verskille tussen Zr en Hf verwag is, wel kan bydra tot die redelike lae skeidingseffektiwiteit van fraksionele kristallisasie.

Die lae korrelasie tussen die eksperimentele- en modelleringsresultate kan toegeskryf word aan verskillende faktore wat nie vir die teoretiese berekeninge in ag geneem is nie. So is byvoorbeeld aangetoon dat die verandering in die vibrasie-entropie, wat aanvanklik ook vir die teoretiese berekening van die skeidingseffektiwiteit geïgnoreer is, 'n beduidende invloed het.

Table of Contents

Nomenclature

Latin Symbols

a, b, c	Unit cell basis vectors	nm or Å
bi	Mole fraction of component i	[-]
c_i	Solute concentration of component i	Any suitable unit
$c_{tot}(T_2)$	Concentration of the dissolved solute at temperature T_2	g/500 mL solvent
$D(y)$	Debye function	[-]
E_A	Electronic energy of A = Zr, Hf, K, F, Al, per atom	eV
$E_C[\rho(r)]$	Coulomb electrostatic contribution to $E_t[\rho(r)]$	au
E_i	Total electronic energy of state i	eV or Ha
$E_K[\rho(r)]$	Kinetic energy of a system of non-interacting electrons	au
$E_t[\rho(r)]$	Total electronic energy due to electron charge density	au
E_{tot}	Total electronic energy of a $K_2Zr_{(1-z)}Hf_zF_6$ supercell	au
$E_{xc}[\rho(r)]$	Exchange-correlation functional	au
f_i^j	Total mass fraction of elemental j = Zr/Hf in stream i	[-]
h	Planck constant	J.s
k	Boltzmann constant	$J.K^{-1}$
K_i	Distribution coefficient of component i	[-]
M_i	Total mass of $K_2Zr(Hf)F_6$ in stream i (batch crystal.)	g
M_i^j	Fractional mass of elemental j = Zr/Hf in stream i (batch crystal.)	g
M_W^j	Molecular weight of elemental j = Zr/Hf	$g.mol^{-1}$
n_i	Total number of moles with respect to Zr and Hf in stream i	mol
n_i^j	Total number of moles of j = Zr/Hf in stream i (batch crystal.)	mol
n	Total number of stages in the Ideal cascade	[-]
n_E	Number of stages in the enriching section of an Ideal cascade	[-]
n_S	Number of stages in the stripping section of an Ideal cascade	[-]
R	Universal gas constant	$J.mol^{-1}.K^{-1}$
r_i^j	Relative mole fraction of j = Zr/Hf in stream i	[-]
S	Supersaturation ratio	[-]
S_{vib}	Vibrational entropy of a solid	$J.K^{-1}.mol^{-1}$

T	Temperature	K or °C
v_i	Quantum number of the i'th energy level	[-]
w_α^I	Weight of an atom of type α at lattice site I	[-]
x_i	Mole fraction of component i in the liquid phase (batch crystal.)	[-]
y_i	Mole fraction of component i in the unprocessed material	[-]
z_i	Mole fraction of component i in the solid phase (batch crystal.)	[-]
x_i^{sat}	Saturation concentration (solubility) of component i	Any suitable unit
$x_{tot}^{sat}(T_1)$	Total solubility of impure solute at temperature T_1	g/500 mL solvent
$x_{i,j}$	Mole fraction of Zr in mother solution leaving stage i or j	[-]
$y_{i,j}$	Mole fraction of Zr in the feed stream to stage i or j	[-]
$z_{i,j}$	Mole fraction of Zr in th crystalline product leaving stage i or j	[-]
i	Stage number in the enriching section of a Ideal cascade	[-]
j	Stage number in the stripping section of a Ideal cascade	[-]
x_W	Mole fraction of Zr in mother solution leaving the waste stream	[-]
y_F	Mole fraction of Zr in the feed stage of the Ideal cascade	[-]
z_P	Mole fraction of Zr in the solid leaving the product stream	[-]
Δc_i	Concentration driving force for component i	Any suitable unit
ΔE_{dis}	Dissociation energy	kJ.mol^{-1}
ΔG_{mix}	Gibbs free energy of mixing	kJ.mol^{-1}
ΔH_{2s}^{dis}, ΔH_{mix}	Dissolution (mixing) enthalpy for lattice substitution	kJ.mol^{-1}
ΔH_{cr}	Enthalpy of crystallization	kJ.mol^{-1}
ΔH_{form}	Formation enthalpy	kJ.mol^{-1}
ΔH_{sol}	Enthalpy of solvation of ions	kJ.mol^{-1}
ΔS_{2s}^{dis}	Dissolution (mixing) entropy for lattice substitution	kJ.mol^{-1}.K^{-1}
ΔS_{2s}^{mix}, ΔS_{mix}	Ideal mixing entropy	kJ.mol^{-1}.K^{-1}
ΔS_{2s}^{vib}, ΔS_{vib}	Vibrational entropy change for lattice substitution	kJ.mol^{-1}.K
$\mathbf{R}_I$	Vector, indicating the position of lattice site I	[-]
$V_{ext}(\mathbf{r},\mathbf{r}')$	Total external potential for a virtual atom	au
$V_{ion}(r)$	All-electron effective potential	au
$V_{ps}(r)$	Pseudopotential	au
V_{ps}^{α}	Pseudopotential of an atom of type α	au

Greek Symbols

α, β, γ	Unit cell angles	Degrees, °
ν_D	Vibration frequency of the highest vibrational mode	s^{-1}
$\alpha_{Zr,Hf(i)}$	Separation factor for Zr relative to Hf (with respect to stage *i*)	[-]
β_0	Thermodynamic relative distribution coefficient	[-]
$\beta_{2,1}$	Relative distribution coefficient, 2 : impurity, 1 : host	[-]
$\beta_{Hf,Zr}$	Relative distribution coefficient with respect to Zr and Hf	[-]
γ_i'	Activity coefficient of compound *i* in solution	[-]
γ_i	Activity coefficient of species *i*	[-]
γ_i^{sat}	Pure-component activity coefficient for a saturated solution of *i*	[-]
$\gamma_{Zr,Hf(i)}$	Tails separation factor for Zr relative to Hf (with respect to stage *i*)	[-]
$\delta_{Zr,Hf(i)}$	Heads separation factor for Zr relative to Hf (with respect to stage *i*)	[-]
$\Delta\mu_{2s}^{dis}$	Change in chemical potential during lattice substitution	$kJ.mol^{-1}$
ε	Total energy of a harmonic oscillator	J
ε_i	Energy of the i'th vibrational level	J
Θ_D	Debye temperature of a solid	K
μ_i	Chemical potential of compound *i*	$kJ.mol^{-1}$
μ_i^*	Chemical potential of an infinitely dilute solution of *i*	$kJ.mol^{-1}$
μ_i^0	Standard chemical potential of compound *i*	$kJ.mol^{-1}$
ν	Vibrational frequency	s^{-1}
σ	Relative supersaturation	[-]
Σ	Relative excess amount of solute at T_2 relative to T_1	[-]
Ω	Regular solution interaction parameter	$kJ.mol^{-1}$
$\rho(r)$	Electronic charge density	[-]
$\psi_i(r)$	One-electron wave functions	[-]

Conversion Factors

1 eV	96.4853 $kJ.mol^{-1}$
1 Ha	2625.5 $kJ.mol^{-1}$
1 Å	10^{-10} m

CHAPTER 1

Introduction

1.1. Problem Statement

Due to its excellent metallurgical properties, corrosion resistance and low neutron absorption cross section; zirconium metal (Zr) is a suitable construction material for nuclear reactors [1 - 3], specifically as cladding material for nuclear fuel rods. For this purpose, zirconium alloys such as Zircaloy 2 or Zircaloy 4 are commonly used, in which alloying elements such as Sn, Fe, Cr and Ni are mostly used, although Nb and Mo alloys have also been applied [1].

Zr-metal must be free of strongly neutron-absorbing impurities such as Cd, B and Hf, to ensure optimum neutron efficiency for nuclear applications [4]. Producing hafnium-free zirconium (< 100 ppm Hf) [2, 4, 5] is a particularly difficult problem because these elements occur together in the mineral zircon, the primary source of Zr, which contains approximately 2 % Hf relative to Zr (Section 2.1.1) [6, 7]. The separation of Zr and Hf is further complicated by their close chemical similarity, which can be attributed to the similar configuration of their valence electrons, namely $4d^2 5s^2$ and $5d^2 6s^2$ for Zr and Hf respectively, and the lanthanide contraction which causes the two elements to have very similar atomic and ionic radii, i.e. 1.45 Å and 0.86 Å for Zr and Zr^{4+}, and 1.44Å and 0.85 Å for Hf and Hf^{4+} respectively [6 - 8]. This close similarity is reflected in the physical properties of Zr and Hf compounds. For example, the tetrachlorides, $Zr(Hf)Cl_4$, have very similar sublimation and triple point temperatures that differ only by a few degrees Celsius [4]. As a result, the production of nuclear grade Zr-metal is costly, partly because of the expensive multistage separation processes required to reduce the Hf-content to an acceptable level [2, 4, 9].

Extraction of Zr from the inert zircon is a daunting task in itself, for which extreme temperature conditions are required. While different methods can be used commercially (Section 2.1.2), carbochlorination, where $Zr(Hf)Cl_4$ is produced that is used in the majority of separation methods (Section 2.1.4), has been the most successful method to date. The

development of alternative separation methods to replace the widely used MIBK (Section 2.1.4.1.A), TBP (Section 2.1.4.1.B), and CEZUS (Section 2.1.4.2) processes were required to ensure compatibility with the carbochlorination step [9]. The use of plasma technology to produce chemically amenable plasma dissociated zircon (PDZ) (Section 2.1.5) [10], as was developed by the Nuclear Energy Corporation of South Africa (Necsa), could facilitate the development of an alternative method for the beneficiation, purification and reduction of Zr.

Using the novel plasma dissociation route, potassium hexafluorozirconate(hafnate), $K_2Zr(Hf)F_6$, can be produced by digestion of PDZ with aqueous hydrofluoric acid (Section 2.1.5.1) in one embodiment of the method [10]. The use of fractional crystallization of $K_2Zr(Hf)F_6$, i.e. crystallization from aqueous solutions in which K_2ZrF_6 has a slightly lower solubility than K_2HfF_6 and therefore a higher tendency to crystallize, has been applied in the past (Section 2.1.5.2) [3, 11, 12] for Zr-Hf separation. However, relatively little literature information exists on this subject. Therefore, to investigate the viability of Zr-Hf separation by fractional crystallization of $K_2Zr(Hf)F_6$, and therefore also the applicability of the production of $K_2Zr(Hf)F_6$ by the plasma dissociation route, fractional crystallization of $K_2Zr(Hf)F_6$ was studied from two main perspectives as discussed in the next section.

1.2. Scope of this Study

Due to the chemical similarities of Zr and Hf, K_2ZrF_6 and K_2HfF_6, like other crystalline solids of these two elements, have isomorphic crystal structures which can lead to solid solution formation during crystallization from a solution that contains both entities, causing poor separation efficiency, as has been observed during the crystallization from solution of other isomorphic compounds [13]. To determine this effect, the efficiency of fractional crystallization to separate Zr and Hf was first studied from a theoretical perspective in which a thermodynamic model for the relative distribution coefficient was used to evaluate the separation efficiency. Molecular modelling techniques were used to determine the thermodynamic mixing properties of $K_2Zr_{(1-z)}Hf_zF_6$ solid solutions (mixed crystals) with varying composition. By substituting the calculated mixing enthalpy into a simplified form of the thermodynamic model, the separation efficiency could be theoretically estimated. In addition, molecular modelling of the ZrF_6^{2-} and HfF_6^{2-} ions was also used to determine whether any significant difference in the stability of the ions in solution exists, that could also influence the efficiency of separation.

Although the solid-state thermodynamics, as studied via molecular modelling of $K_2Zr_{(1-z)}Hf_zF_6$ solid solutions, is an important contributing factor to the overall separation efficiency for crystallization of these and other isomorphic compounds from solution, the influence of the solvent, or solution thermodynamics is equally important, as shown by studies on solution crystallization of other isomorphic systems [13]. Therefore, since fractional crystallization of $K_2Zr(Hf)F_6$ has been studied in the past using aqueous solutions of potassium fluoride (KF) and hydrofluoric acid (HF) [11], crystallization was also evaluated experimentally using KF solutions of varying concentration with and without HF in this study. Hereby, the influence of KF and HF as additives on the separation efficiency was studied, and the results were compared with the theoretical predictions.

Using the experimental results, the efficiency of fractional crystallization of $K_2Zr(Hf)F_6$ for Zr-Hf separation was further evaluated by estimating the number of crystallization stages required in a continuously operated recycle-type cascade process. For this purpose, it was assumed that the separation efficiency remains constant with each stage and that the separation efficiency remains unchanged from that determined for the batch experiments.

1.3. Structure of this Dissertation

In Chapter 2, an overview of the production of nuclear grade Zr is presented including various techniques that have been used to unlock the inert zircon ore, purification of Zr from Hf, and reduction to produce Zr-metal. A more detailed description of the plasma dissociation route is presented as well as a summary of the available literature on the fractional crystallization of $K_2Zr(Hf)F_6$. The principles of crystallization are also reviewed, in which the theory of the thermodynamic model used to estimate the separation efficiency, is discussed. Molecular modelling techniques were used to calculate the necessary thermodynamic properties needed to theoretically evaluate the separation efficiency. Therefore, the basic principles of the molecular modelling programs used in this study are also discussed.

In Chapter 3 the molecular modelling results are presented along with a detailed description of the methods used in this study. It is shown how the molecular modelling results can be applied to predict the separation efficiency of the crystallization from solution of two isomorphic solutes, in this case K_2ZrF_6 and K_2HfF_6, using a simplified form of the thermodynamic model mentioned previously (Section 1.2). In addition, the methods and

parameters used for the modelling of $K_2Zr_{(1-z)}Hf_zF_6$ solid solutions were applied to model two different test systems. The results were compared with published data to evaluate the validity of the parameters used in this study.

The experimental results of crystallization of $K_2Zr(Hf)F_6$ from aqueous solutions of KF and HF with varying composition is presented in Chapter 4. In addition to the KF concentration, the $K_2Zr(Hf)F_6$ concentration was also varied in a separate set of experiments to create comparable crystallization conditions when the solution composition was varied, whereby the effects of the additives could be more clearly evaluated.

In Chapter 5, a summary and comparison of the molecular modelling and experimental results is given. It is shown that there is a rather poor correlation between the modelling and experimental results. Subsequently, these discrepancies are evaluated with specific reference to the change in the vibrational entropy, which was initially neglected in the theoretical predictions. It is shown that the inclusion of this term, which was estimated using a mathematical model, results in an improved correlation between the modelling and experimental results. The semi-quantitative process evaluation, as mentioned above, is also given in this chapter in which the efficiency of fractional crystallization is assessed from a more industrial point of view. Based on the results obtained in this study, other future research possibilities are finally recommended.

1.4. References

1. Nielsen, R.H., Schlewitz, J.H. and Nielsen, H. 2001. Zirconium and zirconium compounds. In Kirk-Othmer encyclopaedia of chemical technology. 5th ed. John Wiley & Sons. Volume 26. p. 621 – 664.

2. Poriel, L., Favre-Réguillon, A., Pellet-Rostaing, S. & Lemaire, M. Zirconium and hafnium separation, part 1. Liquid/liquid extraction in hydrochloric acid aqueous solution with aliquat 336. *Sep. Sci. Technol.* **41** (2006) 1927 - 1940.

3. Vinarov, I.V. Modern methods for separating zirconium and hafnium. *Russ. Chem. Rev.* **36** (7) (1967) 522 – 536.

4. Skaggs, R.L., Rogers, D.T. & Hunter, D.B. Review of anhydrous zirconium-hafnium separation techniques. Report No. BuMines IC 8963, U.S. Bureau of Mines: Albany, OR, 1984.

5. Stephens, W.W. 1984. Extractive metallurgy of zirconium – 1945 to the present. In Franklin, D.G. & Adamson, R.B., eds. Zirconium in the nuclear industry: Sixth international symposium. *ASTM Spec. Tech. Publ. 824*. American Society of Testing and Materials. p. 5 – 36.

6. Nielsen, R.H. 2001. Hafnium and hafnium compounds. In Kirk-Othmer encyclopaedia of chemical technology. 5th ed. John Wiley & Sons. Volume 13. p. 78 – 97.

7. Cotton, F.A., Wilkinson, G., Murillo, C.A. & Bochmann, M. 1999. Advanced inorganic chemistry. New York: John Wiley & sons. p. 878 – 895.

8. Blumenthal, W.B. 1958. The chemical behaviour of zirconium. New York: D. van Nostrand Company Inc. 398 p.

9. da Silva, A.B.V. and Distin, P.A. Zirconium and hafnium separation without waste generation. *CIM Bull.* **91** (1998) 221 - 224.

10. Nel, J.T. Process for reacting a zirconia based material. U.S. Pat. 5,958,355 (1999).

11. Coster, D. and von Hevesy, G. Process of separating zirconium and Hafnium. U.S. Pat. 1,618,960 (1927).

12. Sajin, N.P. & Pepelyaeva, E.A. Separation of hafnium from zirconium and production of pure zirconium dioxide. In Proceedings of the Second united Nations International Conference on the Peaceful uses of Atomic Energy, Geneva, 1958. Vol. 8, Paper P/634, pp 559–562.

13. Nie, Q., Wang, J. & Yin, Q. Effect of solution thermodynamics on the purification of two isomorphic steroids by solution crystallization. *Chem. Eng. Sci.* **61** (2006) 5962 – 5968.

CHAPTER 2

Literature Review

2.1. Zirconium and Hafnium: Chemistry and Separation

2.1.1. Zirconium and Hafnium Applications and Occurrence

Despite the use of Zr in the nuclear industry, for which a high purity (< 100 ppm Hf) is required with regard to the Hf counterpart as explained in Chapter 1, other uses of zirconium includes zircon ceramics, opacifiers, refractories, abrasives, chemicals, metal alloys and welding rod coatings [1]. Commercial grade zirconium (which is not purified from Hf), is also used in chemical process industries due to its high corrosion resistance, while ZrF_4 can be used in the manufacture of fluoride-glasses [1] because of its excellent optical properties. Compounds such as $ZrCl_4$ and ZrO_2 can also be applied as catalysts. Zirconia (ZrO_2) is used for the manufacture of refractories, as mentioned above, that are resistant against high temperatures, fluxes, slags, acids and fused alkalies [2].

Hafnium is often used as an alloying element [3] to improve the high temperature tensile and creep strength for high temperature application alloys and superalloys that are used in jet aircraft engines. In pure form, Hf-metal may be used as control rods in nuclear reactors that power many naval vessels [3], due to its excellent corrosion resistance in hot water and large neutron absorption cross section. Like ZrO_2, HfO_2 is also used in the manufacture of refractories, and can be used as insulating sheaths for tungsten-rhenium thermocouples operating above 1500 °C [3].

The most common sources of Zr are zircon ($ZrSiO_4$), and baddeleyite [1 - 6], which has also been called zirkite [2, 5], and consists mainly of $Zr(Hf)O_2$ and ferrous impurities. As noted in Chapter 1, zirconium and hafnium always occur together in nature. Therefore, zircon and baddeleyite also serve as important sources of Hf, in which the Hf-content is commonly 2 wt% with respect to Zr when derived from zircon [5]. Zircon is the primary source of Zr however [1, 4, 5], and occurs in beach sands of Richard's Bay in South Africa, Florida in the

USA, Australia, Sri Lanka and India. Zircon contains radioactive impurities such as U and Th [7] in the form of their oxides due to their isomorphism with ZrO_2 [5], and it has been observed that the amount of radioactivity increases as the Hf-content increases [3].

2.1.2. Zircon Beneficiation

Extracting Zr from zircon is difficult due to the inert nature of the ore, which resists digestion by regularly used mineral acids. Aggressive reagents under extreme temperature conditions are required to unlock the ore. Techniques that have been used for decomposition include the following:

- carbochlorination,
- reduction by carbon,
- caustic fusion, and
- fluorosilicate fusion.

In the following sections these techniques will be discussed in more detail. Note that when reference is made to different Zr-compounds, it should be understood as being a mixture of Zr and the corresponding Hf-analogue, as separation does not occur during the decomposition stage by any of these methods due to the close chemical similarity of Zr and Hf. Also, trace impurities are not included in the reaction schemes illustrated below.

2.1.2.1. Carbochlorination

In general, carbochlorination has been the most successful method, as $Zr(Hf)Cl_4$ can be produced which is suitable for liquid-liquid extraction for the separation of Zr and Hf. Direct carbochlorination, i.e. without producing the ZrC intermediate (Section 2.1.2.2) can be achieved by the treatment of zircon sand-carbon (coke) mixtures with chlorine at 1150 °C in a fluidized bed reactor, where chlorine gas is used as the fluidizing medium. The process can be represented by the following reaction scheme [1, 3, 4, 8]:

$$ZrSiO_4 + 2C + 4Cl_2 \xrightarrow{1150\,^{\circ}C} ZrCl_4 + SiCl_4 + 2CO_2\uparrow \qquad (2.1)$$

The high temperature required for the endothermic reaction is usually provided by an electric arc furnace, but can also be sustained by the addition of silicon carbide, SiC, which

chlorinates exothermically [3]. The $SiCl_4$ by-product is readily separated from $ZrCl_4$ due to the large difference in the volatility of the two substances [4]. This is done by first cooling the product gasses to below 200 °C whereby zirconium tetrachloride snow, as it is called, is selectively condensed in a large space condenser [1]. $SiCl_4$ is condensed in a quench-condenser in which the warm gasses are scrubbed counter-currently with liquid $SiCl_4$ at -20 °C. $SiCl_4$ can then be purified by stripping and distillation [1].

2.1.2.2. Reduction by Carbon

Instead of direct carbochlorination, zircon may also be heated with carbon (of which coke serves as a convenient source), to produce ZrC according to the following reaction [1, 2, 4, 5, 8]:

$$ZrSiO_4 + 3C \xrightarrow{2500\,^{\circ}C} 2ZrC(N,O) + SiO\uparrow + 3CO\uparrow \qquad (2.2)$$

The formation of $SiCl_4$ is avoided by this method and SiO forms with a deficiency of carbon [1], which is vaporized at the reaction temperature. The formation of ZrN and ZrO also occurs due to the presence of air in the system. The crude carbide is then chlorinated, the reaction of which proceeds exothermically [1, 5]:

$$ZrC(N,O) + 2Cl_2 \xrightarrow{700-1200\,^{\circ}C} ZrCl_4 + (CO + N_2)\uparrow \qquad (2.3)$$

In one modification of the process represented by Equation (2.2), the use of CaC_2 instead of carbon alone has been reported to give better conversion [2].

2.1.2.3. Caustic Fusion

Commercially, the fusion of zircon with dry NaOH has also been used, resulting in a solid frit as represented by the following reaction equation [1, 2, 4]:

$$ZrSiO_4 + 4NaOH \xrightarrow{600-650\,^{\circ}C} Na_2ZrO_3 + Na_2SiO_3 + 2H_2O \qquad (2.4)$$

The product is washed with water to dissolve the sodium silicate that can be separated from the newly formed hydrous zirconium oxide [1, 4]. Nitric or sulphuric acid can then be used to dissolve the zirconium fraction, which can then be used for zirconium-hafnium separation by the TBP solvent extraction process (Section 2.1.4.1.B).

2.1.2.4. Fluorosilicate Fusion

Fusion of zircon with potassium hexafluorosilicate, K_2SiF_6, has been used commercially in the United States and former USSR [1], although the use of potassium hydrogen fluoride has also been reported for the preparation of potassium hexafluorozirconate, K_2ZrF_6. The fusion reaction of zircon with K_2SiF_6 (Equation 2.5) is performed in a rotary furnace at 700 °C [1, 3, 5, 9, 10]:

$$ZrSiO_4 + K_2SiF_6 \xrightarrow{700\,^{\circ}C} K_2ZrF_6 + 2SiO_2 \qquad (2.5)$$

The addition of K_2CO_3 or KCl to the mixture i) reduces the slight tendency of K_2SiF_6 to dissociate whereby SiF_4 is formed that is lost by sublimation, ii) promotes completion of the reaction [1, 3, 9].

The product is leached with a hot acidic solution (1% HCl by volume) [9], where the insoluble silica can be separated from the solution by filtration. K_2ZrF_6 is recovered by cooling the hot, clear solution, producing a solid crystalline product that is then washed with water [1, 3, 9].

2.1.3. Zirconium Reduction

After extraction of Zr from the zircon mineral, purification from trace impurities and separation from Hf (Section 2.1.4), the production of Zr-metal can proceed via different routes. The most common and historically important reduction methods are listed below:

- reduction of K_2ZrF_6 with sodium or potassium,
- reduction of $ZrCl_4$ with Na or Al,
- the Thermite Process,
- the Iodide Process, and
- the Kroll Process.

2.1.3.1. Reduction of K_2ZrF_6 with Sodium or Potassium

Berzelius was the first to produce an impure, blackish Zr powder in 1824 by the reduction of K_2ZrF_6 with potassium [1, 2, 5, 11]. He heated an iron tube that was closed at one end over a spirit lamp to facilitate the reaction. The product was washed with diluted hydrochloric acid, a solution of ammonium chloride and finally with water. Various modifications have been used. For example, Weiss and Neumann found that the product obtained by this process consisted of amorphous Zr, of which the purity could be improved by first washing the product with absolute alcohol, and then with diluted hydrochloric acid [2]. Wedekind, Weiss and Neumann later found that even better results can be obtained using sodium instead of potassium [2].

In later years, it became clear that elementary, or crystalline zirconium, which has a hexagonal close-packed structure, is stable up to 862 °C, but becomes reactive towards N, C, and O at the red-hot temperatures used for the reduction of Zr [5]. Adsorption of these elements affects the ductility and hardness of the metal, leading to an altered crystal structure (face-centred cubic type), if appreciable amounts of the elements are adsorbed. Therefore, the product obtained by the method described above, where an evacuated, sealed tube was not used for the preparation of Zr, cannot be classified as crystalline Zr and was probably a mixture of different Zr-intermetallics [5].

2.1.3.2. Reduction of $ZrCl_4$ with Na or Al

Troost prepared impure Zr by the reduction of gaseous $ZrCl_4$ with magnesium or sodium in 1865, and in doing so was the first to use the tetrachloride salt as the source of Zr [2, 5, 11]. By passing the $ZrCl_4$ vapour over the red-hot metals, an amorphous product was yet again formed. However, by using heated aluminium instead, he obtained a sponge that consisted of a crystalline top-layer [2].

Lely and Hamburger were the first to prepare Zr-metal with an appreciable purity by heating the resublimed tetrachloride with sodium in a sealed bomb in 1914 [2, 5, 11]. Malleable pellets were produced by this method that could be rolled into rods. However, using the technique of Lely and Hamburger, it was found that calcium or magnesium could also be used, where magnesium presented a satisfactory alternative because of the ease of manufacturing and maintaining it in an oxygen-free form [5].

2.1.3.3. The Thermite process

The Thermite Process of Goldschmidt and Vautin has also been used to prepare Zr via zirconia according to the reaction [2, 5]:

$$3ZrO_2 + 4Al \longrightarrow 2Al_2O_3 + 3Zr \qquad (2.6)$$

The main problem of this process however was that the product consisted of a mixture of unreduced zirconia and alumina and zirconium-aluminium alloys, from which the Zr-metal could not easily be isolated. According to Weiss and Neumann [2], there is not sufficient difference between the heats of formation of zirconia and alumina to give efficient conversion by the thermite process.

In general, the reduction of ZrO_2 is technically difficult due to the formation of ZrO intermetallics at the high temperatures used for the reduction reaction, where oxygen has an appreciable solubility in Zr. Zirconium containing only 0.7 % dissolved oxygen or higher causes the metal to be brittle which impairs its use as a structural material [1, 5]. Therefore, the use of oxygen-free compounds such as the tetrahalides has found the most widespread application.

2.1.3.4. The Iodide Process

The first real success in the preparation of ductile Zr-metal came in 1925 when van Arkel and de Boer used the pyrolysis of ZrI_4, which presented a practical method for Zr-reduction [1, 5, 8, 11]. They recognized that ZrI_4 vapour dissociates to a larger extent than the chloride or bromide at a given temperature, and could therefore be used for the pyrolytic preparation of the metal. Furthermore, at the operating temperature, Zr-metal exists as a solid and its vapour pressure is less than its partial pressure when in the gaseous form [5], thereby facilitating the convenient separation of the deposited metal from the iodide vapours. At first, van Arkel and de Boer heated a tungsten filament to 2000 °C in the presence of ZrI_4 vapour that was contained in a chamber that was maintained at 650 °C. As a result, extremely pure Zr-metal is deposited after a few hours, the reaction of which is given below.

$$ZrI_4 \xrightarrow{1200 - 1400\ ^\circ C} Zr + 2I_2 \qquad (2.7)$$

In due course, they determined that the filament temperature only needs to be between 1200 and 1300 °C with a chamber temperature of 340 °C, since a tungsten-zirconium alloy can form above 1800 °C causing the filament to melt [5].In one modification of the method, crude zirconium metal (either powder or sponge) that was prepared by another process was loaded into an evacuated chamber with a specific amount of iodine, which upon heating caused the iodine vapours to react with the Zr-metal, thus producing ZrI_4 vapours [8]:

$$Zr + 2I_2 \xrightarrow{200\,°C} ZrI_4 \qquad (2.8)$$

It was found that a Zr-filament could also be used, where the liberated iodine could again bind with the crude zirconium until all of the zirconium from the raw material is deposited onto the filament [5].

The product produced by this method contains very little carbon, oxygen and nitrogen impurities which are not transferred from the crude product during the formation of ZrI_4. It does however contain some metallic impurities such as titanium and aluminium [5, 8, 11]. Furthermore, this method is very expensive and economically inefficient because only small quantities of Zr can be produced [11].

2.1.3.5. The Kroll Process

Since its development by Dr. Kroll and co-workers at the U.S. Bureau of Mines in the 1940's, the Kroll process has been the most successful method for the production of Zr-metal suitable as a construction material in nuclear reactors. The process basically consists of the reduction of gaseous $ZrCl_4$ with molten magnesium in an inert atmosphere [1, 3, 4, 8, 11]:

$$ZrCl_4(g) + 2Mg(l) \xrightarrow{825\text{-}875\,°C} Zr(s) + 2MgCl_2(l) \qquad (2.9)$$

The use of gaseous $ZrCl_4$ was crucial for the successful development of the process [11], which prevents the incorporation of oxygen into the Zr-metal. Oxygen originates from the formation of the oxychloride, $ZrOCl_2$ due to hydrolysis of $ZrCl_4$ when it comes into contact with the moisture in the air [11]. Therefore, suitable equipment was needed to bring the $ZrCl_4$ vapour into contact with the molten magnesium, wherein the whole system is kept under a

helium or argon atmosphere to limit the hydrolysis reaction of the tetrachloride. Detailed information on the equipment used, and various modifications of the process that exists can be found in the review of Stephens [11].

The reduction by the Kroll process is a batch-wise opperation, and consists of the following basic steps [1, 4, 8]:

- *Sublimation of $ZrCl_4$.* Hf-purified $ZrCl_4$ is heated to gaseous $ZrCl_4$ in an inert atmosphere. This removes the $ZrCl_4$ from the oxychloride formed by partial hydrolysis, but also any other non-volatile impurities.
- *Reduction of gaseous $ZrCl_4$.* The $ZrCl_4$ vapours are brought into contact with an excess amount of molten magnesium, also in an inert atmosphere, whereby solid Zr-sponge is formed together with molten $MgCl_2$ and unreacted Mg.
- *Separation of reaction products.* The product mixture is heated to approximately 925 °C under vacuum, wherein the liquid $MgCl_2$ is removed from the inverted container by drainage while Mg is removed by distillation, leaving a highly reactive and porous Zr-sponge.
- *Conditioning.* The hot sponge is cooled under an inert atmosphere to prevent reaction with oxygen. The sponge is then compacted using arc melting, in an inert atmosphere.

Ultrapure zirconium metal, for research purposes, can be obtained by further purifying the metal obtained from the Kroll process by the Iodide process [1], which can also be used to purify Hf that can also be produced by the Kroll process [3].

2.1.4. Zirconium–Hafnium Separation Methods

Although the purification of Zr (i.e. separation of Hf from Zr) to produce nuclear grade Zr(IV) occurs before the reduction step, the subject is treated separately to emphasize its importance in the production of nuclear grade zirconium metal. As explained in Section 1.1, the separation of Zr and Hf is particularly difficult due to their chemical similarities. In fact, the level of difficulty associated with separating the two different elements has been compared to the separation of two isotopes of the same element [11]. Many different separation techniques have been developed, although only a handful of these have been successfully applied on an industrial scale. In this section, an overview of some of the most successful separation methods is presented. Other separation methods that have been investigated recently by Poriel

et al. are ion exchange using anion exchange resins [12], and ligand-enhanced separation by nanofiltration [13], in addition to many other techniques that have also been proposed and tested, for example fractional sublimation [4] and liquid-vapour distillation [14]. The different separation methods that will be discussed in this section are:

- solvent (or liquid-liquid) extraction:
    - the MIBK process,
    - the TBP process, and
    - ammine extraction
- the CEZUS extractive distillation process, and
- the preferential reduction of zirconium tetrachloride.

Solvent extraction separation methods can be categorized as an aqueous separation method, because they rely on the use of an aqueous phase that serves as the substrate for the Zr-Hf salt mixture. Anhydrous separation methods such as the CEZUS process, preferential reduction and fractional sublimation are however attractive alternatives from an economic point of view. This is because the separation by aqueous routes often produces zirconia that needs to be rechlorinated to produce the zirconium-metal by the Kroll process for example. The use of aqueous separation methods are therefore inefficient with respect to the overall process cost and energy requirements. A detailed overview of different anhydrous separation techniques can be found in the review of Skaggs et. al. [4].

For the aqueous separation methods, the aqueous chemistry of Zr and Hf, including speciation, plays an important role in the separation mechanisms, such as the extraction equilibria for solvent extraction methods. Because speciation studies were not conducted in this study, a detailed discussion will not be presented here. However, some information on the speciation of Zr(IV) and Hf(IV) in aqueous media may be found in references [15 - 20].

2.1.4.1. Solvent Extraction Methods

Despite the shortcomings of the aqueous separation methods, solvent extraction has been one of the most successful methods used for Zr-Hf separation, especially the MIBK process.

2.1.4.1.A. The MIBK Process

This process was originally developed by Union Carbide, where methylisobutyl ketone (MIBK) serves as the organic extractant. The process has the following steps [1, 3, 11, 21, 22]:

- Impure $Zr(Hf)Cl_4$ is dissolved in an aqueous solution whereby the tetrachlorides are converted to the oxychlorides, $Zr(Hf)OCl_2$.
- An initial extraction is performed in which the oxychloride solution is purified from ferrous impurities by extraction with MIBK.
- The purified aqueous solution is mixed with NH_4SCN and NH_4OH which causes the formation of zirconyl and hafnyl thiocyanate, i.e. $Zr(Hf)O(SCN)_2$, which forms the feed solution.
- By liquid-liquid extraction in a series of countercurrent stages with MIBK as the organic phase, $HfO(SCN)_2$ is extracted preferentially from the aqueous phase.
- The Zr-enriched aqueous solution is treated with sulphuric acid whereby pentazirconyl sulphate, $[Zr_5O_8(SO_4)_2.XH_2O]$, is precipitated by adjusting the pH using NH_4OH, which is filtered and washed. Treatment of the aqueous solution with HCl first, to produce $ZrOCl_2$ before treatment with H_2SO_4, is also possible.
- The sulphate is then either calcined to produce zirconia, or is mixed with an ammonia solution to form $Zr(OH)_4$ which is refiltered, rinsed and calcined to form the oxide.

The MIBK process does however suffer from some drawbacks, of which the inherent production of large quantities of toxic by-products and unpleasant odours that requires treatment to minimize pollution [21, 22, 23] seems to be the most severe. The solvent (MIBK) is also highly volatile and explosive and is only marginally soluble in water. Takahashi et al. reported that the use of the MIBK process by Nippon Mining Co., Ltd. resulted in the following problems [23]:

- High operation cost because of the consumption of expensive chemicals. This was related to problems associated with the decomposition of the thiocyanate and thiocyanic acid, as well as by the degradation of MIBK.
- High cost of equipment maintenance because of the corrosion caused by acids and the organic solvent.

To combat these shortcomings, Nippon Mining Co., Ltd. developed a different solvent extraction process in which zirconium oxysulphate is extracted by a high-molecular alkyl amine [23].

The use of the MIBK process does offer some advantages [22]. Since Hf is in effect stripped from the desired component, Zr, efficient separation can be attained which enables the production of both Zr and Hf according to nuclear specifications. MIBK also has a high load capacity and excellent settling characteristics which is advantageous when using a mixer-settler type solvent extraction setup.

2.1.4.1.B. The TBP Process

As mentioned previously, the feed for the TBP process can be obtained by dissolving the washed product of the caustic fusion of zircon in nitric acid [11]. Zirconium is selectively extracted from the acidic aqueous phase using a 50 % solution of tributyl phosphate (TBP) in n-heptane or kerosene as the organic phase. $NaNO_3$ is added to the HNO_3 aqueous solution, which acts as a salting-out agent [1, 11, 22]. Most other impurities remain in the aqueous phase together with Hf(IV). Zirconium is recovered from the organic solvent by stripping with deionized water, while the Hf leaves the process in the aqueous stream. Nitric acid is recycled from both metal streams by distillation, and the solutions are neutralized to precipitate the hydrates. The hydroxides are then calcined to yield the oxides [11].

In contrast to the MIBK process, Zr is selectively extracted by the organic solvent whereby high-purity Zr(IV) can be produced, which does not need any further purification [1]. Production of Hf(IV) with a low Zr-content is difficult from a practical standpoint [4, 11, 22]. Other disadvantages include the constrictions with respect to the low metal concentrations attainable in both phases, and the high consumption rates of chemicals. This ultimately led to companies both in the U.S.A and France abandoning the TBP process.

2.1.4.1.C. Ammine Extraction

As mentioned in Section 2.1.4.1.A, Takahashi et al. used a solvent extraction process by using a high-molecular alkyl amine to replace the MIBK process [23]. Their process comprised of the following steps:

- The feed was prepared by sulphuric acid digestion of sodium zirconate, produced by the caustic fusion of zircon. This results in the formation of the zirconium and hafnium oxysulphates that are soluble in water.
- The organic phase was prepared using a mixture of tri-*n*-octyl amine, which serves as the extractant, which is diluted in tridecanol and *n*-paraffin that has been saturated with sulphuric acid.
- Extraction was carried out countercurrently using a mixer-settler setup whereby the zirconium fraction is selectively extracted by an anionic exchange mechanism. The selectivity is influenced by the pH of the aqueous solution.
- The Hf-content in the organic solvent is reduced by an additional scrubbing section where the organic solvent is contacted with an aqueous scrubbing solution.
- Zr(IV) is recovered from the organic solvent using a NaCl aqueous strip solution. The resulting chloride amine is regenerated to the free amine by neutralization with Na_2CO_3.
- The Zr(IV)-enriched aqueous solution is neutralized with NaOH resulting in the precipitation of $Zr(OH)_4$, which is filtered and washed with water to eliminate the sulphate salt from the precipitate.
- The hydroxide precipitate is calcined at 850 °C to form pure zirconia.

The process has the advantage that most of the trace-element impurities that are associated with the Zr/Hf feed are also separated from zirconium except for uranium that is co-extracted. It was found that this could be avoided using a pre-extraction stage before the bulk Zr-extraction is performed.

Recently, Poriel et al. [24] studied the extraction of Zr and Hf from aqueous HCl solutions using Aliquat 336, a quaternary amine, with respect to different variables such as the influence of the HCl concentration, the Aliquat 336 concentration, and different diluents. The experimental studies were conducted using $Zr(Hf)Cl_4$ that was diluted in hydrochloric acid solutions of varying concentration. The organic phase consisted of the quaternary amine with different concentrations that was dissolved in different organic solvents, or diluents. Using Aliquat 336, Zr is preferably extracted via an anionic exchange mechanism, in which the separation efficiency is influenced by the HCl concentration. This may be due to the inhibition of hydrolysis reactions at the high HCl concentrations that were found to improve both the

extraction and separation efficiency. An increase in the Aliquat concentration resulted in an improved extraction and separation efficiency, while toluene exhibited the most favourable solvent characteristics. Based on these results, Poriel et al. concluded that it is possible to apply this system for the separation of Zr and Hf, provided that the tetrachlorides are dissolved in aqueous HCl with a high concentration to prevent the formation of polynuclear hydroxo-bridged compounds that hamper the extraction equilibrium.

Other studies have shown that primary, secondary and tertiary amines can also be used for the separation of Zr and Hf by solvent extraction using HCl aqueous solutions [1]. Reportedly, the selectivity of the amines is in the order tertiary > secondary > primary.

2.1.4.2. The CEZUS Extractive Distillation Process

To combat the disadvantages of the MIBK process, the CEZUS process was developed wherein extractive distillation of the tetrachlorides is performed at atmospheric pressure using molten potassium chloride – aluminium chloride ($KCl\text{-}AlCl_3$) as the solvent [1, 21]. The process consists of the following steps [3, 4, 21, 22]:

- $Zr(Hf)Cl_4$ is first purified from trace-element impurities by sublimation.
- The $Zr(Hf)Cl_4$ mixture is continuously fed near the middle of a separating column wherein the molten solvent circulates from top to bottom in the column, which is maintained at 350 °C.
- Tetrachloride vapours are produced at about 500 °C in a boiler that is situated at the bottom of the separating column. The vapours rise and countercurrently contacted with the $KCl\text{-}AlCl_3$ solution which becomes saturated with $ZrCl_4$ and $HfCl_4$ during a continuous run.
- The rising vapour is steadily enriched with $HfCl_4$ whereby the solvent stream is depleted of the impurity.
- The Zr(IV)-enriched solvent is passed to a stripping column where the $ZrCl_4$ is completely recovered. Nitrogen is used to strip and transport the $ZrCl_4$ to a condenser where solid $ZrCl_4$ is produced.
- The solvent, which has been stripped of $ZrCl_4$, is recycled and fed to an absorber-condenser where a large fraction of the $HfCl_4$-enriched vapours are dissolved. The fraction of vapours that are not dissolved are condensed by cooling.

- This Hf(IV) enriched product is then reprocessed using the same method, with some adjustments, to produce pure $HfCl_4$.
- The $ZrCl_4$ produced during the first cycle can be used directly in the Kroll process to produce Zr-sponge.

Although the need for a second chlorination stage is eliminated during the use of the CEZUS process (purified $ZrCl_4$ is produced directly), the energy requirements are equivalent to that of the MIBK process in which rechlorination is required [21]. This is because of the high temperatures needed for the CEZUS process. The process also requires corrosion resistant alloys and complicated process technologies to avoid moisture contamination of the vapour streams [22]. However, this process does offer other advantages, including [4, 21]:

- the fact that distillation is performed at atmospheric pressure, which is permitted by the use of the molten salt mixture, as opposed to the high-pressure liquid-vapour distillation of $Zr(Hf)Cl_4$,
- no hazardous organic solvents are used,
- consequently no by-products are produced, and
- purified $ZrCl_4$ can be produced with improved yield, due to a reduction in the required number of stages.

2.1.4.3. Preferential Reduction of Zirconium Tetrachloride

In the review of Skaggs et al. [4], where sixteen different anhydrous Zr-Hf separation methods were reviewed, the preferential reduction of $ZrCl_4$, a purely chemical separation method, was identified as one of the most promising separation methods. In 1957, Newham pioneered this method by observing that the reduction of $ZrCl_4$ to the trichloride is thermodynamically favoured over that of $HfCl_4$ [4, 8]. This can be illustrated by the following reaction in which the Gibbs free energy change is about -92 $kJ.mol^{-1}$:

$$HfCl_3(s) + ZrCl_4(g) \xrightarrow{427\,^{\circ}C} HfCl_4(g) + ZrCl_3(s) \qquad (2.10)$$

Zr-metal is preferred as the reducing agent because no impurities are introduced into the system, although other reducing agents can also be used. The resulting tetrachloride remains in condensed form whereas the more volatile $HfCl_4$ and unreacted $ZrCl_4$ remain in the gaseous

form. This greatly increases, the separation efficiency in comparison with a fractional sublimation process that only uses the slight differences in the volatilities of $ZrCl_4$ and $HfCl_4$ [4].

The tetrachloride may be recovered, for use in the Kroll process for example, by heating the trichloride to about 460 °C which causes the trichloride to disproportionate by a series of complicated reactions that can be summarized as [4]:

$$2ZrCl_3(s) \xrightarrow{460\,^{\circ}C} ZrCl_2(s) + ZrCl_4(g) \qquad (2.11)$$

$ZrCl_2$ produced by the disproportionation reactions can be recycled and used as a reducing agent instead of the Zr-metal. Newham later modified the method to perform the reduction in a molten salt mixture of $AlCl_3$-NaCl or LiCl-KCl that maintains the optimum temperature required for selective reduction [4]. Other modifications have been developed by Larson and Mauser to combat one major problem of the solid-gas reaction; i.e. that a $ZrCl_3$ coating forms around the metallic reductant which quenches the reduction reaction [4]. Frampton and Feldman also studied the process and reported a three-stage separation process [4], although no evidence could be found to date that this method has been adopted on an industrial scale.

2.1.5. Plasma Dissociation of Zircon and Fluorochemical Processing

Following the above discussion, it is clear that processing of zircon to produce Hf-purified Zr has been dominated by chloride technologies. Plasma dissociation of zircon to produce chemically amenable plasma dissociated zircon (PDZ), which was developed by Necsa [7], is a novel alternative for the beneficiation of zircon. Various chemicals can be produced via the reaction of the more chemically reactive PDZ with digestive agents, which will normally be ineffective against the inert zircon. In particular, fluorochemical processing may be applied for beneficiation, purification and production of nuclear grade Zr.

2.1.5.1. Plasma Dissociation of Zircon

Above 1650 °C zircon can be thermally dissociated, to form a zirconia and a silica phase that recombines during slow cooling [1, 8, 25]. However, by allowing particulate zircon particles to free-fall through the heating zone of a plasma furnace, with immediate, subsequent

quenching yields PDZ [1, 7, 25]. During this process, submicron zirconia particles are formed that are embedded in an amorphous silica matrix [25]. Consequently, the plasma dissociated zircon is designated by the formula $ZrO_2.SiO_2$ [7, 25].

Subsequently, the inventors of the process documented two different processing routes using HF as reagent. In the gaseous route, PDZ can be reacted with gaseous (anhydrous) HF, at a specific temperature, whereby the raw material is effectively desilicated [25]:

$$ZrO_2.SiO_2 + 4HF \longrightarrow ZrO_2 + SiF_4 + 2H_2O \qquad (2.12)$$

The gaseous SiF_4 formed can be easily separated from the solid zirconia and re-processed to recover HF. The Zr-component may however also be fluorinated by accurately controlling the temperature of the reaction, which can then be expressed as [25]:

$$ZrO_2.SiO_2 + 8HF \longrightarrow ZrF_4 + SiF_4 + 4H_2O \qquad (2.13)$$

Zirconium tetrafluoride is easily separated from the more volatile SiF_4 and may be purified by sublimation.

In the aqueous route, PDZ can be dissolved in 40 % HF according to [7, 25]:

$$ZrO_2.SiO_2 + 12HF \longrightarrow H_2ZrF_6 + H_2SiF_6 + 4H_2O \qquad (2.14)$$

In addition to H_2ZrF_6, the formation of $ZrF_4.2HF.xH_2O$, with x = 0 to 5, H_2ZrOF_4 and/or hydrates thereof may also form. The reaction products, H_2ZrF_6 and H_2SiF_6 are soluble in aqueous HF and can be separated from undissociated zircon and poorly soluble trace impurities such as U, Th, Ti, Al and Ca [7, 25]. This method therefore provides an effective means of removing these trace element impurities that accompany Zr and Hf in zircon. After removing H_2SiF_6 from the solution by distillation, the H_2ZrF_6 solution can be further purified by ion exchange.

$K_2Zr(Hf)F_6$, which can be produced from PDZ using the aqueous route by reaction of H_2ZrF_6 with KOH or KF, could be used as a possible intermediate product for the separation of Zr

and Hf by fractional crystallization, for example. This route is illustrated in Fig. 2.1, along with a summary of the most prominent processing routes as discussed in Sections 2.1.2 to 2.1.4.

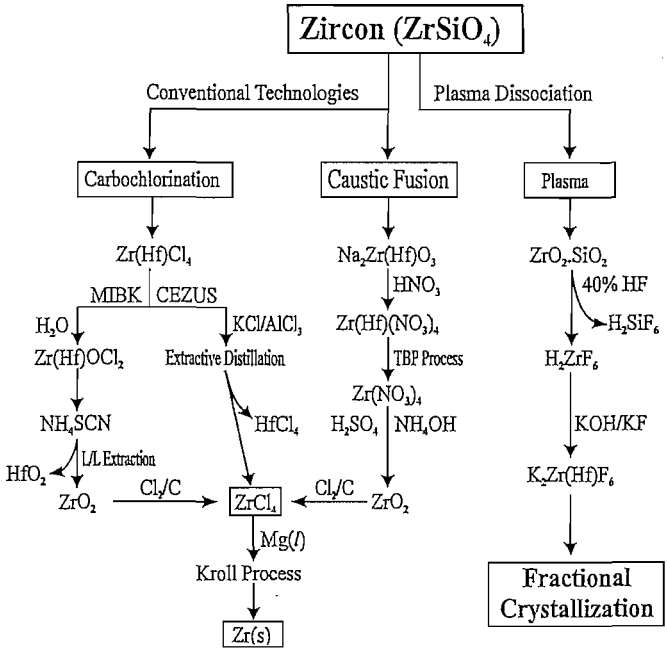

Figure 2.1: Schematic illustration of various routes for zircon beneficiation and Zr-Hf separation, including the possible alternative of plasma dissociation of zircon, processing via an aqueous fluorochemical route and separation via fractional crystallization of $K_2Zr(Hf)F_6$.

2.1.5.2. Fractional Crystallization of $K_2Zr(Hf)F_6$

Fractional crystallization of $K_2Zr(Hf)F_6$ was the first method used by Coster and von Hevesy [3, 8, 10, 26] for the separation of Zr and Hf, although the method entailed a tedious recrystallization procedure. They reported that the ammonium hexafluorometallates of Zr and Hf, which have higher solubilities than the potassium salts although the potassium salts have a larger difference in solubility, could also be used during fractional crystallization [26]. It was shown that the Hf-salts have a higher solubility than the Zr-salts, thereby facilitating

separation by the slightly higher tendency of Zr to crystallize upon cooling from a warm unsaturated solution.

In their studies, they used a fusion reaction between a commercially obtained oxide of Zr (most probably baddeleyite, i.e. the zirconia mineral), and a mixture of KF and HF [10] to produce $K_2Zr(Hf)F_6$. However, they also reported the use of another method in which baddeleyite was first dissolved with HF, before KF was added to the solution to furnish $K_2Zr(Hf)F_6$. It is assumed that both methods were applied to produce the ammonium salts, which was also used for fractional crystallization studies. Using the potassium salt obtained by these methods, they stated that fractional crystallization can then be performed from aqueous solutions of HF, or a mixture of HF and KF [10].

Using the ammonium salts, due to their higher solubilities, von Hevesy [26], reported that after a large number of recrystallizations, a total of 300 g of the Hf-enriched salt that was divided in multiple fractions of different concentrations, was obtained from an initial 2 kg of the impure salt. Using various other operations, pure Hf was obtained that was used for its atomic weight determination.

In the former Soviet Union, Sajin et al. [9, 27] used fractional crystallization of $K_2Zr(Hf)F_6$, and subsequent precipitation to produce pure ZrO_2. In their method, they used only deionised water as solvent, where $K_2Zr(Hf)F_6$ was prepared by the fluorosilicate fusion of zircon. They were able to produce purified Zr(IV) using approximately 16 recrystallization steps, where cooling was applied to effect crystallization. As a result of the large number of crystallizations, a poor yield (10 %) of the initial raw material was obtained. By reprocessing the resulting mother liquors, they were able to obtain an increased product yield of 80 %. This was done by successively recrystallizing $K_2Zr(Hf)F_6$, where deionised water was used in the initial stages of the process. The resulting mother liquors obtained from the first two stages were discarded. In subsequent steps, the crystals produced in one stage were dissolved using the mother liquor obtained from the previous stage. $K_2Zr(Hf)F_6$ was thus crystallized from mother solutions of decreasing Hf-content. Deionised water was again used as solvent in the final two stages of the process. The mother liquors obtained from the first two stages were concentrated by evaporation whereby a Hf(IV)-enriched hydroxide was precipitated using an ammonia solution. From this product, enriched HfO_2 obtained by ion exchange [9, 27].

Zirconium hydroxide was also precipitated from a solution of purified K_2ZrF_6 using a 25 % ammonia solution, which was subjected to calcination to produce purified ZrO_2.

Despite the abovementioned examples where fractional crystallization of $K_2Zr(Hf)F_6$ was used for Zr-Hf separation, there is little literature information regarding this technique and whether or not it was ever commercialized is uncertain. Therefore, as explained in Chapter 1, fractional crystallization of $K_2Zr(Hf)F_6$ was investigated further in this study. Subsequently, the fundamental principles of crystallization are discussed in next section of this chapter.

2.2. Crystallization

Crystallization can be described as the formation of a solid crystalline phase from a solution whereby the resulting two phases can be separated by mechanical means, to obtain (in most cases) the desired crystalline product. The solution can be a mixture of two or more compounds that form a homogeneous phase and can be liquids, gasses and even solids [28]. Therefore, one can distinguish between crystallization from solution, which involves the crystallization of a dissolved substance from a liquid solvent, and melt crystallization which refers to the solidification of a compound from a homogeneous molten liquid (the melt). A third possibility is the formation of crystals from a gaseous phase; however this case is beyond the scope of this study and therefore only the first two cases, the underlying principles of which are similar, will be considered. However, because crystallization from solution presents a more general case and because this is the method employed in fractional crystallization of $K_2Zr(Hf)F_6$, the fundamental principles involved in crystallization will be discussed using this general case.

As a unit operation, crystallization can be used to achieve different objectives, where separation and purification is often the most desirable. The objective is usually to obtain a pure product, or to enhance the purity of a compound by crystallization from a relatively impure solution. An advantage is that the energy requirements of crystallization processes are often less than those required for conventional separation processes, such as distillation. Furthermore, it can be performed under mild temperature and pressure conditions as is the case in crystallization from solution [29]. In addition to separation and purification, other functions that can be achieved by crystallization are concentration and solidification [30]. Crystallization can for example be used to concentrate solutions with a low solute

concentration by freeze crystallization of the solvent, as is done in the production of fruit juice [30]. It may also be desirable to obtain a product in crystalline form for convenient storage and transportation, for example in the pharmaceutical industry where in many cases the product is required to be crystalline. Moreover, for the determination of molecular structure, various analytical procedures (for example XRD) require that an unknown compound is crystalline.

A sound understanding of the underlying phenomena that govern the crystallization process is essential for the effective application of the technique in its many different forms. Since it is not possible to discuss every aspect involved in crystallization in detail in this chapter, the discussion will be focused on the principle of supersaturation – the driving force of crystallization, a brief discussion of the kinetics of crystallization, and some of the factors that influence the separation efficiency of a crystallization process. More detailed information on the different aspects of crystallization such as phase equilibria, and nucleation and growth theories (which will be discussed only briefly in this chapter), can be found in the cited literature.

2.2.1. Crystal Structures

Since crystallization is about crystals, the classification of crystal systems, i.e. the science of crystallography, has to be considered more closely

2.2.1.1. The Unit Cell

Crystals consist of an array of three dimensional, regularly repeating ordered units, and the external shape (morphology) of crystals is largely dependent on this internal order [31]. These ordered units are called unit cells and are the elementary volumes that contain the atoms or molecules of a crystal in a periodic pattern that is unique to each crystalline solid.

The unit cell geometry can be classified into one of seven basic crystals systems [31 - 33]:

- cubic,
- tetragonal,
- rhombic,
- monoclinic,

- triclinic,
- hexagonal, and
- rhombohedral.

These seven basic crystal systems are sets of reference axes, labelled **a**, **b**, and **c**, called basis vectors which define the elementary volume that form the unit cell [31, 32]. The basis vectors **a**, **b**, and **c** (Fig. 2.2) correspond to the *x*, *y*, *z* crystallographic axes respectively with the angles α, β, and γ, that lie between them, with α opposing **a**, β opposing **b**, and γ opposing **c**.

The axis lengths define the relative lengths of the unit cell sides, and the absolute lengths, written a, b and c, can be determined by diffraction techniques which together with the angles α, β, and γ yield the lattice parameters of the unit cell [31]. A crystal is build by translational displacement of the unit cell in three dimensions without any rotational or orientational operations. One can then qualitatively state that the growth rate of individual crystal faces depends on the rate at which the unit cells are stacked in different directions. This differential stacking rate causes different faces of the crystal to become emphasized, while others are suppressed leading to different external crystal morphologies that can be produced. The rate at which different faces propagate outward, which in turn determines the external shape of a crystal, is therefore partly dependent on the crystal structure, as described by the BFDH law (Section 2.2.3.2.A). The crystal morphology can however also be influenced by external factors such as the adsorption of additives or impurities onto growing crystal faces that have to be desorbed or overgrown before growth can proceed [34]. The resulting external shape of a crystal is commonly known as the "habit" of the crystal. Here, a distinction should be made between crystal morphology and polymorphism. With the modification of the crystal morphology relative to the equilibrium or ideal morphology by the growth conditions, the internal crystal structure remains unchanged. However, some substances have the ability to crystallize in different crystal structures but with the same chemical composition [33, 35, 36], which is referred to as polymorphism.

2.2.1.3. The Description of Crystal Structures

In Section 2.2.1.1, we have seen that the unit cell acts as the basic "building blocks" of crystals. To describe specific crystal structures, the positions of all the atoms in the unit cell must also be specified in addition to the unit cell type and parameters.

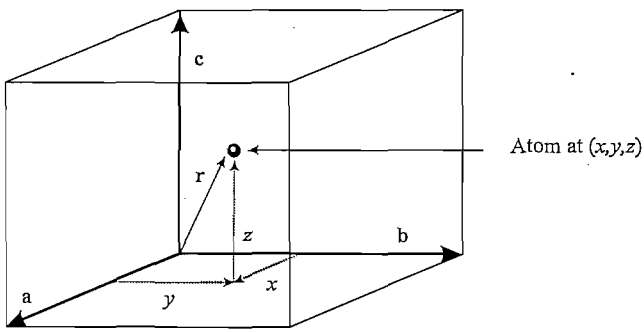

Figure 2.2: Specification of the position of an atom in terms of the unit cell basis vectors. Adapted from [31].

This is conveniently done in terms of fractional coordinates, which is to say the positions of the atoms are given in terms of the fractions of the vectors **a**, **b**, and **c**. The position of an atom (Fig. 2.2) can then be expressed by a vector **r** as [31]:

$$\mathbf{r} = x\mathbf{a} + y\mathbf{b} + z\mathbf{c} \tag{2.15}$$

2.2.1.3.A. Lattices and Symmetry

Due to the complexity of some systems (Section 2.2.1.1), the amount of information needed to specify crystal structures can be greatly reduced by using the concept of symmetry. This requires that a distinction is made between crystal structures and lattices [31]:

- A crystal structure is build from atoms that can form molecules or ion pairs.
- A lattice is a mathematical concept where single atoms or groups of atoms are taken collectively as lattice points.

In combination with the seven basic crystal systems, 14 possible three dimensional lattices can be obtained which are known as the Bravais lattices (Fig. 2.3) [31 - 33, 37].

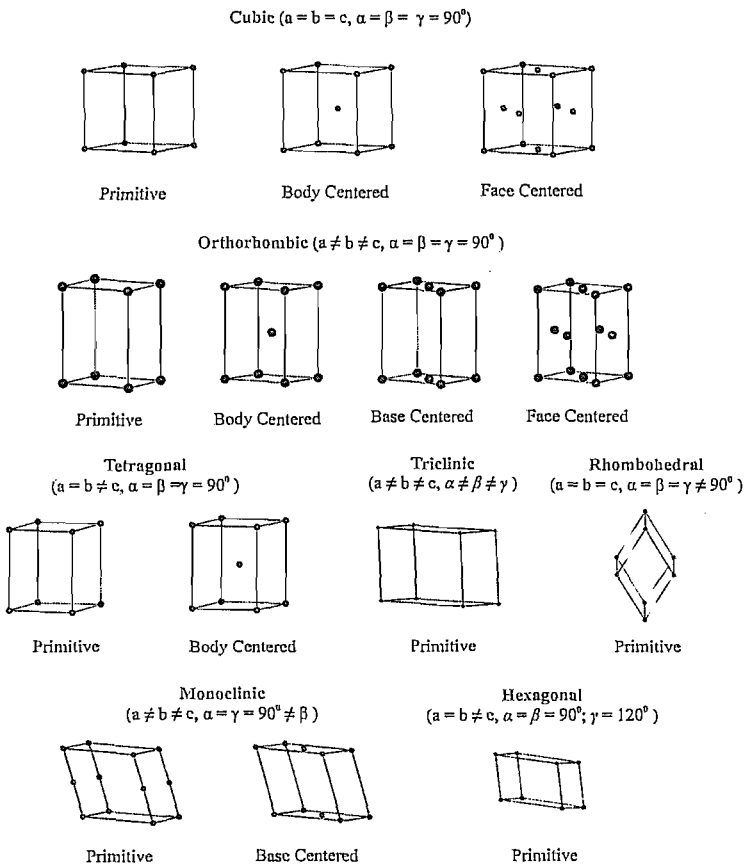

Figure 2.3: The 14 Bravais lattices. Images were drawn using the Materials Studio Modelling Environment [38].

Lattices that have lattice points only on the corners of the unit cell are called primitive, and these lattice points can be chosen for convenience according to the symmetry of the specific lattice. More information on the other types of Bravais lattices are given in Fig. 2.3.

The transformation of an object (for example a unit cell) by some symmetry element, i.e. a mirror plane or a rotational axis that leaves the object unchanged after the transformation has been carried out (called a symmetry operation) characterizes the symmetry of the object. The combination of various symmetry elements that an object might possess is defined as the point group and is collected into the point group symbol [31]. In crystallography, the Hermann-Mauguin system is used to specify the point group symmetry. An alternative system that is mostly used to describe the symmetry of molecular structures is the Schoenflies system [31]. Usually however, the symmetry of a crystal structure is given in terms of both systems.

If the possible symmetry elements are restricted (for example the rotation axes) to those that are compatible with the crystallographic lattices (see references [31, 32] for more information), 32 possible point groups are obtained. Combining these 32 crystallographic point groups with the 14 Bravais lattices, and an additional symmetry element, the screw axis, allows all possible crystallographic patterns to be classified [31, 32]. The resulting 230 combinations are known as the crystallographic space groups. Any crystal structure will have a unit cell that conforms to one of the 230 space groups. However with variations in the chemical composition an infinite number of unique crystal structures can be obtained. Using this system all crystal structures can be described in a conveniently manageable way.

2.2.2. Phase Equilibria

2.2.2.1. Solutions and Solubility

During crystallization from solution, a solvent, which can be a mixture of miscible substances that maximizes the yield and quality of the crystallized product, is desirable. According to Mullin [39], a solvent should have the following properties:

- The solute should be readily soluble in the solvent.
- The solute should be easily deposited from the solution in the desired crystalline form after cooling, evaporation or salting out (see Section 2.2.2.2).
- Close similarity between the solute and solvent (for example in the case of organic compounds) should be avoided as their mutual solubility will probably be high and the crystallization process may become uneconomical.

In some cases a compromise must be found between different solvent properties to ensure the implementation of one or more important solvent properties. The solubility of a compound in a solvent is one of these important factors, which is determined by the maximum amount that is soluble at a specific temperature and pressure and system composition. However, for most systems, the change in solubility with pressure is small and can be neglected [29, 30, 33]. Solubility data of a pure compound in a liquid solvent can therefore be represented graphically as a function of temperature in a solubility diagram (see Fig. 2.4) which can aid in the decision of a suitable mode of crystallization for a particular system. For example, a small increase in solubility with temperature, i.e. a small positive slope, as is the case with NaCl for example [30], methods other than cooling, like evaporation, would be required to obtain a reasonable product yield.

Many different concentration units can be used to express the solubility of a substance in a solvent. These can be divided into [28, 33, 39]:

- volumetric units, for example $mol.m^{-3}$,
- units that are ratios of the mass (or moles) of the solute to the mass (or moles) of the solvent, and
- units that are ratios of the mass (or moles) of the solute to that of the solution.

To convert the first type, to the other types of units requires knowledge of the density as a function of temperature. For this reason mass ratios and mass fractions are usually the most convenient to use.

As shown above, solubility data can yield some information regarding the crystallization process. To gain a more complete understanding of the behaviour of a given system over a wider range of conditions, a phase diagram, of which the solubility diagram represents a small portion, can be used. As noted previously this aspect will not be treated here. More information on the subject can be found by consulting the following references [28, 30, 33, 39, - 41].

2.2.2.2. Supersaturation – The Driving Force of Crystallization

While the solubility and phase equilibria of compounds affect the crystallization process with respect to the yield, efficiency and purity, it does not provide any information regarding the

rate of crystallization. The rate of crystallization must depend on some driving force, and this driving force is the supersaturation [28]. In other words, the system must be in a higher energy state, or activated state, with respect to equilibrium conditions which "drives" the system back towards equilibrium using the energy for nucleation and growth thereby relieving the supersaturation. The degree of supersaturation greatly influences the crystallization kinetics, i.e. the processes of nucleation and growth (Section 2.2.3) [42, 43].

Supersaturation, in which the concentration of a solute exceeds the equilibrium solubility of the solute in a solvent, which will be described more clearly in the subsequent sections, can be achieved in the following ways [28, 33, 43]:

- *Temperature change*: For example, by cooling a solution in which the solute solubility increases with increasing temperature, or by heating a solution in which the solute solubility decreases with increasing temperature,
- *By evaporation*: This can be adiabatic evaporation where the solution cools as the solvent evaporates, due to the heat of vaporization under reduced pressure, often called evaporative cooling. It can also be by evaporating the solvent under heating,
- *Changing solvent composition*: For example, by adding a less efficient solvent that is miscible with the original solvent. This can also be achieved using a technique called salting out where the addition of other substances can cause the solubility of the crystallizing substance to decrease,
- *By chemical reaction*: A chemical reaction in a solution can lead to the formation of a poorly soluble crystalline substance, this is normally called precipitation.

2.2.2.2.A. Supersaturation and Metastability

The concept of supersaturation can be described using a solubility diagram of a hypothetical system illustrated in Fig. 2.4. When a solution with a solute concentration indicated by point A is cooled and reaches point B, it is saturated which corresponds with the solubility of the solute. When the solution is cooled further to point C, the concentration of the solute exceeds that of the equilibrium saturation and the solution is said to be supersaturated. However, spontaneous crystallization may not occur until the metastable limit is reached, point D [28, 30, 42, 43]. At this point, the solution is no longer stable and spontaneous crystallization takes place (see Section 2.2.3.1). Although the definition of the metastable limit is ill-defined [39], there is sufficient proof that an area of metastability exists above the solubility curve.

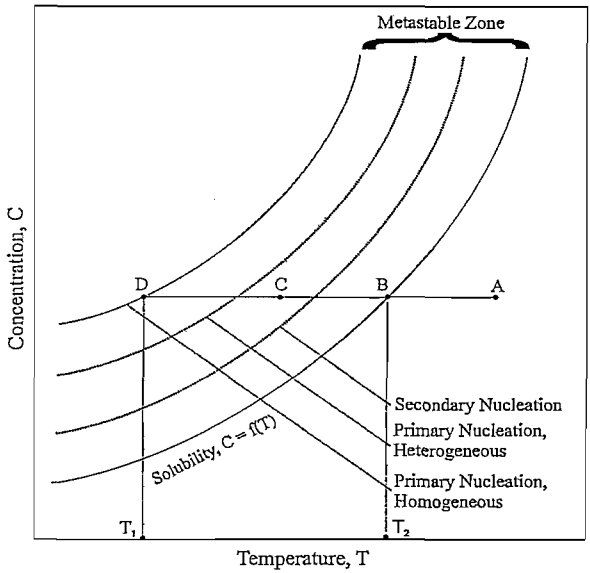

Figure 2.4: Metastability and supersaturation. Adapted from [45].

The area between the solubility curve and the maximum attainable supersaturation is called the metastable zone. The metastable zone width, or maximum attainable supersaturation can be characterized by the maximum attainable supercooling, i.e. $\Delta T = T_2 - T_1$ [43]. The additional information presented in Fig. 2.4 relates to Section 2.2.3.1.

2.2.2.2.B. Expressions of Supersaturation

Following the explanation of Fig. 2.4, the supersaturation can be defined in three ways. It can be expressed in terms of the deviation of the actual concentration from the equilibrium concentration, known as the concentration driving force [28, 33, 39, 43]:

$$\Delta c_i = c_i - x_i^{sat} \tag{2.16}$$

or as the relative supersaturation:

$$\sigma = \frac{c_i - x_i^{sat}}{x_i^{sat}} \tag{2.17}$$

or as the supersaturation ratio:

$$S = \frac{c_i}{x_i^{sat}} = \sigma - 1 \tag{2.18}$$

where c_i is the actual solution concentration and x_i^{sat} is the equilibrium concentration or solubility, where the symbol x_i^{sat} (instead of c_i^{sat} for example) is used to be consistent with other formulas that will be defined in later sections. Any suitable concentration units, as described in Section 2.2.2.1, can be used in the above equations. However, the numerical value of each of these expressions is dependent on the choice of units in which the concentration is given. This is because the more accurate expression of concentration is that of the activity of the solute and the above equations are therefore only an approximation [43]. Thermodynamic considerations can be used to obtain an exact expression of the supersaturation [28, 33, 43], however this aspect will not be treated here in further detail.

2.2.3. Crystallization Kinetics

The crystallization process can be divided into the formation of clusters, atoms, molecules or ion pars of the crystallizing substance, which is known as nucleation, and the growth of the nuclei to substantial sizes. It is therefore understandable that the kinetics of nucleation and growth can have large influences on product characteristics such as crystal size, morphology, and purity. In this section, the theoretical concepts of crystallization kinetics are briefly outlined to provide insight into the mechanisms of nucleation and growth.

2.2.3.1. Nucleation

Nucleation can occur through any of the following mechanisms [30, 39, 43, 44]:

- *Primary nucleation* which occurs in the absence of crystals of the crystallizing compound, and consists of:
    - *Homogeneous Nucleation.* This mechanism is dependant on the degree of supersaturation as indicated in Fig. 2.4. This is because an energy barrier

must be overcome for the formation of stable nuclei, which requires that the system is near, or exceeds, the metastable limit. This energy barrier is characterized by the Gibbs free energy change between the solute in solution and the nuclei; where its value determines the critical nuclei radius. The Gibbs free energy change, and consequently the critical nuclei radius decreases as the supersaturation increases, whereby the rate of homogeneous nucleation increases as the supersaturation increases [28, 39, 43, 45].

- *Heterogeneous Nucleation.* Primary nucleation may be catalyzed by foreign particles, such as dust, that can be introduced into supersaturated solutions unintentionally. These particles acts as heteronuclei which lowers the energy barrier for the formation of stable nuclei, due to adsorption of solute molecules onto the foreign particles, and therefore facilitates the formation of smaller nuclei. This also means that the required supersaturation is effectively lowered as indicated in Fig. 2.4 [30, 39, 43, - 45].

- *Secondary nucleation*, which occurs due to the presence of crystals of the crystallizing compound, where nuclei are formed at still lower supersaturation, as illustrated in Fig. 2.4, because the nuclei are no longer produced via the energy intensive phase transition but are produced from the already formed parent crystals of the crystallizing component. Secondary nuclei can be produced by the following mechanisms [30, 39, 43, 44, 46, - 48]:
  - *Apparent or initial breeding.* This mechanism occurs through the presence of small crystallites or "crystal dust" that is introduced into supersaturated solutions during seeding.
  - *Polycrystalline breeding.* At high supersaturation, crystals can start to agglomerate and polycrystalline growth can set in. The aggregates can then break up due to changes in supersaturation or via mechanical forces to give new crystals that can grow further.
  - *Dendritic breeding.* Dendritic growth can also occur when the supersaturation is sufficiently high. The needle-like structures can be broken off by hydrodynamic forces, or they can be detached from the bulk crystal by dendrite coarsening.

- *Fluid shear*. The formation of secondary nuclei by the fracture of dendrites or other macroscopic crystal features can be brought about by turbulent forces caused by the flow of the solution over the crystal surface. However, production of nuclei via this mechanism is believed to be negligible in comparison with breakage due to mechanical forces.
- *Collision breeding*. This mechanism is thought to be the most dominant, especially in stirred crystallizers. Collision breeding occurs due to collisions between crystals, or between crystals and the crystallizer walls or stirrer where small fragments are produced.

2.2.3.2. Crystal Growth

Once stable nuclei have formed in a supersaturated solution, growth can take place. The growth process, just like nucleation, also has a significant influence on the final crystal properties, including size, shape and purity. While no complete crystal growth theory exists, many different theories have been developed that attempt to describe a certain aspect of the growth process. Two main groups of theories can be distinguished:

- theories that describe crystal morphology, and
- theories that describe the kinetics of growth.

Some theories belonging to each of these two groups will be discussed shortly in the following sections to provide a holistic overview of the growth process.

2.2.3.2.A. Morphology Theories

The morphology of a crystal can be characterized by the different faces that enclose a given volume. As noted in Section 2.2.1.1, the different faces can experience different growth rates (which are measured as the rate of propagation in the direction perpendicular to the face), leading to some faces being emphasized with respect to other faces, which determines the morphology of the crystal [39, 49]. The relative growth rates of individual faces can be influenced by the solvent, impurities or additives that can be adsorbed on crystal faces thereby influencing the growth process. Temperature, and therefore the supersaturation, also influences the growth kinetics [34, 49 - 51]. The understanding and control of the morphology of crystals can be valuable, especially in industrial crystallization where the crystal

morphology can have economic impacts on the entire process, where it can influence the efficiency of different downstream processes such as the filterability of the crystals, caking, packing density, handling and storage, and dissolution rate [50 - 52].

Thus, control of the crystal morphology is important for process optimization. Different theories relating to the description of crystal morphology are listed below.

- *Surface Energy Theories.* In these theories, the influence of external factors on the crystal habit are not taken into account. The equilibrium habit (at slow growth rates) is thought to assume that for which the total surface energy is minimized [39, 43, 49, 50]. Crystal faces grow at rates proportional to their surface energy, where faces with a low surface energy grow at slower rates which results in large faces, and faces with a high surface energy grow faster resulting in smaller faces. Thus, a crystal face with a low surface energy will have a low growth rate resulting in a large surface area. These faces will dominate and will therefore have the highest morphological importance (MI).
- *The BFDH Law.* This law, which was named after its contributors Bravais, Friedel, Donnay and Harker, is based on the fact that the interplanar spacing, or repeat distance between crystallographic units (lattice points which can for example be atoms or molecules), varies between different faces which is related to the unit cell dimensions [49, 51, 52]. Those faces that have the largest interplanar spacing, d_{hkl} will also have the greatest morphological importance (MI), as the growth rate is inversely proportional to the interplanar spacing. This is because it takes longer for crystallographic units to be arranged one after another if they are far apart rather than if they were more closely spaced.
- *The Hartman Perdok (HP) Theory.* Because the bonding between atoms is not explicitly taken into account with the BFDH law, it may fail to accurately predict the morphology in some cases [49, 51]. Therefore, Hartman and Perdok related the growth of individual faces to the energy requirements associated with the formation, and attachment of chains of crystallographic units, with the periodicity of the lattice that forms at the interface of the crystal and bulk liquid and are attached to the crystal surface during growth [28, 49, 51, 52]. They called theses chains of crystallographic units Periodic Bond Chains (PBC's), and then proposed that the growth rate of different faces is proportional to the energy change upon attachment of a PBC.

Using the BFDH law and the HP-theory together with molecular modelling techniques, the influence of additives and impurities on the crystal morphology can be predicted [50, 51, 53, 54].

2.2.3.2.B. Kinetic Theories

The growth process is accompanied by different phenomena that have to occur before growth units from the supersaturated solution are build into the crystal. The main steps are [30, 34, 43, 55]:

- transport of growth units from the bulk supersaturated solution by volume diffusion and convection to the solid-liquid interface,
- transport of growth units over the crystal surface by surface diffusion towards an integration site, and
- incorporation into the crystal at the integration site.

The supersaturation is a fundamental requirement for each of these processes and the rate of crystal growth is governed by the slowest of these processes which is the rate limiting step. The ease of transport through the bulk solution is determined by the diffusivity of the growth units and is related to the concentration, and therefore the supersaturation, of the crystallizing component. The integration process can be hindered by adsorbed additives or impurities which must then be desorbed or overgrown for which a higher supersaturation is required [34].

The surface diffusion process is influenced by the microstructure, viz. the surface roughness of the growing crystal faces. The surface roughness can be described by the structural attributes of a crystal interface, in which the Kossel model is useful [49]. Accordingly, the crystal surface can be classified into regions that show different properties as illustrated in Fig. 2.5:

- flat surfaces or terraces that are atomically smooth,
- steps which forms a dividing barrier between terraces, and
- kink sites formed by incomplete regions on the steps.

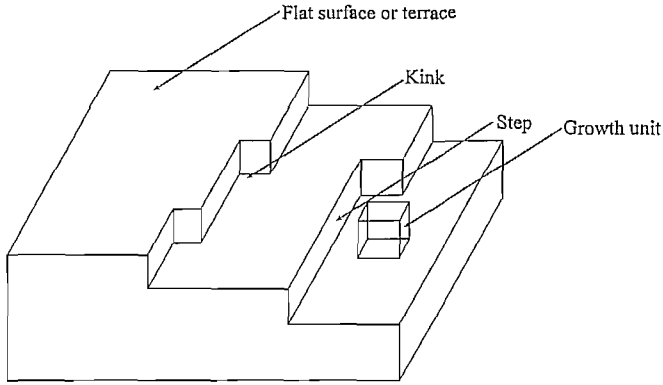

Figure 2.5: Kossel model of a growing crystal surface. Adapted from [34].

Steps and kink sites form a fundamental requirement for growth as the incorporation of growth units at kink sites are energetically favoured in comparison with a smooth surface due to the lowering of the required supersaturation [34, 43, 56]. Also, when more kink sites are available, less surface diffusion is necessary before growth units are incorporated into the crystal surface, thus leading to higher growth rates [49, 56]. The surface roughness is influenced by different factors including solubility of the crystallizing component, the degree of interaction between the solution and the crystal surface, and the temperature [56], which will not be discussed here in further detail.

Thus, energetically favourable surface sites must be present to facilitate the incorporation of growth units into the crystal surface whereby growth takes place. This requires a rough crystal surface with many step and kink sites. If this requirement is met, continuous growth can occur, even at low supersaturation, and volume diffusion becomes the rate limiting step [34], although the growth rate increases linearly with supersaturation. When the surface is not sufficiently rough, growth takes places either by the screw dislocation mechanism, the surface nucleation mechanism, or the spiral nucleation mechanism.

- *The BCF Screw Dislocation Mechanism.* At low supersaturation, energetically favoured integration sites can only be provided by the structural imperfections of crystals, i.e. by screw dislocations. Surface diffusion is the rate-limiting step for this mechanism and the growth rate changes from a quadratic dependence on

supersaturation to a linear dependence as the supersaturation is increased [34, 43, 49, 57 - 59].

- *The Surface (or Two-dimensional) Nucleation Mechanism.* At higher supersaturation, the energy barrier for the formation of two-dimensional nuclei (nuclei that are formed on the crystal surface and which only changes size in two dimensions), via the surface nucleation mechanism becomes possible. The growth rate depends on the relation between the growth of the nuclei and the nucleation rate, and three mechanisms can be distinguished. These are the mononuclear nucleation, polynuclear nucleation and the birth and spread mechanisms. The growth rate of the nuclei exceeds the nucleation rate for mononuclear nucleation, but at higher supersaturation the nucleation rate overshadows the growth process and polynuclear nucleation proceeds covering the crystal surface in a growth layer. In between these two surface nucleation mechanisms is the birth and spread model where nucleation and growth occurs simultaneously [34, 43].
- *The Spiral Nucleation Mechanism.* Although widely applied to describe the growth of different crystal systems [59], the preceding two mechanisms fail to adequately describe the experimental growth rates observed in some cases. Martins and co-workers [57] developed a new theory however, called the Spiral Nucleation Model. Screw dislocations serve as origins of growth, and surface nucleation occurs at the dislocations to form a conical spiral which is induced by the screw component of the dislocation. This mechanism, according to the authors, is consistent with Atomic Force Microscopy (AFM) analysis, and the energy requirements for the formation of critical sized nuclei via spiral nucleation are greatly reduced. Growth units are incorporated into the steps created by stable spirals and the rate increases with the spiral surface area. The growth rate also increases the higher the density of spirals, which is dependent on the supersaturation, temperature and the dislocation structure of the crystal surface.

2.2.4. Incorporation of Impurities

Because crystallization is often used for the separation of two or more compounds, the understanding of impurity incorporation into product crystals becomes very important, especially during crystallization from solutions containing both the desired compound and one or more impurities. Although complete separation of two or more solutes can theoretically be

achieved, if the crystallization is performed under the correct conditions as dictated by the appropriate phase diagram (consult references cited in Section 2.2.2.1), non-ideal separation can still occur due to impurities that are incorporated into the product either through adhering mother liquor, inclusion formation or the formation of solid solutions, whereby impurities are incorporated directly into the crystal structure of the crystallizing compound via lattice substitution or by a combination of these mechanisms [29, 60].

In the case of adhering mother liquor, product crystals can retain some of the impure solution during solid-liquid separation and the amount that is absorbed depends on the crystal habit, size distribution and the viscosity of the liquid [29]. Small crystals, for example, will absorb relatively more liquid than larger crystals. This unwanted effect on the product purity can be reduced by washing crystals with pure solvent. However, this causes partial dissolution of the product, which can be avoided using an inert washing liquid (one in which the product is not soluble). The incorporation of impurities via the other two mechanisms however, cannot so easily be avoided and will therefore be discussed separately in the following sections.

2.2.4.1. Inclusion Formation

Crystals grown from impure solutions can contain entrapped liquid in the form of macroscopic pockets which are termed inclusions [49]. This mode of impurity incorporation, which can have a significant effect on purification, is caused by unstable growth conditions that can be induced by [49]:

- the growth rate (and therefore supersaturation),
- inhomogeneous mixing, and
- damage to growing crystal surfaces.

When crystals grow at a high growth rate, the supersaturation decreases rapidly resulting in insufficient supply of the supersaturated solution to parts of the growing crystal surface. This causes solvent to be enclosed within the pockets formed that result from inhomogeneous growth of the crystal surface [59]. This condition can also be induced by inhomogeneities in the solute as well as the temperature [49]. The resulting inhomogeneous growth can be explained by a phenomenon called step bunching. A region on the crystal surface with a high step density is called step bunching, which also causes a high growth rate. Therefore, a region of inhomogeneous solute concentration above such an area will cause steps to compete for

nutrients in the solution, leading to the formation of macrosteps which eventually cause liquid to be trapped within the vacancies formed while growth continues [58, 60]. Such macrosteps can also be induced due to damage to growing crystal surfaces as well as some impurities that are adsorbed on steps sites that influence the development of steps [58].

2.2.4.2. Solid Solution Formation

Efficient separation can in most cases be achieved by crystallization, because of the ordered structure of the crystalline phase. This order can be disrupted by host atoms or molecules in the crystal lattice being substituted by impurities, especially when the host and impurity have an isomorphic crystal structure. Therefore, if the host crystal structure is not appreciably distorted during the incorporation of impurities, solid solution formation can become the dominant mechanism of impurity incorporation. Such a system, that forms solid solutions, exhibits non-eutectic behaviour and the phase equilibria are very complex.

Disregarding for the moment the other two means of impurity incorporation, the extent to which impurities are incorporated into the lattice of the desired compound can be quantitatively related to the energy change upon integration of the impurities into the crystal lattice relative to that of the host atoms or molecules [49]. If solid solution formation via lattice substitution of impurities occurs, the host and impurities will be distributed between the solid and liquid phases in a way that is determined largely by the thermodynamics of the system. This phenomenon of separation of the desired compound and the impurities at the growing crystal interface is termed segregation [49]. The relative segregation, or distribution coefficient, can be used to quantify the degree of impurity incorporation into the host crystal structure via lattice substitution, and therefore also to describe the separation efficiency.

The relative distribution coefficient is defined as the equilibrium distribution of the impurity between the two phases relative to that of the desired compound. If the subscript 1 is used to denote the desired (host) compound and the subscript 2 is used for the impurity, the relative distribution coefficient is numerically equal to [49, 61, 62]:

$$\beta_{2,1} = \frac{z_2/x_2}{z_1/x_1} = \frac{K_2}{K_1} \tag{2.19}$$

where $\beta_{2,1}$ is the relative distribution coefficient, which is a ratio of the distribution coefficients of the impurity and the desired compound. z_i, which can be conveniently expressed in terms of mole fractions, is the concentration of compound i in the solid phase and x_i the concentration of compound i in the liquid phase.

A value of $\beta_{2,1}$ less than unity corresponds to enrichment of the crystalline phase with the desired compound, whereas a value larger than unity corresponds with enrichment of the crystalline phase with the impurity. Both cases therefore relate to purification; however the relative value can give an indication of the efficiency of the process. Furthermore, because the concentration of impurities is normally small in comparison with that of the desired compound, the smaller the value of $\beta_{2,1}$ (when $\beta_{2,1} < 1$), the higher the efficiency of the crystallization process due to the enrichment of the crystalline product with the desired compound. It should be borne in mind however, that an experimentally determined value can be influenced by other means of impurity incorporation and care must therefore be taken to ensure that such effects are minimized by employing slow crystal growth and effective solid-liquid separation.

Rossenberger and Riveros [61, 62] derived a theoretical expression (Equation 2.43) for the relative distribution coefficient using thermodynamic considerations of solid-liquid systems. The derivation, which is shown below, makes use of the following principles:

The chemical potential, μ, of a solute i in solution is written as:

$$\mu_i = \mu_i^0 + RT\ln(\gamma_i b_i) \tag{2.20}$$

where μ_i^0 is a standard chemical potential chosen to only be dependent on state-functions such as temperature and pressure, and not on the composition. γ_i is the activity coefficient which has a value of $\gamma_i = 1$ when ideal behaviour is applicable, and b_i is the relative concentration.

Using the notation where l and s denote "liquid" and "solid" respectively, and using $b_i = x_i$ for the liquid phase, and $b_i = z_i$ for the solid phase, an expression for the thermodynamic relative distribution coefficient, which is represented by β_0 to indicate its dependence on the thermodynamics of the solid-liquid system, can be obtained as follows:

The chemical potential of the impurity in the solid (host crystal structure) is:

$$\mu_{2s}=\mu_{2s}^{0}+RT\ln\left(\gamma_{2s}\, z_2\right) \tag{2.21}$$

where μ_{2s}^{0} is the chemical potential of the pure solid of the impurity, z_2 is the relative concentration, and γ_{2s} is the activity coefficient. The concentration of the desired compound is usually much more than that of the impurity, i.e. $z_1 \approx 1$ and ideal behaviour can therefore be assumed ($\gamma_1 = 1$), thus:

$$\mu_{1s}=\mu_{1s}^{0} \tag{2.22}$$

For the impurity in the liquid phase:

$$\mu_{2l}=\mu_{2l}^{*}+RT\ln\left(\gamma_{2l}^{'} x_2\right) \tag{2.23}$$

$\gamma_{2l}^{'}$ gives an indication of the degree of interaction of the impurity with the solvent, in which the desired compound is also dissolved. This also holds for the desired compound in the liquid phase:

$$\mu_{1l}=\mu_{1l}^{*}+RT\ln\left(\gamma_{1l}^{'} x_1\right) \tag{2.24}$$

Accordingly, $\gamma_{1l}^{'}$ accounts for the host-solvent interaction, in the presence of the dissolved impurity. In Equations (2.23) and (2.24), μ_{il}^{*} corresponds with the chemical potential of an infinitely dilute solution of compound i where ideal behaviour is also approached (see the original works of Rosenberger et al. [61, 62]). At equilibrium, the chemical potential of the different species in the solid phase is equal to that in the liquid phase, therefore:

$$\mu_{is}=\mu_{il} \tag{2.25}$$

The premise that the degree of segregation is dependent on the difference between the change in the chemical potential of the desired compound and impurity during the phase transition forms the basis of this model, which can be expressed according to Equation (2.26).

$$\left(\mu_{2s} - \mu_{21}\right) - \left(\mu_{1s} - \mu_{11}\right) = 0 \tag{2.26}$$

where the condition of Equation (2.25) is used. By substitution of Equations (2.21) to (2.24), Equation (2.27) is obtained:

$$\mu_{2s}^{0} + RT\ln\left(\gamma_{2s} z_2\right) - \mu_{21}^{*} - RT\ln\left(\gamma_{21}^{'} x_2\right) - \mu_{1s}^{0} + \mu_{11}^{*} + RT\ln\left(\gamma_{11}^{'} x_1\right) = 0 \tag{2.27}$$

$$\therefore \left(\mu_{2s}^{0} - \mu_{21}^{*}\right) - \left(\mu_{1s}^{0} - \mu_{11}^{*}\right) + RT\ln\frac{\gamma_{2s} z_2 \gamma_{11}^{'} x_1}{\gamma_{21}^{'} x_2} = 0 \tag{2.28}$$

$$\therefore -RT\ln\frac{\gamma_{2s} z_2 \gamma_{11}^{'} x_1}{\gamma_{21}^{'} x_2} = \left(\mu_{2s}^{0} - \mu_{21}^{*}\right) - \left(\mu_{1s}^{0} - \mu_{11}^{*}\right) \tag{2.29}$$

$$\therefore \frac{\gamma_{2s}\gamma_{11}^{'}}{\gamma_{21}^{'}}\frac{z_2 x_1}{x_2} = exp\left[-\frac{\left(\mu_{2s}^{0} - \mu_{21}^{*}\right) - \left(\mu_{1s}^{0} - \mu_{11}^{*}\right)}{RT}\right] \tag{2.30}$$

However, because

$$\beta_0 = \frac{z_2 x_1}{z_1 x_2}, \text{ and } z_1 \approx 1 \tag{2.31}$$

$$\beta_0 \approx \frac{z_2 x_1}{x_2} = \frac{\gamma_{21}^{'}}{\gamma_{2s}\gamma_{11}^{'}} . exp\left[-\frac{\left(\mu_{2s}^{0} - \mu_{21}^{*}\right) - \left(\mu_{1s}^{0} - \mu_{11}^{*}\right)}{RT}\right] \tag{2.32}$$

μ_{11}^{*} and μ_{21}^{*} can be written in terms of the chemical potential of the pure solid components that are in equilibrium with the corresponding saturated solutions:

$$\mu_{is}^{0} = \mu_{il}^{*} + RT\ln\left(\gamma_{il}^{sat} x_i^{sat}\right) \tag{2.33}$$

where x_i^{sat} is the concentration of component i in a saturated solution, or in other words the solubility of component i. Thus:

$$\left(\mu_{2s}^{0} - \mu_{2l}^{*}\right) = \mu_{2l}^{*} + RTln\left(\gamma_{2l}^{sat} x_2^{sat}\right) - \mu_{2l}^{*} = RTln\left(\gamma_{2l}^{sat} x_2^{sat}\right) \tag{2.34}$$

$$\left(\mu_{1s}^{0} - \mu_{1l}^{*}\right) = \mu_{1l}^{*} + RTln\left(\gamma_{1l}^{sat} x_1^{sat}\right) - \mu_{1l}^{*} = RTln\left(\gamma_{1l}^{sat} x_1^{sat}\right) \tag{2.35}$$

$$\therefore \left(\mu_{2s}^{0} - \mu_{2l}^{*}\right) - \left(\mu_{1s}^{0} - \mu_{1l}^{*}\right) = RT\, ln\left(\frac{\gamma_{2l}^{sat} x_2^{sat}}{\gamma_{1l}^{sat} x_1^{sat}}\right) \tag{2.36}$$

$$\begin{aligned} \therefore \beta_0 &= \frac{\gamma_{2l}^{'}}{\gamma_{2s}\gamma_{1l}^{'}}.exp\left[-\frac{RT\, ln\left(\gamma_{2l}^{sat} x_2^{sat} / \gamma_{1l}^{sat} x_1^{sat}\right)}{RT}\right] \\ &= \frac{\gamma_{2l}^{'}}{\gamma_{2s}\gamma_{1l}^{'}}.exp\left[\frac{RT\, ln\left(\gamma_{1l}^{sat} x_1^{sat} / \gamma_{2l}^{sat} x_2^{sat}\right)}{RT}\right] \\ &= \frac{\gamma_{2l}^{'}\gamma_{1l}^{sat}}{\gamma_{2s}\gamma_{1l}^{'}\gamma_{2l}^{sat}} \frac{x_1^{sat}}{x_2^{sat}} \end{aligned} \tag{2.37}$$

With $\gamma_{1l}^{'} = \gamma_{1l}^{sat}$, Equation (2.37) reduces to:

$$\beta_0 = \frac{\gamma_{2l}^{'}}{\gamma_{2s}\gamma_{2l}^{sat}} \frac{x_1^{sat}}{x_2^{sat}} \tag{2.38}$$

According to Equation (2.21), γ_{2s} can be written as:

$$\gamma_{2s} = exp\left(\frac{\mu_{2s} - \mu_{2s}^{0}}{RT}\right) \Big/ z_2 \tag{2.39}$$

$$\therefore \beta_0 = \frac{\gamma_{2l}^{'}}{\gamma_{2l}^{sat}} \frac{x_1^{sat}}{x_2^{sat}}.z_2.exp\left(-\frac{\mu_{2s} - \mu_{2s}^{0}}{RT}\right) \tag{2.40}$$

The difference $\mu_{2s} - \mu_{2s}^{0}$ corresponds with the change in the chemical potential for the dissolution of the solid impurity in the host crystal structure, which is equal to the change in the Gibbs free energy, thus:

$$\mu_{2s} - \mu_{2s}^{0} = \Delta\mu_{2s}^{dls} = \Delta H_{2s}^{dls} - T\Delta S_{2s}^{dls} \tag{2.41}$$

The entropy consists of a mixing term and a vibrational term:

$$\begin{aligned} \Delta S_{2s}^{dls} &= \Delta S_{2s}^{mix} + \Delta S_{2s}^{vib} \\ \Delta S_{2s}^{mix} &= -R\, lnz_2 \end{aligned} \tag{2.42}$$

whereby it can be shown that Equation (2.40) reduces to:

$$\beta_0 = \frac{z_2/x_2}{z_1/x_1} \approx \frac{z_2 . x_1}{x_2} \simeq \frac{\gamma_{21}^{'}}{\gamma_{21}^{sat}} \frac{x_1^{sat}}{x_2^{sat}} exp\left(-\frac{\Delta H_{2s}^{dis} + T\Delta S_{2s}^{vib}}{RT} \right) \tag{2.43}$$

In Equation (2.43), β_0 represents the thermodynamic, relative distribution coefficient where the subscript is used to indicate that the kinetics of crystal growth are neglected. The assumption is made that $z_1 \approx 1$, the concentration of the desired compound in the solid phase. $\gamma_{21}^{'}$ and γ_{21}^{sat} represents, the activity coefficients of the impurity in a solution of the host and in a saturated solution of the pure impurity respectively. The ratio x_1^{sat}/x_2^{sat}, corresponds with the pure component solubility ratio of the host and impurity, ΔH_{2s}^{dis} is the heat of dissolution ($kJ.mol^{-1}$) of the impurity in the host crystalline phase, and ΔS_{2s}^{vib} is the change in the vibrational entropy ($kJ.K^{-1}.mol^{-1}$) in transferring the impurity from the solution to the solid phase, thereby replacing the host compound.

The thermodynamic relative distribution is therefore dependent on:

- The degree of interaction of the impurity with the host solution, as described by the ratio $\gamma_{21}^{'}/\gamma_{21}^{sat}$.
- The solubility ratio of the pure compounds in the solvent.
- The energy requirements for the substitution of impurities for host molecules in the crystal lattice, which is described by the heat of mixing and the vibrational entropy change.

This can be summarized as [49]:

$$\beta_0 = f(\text{Solution thermodynamics, Solid-state thermodynamics})$$

Some simplifications that can be made include [49, 61, 62]:

The activity coefficient ratio can be approximated as unity because the values at low concentrations and at saturated conditions would normally be of the same order of magnitude. The vibrational entropy is usually also negligible in comparison with the enthalpy term and can therefore be neglected in most cases.

This implies that the higher the solubility of the impurity in relation to that of the desired compound in the same solvent, the lower the amount of incorporation, according to Ruff's rule [49]. This dependence on the solubility ratio has been confirmed by some researchers [60, 63, 64]. Also, the amount of impurity incorporation decreases as the heat of mixing of the impurity in the solid phase increases [49].

Another important factor that effects the incorporation of substitutional impurities is the growth rate. The theory is that as the growth rate increases, the impurities are rejected at a faster rate than they can diffuse back to the bulk solution. This leads to an increase in the incorporation in the solid phase relative to that predicted by thermodynamics, because at the interface the impurity concentration will be higher than in the bulk solution [49]. Burton, Prim and Slichter developed a model (the BPS model), that relates the effective distribution coefficient to the thermodynamic distribution coefficient and the growth rate [49, 65]. The result is that the efficiency of separation increases as the growth rate decreases, because the diffusivity of impurities increases with respect to the growth rate.

Although, as mentioned before, the model for the thermodynamic distribution coefficient does not include impurity incorporation via the other mechanisms, it can be used for the prediction of the effectiveness of a purification process via crystallization. Similar models have been developed and used in the past [61]; for example, Geertman and Diepen used similar models to predict the separation efficiency for crystallization of isomorphic organic compounds [65, 66]. The model of Rosenberger and Riveros, described above, was subsequently applied to the fractional crystallization of $K_2Zr(HF)F_6$ (this study) in conjunction with the results obtained from the molecular modelling in this study.

2.3. Molecular Modelling

As will be explained in Section 3.3.1.5, the molecular modelling of $K_2Zr_{(1-z)}Hf_zF_6$ solid solutions was used to calculate the mixing enthalpy for the lattice substitution of Zr by Hf. These results were used, together with a simplified form of Equation (2.43), to theoretically evaluate the separation efficiency of fractional crystallization. The majority of solid state simulations were performed using the ab initio simulation program CASTEP (Section 3.3.1), although DMol^3 was also used to a lesser extent (Section 3.3.2). Both of these programs are available as part of the Materials Studio Modelling Environment [38]. The basic theory of these methods is therefore discussed in the subsequent sections. For determining the efficiency of fractional crystallization by the abovementioned strategy, the vibrational entropy contribution was assumed to be negligible (Section 2.2.4.2). The determination of the vibrational entropy contribution by molecular simulations is very intensive. However, it is shown in Section 5.3.1 how the vibrational entropy may be estimated mathematically.

2.3.1. Density-Functional Theory – CASTEP

While both CASTEP and DMol^3 use Density-Functional Theory (DFT), only its implementation in CASTEP will be briefly outlined in this section. The basic principles of the application of the theory in DMol^3 is treated in Section 2.3.3.

Quantum mechanics are used to describe the behaviour of subatomic particles such as electrons and nuclei, which in turn determines the properties of materials; as chemical bonds within a compound can be viewed as being the result of the interactions of these particles with each other [67]. The Schrödinger equation describes the behaviour of the electrons and nuclei within a system, however the degree of interaction, even in the simplest of molecules, are too complex to describe mathematically. As a result, an exact solution to the Schrödinger equation can effectively only be solved for a one-electron system such as a hydrogen atom. The Born-Oppenheimer approximation can be used to reduce the complexity of the problem to a system of interacting electrons only [37, 67, 68]. Within this approximation, it is assumed that because the electrons move so rapidly with respect to the nuclei, the nuclei can be considered to be stationary. Thereby, the system is reduced to a set of interacting electrons only. However, even with this simplification, describing the interactions of the electrons with each other remains challenging. To make calculations practically feasible, further simplifications and computational techniques must be used.

The problem of interacting electrons can be solved in terms of a system of non-interacting electrons moving in an effective potential field. This potential acts on each individual electron of a system whereby the problem of a multi-electron system is reduced to a set of one-electron systems wherein the effective potential accounts for the interactions between the electrons [67]. Density-functional theory (DFT) developed by Hohenberg, Kohn and Sham provides a scheme to solve the problem of interacting electrons in terms of individual electrons moving in an effective potential [68]. According to DFT, the total energy of any system can be expressed as functionals of the electron density, where a function gives a value from a variable and a functional gives a value from a function. The ground state properties are then given by minimizing the total energy which is written as [67 - 69]:

$$E_t\left[\rho(r)\right] = E_k\left[\rho(r)\right] + E_C\left[\rho(r)\right] + E_{xc}\left[\rho(r)\right] + \int V_{ion}(r)\,\rho(r)\,dr \qquad (2.44)$$

where the charge density, $\rho(r)$, which is calculated from a set of one-electron wave functions ψ_i (in terms of non-interacting electrons), according to [67 - 69]:

$$\rho(r) = \sum_i \left|\psi_i(r)\right|^2 \qquad (2.45)$$

In Equation (2.44), E_K is the electron kinetic energy of a system of non-interacting electrons, E_C is the purely Coulomb electrostatic contribution due to the electrostatic interaction of the electrons with each other and E_{xc} is the exchange-correlation functional. V_{ion} represents the effective potential that accounts for the interactions of the electrons with the nuclei, and together with the E_{xc}-term accounts for the interaction of the electrons with each other [68, 69]. This exchange-correlation energy term is in fact a correction term that is included to account for the interaction between electrons of the same spin, and is one semi-empirical element within the DFT framework as applied to otherwise purely ab initio simulation methods [67, 68].

The most fundamental exchange-correlation functional is the Local Density Approximation (LDA) in which the exchange-correlation energy is calculated for a uniformly distributed system of electrons [67 - 69]. Thus, the term electron gas is often used to denote a uniform distribution of the electron density. The LDA is therefore an oversimplification as the electron density is non-uniformly distributed around real molecules. Therefore, other functionals have

been developed such as the Generalized Gradient Approximation [70] wherein consideration is also given to the non-linearity of the density distribution [67]. However, regardless of the different types of exchange-correlation functionals, the applicability of each functional varies according to the system under consideration.

As indicated in Equation (2.45), the electron density is calculated in terms of the one-electron wave functions, which gives the probability of finding an electron at a given point in space, and therefore an effective method is required to express these wave functions. In a periodic structure, i.e. condensed matter, each of the single-electron wave functions can be expanded in terms of the sum of a set of plane-waves that serves as basis functions, and which coincides with the periodicity of the lattice [67, 68]. In principle, an infinite number of plane-waves, with an infinite number of wave-vectors, should be applied to accurately describe each electronic wavefunction in a multi-electron system. However, by applying Bloch's theorem, the wave functions can be calculated at discrete points, or *k*-points within the Brillouin zone, wherein the accuracy of the representation increases as the density of *k*-points increases [67, 68, 71]. The density of the *k*-point grid is known as *k*-point sampling. The Brillouin zone, or reciprocal space, is used as an effective mathematical description of the unit cell that permits calculation of the wave functions using a specific *k*-point sampling [67]. Furthermore, using this description, symmetry considerations dictates that only the *k*-points within the irreducible section of the Brillouin zone need to be taken into account. Fast Fourier transformation is then applied to relate the information calculated within the reciprocal space to real space [67, 69]. In addition to the density of the *k*-point sampling, another parameter influences the accuracy of the wavefunction calculations. This parameter is termed the plane-wave cutoff energy [67, 68]. As a result, only plane waves with kinetic energies smaller than a certain cutoff are considered, where the accuracy of the representation increases as the cutoff energy increases. A practical cutoff energy for a specific system must however be found by performing a cutoff energy convergence test.

However, even with the abovementioned approximations and computational techniques, it is practically impossible to include all of the electrons of a system in the calculation of the wave functions in terms of plane-waves, as this would still require an infinite number of these functions. This problem is overcome by the pseudopotential approximation which allows the expansion of the electronic wave functions using a much smaller number of plane-wave basis functions. This is because only the valence electrons are considered [72], in which the

interaction of the valence electrons with the nuclei and core electrons, which is collectively taken as the ion-core, is accounted for by a pseudopotential that mimics the full ionic potential. Equation (2.44) may then be written as [67 - 69]:

$$E_t\left[\rho(r)\right] = E_k\left[\rho(r)\right] + E_C\left[\rho(r)\right] + E_{xc}\left[\rho(r)\right] + \int V_{ps}(r)\rho(r)\,dr \qquad (2.46)$$

The pseudopotential formalism is thus implemented in DFT by modification of the effective potential, V_{ion}, [68, 69] to account for the interactions of the valence electrons with the ion-cores, as represented by V_{ps}, which is written in a simplified form. Furthermore, E_C now only accounts for the collective electrostatic interactions of the ion-cores with each other, and the valence electrons with each other. Within this regard, the valence electrons can be arbitrarily chosen whereby different pseudopotentials can often describe core regions with different radii. Also, different types of pseudopotentials have been developed, i.e. norm-conserving pseudopotentials and ultrasoft pseudopotentials [67, 69, 72]. Although very effective, norm-conserving pseudopotentials require the use of large plane-wave basis sets. Ultrasoft pseudopotentials were subsequently developed [73] that also reduce the number of plane waves required, without compromising the level of accuracy [67]. Pseudopotentials are therefore also a semi-empirical approximation, and as a result, the construction of pseudopotentials of adequate accuracy requires rigorous testing procedures [67].

The approximations and techniques described above are implemented using sets of coupled equations called the Kohn-Sham equations, which are a set of one-electron Schrödinger-like equations with the pseudopotential acting on the valence wave functions, whereby the total energy is minimized using minimization algorithms such as molecular dynamics and the BFGS algorithm [72]. Consequently, the ground-state properties of the system can be calculated. Therefore, using k-point sampling together with pseudopotentials and Fast Fourier transform provides a computationally tractable method for the simulation of solids with complex structures.

2.3.2. Calculating Thermodynamic Quantities

2.3.2.1. Simulation Methods

As mentioned previously, solid-state modelling was applied to study the thermodynamics of $K_2Zr_{(1-z)}Hf_zF_6$ solid solution formation, i.e. the thermodynamic energy changes accompanied by the substitution of Hf into the crystal structure of K_2ZrF_6. Therefore, the methods, that can be used to study such substitutional disorder in crystals, are briefly discussed below.

2.3.2.1.A. The Virtual Crystal Approximation

One method whereby solid solutions formed by the incorporation of substitutional impurities can be modelled is the so-called Virtual Crystal Approximation (VCA) [74 - 76]. In the VCA approach the composition of the atoms at each crystallographic site can be modelled as a mixture of two or more atoms. The "mixture-atoms" possess properties of both the pure species in the corresponding ratio of their concentrations in the solid solution. Using this approach, the problem associated with treating the configurational disorder with the supercell method, as discussed below is prevented as the VCA, according to Winkler et al. [76], also "mimics the statistical distribution of different atomic species at each crystallographic site". Furthermore, the modelling of solid solutions with compositions close to the pure structures can be easily performed on unit cells, which is a major advantage over the use of large supercells (Section 2.3.2.1.B), which are computationally very time intensive. The basis of the VCA lies in the pseudopotential approximation, as the implementation of the VCA relies on the averaging of the pseudopotentials of the participating species to form a composite potential with which the mixture-atoms can be accurately described. The approach of Bellaiche and Vanderbilt consists of using a VCA operator equation to generate a compositionally averaged pseudopotential of the participating species which can be written as [75]:

$$V_{ext}(\mathbf{r},\mathbf{r}') = \sum_I \sum_\alpha w_\alpha^I V_{ps}^\alpha (\mathbf{r}-\mathbf{R}_{I\alpha}, \mathbf{r}'-\mathbf{R}_{I\alpha}) \qquad (2.47)$$

In Equation (2.47), V_{ext} is the total external potential, w_α^I is the weight of an atom of type α, i.e. the statistical composition, at lattice site I ($\mathbf{R}_I$ denotes the position of site I), and V_{ps}^α is the pseudopotential of an atom of type α. The advantage of this approach is that the only input

required to model a solid solution system is the weight of the participating atomic species along with their positions in the unit cell, which is then used for the construction of the total external pseudopotential for the description of the valence-electron wave functions by the plane-wave basis functions. This method has been shown to be useful for the modelling of Al/Si disorder in silicates [76], as well as to describe the electronic properties of perovskites [75]. However, although this method has some advantages over the supercell method discussed in the next section, it was not used in this study as is explained in Section 3.2.1.2.

2.3.2.1.B. The Supercell Method

In the supercell method, or "configurational approach", a specific atom distribution is used to study disorder [76]. Supercells are constructed from the unit cells used to model the pure structures of two or more crystalline solids that form solid solutions, which are extended in the basis vector directions to produce a larger model. This permits modelling of solid solutions with varying composition by varying the amount of atoms that are substituted within the supercell. For example, for the simple hypothetical system AB that forms solid solutions with a similar structure AC, by the substitution of the atoms of type B by those of type C, AB_xC_{1-x} solid solutions with varying molar composition, x, can be modelled by varying the amount of atoms of type B that are substituted with atoms of type C.

An advantage of the supercell method is that local distortions at specific lattice sites can be modelled, such as Al/Si disorder in silicates [76]. This supercell method places unfortunate restrictions on the concentration ratios that can be modelled however, because the range of compositions that can be studied [76] is determined by the size of the supercell, and due to the increase in computational time with increasing size of the system, one is limited to a finite sized system that is computationally accessible in terms of computational time and "power". For example, as is the case in this study, discrete ratios of Zr and Hf molar fractions in the crystal structure of $K_2Zr_{(1-z)}Hf_zF_6$ are modelled and the results are then used to extrapolate over the entire concentration range (Section 3.3.1.5). At low concentrations of Hf for example, a different trend may be observed than at higher concentrations which might lead to inaccurate conclusions. The VCA method has a major advantage in this regard as mentioned above, because any concentration ratio may be modelled using only the unit cell, however only if the method is applicable to the system under consideration [76].

In the case of the $K_2Zr_{(1-z)}Hf_zF_6$ system, the model, as described in Section 3.2.1, was used whereby the configurationally average properties of the different compositions were approximated by treating only a single configuration due to the complexity of the $K_2Zr_{(1-z)}Hf_zF_6$ crystal structure. However, a more accurate description of the desired properties of a system, when employing such an approach, should be obtained by investigating all possible configurations within the limitations of the supercell, i.e. different atoms or pairs of atoms can be substituted to obtain a specific composition [76, 77]. With increasing size of the supercell, the accuracy is therefore improved as a larger dataset can be used and unwanted interactions between substituted species can be avoided [78], however computational time is increased and the amount of calculations become unmanageable. This is another shortcoming of the supercell method, although it may be resolved using Monte Carlo simulations [79] or using other approximations [77, 78]. In the Monte Carlo approach, interaction parameters are determined using relatively small supercells. The interaction parameter data is then incorporated into the Monte Carlo simulations where large supercells are used in which literally thousands of configurations can be tested, as was done by Reich and Becker [79]. This was not performed in the present study however, but the determination of the thermodynamic and structural properties as a function of composition, using only a single configuration for each composition has also been performed by other investigators. For example, to the best of my knowledge, this same approach was used by Ding et al. [80] and El Haj Hassan et al. [81] in their respective studies of $Be_xZn_{1-x}O$ and BP_xAs_{1-x} alloys.

Nevertheless, the supercell method has been successfully applied to study solid solution formation in various different systems. For example, $Zn_{1-x}Be_xSe$ alloys [77], $Be_xZn_{1-x}O$ alloys [80], $Mg_xZn_{1-x}O$ alloys [82], BP_xAs_{1-x} alloys, and $Al_xGa_{1-x}N$ alloys have all been studied with respect to structural, electronic and thermodynamic properties using the supercell approach. Because of the large size of the crystallographic models needed for implementation of the supercell method, temperature correction by vibrational analysis was not performed in the abovementioned studies which were concerned with the construction of phase diagrams [77, 81 - 83]. Instead, the temperature dependent ideal mixing entropy, which can be calculated mathematically, was used to obtain a temperature dependent expression for the Gibbs free energy of mixing that was used for the construction of phase diagrams as a function of the composition. Although phase diagrams were not constructed in this study, the same basic approach was also applied to study $K_2Zr_{(1-z)}Hf_zF_6$ solid solutions. Consequently, just as in the abovementioned studies, the mixing enthalpies that were calculated from the total electronic

energies (Section 3.2.1.2), was correlated with the regular solution model (Section 3.3.1.5), which yields a functional relationship between the mixing enthalpy and the composition as will be illustrated in Chapter 3. Using the results obtained from this procedure, the separation efficiency of Zr and Hf by fractional crystallization of $K_2Zr(Hf)F_6$ was theoretically evaluated in this study.

2.3.3. DMol^3 and the COSMO Approach

DMol^3 is a quantum mechanical molecular modelling program in which the basic principles of DFT (Section 2.3.1) are also applied. However, the level of parameterization is more extensive than that of CASTEP. In general, DMol^3 is conveniently applied to molecular systems and the major difference between the DFT implementation of CASTEP and DMol^3 is the method with which the electronic wave functions are described. To describe the bonds between atoms, the molecular orbitals need to be calculated, which can conveniently be done by linear combination of the atomic orbitals (LCAO) [84]. In contrast to the CASTEP approach where only the valence electrons are considered in the plane-wave pseudopotential method, all the electrons are typically treated within the DMol^3 implementation [84]. Numerical atomic orbitals, i.e. tabulated values that are determined semi-empirically, are used for the construction of the molecular orbitals by the LCAO method [84]. Consequently, all-electron full potentials are used instead of pseudopotentials, although the use of pseudopotentials is sometimes beneficial especially when dealing with heavier atoms [85]. Different numerical orbitals, or basis sets, are currently available and the use of a specific type should be carefully selected depending on the physical problem at hand. Despite these modifications, exchange-correlation functionals are also used within this formalism [84].

By the implementation of numerical basis sets, it is also possible to model periodic structures with DMol^3 [85] for which the principles of *k*-point sampling is also applied. However, because numerical basis functions are used, modelling of crystalline structures is time efficient, although maybe not as accurate as the plane-wave pseudopotential method. Therefore, DMol^3 was also used in this study to calculate the thermodynamic properties of $K_2Zr_{(1-z)}Hf_zF_6$ solid solutions using single-point energy calculations only, i.e. no geometry optimizations were performed. The CASTEP-optimized structures were used for this purpose, the results of which are discussed in Section 3.3.2.1.

In addition, the DMol^3 method was also used to study solvation effects of the $Zr(Hf)F_6^{2-}$ ions as explained in Section 3.2.2.2. DMol^3 provides a convenient model, the COSMO model, whereby solvation effects can be studied. COSMO, or Conductor-like Screening Model [86, 87], is a continuum solvation model (CSM) where the solvent is represented by a dielectric continuum with a specific permittivity within which the solute molecule forms a cavity. The polarization of the dielectric medium resulting from the charge distribution of the solute is described by screening (or polarization) charges acting on the cavity surface, i.e. the Solvent Accessible Surface (SAS) [86].

In general, COSMO is a simplification of the normal CSM approach, but it allows efficient implementation into quantum mechanical programs such as DMol^3 [86, 87]. In short, this is done by incorporating the electrostatic COSMO potential, due to the interaction between the solute and the dielectric medium, into the Kohn-Sham equations used to calculate the electron density distribution. As a result, the all-electron and COSMO potentials collectively act on the molecular wave functions from which the solvent-corrected electron density distribution is calculated and minimized [86, 87]. These calculations are dependent however on a realistic construction of the SAS, for which the van der Waals radii of the atoms in the molecule can be applied [86, 87]. By comparison of the vacuum geometry and electronic energy calculated using a DMol^3 calculation with a DMol^3/COSMO simulation, the effects of solvation can be evaluated [86].

This basic approach has been successfully applied to study the solvation of cations such NH_4^+, $N(CH_3)_4^+$ and $N(C_2H_5)_4^+$ using semi-empirical modelling methods [86], the mutual solubilities of hydrocarbons and water [88], and has also been extended to polymers with periodic boundary conditions [89].

2.4. Conclusions

Following the above discussion, the thermodynamics of solid solution formation and solution composition was identified as two important aspects that were investigated in this study to evaluate the efficiency of fractional crystallization to separate Zr and Hf.

Based on the thermodynamic model presented in Section (2.2.4.2.), it was shown that the separation efficiency of two or more isomorphic crystalline substances by crystallization from

solution is influenced by the solution thermodynamics and the solid-state thermodynamics of the system. Therefore, the thermodynamic energy changes associated with $K_2Zr_{(1-z)}Hf_zF_6$ solid solution formation (solid state thermodynamics) were investigated by solid state modelling, to determine whether the separation efficiency might be controlled by the thermodynamics of the isomorphic $K_2Zr(Hf)F_6$ system (Chapter 3). For this purpose, the pseudopotential plane-wave method as implemented in CASTEP was mostly used, where two different ultrasoft pseudopotential schemes were employed. In addition, the numerical basis sets of DMol^3 were also used, although to a lesser extent, for comparison with the CASTEP results.

However, although the thermodynamics of solid solution formation is an important aspect, the solvent composition has also been shown to have a significant influence on separation efficiency of other isomorphic substances as discussed in Section 2.2.4.2. In those cases, the solvent composition seemed to affect the solubility ratio of the impurity and desired compounds, which according to Equation (2.43) is another important factor that influences the separation efficiency. Because KF and HF was used as additives in fractional crystallization of $K_2Zr(Hf)F_6$ in the past (Section 2.1.5.2), its influence on the separation efficiency was also investigated experimentally in this study. Consequently, the fractional crystallization of $K_2Zr(Hf)F_6$ from aqueous solutions of KF with varying concentrations, with and without HF with a constant concentration was studied (Chapter 4). Following the importance of the supersaturation and crystallization kinetics on the different aspects of crystallization (Sections 2.2.2.2 and 2.2.3), an attempt was made to create comparable crystallization conditions for crystallization of $K_2Zr(Hf)F_6$ from aqueous solutions of varying composition as explained in Chapter 4.

2.5. References

1. Nielsen, R.H., Schlewitz, J.H. and Nielsen, H. 2001. Zirconium and zirconium compounds. In Kirk-Othmer encyclopaedia of chemical technology. 5th ed. John Wiley & Sons. Volume 26. p. 621 – 664.

2. Mellor, J.W. 1952. A comprehensive treatise on inorganic and theoretical chemistry. London: Longmans, Green and Co. Volume 7. p. 98 – 165.

3. Nielsen, R.H. 2001. Hafnium and hafnium compounds. In Kirk-Othmer encyclopaedia of chemical technology. 5th ed. John Wiley & Sons. Volume 13. p. 78 – 97.

4. Skaggs, R.L., Rogers, D.T. & Hunter, D.B. Review of anhydrous zirconium-hafnium separation techniques. Report No. BuMines IC 8963, U.S. Bureau of Mines: Albany, OR, 1984.

5. Blumenthal, W.B. 1958. The chemical behaviour of zirconium. New York: D. van Nostrand Company Inc. 398 p.

6. Cotton, F.A., Wilkinson, G., Murillo, C.A. & Bochmann, M. 1999. Advanced inorganic chemistry. New York: John Wiley & sons. p. 878 – 895.

7. Nel, J.T. Process for reacting a zirconia based material. U.S. Patent 5,958,355 (1999).

8. Bradley, D.C. and Thornton, P. 1973. Zirconium and Hafnium. In: Bailar, J.C., Emeleus, H.J., Nyholm, R. & Trotman-Dickenson, A.F., eds. Comprehensive inorganic chemistry. Oxford: Pergamon Press. p. 419-490.

9. Sajin, N.P. & Pepelyaeva, E.A. Separation of hafnium from zirconium and production of pure zirconium dioxide. In Proceedings of the Second united Nations International Conference on the Peaceful uses of Atomic Energy, Geneva, 1958. Vol. 8, Paper P/634, pp 559–562.

10. Coster, D. and von Hevesy, G. Process of separating zirconium and Hafnium. U.S. Pat. 1,618,960 (1927).

11. Stephens, W.W. 1984. Extractive metallurgy of zirconium – 1945 to the present. In Franklin, D.G. & Adamson, R.B., eds. Zirconium in the nuclear industry: Sixth international symposium. *ASTM Spec. Tech. Publ. 824.* American Society of Testing and Materials. p. 5 – 36.

12. Poriel, L., Pellet-Rostaing, S., Lamotte, V., Lemaire, M., Favre-Réguillon, A. Zirconium and hafnium separation, part 2. Solid/liquid extraction in hydrochloric acid

aqueous solution with anion exchange resins. *Sep. Sci. Technol.* **41** (2006) 2711 - 2722.

13. Poriel, L., Chitry, F., Pellet-Rostaing, S., Lemaire, M. & Favre-Réguillon, A. Zirconium and hafnium separation, part 3. Ligand-enhanced separation of zirconium and hafnium from aqueous solution using nanofiltration. *Sep. Sci. Technol.* 41 (2006) 2883 - 2893.

14. Ishizuka, H. Process for separation of zirconium- and hafnium tetrachlorides from a mixture comprising such chlorides and apparatus therefore. Eur. Pat. Appl. EP 45,270 (1982).

15. Veyland, A., Dupont, L., Pierrard, J-C., Rimbault, J. and Aplincourt, M. Thermodynamic stability of Zirconium(IV) complexes with hydroxyl ions. *Eur. J. Inorg. Chem.* **11** (1998) 1765-1770.

16. Varga, L.P. & Hume, D.N. Computer analysis of potentiometric and thenoyltrifluoroacetone (TTA) solvent extraction studies on the fluoride complexes of hafnium. *Inorg. Chem.* **2** (1) (1963) 201 – 206.

17. Deshpande, R.G., Khopkar, P.K., Rao, C.L. & Sharma, H.D. The aqueous chemistry of hafnium(IV), solvent extraction and ion exchange studies. *J. Inorg. Chem.* **27** (1965) 2171 – 2181.

18. Norén, B. The hydrolysis of Zr^{4+} and Hf^{4+}. *Acta. Chem. Scand.* **27** (1973) 1369 – 1384.

19. Kragten, J. & Parczewski, A. Photometric complex-formation titration of submicromolar amounts of zirconium. *Talanta.* **28** (1981) 149 – 155.

20. Ahrland, S., Hefter, G. & Norén, B. A calorimetric study of the mononuclear fluoride complexes of zirconium(IV), hafnium (IV), thorium(IV) and uranium(IV). *Acta. Chem. Scand.* **44** (1990) 1 – 7.

21. Moulin, L., Thouvenin, P. & Burn, P. 1984. New process for zirconium and hafnium separation. In Franklin, D.G. & Adamson, R.B., eds. Zirconium in the nuclear industry: Sixth international symposium. *ASTM Spec. Tech. Publ. 824.* American Society of Testing and Materials. p. 37 – 44.

22. da Silva, A.B.V. and Distin, P.A. Zirconium and hafnium separation without waste generation. *CIM Bull.* **91** (1998) 221 - 224.

23. Takahashi, M., Miyazaki, H. & Katoh, Y. 1984. New solvent extraction process for zirconium and hafnium. In Franklin, D.G. & Adamson, R.B., eds. Zirconium in the nuclear industry: Sixth international symposium. *ASTM Spec. Tech. Publ. 824.* American Society of Testing and Materials. p. 45 – 56.

24. Poriel, L., Favre-Réguillon, A., Pellet-Rostaing, S. & Lemaire, M. Zirconium and hafnium separation, part 1. Liquid/liquid extraction in hydrochloric acid aqueous solution with aliquat 336. *Sep. Sci. Technol.* **41** (2006) 1927 - 1940.

25. Retief, W.L. 1997. Plasma chemical conversion – a revolutionary new beneficiation tool. Heavy Minerals. Johannesburg, South African Institute of Mining and Metallurgy. p. 157 – 160.

26. von Hevesy, G. The discovery and properties of hafnium. *Chem. Rev.* **2** (1) (1925) 1 – 41.

27. Vinarov, I.V. Modern methods for separating zirconium and hafnium. *Russ. Chem. Rev.* **36** (7) (1967) 522 – 536.

28. Schwartz, A.M. & Myerson, A.S. 2002. Solutions and solution properties. In Myerson, A.S., ed. Handbook of industrial crystallization. 2nd ed. Boston: Butterworth-Heinemann. p. 1 – 31.

29. Perry, R.H. & Green, D.W. 1997. Perry's chemical engineering handbook. 7th ed. New York: McGraw-Hill. p. 18-35 -18-54.

30. Ulrich, J. 2001. Crystallization. In Kirk-Othmer encyclopaedia of chemical technology. 5th ed. John Wiley & sons. Volume 8. p. 95 – 147.

31. Tilley, R.J.D. 2006. Crystals and crystal structures. New York: John Wiley and sons. 255 p.

32. Giacovazzo, C., ed. 2002. Fundamentals of crystallography. 2nd ed. New York: Oxford university press. 825 p.

33. Mersman, A. 2001. Physical and chemical properties of crystalline systems. In Mersman, A., ed. Crystallization technology handbook. 2nd ed. New York: Marcel Dekker. p. 1 – 44.

34. Mersman, A., Eble, A. & Heyer, C. 2001. Crystal growth. In Mersman, A., ed. Crystallization technology handbook. 2nd ed. New York: Marcel Dekker. p. 81 - 143.

35. Cornel, J., Lindenberg, C. & Mazotti, M. 2007. Polymorph transformation monitoring using in-situ vibrational spectroscopy. In Lewis, A.E. & Olsen, C., eds. BIWIC 2007: 14th International workshop on industrial crystallization. Cape Town, South Africa. Amsterdam: IOS press. p. 65 – 72.

36. Flaten, E.M. & Andreassen, J.-P. 2007. Polymorphism and nucleation kinetics. In Lewis, A.E. & Olsen, C., eds. BIWIC 2007: 14th International workshop on industrial crystallization. Cape Town, South Africa. Amsterdam: IOS press. p. 57 – 64.

37. Atkins, P. & de Paula, J. 2002. Atkins' physical chemistry. 7th ed. Trento: Oxford university press. 1150 p.

38. Accelrys Software Inc., Materials Studio Modelling Environment, Version 4.0 and 4.2, San Diego: Accelrys Software Inc., 2007.

39. Mullin, J.W. 2001. Crystallization. 4th ed. Boston : Butterworth-Heinemann. 594 p.

40. Dye, S.R. & Ng, K.M. Fractional crystallization: Design alternatives and tradeoffs. *AIChE J.* **41** (11) (1995) 2427 - 2438.

41. Bowden, S., Brown, D., Gilday, J., Langer, T., Lockwood, M., Snape, E. & White, W. 2007. The development of a reverse classical resolution. In Lewis, A.E. & Olsen, C., eds. BIWIC 2007: 14th International workshop on industrial crystallization. Cape Town, South Africa. Amsterdam: IOS press. p. 40 – 49.

42. Ulrich, J. & Strege, C. Some aspects of the importance of metastable zone width and nucleation in industrial crystallizers. *J. Cryst. Growth.* **237 – 239** (2002) 2130 – 2135.

43. Nývlt, J., Söhnel, O., Matuchová, M. & Broul, M. 1985. The kinetics of industrial crystallization. Amsterdam: Elsevier science publishers. 350 p.

44. van Rosmalen, G.M. & van der Heyden, A.E. 1995. Secondary nucleation. In van der Eerden, J.P. & Bruinsma, O.S.L., eds. Science and technology of crystal growth. Dordrecht: Kluwer academic publishers. p. 259 - 277.

45. Mersman, A., Heyer, C. & Eble, A. 2001. Activated nucleation. In Mersman, A., ed. Crystallization technology handbook. 2nd ed. New York: Marcel Dekker. p. 45 - 79.

46. Stricland-Constable, R.F. 1972. The breeding of crystal nuclei – a review of the subject. In Estrin, J., ed. Crystallization from solution: nucleation phenomena in growing crystal systems. New York: American institute of chemical engineers. Volume 121 (68). p. 1 – 7.

47. Botsaris, G.D. 1976. Secondary nucleation – a review. In Mullin, J.W., ed. Industrial crystallization. New York: Plenum press. p. 3 – 22.

48. Beck, R., Sørenssen, D.M. & Andreassen, J.-P. 2007. The onset of polycrystalline growth in precipitation of L-glutamic acid. In Lewis, A.E. & Olsen, C., eds. BIWIC 2007: 14th International workshop on industrial crystallization. Cape Town, South Africa. Amsterdam: IOS press. p. 177 – 184.

49. Meenman, P.A., Anderson, S.R. & Klug. D.L. 2002. The influence of impurities and solvents on crystallization. In Myerson, A.S., ed. Handbook of industrial crystallization. 2nd ed. Boston: Butterworth-Heinemann. p. 67 - 100.

50. Lu, J.J. & Ulrich, J. An improved prediction model of morphological modifications of organic crystals induced by additives. *Cryst. Res. Technol.* **38** (1) (2003) p. 63 – 73.

51. Clydesdale, G. & Roberts, K.J. 1995. Modelling of the habit modification of molecular crystals by the action of "tailor-made" additives. In van der Eerden, J.P. & Bruinsma, O.S.L., eds. Science and technology of crystal growth. Dordrecht: Kluwer academic publishers. p.179 - 192.

52. Bennema, P. 1995. Morphology of crystals: past and future. In van der Eerden, J.P. & Bruinsma, O.S.L., eds. Science and technology of crystal growth. Dordrecht: Kluwer academic publishers. p.149 – 164.

53. ter Horst, J.H., Geertman, R.M., van der Heijden, A.E. & van Rosmalen, G.M. The influence of a solvent on the crystal morphology of RDX. *J. Cryst. Growth* 189 – 199 (1999) 773 – 779.

54. Lu, J.J. & Ulrich, J. The influence of supersaturation on crystal morphology – experimental and theoretical study. *Cryst. Res. Technol.* **40** (9) (2005) 839 – 846.

55. Liu, C.Y. Tsuei, H.S. & Younquist, G.R. 1971. Crystal growth from solution. In Larson, M., ed. Crystallization from solution: factors influencing size distribution. New York: American institute of chemical engineers. Volume 110 (67). p. 43 - 52.

56. Bourne, J.R. 1980. The influence of solvent on crystal growth kinetics. In Randolph, A.D., ed. Design, control and analysis of crystallization processes. New York: American institute of chemical engineers. Volume 193 (76). p. 59 – 64.

57. Martins, P.M. & Rocha, F. Characterization of crystal growth using a spiral nucleation model. *Surf. Sci.* **601** (2007) 3400 – 3408.

58. Chernov, A.A. & Komatsu, H. 1995. Topics in crystal growth kinetics. In van der Eerden, J.P. & Bruinsma, O.S.L., eds. Science and technology of crystal growth. Dordrecht: Kluwer academic publishers. p 67 – 80.

59. Bennema, P. 1976. Theory and experiment for crystal growth from solution: implications for industrial crystallization. In Mullin, J.W., ed. Industrial crystallization. New York: Plenum press. p. 91 – 112.

60. Givand, J.C., Teja, A.S. & Rousseau, R.W. Effect of relative solubility on amino acid crystal purity. *AIChE J.* **47** (12) (2001) 2705 – 2712.

61. Rosenberger, F. and Riveros, H.G. Segregation in alkali halide crystallization from aqueous solutions. *J. Chem. Phys.* **60** (2) (1974) *668 – 673.*

62. Rosenberger, F. 1979. Fundamentals of crystal growth. New York: Springer-Verlag. 530 p.

63. Givand, J., Chang, B-K. Teja, A.S. & Rousseua, R.W. Distribution of isomorphic amino acids between a crystal phase and an aqueous solution. *Ind. Eng. Chem. Res.* **41** (2002) 1873 – 1876.

64. Nie, Q., Wang, J. & Yin, Q. Effect of solution thermodynamics on the purification of two isomorphic steroids by solution crystallization. *Chem. Eng. Sci.* **61** (2006) 5962 – 5968.

65. Diepen, P.J. Cooling crystallization of organic compounds: processes, purity and permeability. Ph.D-thesis, Technische Universiteit, Delft, 1998.

66. Geertman, R.M. Crystallization of organic compounds: Studies on crystal morphology and purity. Ph.D-thesis, Katholiek Universiteit, Nijmegen, 1993.

67. Segall, M.D., Lindan, P.J.D., Probert, M.J., Pickard, C.J., Hasnip, P.J., Clark, S.J. & Payne, M.C. First-principles simulation: ideas, illustrations and the CASTEP code. *J. Phys.: Condens. Matter.* **14** (2002) 2717 – 2744.

68. Payne, M.C., Teter, M.P., Allan, D.C., Arias, T.A. & Joannopoulos, J.D. Iterative minimization techniques for ab initio total-energy calculations: molecular dynamics and conjugate gradients. *Rev. Mod. Phys.* **64** (4) (1992) 1045 – 1097.

69. Baroni, S., de Gironcoli, S. & Dal Corso, A. Phonons and related crystal properties from density-functional pertrubation theory. *Rev. Mod. Phys.* **73** (2) (2001) 515 – 562.

70. Perdew, J.P., Burke, K. and Ernzerhof, M. Generalized gradient approximation made simple. *Phys. Rev. Lett.* 77 (18) (1996) 3865 – 3868.

71. Monkhorst, H.J. and Pack, J.D. Special points for Brillouin-zone integrations. *Phys. Rev. B.* **13** (12) (1976) 5188 - 5192.

72. Milman, V., Winkler, B., White, J.A., Pickard, C.J., Payne, M.C., Akhmatskaya, E.V. & Nobes, R.H. Electronic structure, properties, and phase stability of inorganic crystals: a pseudopotential plane-wave study. *Int. J. Quantum. Chem.* 77 (5) (2000) 895 – 910.

73. Vanderbilt, D. Soft self-consistent pseudopotentials in a generalized eigenvalue formalism. *Phys. Rev. B.* **41** (1990) 7892 – 7895.

74. Ramer, N.J. & Rappe, A.M. Virtual-crystal approximation that works: locating a compositional phase boundary in $Pb(Zr_{1-x}Ti_x)O_3$. *Phys. Rev. B.* **62** (2) (2000) R743 – R746.

75. Bellaiche, L. & Vanderbilt, D. Virtual crystal approximation revisited: application to dielectric and piezoelectric properties of perovskites. *Phys. Rev. B.* **61** (12) (2000) 7877 – 7882.

76. Winkler, B., Pickard, C. & Milman, V. Applicability of a quantum mechanical "virtual crystal approximation" to study Al/Si-disorder. *Chem. Phys. Lett.* **362** (2002) 266 – 270.

77. Berghout, A., Zaoui, A., Hugel, J. and Ferhat, M. First-principles study of the energy-gap composition dependence of $Zn_{1-x}Be_xSe$ ternary alloys. *Phys. Rev. B.* **75** (2007) 205122-1 – 205112-9.

78. Amrani, B., El Haj Hassan, F. & Zoaeter, M. First-principles study of rock-salt $AgCl_xBr_{1-x}$ alloys. *Phys. B.* **396** (2007) 192–198.

79. Reich. M. & Becker, U. First-principles calculations of the thermodynamic mixing properties of arsenic incorporation into pyrite and marcasite. *Chem. Geol.* **225** (2006) 278 – 290.

80. Ding, S.F., Fan, G.H., Li, S.T., Chen, K. & Xiao, B. Theoretical study of $Be_xZn_{1-x}O$ alloys. *Phys. B.* **394** (2007) 127 – 131.

81. El Haj Hassan, F. & Akbarzadeh, H. First-principles investigation of BN_xP_{1-x}, BN_xAs_{1-x} and BP_xAs_{1-x} ternary alloys. *Mater. Sci. Eng. B.* **121** (2005) 170 -177.

82. Amrani, B., Ahmed, R. & El Haj Hassan, F. Structural, electronic and thermodynamic properties of wide band gap $Mg_xZn_{1-x}O$ alloy. *Comp. Mater. Sci.* **40** (2007) 66 – 72.

83. de Paiva, R., Alves, J.L.A., Nogueira, R.A. de Oliveira, C. Alves, H.W.L., Scolfaro, L.M.R. & Leite, J.R. Theoretical study of the $Al_xGa_{1-x}N$ alloys. *Mater. Sci. Eng. B.* **93** (2002) 2 – 5.

84. Delley, B. An all-electron numerical method for solving the local density functional for polyatomic molecules. *J.Chem. Phys.* **92** (1) (1990) 508 – 517.

85. Delley, B. From molecules to solids with the $DMol^3$ approach. *J.Chem. Phys.* **113** (8) (2000) 7756 – 7764.

86. Klamt, A. and Schüürman, G. COSMO: A new approach to dielectric screening in solvents with explicit expressions for the screening energy and its gradient. *J. Chem. Soc. Perkin Trans.* **2** (1993) 799-805.

87. Tomasi, J. and Persico, M. Molecular interactions in solution: an overview of methods based on continuous distributions of the solvent. *Chem. Rev.* **94** (1994) 2027 – 2094.

88. Klamt, A. Prediction of the mutual solubilities of hydrocarbons and water with COSMO-RS. *Fluid Phase Equilibr.* **206** (2003) 233 – 235.

89. Delley, B. The conductor-like screening model for polymers and surfaces. *Mol. Simul.* **32** (2) (2006) 117 – 123.

CHAPTER 3

A Molecular Modelling Approach to the Separation of K_2ZrF_6 and K_2HfF_6 via Crystallization

3.1. Introduction

The fractional crystallization of K_2ZrF_6 and K_2HfF_6 has been used for the separation of Zr and Hf in the past [1 - 3], although mostly only on a laboratory scale. Therefore, fractional crystallization could possibly also be applied for separating Zr and Hf by using the plasma dissociation route to produce $K_2Zr(Hf)F_6$. However, it has been reported that separation via fractional crystallization requires multiple crystallization steps to produce K_2ZrF_6 of sufficient purity for nuclear applications, [2].

During the fractional crystallization from impure solutions (solutions containing both the desired compound and one or more impurities), impurities can be incorporated in the desired compound through a number of mechanisms. These include lattice substitution of the impurity in the host crystal lattice (crystal structure of the desired compound), inclusions of the impure solution in growing crystals, adsorption of the impurity on the crystal surface, or by wetting of filter cakes by the residual mother liquor [4]. Lattice substitution, or solid solution formation, can play a dominant role when the desired compound and impurity have similar molecular and crystal structures [4, 5]. This might be the case with K_2ZrF_6 and K_2HfF_6, since the compounds have an isomorphic crystal structure [6] as will be illustrated in this chapter. Furthermore, Zr and Hf have very similar chemical properties, thus solid solution formation might be another reason that many recrystallization steps are needed to sufficiently separate the two salts. Since the distribution of an impurity between the solid and liquid phases during equilibrium crystal growth is determined by the thermodynamics of the solid-liquid system [4, 5, 7], the incorporation of an impurity in the host lattice will be determined by the energy change occurring during lattice substitution. In other words, the degree to which impurities are incorporated in the host lattice will be determined by the stability of the resulting solid solutions. The relative distribution coefficient can be used to quantify the distribution of the

impurity between the solid and liquid phases. Therefore, the relative distribution coefficient can also be used to evaluate the efficiency of a crystallization process for the separation of two or more compounds. The thermodynamic model developed by Rosenberger and Riveros [8, 9] can be conveniently applied to theoretically assess the separation efficiency of a crystallization process to separate isomorphic compounds forming solid solutions. According to the model the separation efficiency is determined by different factors. One of these factors is the enthalpy changes occurring during solid solution formation by lattice substitution of the impurity in the host lattice. The other important factor that must be considered is the relative solubility of the pure compounds, which has been confirmed by some authors to have a definite influence on the separation efficiency of different isomorphic compounds [4, 5, 7]. Section 2.2.4 may be consulted for a more detailed discussion of these effects.

In this study we have used molecular modelling software in an attempt to predict the thermodynamic stability of $K_2Zr_{(1-z)}Hf_zF_6$ solid solutions, similarly to Geertman and Diepen [10, 11] who used similar techniques for studying melt crystallization of organic substances. In this chapter it is illustrated how the modelling data can be applied to evaluate the separation efficiency of K_2ZrF_6 and K_2HfF_6 via crystallization if it is assumed that solid solution formation is the only mechanism whereby the separation of the two compounds is restricted. For this purpose, a simplified form of the thermodynamic model of Rosenberger and Riveros [8,9], for the relative distribution coefficient, which can also be applied to other isomorphic systems, was used. Furthermore, molecular modelling was also used to determine whether a significant difference in thermodynamic stability exists between the solvated species, which would also influence the efficiency of separation via crystallization. In addition, different modelling methods and parameters were evaluated to determine the validity of applying this approach to the current Zr-Hf system as will be described in the subsequent sections. Modelling was also done using test systems whereby the results could be compared with published data to evaluate the reliability of the current modelling method.

3.2. Computational Methodology

Two different modelling methods were used for the determination of the ground-state (at 0 K) thermodynamic properties of the formation of $K_2Zr_{(1-z)}Hf_zF_6$ solid solutions. These are firstly, the use of the pseudopotential plane-wave method as implemented in the program CASTEP [12] and secondly, numerical basis functions as is available in the program DMol^3. DFT forms

the basis of both methods, the main difference between the two being that different methods are used to describe the electronic wave functions, or in other words to calculate the molecular orbitals. These programs are both available as part of the Materials Studio Modelling Environment [13]. DMol^3 was also used to determine the liquid-phase thermodynamic properties of K_2ZrF_6 and K_2HfF_6, i.e. with respect to the complex ions in solution.

3.2.1. First-Principles Calculations using CASTEP

3.2.1.1. Computational Parameters and Crystallographic Models

CASTEP was used for total energy calculations and geometry optimization of K_2ZrF_6 and K_2HfF_6 unit cells and $K_2Zr_{(1-z)}Hf_zF_6$ solid solutions. As previously mentioned, CASTEP employs DFT and uses the pseudopotential plane-wave method. The plane-wave basis functions used to approximate the valence-electron orbitals (wave functions) were tested for convergence in the cutoff energy range of 330 eV to 510 eV, using the unit cell of K_2ZrF_6 as test system. As will be explained in Section 3.3.1.1, a cutoff energy of 450 eV was chosen to perform further calculations. Although, the calculations were not performed using the cutoff energy of 450 eV in a single run, instead, the structures were first optimized using a cutoff energy of 330 eV after which geometry optimizations were performed on the 330 eV-optimized structures again using the 450 eV cutoff energy. Some calculations were performed using only a cutoff energy of 330 eV to save on computational time as will be shown in Section 3.3.1. The plane-wave basis functions were integrated over the Brillouin-zone [14] that consisted of a mesh of *k*-points with a spacing of approximately 0.04 Å^{-1}. A Gaussian smearing width of 0.1 eV (which seemed to be adequate for all calculations), was used for the electronic energy levels to prevent discontinuities in the energy during the iterative self-consistent procedure, whereby convergence was ensured. The Broyden-Fletcher-Goldfarb-Shanno (BFGS) minimization algorithm was used for geometry optimization in all the calculations whereby both the internal atomic coordinates and cell parameters were optimized. Using these settings, total energy convergence of at least 10^{-5} eV/atom could be achieved.

The calculations were initially performed using the generalized gradient approximation (GGA) of Perdew, Burke and Ernzerhof (PBE) as the exchange-correlation functional [15], and the ultrasoft pseudopotential scheme [16] for approximation of the interactions of the valence electrons with the ion-cores. Since the type of functional that is used can also

influence the accuracy of the modelling results, additional calculations were performed using different exchange-correlation functionals to test the accuracy of the GGA-PBE functional when modelling the K_2ZrF_6 – K_2HfF_6 system. The additional functionals that were tested included the LDA – CA-PZ (Local Density Approximation), GGA-PW91, and GGA-RPBE functionals. The valence states used for each element in the present ultrasoft scheme were as follows: K: $3s^2\ 3p^6\ 4s^1$, F: $2s^2\ 2p^5$, Zr: $4s^2\ 4p^6\ 4d^2\ 5s^2$, and Hf: $5d^2\ 6s^2$. An alternative ultrasoft pseudopotential for Zr was also tested that allowed the number of valence electrons of Zr and Hf to be equal, where the valence electrons used by the alternative pseudopotential for Zr is $4d^2\ 5s^2$. The ultrasoft pseudopotential for Zr that uses 12 valence electrons will be referred to as Ultrasoft A and the alternative pseudopotential that uses only 4 valence electrons will be referred to as Ultrasoft B.

The modelling results as presented in Section 3.3.1, were obtained using the method outlined above. The experimentally determined crystal structure data for K_2ZrF_6 and K_2HfF_6 of Bode and Teufer [6] was used as starting structures in geometry optimizations of the unit cells of the two compounds. $K_2Zr_{(1-z)}Hf_zF_6$ solid solutions were modelled using 1x1x2 supercells, which corresponds with expanding the unit cell twofold in the c-axis direction. The result is a crystal structure containing a total of eight Zr and/or Hf-atoms enabling one to simulate solid solutions with molar compositions of z = 0.0, 0.125, 0. 375, 0.5, 0.625, and 1.0 by the substitution of Zr-atoms with Hf-atoms in the lattice. Therefore, the crystal structure obtained by repeating the unit cell in a specific direction is used to describe solid solutions or mixed crystals [17, 18]. Note that z represents the molar fraction of Hf in the mixed crystals and should be read as z_{Hf} but to simplify subsequent expressions the subscript Hf is ignored. The unit cell, which was reduced to the corresponding primitive cell to increase computational efficiency during geometry optimizations of K_2ZrF_6 (as well as for K_2HfF_6), and the supercell used to model $K_2Zr_{(1-z)}Hf_zF_6$ with z = 0.125, is shown in Fig. 3.1 (a) and (b) respectively.

This crystallographic model used to study the isomorphic crystal structures of K_2ZrF_6 and K_2HfF_6, has an orthorhombic geometry with space group symmetry Cmcm (D_{2h}^{17}). It should be noted that modelling of supercells with the same symmetry as the unit cell were found to be only possible at low cutoff energies; at high cutoff energies the program failed to perform the calculations. However, when the space group is changed to Pmm2 (C_{2v}^1) with the substitution of a Hf-atom for a Zr-atom, calculations at higher cutoff energies are possible.

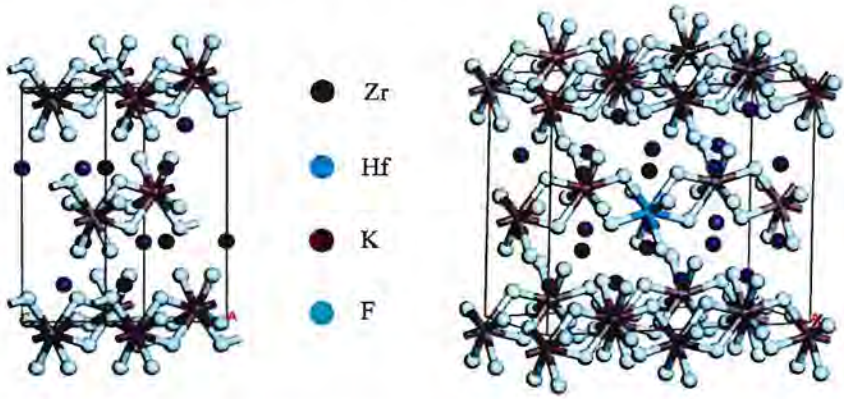

(a) (b)

Figure 3.1: Unit cell of K_2ZrF_6 (a), and supercell of $K_2Zr_{(1-z)}Hf_zF_6$ with $z = 0.125$ (b).

With this change, the structure remains that of an orthorhombic cell but the **b**- and **c**- axis are interposed, while the cell volume remains unchanged. The reason for this problem is apparently related to memory issues with the computer system used for these calculations. Nevertheless supercells of this type were employed for the simulation of solid solutions with compositions of $z = 0.0$ to $z = 1.0$.

3.2.1.2. Thermodynamic Properties

The computed total electronic energies of the mixed crystals with varying composition were referenced to the electronic energy of the constituent elements to calculate the formation enthalpies as a function of composition according to Equation (3.1) [19, 20]:

$$\Delta H_{form} = E_{tot}(K_2Zr_{(1-z)}Hf_zF_6)/8 - z.E_{Hf} - (1-z).E_{Zr} - 2E_K - 6E_F \qquad (3.1)$$

Thus, the formation enthalpy can be viewed as the enthalpy change for the reaction given in Equation (3.2):

$$zHf\,(s) + (1-z)Zr\,(s) + 2K\,(s) + 2F\,(s) \rightarrow K_2Zr_{(1-z)}Hf_zF_6\,(s) \qquad (3.2)$$

In Equation (3.1), $E_{tot}(K_2Zr_{(1-z)}Hf_zF_6)$ is the total energy of the supercells and is divided by 8 to obtain the energy per mole of M^{4+} (M = Zr/Hf, in this case a total of eight Zr and Hf atoms). E_{Zr}, E_{Hf}, E_K and E_F is the energy per atom of Zr, Hf, K and F respectively, where all energies are given in eV from which ΔH_{form} was calculated and converted to $kJ.mol^{-1}$. This method of calculation is similar to that used by Ghosh et al. [20] (Section 3.3.1.2.B) in their study of Al-transition metal alloys and differs only in the sense that the formation enthalpy is calculated here in moles per formula unit and not per mole atom. Calculations that were reproduced from their data on Zr- and Hf-alloys, were also performed to determine the reliability of the computational setup described above, the results of which will be presented in Section 3.3.1.2.B. These formation enthalpy calculations were performed to test the accuracy of the calculated thermodynamic properties against available experimental data of ZrF_4 and HfF_4. To the best of our knowledge no such experimental data has been published for the potassium salts.

The zirconium- and hafnium fluorides ($Zr(Hf)F_4$) have also been modelled using the same methods described above, for comparison with the calculated data of $K_2Zr(Hf)F_6$ and the experimental data of the fluorides, which will be discussed in Sections 3.3.1.4, 3.3.1.5 and 3.3.2.1.A. The energy of Zr, Hf, and K were determined by modelling of the pure compounds in their ground state crystal structures. The ground state structures of elemental Zr and Hf are $P6_3/mm2$ (D^4_{6h}) and that of K is Im-3m (O^9_h). These structures are available in the structural database of CASTEP and were modelled using the same plane-wave basis set cutoff energy, exchange-correlation functional, ultrasoft pseudopotentials, and accuracy as for the $K_2Zr_{(1-z)}Hf_zF_6$ solid solutions. For fluorine, the bond distance of a F_2 molecule was determined with DFT calculations on an isolated F_2 molecule. A periodic structure of F_2 was then modelled with CASTEP by placing F_2 molecules with the determined bond distance at the vertices of a simple, large cubic cell with space group symmetry P1. With this method the electronic energy of fluorine was calculated, again, using the same parameters and accuracy as for the other calculations. The unit cells of Zr, Hf, K, and the F_2-structure as described above are shown in Fig. 3.2.

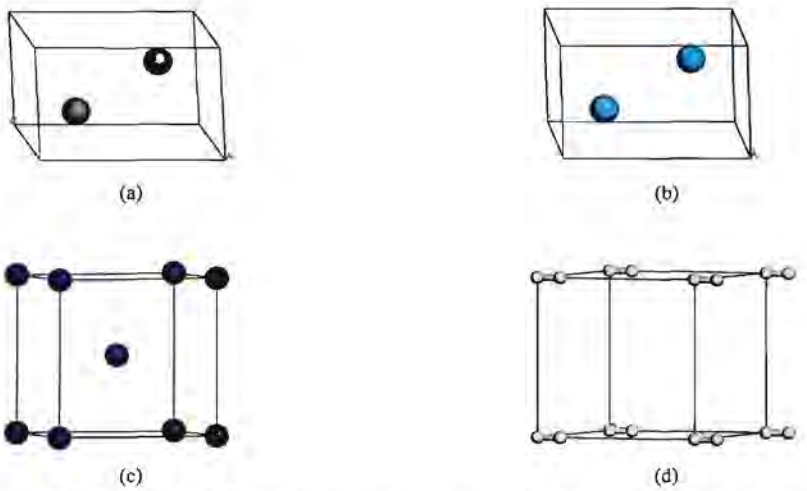

Figure 3.2: Unit cells of Zr (a) and Hf (b) with $P6_3/mm2 - D^4_{6h}$ symmetry, K (c) with $Im\text{-}3m\text{-}O^9_h$ symmetry, and the periodic F_2-P1 structure (d) used for electronic energy calculations with CASTEP of the respective constituent elements of both $K_2Zr_{(1-z)}Hf_zF_6$ and ZrF_4 and HfF_4.

The experimental crystal structure data of the α-polymorph of ZrF_4 [21] was used as input structure for the modelling of both ZrF_4 and HfF_4 unit cells, using the same functional (GGA-PBE), computational accuracy and ultrasoft pseudopotentials (both type A and B) as for the modelling of $K_2Zr_{(1-z)}Hf_zF_6$. The formation enthalpies were calculated using the same method as for the potassium salts. The tetragonal unit cell of α-ZrF_4 with space group symmetry $P4_2/m$ is shown in Fig. 3.3, which was also used for the modelling of HfF_4 by simply replacing the Zr-atoms with Hf-atoms, as it is assumed that the two structures are isomorphic by analogy with the pure metals of Zr and Hf and the potassium salts.

The determination of the thermodynamic properties of mixing, in particular the mixing enthalpy, forms the basis of this study and is crucial for implementation in the thermodynamic model that is used to describe the separation efficiency of the compounds via crystallization.

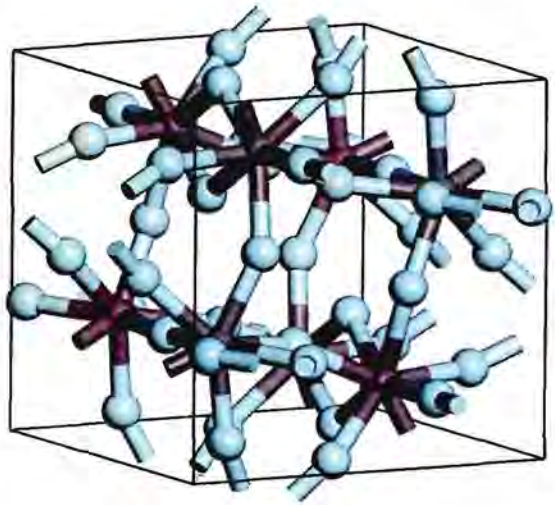

Figure 3.3: Unit cell of α-ZrF_4 with $P4_2/m$ symmetry used for modelling of ZrF_4 and HfF_4.

The mixing enthalpies for the formation of $K_2Zr_{(1-z)}Hf_zF_6$ solid solutions were calculated by subtracting the calculated total energy of the $K_2Zr_{(1-z)}Hf_zF_6$ supercells from the sum of the weighted average energies of the pure structures [17, 18, 22 - 24], which translates to the amount of energy needed to form solid solutions from the pure constituent compounds. This is expressed in Equation (3.3):

$$\Delta H_{mix} = E_{tot}(K_2Zr_{(1-z)}Hf_zF_6) - z.E_{tot}(K_2HfF_6) - (1-z).E_{tot}(K_2ZrF_6) \quad (3.3)$$

where the mixing enthalpy is thus the enthalpy change for the reaction presented in Equation (3.4).

$$zK_2HfF_6\,(s) + (1-z)K_2ZrF_6\,(s) \rightarrow K_2Zr_{(1-z)}Hf_zF_6\,(s) \quad (3.4)$$

In Equation (3.3), E_{tot} is the total energy of the corresponding supercells (eV), from which ΔH_{mix} can be calculated and converted to $kJ.mol^{-1}$. The mixing enthalpy was therefore calculated for each of the modelled compositions, and by using this data it is possible to determine the mixing enthalpy for the entire composition range using the regular solution

model (Section 3.3.1.5). Because the simulations were performed in vacuum and thus there is no external pressure acting on the system, the enthalpy change can be assumed to be equal to the energy changes as calculated with Equations (3.1) and (3.3). Also, because of the small difference between the unit cell parameters of K_2ZrF_6 and K_2HfF_6 (Section 3.3.1.1), it can be shown that the difference in the molar volume of the two compounds are negligible in comparison with the internal energy (or energy calculated via molecular modelling) which also supports the assumption that $\Delta H = \Delta E$.

To summarize, the supercell method using 1x1x2 supercells of the unit cells were used for the simulation of $K_2Zr_{(1-z)}Hf_zF_6$ solid solutions as described above. The thermodynamic properties of solid solution formation could then be determined, which is used to theoretically evaluate the separation efficiency via crystallization, the method of which is discussed in Sections 3.3.1.5 and 3.3.2.1.B. Due to the complex structure of $K_2Zr(Hf)F_6$ which causes calculations to be very time intensive on the workstation setup used in this study, I was restricted to using the relatively small 1x1x2 supercell for modelling the solid solutions. Therefore the restrictions of the method mentioned in Section 2.3.2.1.B could not be overcome. Furthermore, the alternative VCA method (discussed in Section 2.3.2.1.A) seemed to yield unrealistic results with both the $K_2Zr(Hf)F_6$, and the Zn(Be)O [18] test system that was used to gauge the accuracy of the present supercell method with the selected computational parameters to predict the thermodynamic mixing properties (of which some results are presented in Section 3.3.1.2.A). Because of this difficulty and the fact that some calculations with the VCA method failed to converge, this method was not investigated further and only the present supercell method was used. In addition, simulations of the tetrafluorides of Zr and Hf were also performed for quantitative comparison of the thermodynamic data with the corresponding potassium salts and the available experimental data of the fluorides. Other test calculations were also performed using published data of Al-transition metal alloys [20] to test the reliability of the computational setup as employed in this study.

3.2.2. Energy Calculations using DMol^3

In addition to solid-state calculations of $K_2Zr_{(1-z)}Hf_zF_6$ solid solutions using the numerical basis sets of DMol^3, the program has also been used for thermodynamic calculations of the solvation of K_2ZrF_6 and K_2HfF_6 on a molecular level. The COSMO model was employed to study solvation effects as will be described in the subsequent sections.

3.2.2.1. Solid-State Calculations

Although DMol^3 is traditionally applied to molecular systems, the use of its numerical basis functions were investigated for the modelling of $K_2Zr(Hf)F_6$ solid solutions using the same crystallographic models as described in the previous section. For simulation of the solid solutions, geometry optimizations were not performed as is the case with CASTEP. A much simpler and easier approach was followed in which the total energy of the CASTEP-optimized structures were calculated using DMol^3, which is referred to as single point energy calculations. These single point energy calculations were performed to save on computational time. For the purpose of this study the optimized structures of only the 450 eV, GGA-PBE, Ultrasoft A dataset (which included the $K_2Zr_{(1-z)}Hf_zF_6$ supercells as well as the unit cells of ZrF_4 and HfF_4) were used for energy calculations in DMol^3. The results were then used to calculate the different thermodynamic properties using the same methods as for the CASTEP results. For calculating the formation enthalpies using the DMol^3 data, the energies of the optimized structures of Zr, Hf, and K, as well as the energy of the periodic F_2-structure (all from the same dataset as the supercells) were calculated in the same manner.

All these calculations were performed using the same GGA-PBE exchange-correlation functional as with CASTEP along with the DND numerical basis set for the atomic orbitals of the elements. An all-electron treatment of the atomic orbitals was chosen which means that the valence electron and core electron interactions are not approximated using a potential field (pseudopotential as in CASTEP). An orbital cutoff of no larger than 5.6 Å was used in which all calculations were treated as spin restricted, meaning that different orbitals are not used to distinguish between electrons with opposite spin, which would increase computational time, and besides should not play a major role if the studied structures are not spin polarized. The Brillouin-zones of all crystallographic lattices were sampled using the same approximate *k*-point spacing of 0.04 Å^{-1} as with CASTEP. The same computational accuracy and convergence tolerance was used throughout for all calculations.

3.2.2.2. Solvation Energy Calculations

The purpose of these calculations was to determine whether there exists a significant difference between the energy changes during the crystallization of K_2ZrF_6 and K_2HfF_6 from solution. The method used to determine these energy changes will be explained in Section 3.3.2.2, while only the computational details are given in this section. The energy of the pure

K_2ZrF_6 and K_2HfF_6 supercells, calculated using the DMol^3 method described above, was taken as the energy of the pure crystals. The energy of the dissociated ions, namely K^+ and $Zr(Hf)F_6^{2-}$, was calculated separately using the same computational parameters as for the supercells of K_2ZrF_6 and K_2HfF_6 (Section 3.2.2.1). For the MF_6^{2-}-ions, an octahedral molecular structure was used with the appropriate total electronic charge, which was then geometrically optimized using DMol^3. The molecular models of ZrF_6^{2-} and HfF_6^{2-} are shown in Fig. 3.4. These optimizations were performed in vacuum conditions, which is the case with most molecular modelling calculations, and therefore no external effects are considered.

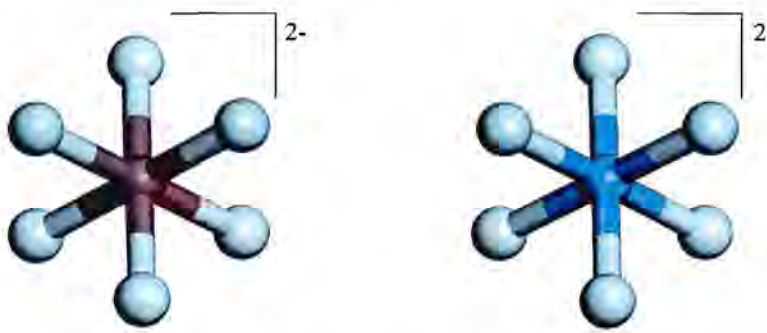

Figure 3.4: Molecular models of ZrF_6^{2-} (left) and HfF_6^{2-} (right) with O_h symmetry used for solvation energy calculations with DMol^3.

For the description of the effect of solvation, the same procedure was used but this time geometry optimizations of the MF_6^{2-}-ions and the energy calculation of the K^+-ion were performed using the COSMO model [25, 26, 27] as implemented in DMol^3 (Section 2.3.3). Accordingly, for the description of the solvation of the ions in water, a dielectric constant of 78.54, corresponding with that of water was used. Therefore, as explained in Section 2.3.3, the ions are modelled as solvated species by placing them in a dielectric continuum whereby polarization effects are taken into account [25].

The DND basis set together with the GGA-PBE functional was also used for all these calculations, as well as the same orbital cutoff and computational accuracy as for the solid phase calculations and vacuum geometry optimizations. In addition, all the calculations described in this section were also repeated using another basis set (DNP) but keeping the

other computational parameters constant. This was done to compare the calculated thermodynamic properties determined using the two basis sets, thus determining the reliability when using the numerical basis sets for the Zr- and Hf-species. The difference between the DND and DNP basis sets is that although the same numerical orbitals are used in the two basis sets, the DNP basis set includes a polarization function that more accurately describes hydrogen-bonding.

3.3. Results and Discussion

3.3.1. First-principles Calculations using CASTEP

3.3.1.1. Optimization of the Modelling Method

The experimentally determined crystallographic data of K_2ZrF_6 and K_2HfF_6 that was used as starting structures for the cutoff energy convergence tests is summarized in Table 3.1, showing the lattice parameters of both unit cells.

Table 3.1: Experimentally determined lattice parameters of the isomorphic, orthorhombic unit cells of K_2ZrF_6 and K_2HfF_6 with space group symmetry Cmcm – D_{2h}^{17} [6].

Lattice Parameter (Å)	K_2ZrF_6	K_2HfF_6
a	6.58	6.58
b	11.40	11.40
c	6.94	6.89

The change in the lattice parameters, as well as the total electronic energy with increasing cutoff energy for the K_2ZrF_6 unit cell, is shown in Table 3.2. These results were obtained using the GGA-PBE functional and the Ultrasoft A pseudopotential along with the other computational parameters outlined in Section 3.2.1.1. The data indicates that (i) the lattice parameters do not change significantly with increasing cutoff energy and (ii) the computed quantities do not converge to a single value, but rather oscillate, especially at higher cutoff energies. By increasing the cutoff energies even further the oscillation might decrease, however the computation time would increase while the accuracy would not change appreciably. The results obtained with a cutoff energy of 450 eV seem to give the most adequate description of the experimental data.

Table 3.2: Lattice parameters and computed total electronic energy of the K_2ZrF_6 unit cell modelled with increasing cutoff energy using the GGA-PBE functional and the Ultrasoft A pseudopotential computational scheme.

Cutoff Energy	330 eV	370 eV	390 eV	430 eV	450 eV	510 eV
a (Å)	6.679	6.645	6.634	6.627	6.628	6.636
b (Å)	11.982	11.713	11.697	11.682	11.677	11.687
c (Å)	6.974	6.952	6.942	6.949	6.949	6.948
Energy (eV)	-13688.31	-13688.79	-13688.82	-13688.85	-13688.89	-13689.09

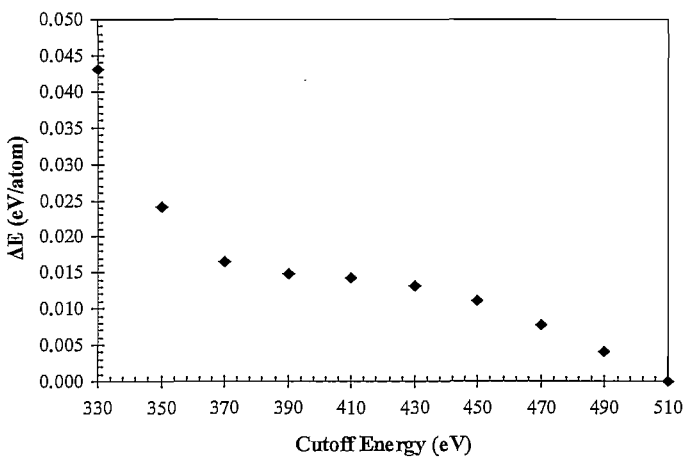

Figure 3.5: Plane-wave energy cutoff convergence for K_2ZrF_6 using the GGA-PBE functional and Ultrasoft A pseudopotential scheme.

Furthermore, as shown in Fig. 3.5, the energy convergence improves as the cutoff energy is increased, in other words the amount by which the computed total energy changes, decreases with increasing cutoff energy. In this case, ΔE represents the difference between the calculated electronic energy at a specific cutoff energy and the electronic energy at a cutoff energy of 510 eV, wherein the energy difference is evaluated per atom. From these results we can also see that convergence seems to be achieved faster as the cutoff energy is increased beyond 450 eV. Therefore, based on these results, the cutoff energy of 450 eV was selected as

being the most appropriate for further modelling studies when considering the increase in computational time with increasing cutoff energy.

The exchange-correlation functional tests were performed with the unit cells of both K_2ZrF_6 and K_2HfF_6 at cutoff energies of 330 eV and 450 eV using the Ultrasoft A pseudopotential scheme and the same computational parameters as for the convergence test. The results obtained from different functionals were compared with the experimental crystal structure data of both compounds respectively by calculating the percentage difference between the experimentally determined lattice parameters and the calculated parameters. Therefore, the lower the percentage differences, the greater the accuracy of a particular functional. The results for K_2ZrF_6 are shown in Table 3.3, in which the GGA-PBE data is also included.

Table 3.3: Results of K_2ZrF_6 exchange-correlation functional tests at cutoff energies of 330 eV and 450 eV. Values represent the percentage deviation from the experimental crystallographic data [6].

Functional	Cell Parameters 330 eV			Cell Parameters 450 eV		
	a	b	c	a	b	c
GGA-PBE	1.509	5.105	0.483	0.729	2.431	0.132
GGA-RPBE	3.440	7.877	3.114	2.804	6.022	2.406
GGA-PW91	1.450	4.861	0.390	0.553	2.344	0.067
LDA-CA-PZ	-2.419	-2.355	-3.039	-3.078	-3.250	-3.425

The results show that the GGA-PBE and GGA-PW91 give the best correlation with each other, and the smallest deviation from the experimental results in comparison with the other two functionals. It is also clear that as the cutoff energy is increased, the accuracy also increases as the percentage deviation decreases for all functionals, except for the LDA functional. Here the calculated cell parameters are underestimated in comparison with the experimental parameters. With increasing cutoff energy the cell parameters decreases further, therefore leading to the reduced accuracy for this functional. The lattice parameters are overestimated by the GGA-RPBE functional to a larger extent than for the other two GGA functionals. Therefore, the GGA-RPBE and LDA-CA-PZ functionals give the poorest results and the GGA-PBE and GGA-PW91 give the best results and correlate well with each other at both low and high cutoff energies.

The corresponding results for K_2HfF_6 are shown in Table 3.4. According to the results, the GGA-PBE and GGA-PW91 functionals again show the best correlation with each other for K_2HfF_6. However, in this case the LDA functional gives better results than the GGA functionals, while the GGA-RPBE functional still yields the poorest results. For solid solutions (mixed crystals) of $K_2Zr(Hf)F_6$, the GGA-PBE or GGA-PW91 functionals therefore are the best options as they give good results for both K_2ZrF_6 and K_2HfF_6. These results therefore confirm the applicability of the GGA-PBE functional as it was used for the convergence test, which was also the functional used for modelling $K_2Zr_{(1-z)}Hf_zF_6$ solid solutions.

Table 3.4: Results of K_2HfF_6 exchange-correlation functional tests at cutoff energies of 330 eV and 450 eV. Values represent the percentage deviation from the experimental data.

Functional	Cell Parameters 330 eV			Cell Parameters 450 eV		
	a	b	c	a	b	c
GGA-PBE	3.625	4.930	2.732	2.638	2.844	2.456
GGA-RPBE	5.762	7.731	5.016	4.962	6.258	4.389
GGA-PW91	3.276	5.163	3.176	2.465	2.784	2.607
LDA-CA-PZ	-0.546	-1.883	-0.445	-1.130	-2.648	-0.878

To determine whether the use of the Ultrasoft B pseudopotential has a significant influence on the results of the thermodynamic calculations of solid solutions, this alternative pseudopotential for Zr was used in addition to the Ultrasoft A pseudopotential. Solid solution simulations were however only performed at a plane-wave cutoff energy of 330 eV for the Ultrasoft B pseudopotential. Firstly however, the applicability of the Ultrasoft B pseudopotential for modelling of $K_2Zr_{(1-z)}Hf_zF_6$ solid solutions was tested using the unit cell of K_2ZrF_6. Note that only pure K_2ZrF_6 has to be tested as the use of the different pseudopotentials for Zr will not influence the pure K_2HfF_6 calculations (both for the unit cell and the 1x1x2 supercell). The GGA-PBE functional was used for this test at cutoff energies of 330 eV and 450 eV together with the rest of the computational parameters used for the other calculations.

The results of both the Ultrasoft A and B pseudopotentials are shown in Table 3.5. From the results we see that, in general, the Ultrasoft A pseudopotential predicts the lattice parameters

more accurately at both 330 eV and 450 eV cutoff energies (compare the calculated parameters with the experimental data shown in Table 3.1). There is not a large difference between the results of the two pseudopotentials however, and therefore the Ultrasoft B pseudopotential was also applied in solid solution modelling, and its influence on the thermodynamic properties of $K_2Zr_{(1-z)}Hf_zF_6$ solid solutions will be discussed in Sections 3.3.1.4 and 3.3.1.5. The large difference observed between the electronic energies of the different pseudopotentials is due to the different valence states used, as explained in Section 3.2.1.1. Therefore, only by comparing the total electronic energies of structures modelled using the same parameters, can meaningful results be obtained.

Table 3.5: Lattice parameters and total electronic energy of K_2ZrF_6 unit cells using ultrasoft pseudopotentials A and B for Zr together with the GGA-PBE functional at cutoff energies of 330 eV and 450 eV.

	Ultrasoft A		Ultrasoft B	
Parameter	**330 eV**	**450 eV**	**330 eV**	**450 eV**
a (Å)	6.679	6.628	6.777	6.722
b (Å)	11.982	11.677	11.879	11.684
c (Å)	6.974	6.949	6.996	6.975
E (eV)	-13688.31	-13688.89	-11285.76	-11286.39

The results presented in this section show that the computational parameters used for solid solution modelling as described in Section 3.2.1.1, give adequate results with respect to experimental data in comparison with the other parameters that have been tested. In short, it was shown that the use of a cutoff energy of 450 eV, as determined from the convergence test, together with either the GGA-PBE or GGA-PW91 exchange-correlation functionals are best suited for solid solution modelling. Subsequently, the GGA-PBE functional was used with a cutoff energy of 450 eV together with the Ultrasoft A pseudopotential for this very purpose. However, the tests showed that there is no significant difference between the Ultrasoft A and B pseudopotentials and therefore the Ultrasoft B pseudopotential (with the GGA-PBE functional) was also used in solid solution simulations, which allows comparison between the thermodynamic data as predicted by the two pseudopotentials. It should be kept in mind though that a cutoff energy of only 330 eV was used for simulations with the Ultrasoft B pseudopotential scheme to save computational time.

3.3.1.2. $Be_xZn_{1-x}O$ and Al-TM Test Systems

3.3.1.2.A. $Be_xZn_{1-x}O$ Alloys

An attempt was made to reproduce some of the published data of Ding et al. [18], who studied $Be_xZn_{1-x}O$ alloys also using CASTEP, to test the reliability of our computational setup. In their publication, they report that 16-atom 2x2x1 $Be_xZn_{1-x}O$ supercells, as shown in Fig. 3.6., with the wurtzite structure were used to simulate the alloys. They also used a cutoff energy of 450 eV with the ultrasoft pseudopotentials. Using the configuration shown in Fig. 3.6, they were able to simulate different alloy compositions by replacing Zn-atoms with Be-atoms, in much the same way as was done with the $K_2Zr_{(1-z)}Hf_zF_6$ solid solutions in this study. For the purpose of the test, only the alloy composition $x = 0.125$ was chosen, which corresponds with replacing one Zn-atom for a Be-atom as illustrated in Fig. 3.6.

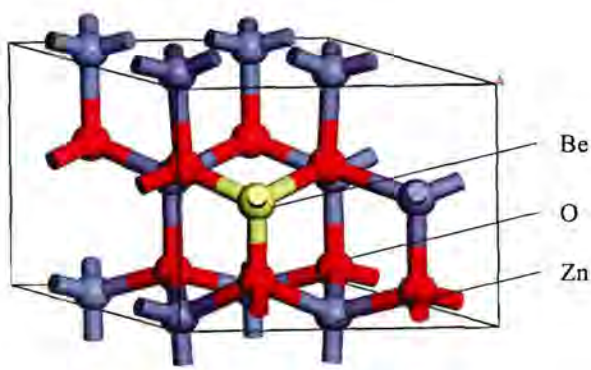

Figure 3.6: 2x2x1 Supercell of $Be_{0.125}Zn_{0.875}O$ with P3m1 (C_{3v}^1) symmetry.

The same cutoff energy and ultrasoft pseudopotentials employed by the authors were used for this test, where the valence states that were used by the ultrasoft pseudopotentials were as follows: Be: $2s^2$, Zn: $3d^{10}$ and O: $2s^22p^4$. The rest of the computational parameters that were used for the test are the same as discussed in Section 3.2.1.1. The ZnO crystal structure is available as part of CASTEP's structural database and was used to construct a 2x2x1 supercell just as the authors did, and was used for modelling the pure ZnO supercell and the $Be_xZn_{1-x}O$ alloy with $x = 0.125$. For this test the published results of the pure BeO supercell were used as

available from literature. In Table 3.6, the results of the modelled ZnO and $Be_xZn_{1-x}O$ at x = 0.125 are compared with the published data.

The authors [18] calculated the mixing enthalpies of the alloys with different compositions, which they referred to as the formation energies, to evaluate the thermodynamic stability of the alloys. This was done with the same method used in this study to determine the mixing enthalpies of $K_2Zr_{(1-z)}Hf_zF_6$ solid solutions according to Equation (3.3), which is discussed in Section 3.3.1.5.

Table 3.6: Comparison between modelling results and published data of ZnO and $Be_{0.125}Zn_{0.875}O$.

Lattice Parameters/	ZnO		$Be_{0.125}Zn_{0.875}O$	
Energy	This Study	Ding et al.[18]	This Study	Ding et al.[18]
a = b (Å)	3.257	3.257	3.191	3.193
c (Å)	5.255	5.258	5.147	5.147
Total Energy (eV)	-17246.584	-17246.584	-15562.672	-15562.672*

* Calculated from published data by rewriting Equation (3.5).

By applying this method to the $Be_xZn_{1-x}O$ system, Equation (3.3) can then be written in the form of Equation (3.5), which was used by Ding et al. to determine the formation energy and is here referred to ΔH_{mix} for consistency:

$$\Delta H_{mix} = E_{tot}(Be_xZn_{1-x}O) - x.E_{tot}(BeO) - (1-x).E_{tot}(ZnO) \qquad (3.5)$$

Using the results of ZnO and $Be_{0.125}Zn_{0.875}O$ presented in Table 3.6, and the published total energy of BeO together with Equation (3.5), gives a value for ΔH_{mix} of 0.497 eV in comparison with a value of 0.498 eV given by Ding et al. [18]. This excellent correlation of the ΔH_{mix}-values, the lattice parameters and total energies with the published data (Table 3.6) therefore confirms that the methods used in this study yields results that are consistent with published data.

3.3.1.2.B. Al-TM Intermetallics

In the previous section it was shown that data from other authors could be satisfactorily reproduced using the computational setup applied in this study. However, with the exception of the experimental data of the tetrafluorides of Zr and Hf, discussed in Section 3.3.1.4, and the experimental crystal structures of K_2ZrF_6 and K_2HfF_6, no other benchmark could be found to validate the modelling results of the Zr- and Hf-systems investigated in this study. Ghosh et al. [20] however, conducted a comprehensive study on 69 aluminium-transition metal alloys (Al-TM) with TM = Ti, Zr and Hf, also using DFT methods. They used a simulation program known as VASP, instead of CASTEP, which also uses the pseudopotential plane-wave method with GGA exchange-correlation functionals. The authors used the VASP implementation of ultrasoft pseudopotentials, which differs from that of CASTEP, with a plane-wave cutoff energy of 281 eV along with the GGA-PW91 exchange-correlation functional. They also used a Gaussian smearing width of 0.1 eV of the electronic energy levels. Using this basic calculation method they evaluated the zero temperature formation enthalpies of alloys with different compositions, amongst other physical properties.

To simulate alloys (solid solutions) of different compositions, they did not use the supercell method (this study), but instead modelled the alloys using physical crystallographic data obtained from a comprehensive literature survey. For example, the crystallographic model used to simulate the alloy Al_3Zr is shown in Fig. 3.7 (a), which has the space group symmetry I4/mmm. This alloy together with its Hf-analogue (Al_3Hf, which is isomorphic to the Zr-alloy) was chosen as test models to gauge the reliability of the CASTEP implementation of the Zr- and Hf-pseudopotentials in particular. Consequently, both the Zr-pseudopotentials (Ultrasoft A and Ultrasoft B) were tested with these structures. This simultaneously presented an opportunity to test my method of calculating the formation enthalpies, because the authors used virtually the same method in their study, where the electronic energies of the alloys are referenced to the electronic energies of the constituent elements according to:

$$\Delta H_{form} = \frac{E_{tot}(Al_mTM_n)}{m+n} - \left[\frac{m}{m+n}E(Al) + \frac{n}{m+n}E(TM)\right] \qquad (3.6)$$

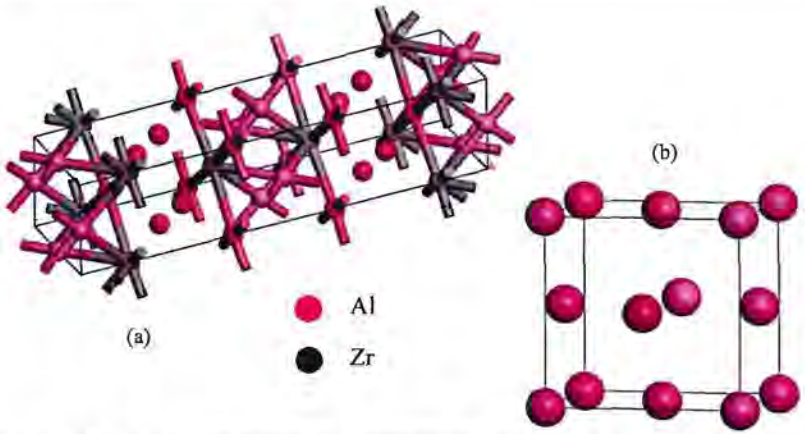

Figure 3.7: Al_3Zr alloy with I4/mmm (D_{4h}^{17}) symmetry and unit cell of Al with Fm-3m (O_h^5) symmetry used for formation enthalpy calculations [20].

In Equation (3.6), m and n represent the total number of atoms of each atomic species in the crystallographic model. Therefore, the energy of the transition metal alloy, and the resulting formation enthalpy is evaluated per atom. E(Al) and E(TM) is the electronic energy per atom of the pure metals which is subtracted from the energy of the alloy in the appropriate fraction. The electronic energies of the atomic species were also calculated by the authors, via the modelling of the equilibrium crystal structures of the elements. The corresponding Zr- and Hf-metals were already modelled for the very purpose of calculating the formation enthalpies of $K_2Zr_{(1-z)}Hf_zF_6$ solid solutions and of ZrF_4 and HfF_4. The structures used for Zr and Hf in this study, were the same crystal structures used by the authors in their study. Therefore, all that was left to do was to model the corresponding Al crystal structure (shown in Fig. 3.7 (b)) to determine its electronic energy, as well as to model the Al_3Zr and Al_3Hf alloys using our CASTEP method. As was mentioned previously, both the Ultrasoft A and B pseudopotentials were tested. This was done with the same computational parameters used in this study (Section 3.2.1.1) at both low and high cutoff energies of 330 eV and 450 eV for both pseudopotentials and employing the GGA-PBE functional throughout. Note that the use of an equation of the type shown in Equation (3.6) with both the data of the $K_2Zr_{(1-z)}Hf_zF_6$ solid solutions and tetrafluorides can easily be implemented. For the solid solutions, one simply needs to divide Equation (3.1) by 9 to obtain the formation enthalpy per mole atom. This also applies to calculations with ZrF_4 and HfF_4 where Equation (3.8) can be divided by the total

number of atoms in one formula unit, which in that case amounts to 5. For the purpose of comparing the calculated formation enthalpies of $K_2Zr_{(1-z)}Hf_zF_6$ solid solutions and $Zr(Hf)F_4$ with the experimental data of the tetrafluorides (Section 3.3.1.4), the formation enthalpies of those compounds will however be given per mole formula unit or in other words per mole M^{4+} (M = Zr/Hf).

The crystal structure of Al was obtained from the structural database of CASTEP, while the isomorphic Al_3Zr and Al_3Hf alloys, of which Al_3Zr is shown in Fig. 3.7, were constructed using the crystallographic data given by Ghosh et al., obtained from their simulations. The results when modelling the different structures at both cutoff energies of 330 eV and 450 eV, using the Ultrasoft A pseudopotential for Zr, and the normal ultrasoft pseudopotentials for the other elements are shown in Table 3.7, together with the published data of Ghosh et al. [20].

Table 3.7: Lattice Parameters and energies of alloys and pure metals modeled using different cutoff energies with the Ultrasoft A pseudopotential for Zr. Also included is published data of Ghosh et al. [20].

	330 eV			450 eV			Ghosh et al. [20]	
Metal/ Alloy	**Lattice Parameters**		**Energy per atom (eV)**	**Lattice Parameters**		**Energy per atom (eV)**	**Lattice Parameters**	
	a (Å)	**c (Å)**		**a (Å)**	**c (Å)**		**a (Å)**	**c (Å)**
Al	3.958	N/A	-57.266	3.958	N/A	-57.267	4.044	N/A
Zr	3.231	5.170	-1285.173	3.227	5.162	-1285.179	3.208	5.133
Hf	3.209	5.082	-410.426	3.208	5.081	-410.430	3.180	5.021
Al_3Zr	3.963	17.157	-364.741	3.963	17.146	-364.743	4.008	17.297
Al_3Hf	3.942	17.025	-145.986	3.942	17.025	-145.988	3.990	17.172

N/A – Not applicable.

From the results it is clear that the data obtained using the CASTEP ultrasoft pseudopotentials with the GGA-PBE functional at both cutoff energies of 330 eV and 450 eV, agree well with the published results of Ghosh et al. [20]. Furthermore, the results change only marginally with an increase in cutoff energy. This is due to the fact that Ghosh and co-workers used a plane-wave cutoff energy of 281 eV, which already provides converged results in comparison with the higher cutoff energies as shown by our results. The observed differences with the

published results can be due to many factors, including the difference in the pseudopotentials of the two programs, the different functional used in this study (i.e. GGA-PBE vs. GGA-PW91) and maybe the most important, the *k*-point spacing that was used by the authors to sample the Brillouin-zone. The data resulting from the use of the Ultrasoft B pseudopotential for Zr is shown in Table 3.8. In general, the lattice parameters contract with the change from the Ultrasoft A pseudopotential to the Ultrasoft B pseudopotential. However, just as with the Ultrasoft A pseudopotential data, the different values only changed marginally with the increase in the cutoff energy.

The resulting formation enthalpies, calculated using Equation (3.6) and converted to $kJ.mol^{-1}$-atom are shown in Table 3.9. Again, the results agree well with those of Ghosh et al.[20].

Table 3.8: Lattice Parameters and energies of the Al_3Zr alloy and pure Zr modeled using different cutoff energies with the Ultrasoft B pseudopotential for Zr. Also included is published data of Ghosh et al. [20].

	330 eV			450 eV			Ghosh et al. [20]	
Metal/ Alloy	Lattice Parameters		Energy per atom (eV)	Lattice Parameters		Energy per atom (eV)	Lattice Parameters	
	a (Å)	c (Å)		a (Å)	c (Å)		a (Å)	c (Å)
Zr	3.129	5.080	-84.667	3.129	5.079	-84.673	3.208	5.133
Al_3Zr	3.910	16.877	-64.700	3.912	16.885	-64.703	4.008	17.297

Note that only the results of Zr-metal and the Al_3Zr-alloy results changes as only the Zr-pseudopotential was changed.

Table 3.9: Formation enthalpies of Al_3Zr and Al_3Hf alloys modelled at different cutoff energies using both Ultrasoft pseudopotentials A and B for Zr. Included is published data of Ghosh et al.

Alloy	Formation Enthalpy, ΔH_{form} ($kJ.mol^{-1}$)				
	Ultrasoft A		Ultrasoft B		Ghosh et al.[20]
	330 eV	450 eV	330 eV	450 eV	
Al_3Zr	-48.079	-48.032	-56.407	-56.404	-49.106
Al_3Hf	-41.530	-41.519	N/A	N/A	-39.632

N/A – Not applicable, values unchanged.

It is clear from Table 3.9 that, the results from the Ultrasoft A pseudopotential deviate less from the published data than the results obtained from the Ultrasoft B pseudopotential scheme. This good correlation for both the Zr- and Hf-alloys indicates that reliable results can indeed be obtained from the computational methods used. Furthermore, the computational parameters used, i.e. different pseudopotentials, a different exchange-correlation functional and different *k*-point grid, yielded satisfactory results compared with that of Ghosh et al. who used a slightly different computational method. Therefore, the suitability of the parameters used in this study to model the different Zr- and Hf-compounds was confirmed both from the viewpoint of the structures modelled in this study (Section 3.3.1.1), as well as of other alloy systems, in particular the Al-alloys of Zr and Hf.

3.3.1.3. Structural Properties of $K_2Zr_{(1-z)}Hf_zF_6$ Solid Solutions

Due to the large amount of computational time needed to model $K_2Zr_{(1-z)}Hf_zF_6$ solid solutions, as mentioned in Section 3.2.1.1, simulations were first carried out at a cutoff energy of 330 eV using the Ultrasoft A pseudopotential. The 330 eV optimized structures were then again optimized using the higher cutoff energy of 450 eV, whereby convergence could be achieved. The resulting structures from the 330 eV Ultrasoft A optimizations were then also used as starting structures for simulations using the 330 eV, Ultrasoft B scheme. In general, the results using a cutoff energy of 450 eV with the GGA-PBE exchange-correlation functional, the Ultrasoft A pseudopotential and the other computational parameters discussed in the method section, will be used in subsequent discussions unless special reference is made to results of the 330 eV cutoff energy Ultrasoft B pseudopotential scheme.

The structural properties of the $K_2Zr_{(1-z)}Hf_zF_6$ solid solutions were studied by observing the change in the lattice parameters of the supercells (Fig. 3.1) with varying composition, z (the mole fraction of Hf). In this regard, Vegard's law [17, 18, 22], which states that the equilibrium physical properties of an alloy or solid solution $A_{(1-z)}B_zC$ may be approximated by the compositional average of the pure-component properties, is useful. For example, if we consider lattice parameter a, its value can be approximated by the linear relationship illustrated in Equation (3.7):

$$a(z) = (1 - z)a_{AC} + z.a_{AB} \qquad (3.7)$$

Representative results of geometry optimizations of the supercells with varying composition are shown in Fig. 3.8. The results of geometry optimizations using the Ultrasoft A pseudopotential at a cutoff energy of 450 eV are shown for lattice parameters a and c in Fig. 3.8 (a) and (b) respectively, and that of the Ultrasoft B pseudopotential at a cutoff energy of 330 eV for lattice parameter b is shown in Fig. 3.8 (c). Note that parameters b and c are interposed in comparison with the unit cells as explained in Section 3.2.1.1. From the results it is evident that minor deviation from Vegard's law exists as indicated by the linear fits, however some fluctuation is also apparent from Fig. 3.8. (b), where the computed data deviates more from linearity.

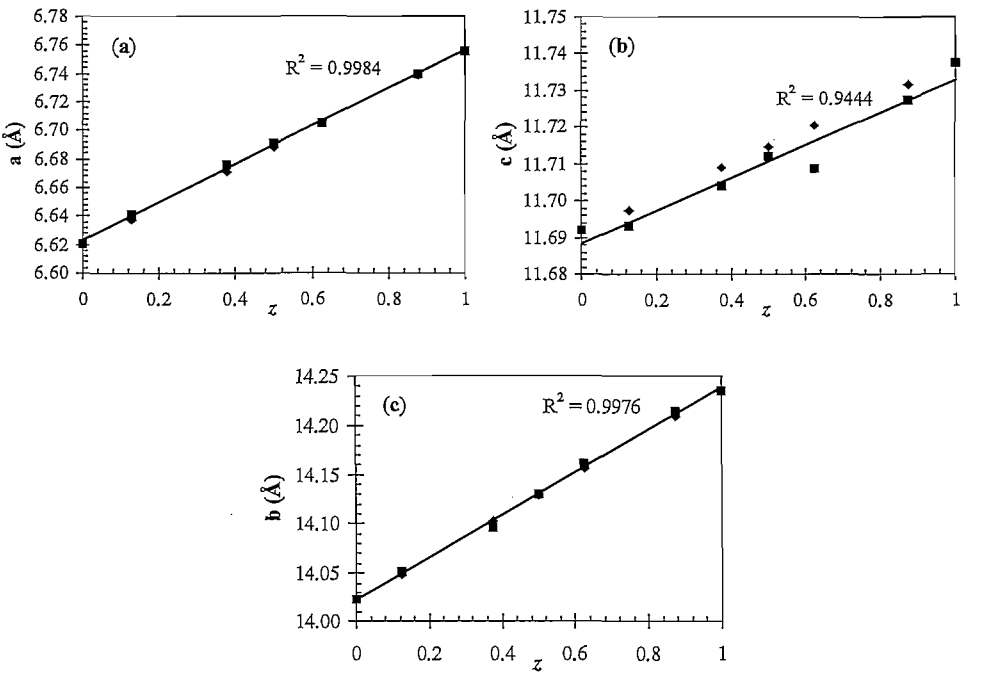

Figure 3.8: Lattice parameters of $K_2Zr_{(1-z)}Hf_zF_6$ supercells as a function of composition, *z*. (a) and (b): lattice parameters a and c respectively resulting from geometry optimizations using the 450 eV, Ultrasoft A scheme. (c): Lattice parameter b resulting from geometry optimizations using the 330 eV, Ultrasoft B scheme. Both the computed (■) and averaged (♦) parameters are shown. Linear fits are for the computed data.

The results from both the 450 eV, Ultrasoft A, and the 330 eV, Ultrasoft B computational schemes therefore show that the lattice parameters increase linearly with increasing Hf-concentration. However, the increase in the lattice parameters is in the order of only 2%, which can be attributed to the isomorphic structures of the two pure compounds as well as the similar ionic radii of Zr and Hf (Section 1.1). The linear dependence of the lattice parameters on composition therefore serves as evidence that the amount of lattice strain resulting from the incorporation of Hf in the K_2ZrF_6 lattice and vice versa may be such that stable crystal structures form during solid solution formation.

3.3.1.4. ΔH_{form} Calculations of $K_2Zr_{(1-z)}Hf_zF_6$ Solid Solutions

The results of the formation enthalpy calculations, using the 450 eV - Ultrasoft A data, and Equation (3.1) is illustrated in Fig. 3.9.

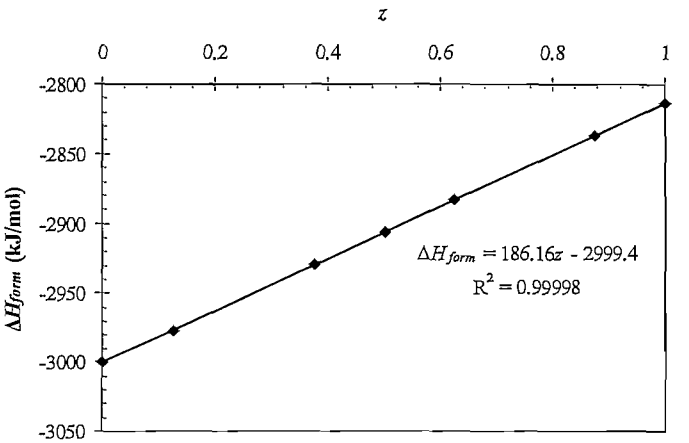

Figure 3.9: Calculated formation enthalpy in $kJ.mol^{-1}$ M^{4+} of $K_2Zr_{(1-z)}Hf_zF_6$ solid solutions with varying Hf-concentration modeled using the Ultrasoft A pseudopotential scheme at a cutoff energy of 450 eV.

The results show that there is an increase in energy associated with the formation of solid solutions of $K_2Zr_{(1-z)}Hf_zF_6$ with respect to pure K_2ZrF_6. The slope indicates the change in energy associated with the incorporation of Hf-atoms in the K_2ZrF_6 crystal lattice. The slope

also represents the difference in the formation enthalpy for pure K_2ZrF_6 and K_2HfF_6, which is about 186.2 kJ.mol^{-1} in this case. These formation enthalpy values were compared with that of the zirconium and hafnium tetrafluorides (ZrF_4 and HfF_4) as experimental data is available for these compounds but not for the potassium salts. The calculated values of ΔH_{form} for K_2ZrF_6, K_2HfF_6 and the experimental data for ZrF_4 and HfF_4 [28] are shown in Table 3.10. The values in the second row of the table represent the differences between the values of the Zr and Hf compounds for the different salts.

Table 3.10: Comparison of the calculated ΔH_{form} values of K_2ZrF_6 and K_2HfF_6 with the experimental data of ZrF_4 and HfF_4 [28].

Compound	ZrF_4	HfF_4	K_2ZrF_6	K_2HfF_6
ΔH_{form} (kJ.mol^{-1})	-1913.4	-1931.8	-2999.7	-2813.6
$\Delta(\Delta H_{form})$ (kJ.mol^{-1})	-18.4		186.2	

From this data we see that in comparison with the experimental values of the tetrafluorides, the difference between the calculated formation enthalpies of the potassium salts are larger and about one order of magnitude higher. To confirm this trend the tetrafluorides were also modelled. The experimental crystal structure data of the fluorides [21] was used for the modelling just as in the case of K_2ZrF_6 and K_2HfF_6. The method as described in Section 3.2.1.2 was followed, and the formation enthalpies were calculated using the same method as for the potassium salts using Equation (3.8), which is analogous to Equation (3.1).

$$\Delta H_{form} = E_{tot}(Zr(Hf)F_4)/8 - E_{Zr(Hf)} - 4E_F \qquad (3.8)$$

In Equation (3.8) the energy of the corresponding fluoride is evaluated per mol M^{4+}, which coincidentally also requires the calculated total energy to be divided by 8 just as for the $K_2Zr_{(1-z)}Hf_zF_6$ solid solutions as the unit cell of the tetrafluorides as shown in Fig. 3.3 also contains a total of 8 Zr- or Hf-atoms. The results obtained for cutoff energies of 330 eV and 450 eV are shown in Table 3.11. From the results we see that the same trend is observed as for the potassium salts with the differences between the formation enthalpies virtually the same as for $K_2Zr(Hf)F_6$ (at both low and high cutoff energies).

Table 3.11: Comparison between calculated and experimental [28] ΔH_{form} values for ZrF_4 and HfF_4.

Dataset	ΔH_{form} (kJ.mol^{-1})		$\Delta(\Delta H_{form})$ (kJ.mol^{-1})
	ZrF_4	HfF_4	
330 eV	-1806.1	-1617.6	188.5
450 eV	-1815.2	-1627.3	188.0
Experimental	-1913.4	-1931.8	-18.4

Furthermore, as is the case for K_2ZrF_6 and K_2HfF_6, the computed enthalpy of the Hf-salt is larger in value than that of the Zr-salt, as is reflected by the positive signs of the $\Delta(\Delta H_{form})$-values, which is contradictory with the experimental data where the formation enthalpy of the Hf-salt is lower than that of the Zr-salt. However, we see that the computed formation enthalpies are in the same order of magnitude as the experimental values and that the higher energy of the Hf-salts for both the tetrafluorides and K_2ZrF_6 and K_2HfF_6, cause the slope of the ΔH_{form}-curve to be positive instead of negative (Fig. 3.10). The deviation of the computed values from the experimental values can be due to the fact that calculations are performed at 0 K. Although, as the large difference between Zr and Hf also indicates, this might also be attributed to the basis functions (pseudopotentials) of Zr and Hf that are not yet accurately defined, or it may be that the inherent effect of the electron density minimization of the DFT method is not fully removed by the numerical method, (Equations (3.1) and (3.8)) used to calculate the physical thermodynamic property. Therefore, systematic errors arise when using inadequately defined pseudopotential basis functions that can lead to artefacts embedded in the final results. Furthermore, the pseudopotential of Zr used in the Ultrasoft A scheme is defined over a larger number of electrons for Zr in its valence shell than for Hf (explained in Section 3.2.1.1), which indicates that the accuracy of the parameters might differ for the two compounds, which can be understandable due to the fact that relatively little thermodynamic data exists for these "exotic" compounds, especially for Hf.

The ΔH_{form} results of the solid solution modelling using the Ultrasoft B pseudopotential scheme at a cutoff energy of 330 eV is shown in Fig. 3.10. Note that for the purpose of ΔH_{form}-calculations, the pure Zr-structure shown in Fig. 3.2 was also modelled using the same ultrasoft pseudopotential as that used in $K_2Zr_{(1-z)}Hf_zF_6$ solid solution modelling in both cases of pseudopotential A and B. The calculated formation enthalpies of K_2ZrF_6 and K_2HfF_6 modelled at 330 eV using both ultrasoft pseudopotentials are summarised in Table 3.12.

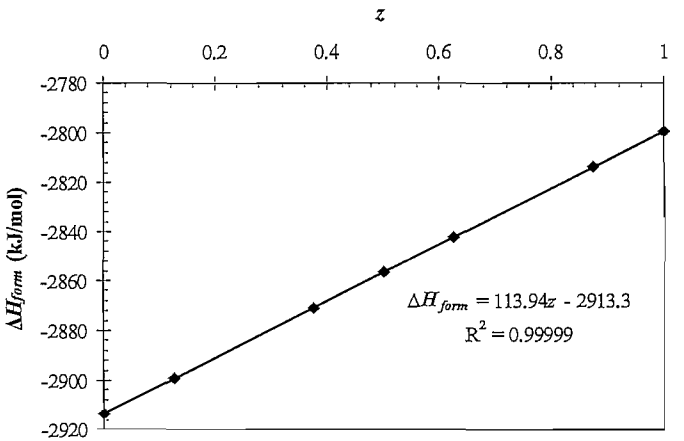

Figure 3.10: Calculated formation enthalpy in $kJ.mol^{-1}$ M^{4+} of $K_2Zr_{(1-z)}Hf_zF_6$ solid solutions with varying Hf-concentration modeled using the Ultrasoft B pseudopotential scheme at a cutoff energy of 330 eV.

Table 3.12: Comparison between ΔH_{form} values calculated using the Ultrasoft A and Ultrasoft B pseudopotentials at a cutoff energy of 330 eV.

Pseudopotential	ΔH_{form} ($kJ.mol^{-1}$)		$\Delta(\Delta H_{form})$ ($kJ.mol^{-1}$)
	K_2ZrF_6	K_2HfF_6	
330 eV Ultrasoft A	-2987.3	-2799.5	187.8
330 eV Ultrasoft B	-2913.3	-2799.5	113.9

The calculated enthalpy of K_2HfF_6 remains unchanged for both pseudopotential schemes as the pseudopotential for only Zr was changed. The results show that the energy of K_2ZrF_6 is slightly higher than that of K_2HfF_6 when compared to the Ultrasoft A pseudopotential data, but the change is not significant. This causes the difference between the formation enthalpies of the compounds to be slightly lower; however the energy of K_2HfF_6 is still higher than that of K_2ZrF_6 which causes the large difference. This was also tested for ZrF_4 and HfF_4 and the same trend was observed for these compounds (results not shown).

The significance of the ΔH_{form}-results is that the increase in the formation enthalpy with increasing z implies that solid solutions are thermodynamically less stable than pure K_2ZrF_6, however, the formation of solid solutions are energetically favoured over pure K_2HfF_6. Therefore, the crystal lattice of K_2HfF_6 may be stabilized by the formation of solid solutions. This increase in the formation enthalpy as depicted by the positive slopes in Figs. 3.9 and 3.10, suggests that there is a large difference in the stability of pure K_2ZrF_6 with respect to solid solutions with increasing Hf-concentration, where the difference in the thermodynamic stability is predicted to be larger by the Ultrasoft A pseudopotential than by the Ultrasoft B pseudopotential data. Therefore, both datasets indicate that solid solution formation might not interfere with the separation of the two pure compounds due to the rapid decrease in thermodynamic stability as the Hf-concentration in $K_2Zr_{(1-z)}Hf_zF_6$ solid solutions increases. However, the discrepancies between the calculated and experimental data, which as was mentioned could be due to either the numerical calculation method or the basis functions of Zr and Hf that are not yet accurately parameterized, might invalidate these conclusions. Nevertheless, the decrease in thermodynamic stability of solid solutions, as depicted by the positive slopes of the ΔH_{form}-curves, means that ΔH_{mix} should also assume positive values, which will be illustrated in the next section.

As explained above, the discrepancies observed between the calculated and experimental thermodynamic data could be attributed to the constant effect of the parameterization of the basis functions. Nevertheless, this "constant error" should not prevent determination of the relative amount of interaction of the impurity with the host crystal. In other words, to determine whether the impurity interacts with the host crystal in such a way that can prevent selective removal of the impurity from the desired compound. The quantification of the degree of interaction of the impurity with the host crystal is the subject of the next section.

3.3.1.5. ΔH_{mix} and the Relative distribution Coefficient

Ultrasoft A 450 eV Results

As already mentioned, the supercell method (Section 2.3.2.1.B.) was used to simulate the different compositions of solid solutions, and from the results ΔH_{mix} is calculated for each of the modelled compositions using Equation (3.3) as explained in Section 3.2.1.2. According to the regular solution model, ΔH_{mix} can be described in terms of an interaction parameter, Ω, as shown in Equation (3.9) [17, 22]:

$$\Delta H_{mix} = \Omega . z(1-z) \tag{3.9}$$

where ΔH_{mix} and Ω are expressed in kJ.mol^{-1} and z is the Hf-fraction. This model can thus be used to obtain an expression for ΔH_{mix} as a function of z. By calculating Ω from the ΔH_{mix}-data using Equation (3.9) as a function of composition, it was found that a parabolic fit gave the most accurate description for the data. The polynomial function was therefore chosen empirically to describe the functional dependence of Ω on z. This expression for Ω is then substituted back into Equation (3.9) to produce a continuous ΔH_{mix}-curve [17, 22 - 24]. The parabolic fit used yields the following expression for Ω:

$$\Omega \text{ (kJ/mol)} = -62.483 z^2 + 61.246 z + 7.327 \tag{3.10}$$

Unfortunately, the accuracy of the fit is not very satisfactory with a correlation coefficient of $R^2 = 0.862$. However, as illustrated in Fig. 3.11, the function reproduces the calculated ΔH_{mix}-values fairly accurately especially at lower concentrations.

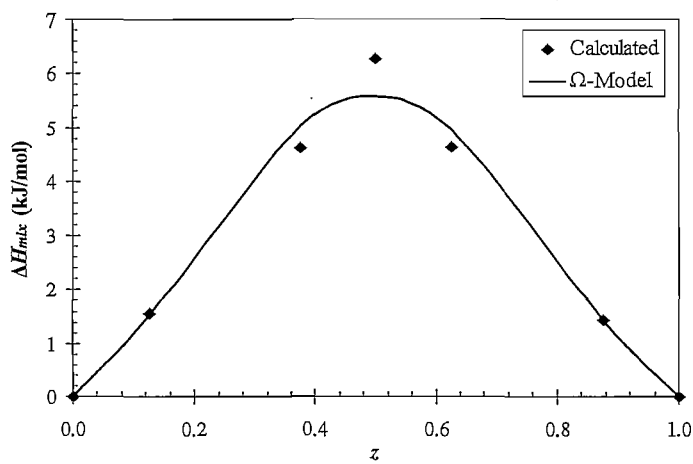

Figure 3.11: Comparison between ΔH_{mix}-values calculated from simulation data and regular solution model.

The ideal mixing entropy can also be calculated using the ideal solution model according to:

$$\Delta S_{mix} = -R[z \ln(z) + (1 - z) \ln(1 - z)] \quad (3.11)$$

where R is the universal gas constant (8.314 $J.K^{-1}.mol^{-1}$).

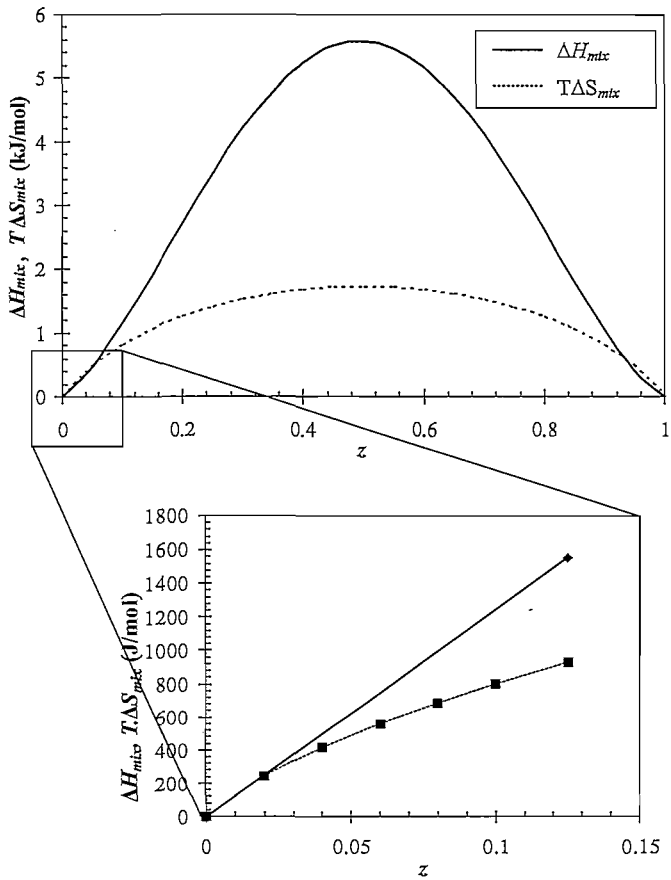

Figure 3.12: Calculated mixing enthalpy and ideal mixing entropy of $K_2Zr_{(1-z)}Hf_zF_6$ solid solutions at 298 K.

Although not used specifically in further discussions on the prediction of the separation efficiency, the Gibbs free energy of mixing can also be calculated according to Equation (3.12):

$$\Delta G_{mix} = \Delta H_{mix} - T\Delta S_{mix} \quad (3.12)$$

where T is the temperature (K) at which the process takes place.

The results of this procedure are shown in Fig. 3.12. From the figure we see that a slightly positive mixing enthalpy is obtained, in accordance with the ΔH_{form}-data (450 eV Ultrasoft A scheme). There is a small difference (with a maximum in the range of 4 kJ.mol^{-1}) between the entropy (at 298 K) and the enthalpy terms. Thus ΔG_{mix} has a small value which implies that the formation of solid solutions from the pure components is slightly thermodynamically unfavoured. This means that the separation efficiency might be hampered by the phenomena of solid solution formation. Therefore, although the ΔH_{form}-results predict a significant difference in the thermodynamic stability of the pure compounds, the ΔH_{mix}-data shows that relatively small energy changes are associated when transferring the impurity to the host crystal. Furthermore, at low and high concentrations of Hf (low and high values of z where either pure K_2ZrF_6 or K_2HfF_6 is approached) ΔH_{mix} is equal to or even smaller in value than the $T\Delta S_{mix}$ term, which would suggest the formation of stable solid solutions for these compositions as ΔG_{mix} approaches zero. This is emphasised in the insert of Fig. 3.12 where the increase in the mixing enthalpy with composition is approximated as a straight line between $z = 0$, and $z = 0.125$ (the first two data points resulting from molecular modelling). The entropy curve follows the same model as expressed in Equation (3.11) where the calculated data points, used to construct the curve, are also shown. It is clear that at a Hf-fraction of $z \approx 0.02$, the slopes of both curves are equal, therefore $d(\Delta G_{mix})/dz = 0$. In principle this would mean that separation cannot proceed, however it should be borne in mind that the data is a result of mathematical approximations and the accuracy is further restricted by the modelling method used. However, it seems that the separation of Zr and Hf at low concentrations of Hf could be difficult due to the small thermodynamic barrier that needs to be overcome to form solid solutions during crystal growth. In other words, the steric interactions of the Hf impurity with the K_2ZrF_6 crystal, especially at low concentrations, are small enough to permit its incorporation in the host crystal structure with relative ease, thereby limiting the separation.

This thermodynamic data can thus now be used to theoretically assess the separation efficiency more quantitatively using the model described in Section 2.2.4.2, which for

convenience is again briefly reviewed. It was shown that the relative distribution coefficient can be used as a measure of the efficiency of a crystallization process, and as explained in Section 2.2.4.2, Equation (2.19), is defined as:

$$\beta_{Hf,Zr} = \frac{z_{Hf}/x_{Hf}}{z_{Zr}/x_{Zr}} = \frac{K_{Hf}}{K_{Zr}} \tag{3.13}$$

which is the distribution of the impurity (in this case the Hf-species) between the liquid and solid phases relative to that of the desired compound (in this case the Zr-species). z_i is the concentration of species i in the product crystals and x_i is the concentration of species i in solution that can be conveniently expressed in terms of mole fractions. The impurity is in this case Hf and the desired product the corresponding Zr-salt. If high selectivity is achieved, between the impurity and the desired compound, the value of $\beta_{Hf,Zr}$ will be smaller than 1 (the impurity is rejected by the crystalline product) and if no separation is achieved $\beta_{Hf,Zr}$ will be unity. Recall that the thermodynamic model for the relative distribution coefficient developed by Rosenberger and Riveros [8, 9] can be expressed as:

$$\beta_0 = \frac{\gamma'_{Hf(l)}}{\gamma^{sat}_{Hf(l)}} \frac{x^{sat}_{Zr}}{x^{sat}_{Hf}} exp\left(\frac{-\Delta H^{dis}_{Hf} + T\Delta S^{vib}_{Hf}}{RT}\right) \tag{3.14}$$

The notation β_0 is used to indicate that this is a thermodynamic prediction where the kinetics of crystal growth are neglected. A full description of the different symbols can be found in Section 2.2.4.2, where the notation is only modified here in accordance to the Zr-Hf system. As noted previously [8, 9], the activity coefficient ratio can be approximated as being unity because the values at low concentrations and at saturated conditions would normally be of the same order of magnitude. The vibrational entropy is assumed here to be negligible in comparison with the enthalpy term in light of the similarities of Zr and Hf with regard to their chemical and physical properties, for example the crystal structures of their different compounds. In other words, because Zr and Hf are so similar, it could be that there does not exist any significant difference in the vibrational entropy change when either of the two is transferred from the solution and incorporated into a growing crystal of K_2ZrF_6.

The relative solubility of the two compounds, in conjunction with the mixing enthalpy, then plays a major role in the incorporation of the Hf-impurity. However, following the argument

above, the relative solubility ratio may then also be approximated as being unity. This aspect is addressed in more detail in Section 3.3.2.2. Therefore this could also hold for the activity coefficient ratios, as it may be assumed that the aqueous chemistry of Zr and Hf are probably similar. With these approximations, the amount of impurity incorporation decreases as the heat of mixing of the impurity in the solid phase increases [9] as summarized in Equation (3.15).

$$\beta_0 = exp\left(\frac{-\Delta H_{mix}}{RT}\right) \tag{3.15}$$

where ΔH_{mix} is the mixing enthalpy (J.mol^{-1}), R the universal gas constant (J.K^{-1}.mol^{-1}) and T is the temperature (K) at which crystal growth takes place. The results of this analysis give a value of β_0 in the range $0.2 < \beta_0 < 1$, which indicates relatively low separation efficiency. If we use the data of β_0, it is possible to calculate the equilibrium concentration (x_{Hf}) of the Hf-salt remaining in solution after a solid solution of composition z_{Hf} has formed. In other words, the data can be used to determine (predict) K_{Hf} whereby the predicted separation efficiency can be better visualized. This can be done by recognising that:

$$\beta_0 = \frac{K_{Hf}}{K_{Zr}} = \frac{z_{Hf}/x_{Hf}}{(1 - z_{Hf})/(1 - x_{Hf})} \tag{3.16}$$

where $z_{Zr} = 1 - z_{Hf}$ and $x_{Zr} = 1 - x_{Hf}$. By solving the equation for x_{Hf}, the equilibrium concentration of Hf in the liquid phase can be determined as a function of β_0 and z_{Hf} only. The results are represented by the solid curve in Fig. 3.13. The dashed line is where $x_{Hf} = z_{Hf}$, thus where the composition of Hf in the liquid and solid phases are equal. When the two curves cross, further separation would therefore not be possible as the distribution of the impurity between the liquid and solid phases remains constant with each recrystallization. This is known as the azeotropic composition. The composition at which the solid and dashed lines start to converge would therefore be where the separation becomes increasingly inefficient. In this case we see from the results that this should occur at a Hf-fraction of $z_{Hf} \approx 0.05$. From the graph it is also clear that regardless of the poor separation efficiency encountered at the low Hf-concentration, the separation efficiency decreases with increasing purity as $K_{Hf} = z_{Hf}/x_{Hf}$ increases in value, approaching unity.

The fact that the same liquid-phase composition can be obtained when solid solutions of different compositions are formed during crystallization (represented by the vertical part of the solid curve, where the same x_{Hf}-value results in different z_{Hf}-values) might seem physically incorrect. However this is a result of the variation in β_0 with the formation of solid solutions with varying composition. More specifically, the β_0-curve takes the inverse form of the mixing enthalpy curve where the efficiency increases with increasing z_{Hf} (value of β_0 decreases) until a 1:1 mixture of Zr and Hf is achieved and then the efficiency decreases with a further increase in z_{Hf} (value of β_0 increases).

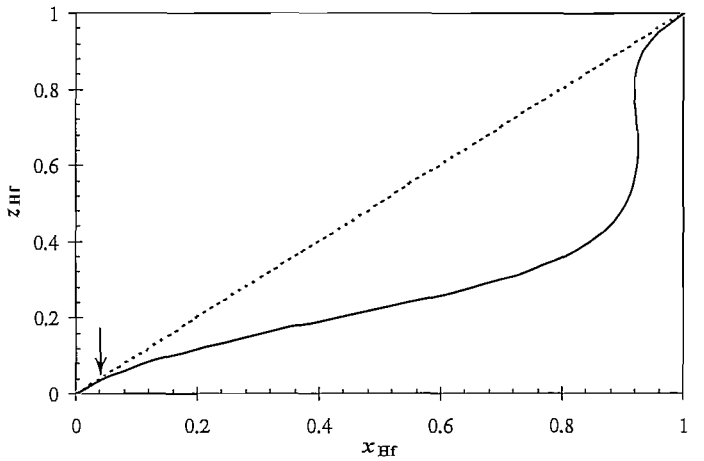

Figure 3.13: Predicted equilibrium distribution of Hf between the solid and liquid phases during crystallization from solution.

Therefore with each crystallization, the degree of separation that is achieved (if solid solution formation is assumed to be the only means whereby the separation is restricted), is governed by the phase equilibria (solid curve in Fig. 3.13) and therefore the separation efficiency decreases with each crystallization as the value of K_{Hf} approaches unity. According to these results, separation beyond a Hf-fraction of ~ 0.05 (indicated by the arrow) will be rather inefficient, due to the small deviation of the distribution curve from the $K_{Hf} = 1$ condition.

Ultrasoft B 330 eV Results

The mixing enthalpies were also determined using the Ultrasoft B, 330 eV data. A parabolic fit was again used for this data, which yields the following expression for Ω with a correlation coefficient of $R^2 = 0.933$.

$$\Omega\ (\text{kJ/mol}) = -44.536z^2 + 59.960z - 12.987 \qquad (3.17)$$

The results of the calculations using Equations (3.3), (3.9), (3.11) and (3.17) are represented in Fig. 3.14.

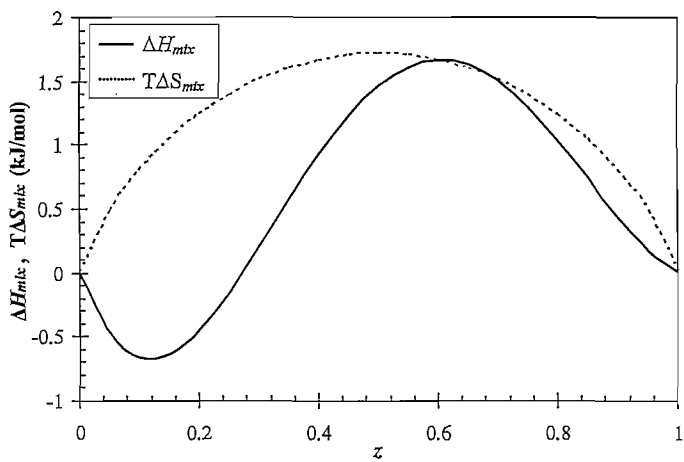

Figure 3.14: Calculated mixing enthalpy and ideal mixing entropy of $K_2Zr_{(1-z)}Hf_zF_6$ solid solutions at 298 K for the 330 eV, Ultrasoft B pseudopotential data.

In comparison with the 450 eV, Ultrasoft A pseudopotential data (Fig. 3.12), a mixing enthalpy is obtained that is considerably lower in value and negative up to a Hf-fraction of about 0.28. Furthermore, the mixing enthalpy is smaller than the ideal mixing entropy at 298 K over the entire composition range, which translates to the Gibbs free energy of mixing being slightly negative. Therefore, solid solutions are predicted to be thermodynamically more stable, which causes a decrease in the separation efficiency in comparison with that predicted by the 450 eV, Ultrasoft A data. The lower mixing enthalpy change predicted by this data is

then also in accordance with the smaller increase in the formation enthalpy with increasing Hf-concentration, in comparison with the other data, as shown in Fig. 3.10. The lower separation efficiency is confirmed by the results obtained using Equations (3.15) and (3.16) as shown in Fig. 3.15. Because of the low mixing enthalpy change, depicted in Fig. 3.14, the azeotropic composition is now significantly higher, i.e. at a Hf-fraction of 0.28. However, at lower concentrations of Hf ($z_{Hf} < 0.28$) separation may proceed because the value of K_{Hf} is larger than unity (the solid curve lies above the $z_{Hf} = x_{Hf}$ line), therefore corresponding with the enrichment of the crystalline product with Hf instead of the mother solution (for the condition of $\beta < 1$).

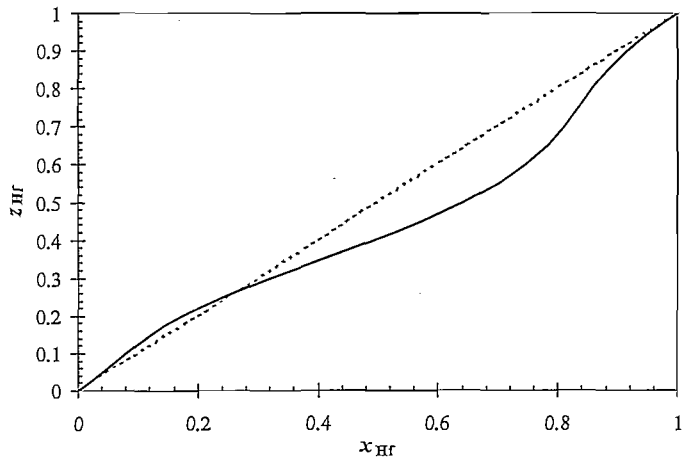

Figure 3.15: Predicted equilibrium distribution of Hf between the solid and liquid phases during crystallization from solution from using the 330 eV, Ultrasoft B pseudopotential data.

Consequently, the resulting mother solution is enriched with Zr contrary to the condition depicted in Fig. 3.13 where the crystalline product is purified from the Hf-impurity. However, from Fig. 3.15, it is clear that this process is predicted to be very inefficient due to the marginal deviation of the K_{Hf}-curve from unity at low Hf-concetrations which is caused by the slightly negative ΔH_{mix} resulting from the use of the 330 eV, Ultrasoft B pseudopotential simulation data. Furthermore, the azeotropic condition would also imply that the recovery of K_2ZrF_6 would be low because no further enrichment of the crystalline phase can be obtained

beyond the azeotropic composition, and therefore the balance of Zr cannot be stripped from the impure solid phase. Thus, the slight thermodynamic stability of the solid solutions, as predicted by the Ultrasoft B-data, would not be enough for the realisation of a separation process in which the mother liquor is purified from, and the crystalline product enriched with the Hf-impurity. Furthermore, just as in the case of Fig. 3.13, the distribution curve in Fig. 3.15 approaches unity at a Hf fraction of approximately 0.05, which is where the enthalpy changes converges to zero, in other words where an appreciable thermodynamic driving force no longer exists that can facilitate the separation of the two compounds.

3.3.2. Energy Calculations using Dmol^3

3.3.2.1. Solid-State Calculations

3.3.2.1.A. ΔH_{form} Calculations of $K_2Zr_{(1-z)}Hf_zF_6$ Solid Solutions

To investigate the discrepancies associated with the formation enthalpy calculations discussed in Section 3.3.1.4, the numerical basis functions of DMol3 were employed for the modelling of the same solid solution structures. As already mentioned, single point energy calculations were performed using the 450 eV, Ultrasoft A pseudopotential, GGA-PBE, CASTEP-optimized $K_2Zr_{(1-z)}Hf_zF_6$ supercells as well as the unit cells of ZrF_4 and HfF_4. The rest of the computational parameters were discussed in Section 3.2.2.1. Although the total electronic energy is given by DMol^3 in Ha (Hartrees), the same method was used to compute the formation enthalpies according to Equation (3.1), where the calculated energies were then converted to kJ.mol^{-1} just as with the CASTEP results.

The results of the formation enthalpy calculations are shown in Fig. 3.16. From these results we see that in contradiction to the CASTEP results, a negative slope of 21.2 kJ.mol^{-1} is obtained. Therefore, the formation enthalpy decreases from K_2ZrF_6 to K_2HfF_6, which however is in accordance with the experimental data of ZrF_4 and HfF_4 [28]. In comparison with the 450 eV data of CASTEP shown in Table 3.13, it is clear that the calculated formation enthalpy values of the two datasets (CASTEP and DMol^3) fall in the same order of magnitude.

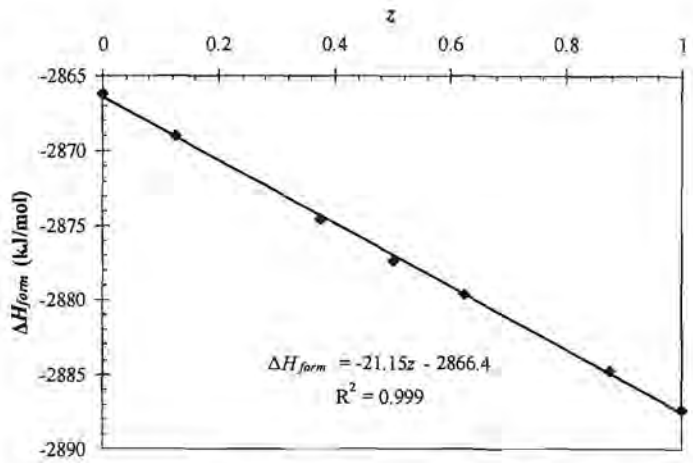

Figure 3.16: Calculated formation enthalpy in $kJ.mol^{-1}$ M^{4+} of $K_2Zr_{(1-z)}Hf_zF_6$ solid solutions with varying Hf-concentration modeled using DMol^3.

Table 3.13: Comparison between the calculated formation enthalpies of K_2ZrF_6 and K_2HfF_6 from the use of the DMol^3- and CASTEP-data.

Method	ΔH_{form} (kJ.mol^{-1})		$\Delta(\Delta H_{form})$ (kJ.mol^{-1})
	K_2ZrF_6	K_2HfF_6	
DMol^3 (DND*)	-2866.1	-2887.4	-21.2
CASTEP (450 eV)	-2999.7	-2813.6	186.2

*Results from using the DND basis set.

The difference between the two methods is that the calculated energy of the Zr-salt is higher in comparison with the Hf-salt which is not the case with the CASTEP values. This causes that the difference between the formation enthalpy values of K_2ZrF_6 and K_2HfF_6 is lower for the DMol^3 results and in the same range as the experimental data of ZrF_4 and HfF_4 (see Table 3.11). Because the same crystallographic models and numerical calculation methods were used with both DMol^3 and CASTEP, the difference that is observed can be largely ascribed to the different basis sets used, viz. the numerical basis sets of Zr and Hf in DMol^3 that seemingly performs better with respect to each other than the CASTEP plane-wave

pseudopotential basis sets. The DMol^3-calculations were also tested with ZrF_4 and HfF_4 and in comparison with the 450 eV CASTEP results the same trend is observed as for K_2ZrF_6 and K_2HfF_6 (Table 3.14).

Table 3.14: Comparison between the calculated formation enthalpies of ZrF_4 and HfF_4 from the use of the DMol^3- and CASTEP-data.

Method	ΔH_{form} (kJ.mol^{-1})		$\Delta(\Delta H_{form})$ (kJ.mol^{-1})
	ZrF_4	HfF_4	
DMol^3 (DND*)	-1701.2	-1723.3	-22.1
CASTEP (450 eV)	-1815.2	-1627.3	188.0

*Results from using the DND basis set.

3.3.2.1.B. ΔH_{mix} and the Relative distribution Coefficient

The data of the DMol^3-modelled mixed crystals (Section 3.3.2.1.A) were also used to calculate the mixing enthalpy using the same approach as with the CASTEP data, i.e. using Equation (3.3). In this case only the results of the calculated compositions are shown in Fig. 3.17, because an appropriate fit could not be found for the DMol^3 simulation data as for the CASTEP results. The single point energy calculation of the mixed crystal with a composition of $z = 0.625$ resulted in a mixing enthalpy that is not consistent with the rest of the data, and for this reason is omitted from the results shown in Fig. 3.17. The results show that the mixing enthalpy is negative for all of the modelled compositions (indicated by the solid line) which is drawn to serve as a guide). This contradicts with the CASTEP results where the mixing enthalpies were positive, which may be expected in light of the negative slope of the ΔH_{form}-curve (Fig. 3.16). The absolute values are still in the same range however, with a maximum change of 5 - 6 kJ.mol^{-1}. The implication of the negative mixing enthalpy values is that the Gibbs free energy of mixing will also be negative for the entire composition range which means that the formation of mixed crystals is thermodynamically favoured over the pure crystals of K_2ZrF_6 and K_2HfF_6. Using equation (3.15), a thermodynamic distribution coefficient can therefore be predicted with a value larger than unity.

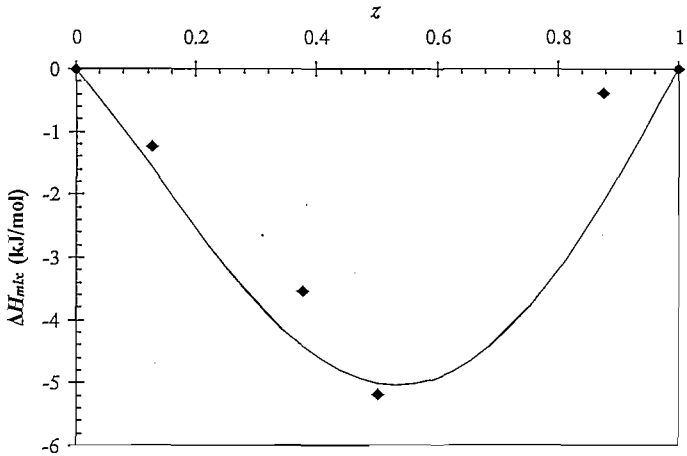

Figure 3.17: Calculated mixing enthalpy of $K_2Zr_{(1-z)}Hf_zF_6$ solid solutions at simulated compositions for the DMol[3] data. Solid curve serves as a guideline.

Thus, as illustrated in Fig. 3.18, the distribution curve would assume the inverse form of that depicted in Fig. 3.13, because solid solutions are thermodynamically favoured over the pure structures due to the negative enthalpy changes (Fig. 3.17). Therefore, if these results were to be correct, Hf would be favourably incorporated in the crystalline product during crystallization. Although this situation might be anticipated as being unwanted, the fact is that separation could still proceed as was the case in Fig. 3.15. The difference is that Hf can be more easily transferred to the crystalline phase according to this dataset due to the greater negative enthalpy change. The increased efficiency of Hf-incorporation in the crystalline product as compared to the 330 eV - Ultrasoft B case (lower part of Fig. 3.15), leads to higher values of K_{Hf} and therefore greater deviation of the distribution curve from $K_{Hf} = 1$. This in turn corresponds with a greater purification efficiency of the mother liquor from the Hf-impurity compared to the predicted efficiency of Fig. 3.15. However, in comparison with the 450 eV – Ultrasoft A results, the same relative separation efficiency would still be obtained as the same amount of energy (absolute values) is required or released for the formation of solid solutions as predicted by the two methods respectively. The possibility of separation by purification of the mother liquor instead of the crystalline product via crystallization is discussed in Chapter 4.

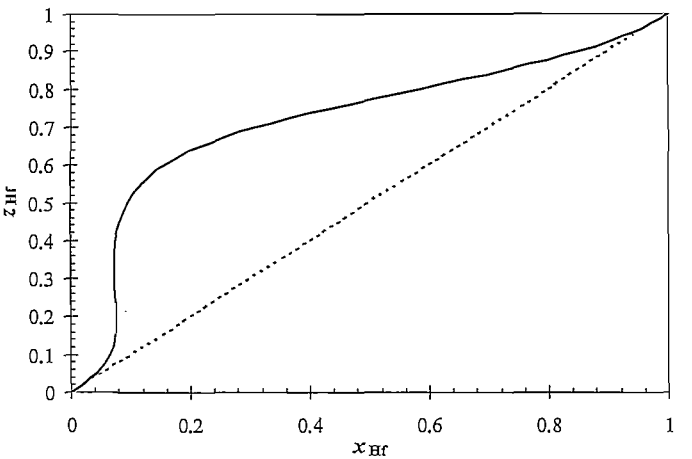

Figure 3.18: Approximated equilibrium distribution of Hf between the solid and liquid phases during crystallization from solution based on the DMol^3 modelling results.

3.3.2.2. Solvation Energy Calculations

The low selectivity that is predicted by the solid solution modelling results as implemented in the thermodynamical model described in the previous sections can be attributed to the small energy requirements that are associated with the formation of solid solutions of $K_2Zr(Hf)F_6$ from the constituting species (CASTEP) reducing the efficiency of separation, since, the impurity (Hf) can be incorporated into the crystallization product (K_2ZrF_6) with relative ease. In the case of the DMol^3 results, it was predicted that solid solutions are even more thermodynamically stable than the pure structures. The solid solutions were predicted to be only marginally stable while they were predicted to be marginally unstable by the CASTEP results. Therefore, whatever the real-world situation may be, the small thermodynamic barrier (either positive or negative) implies that the separation should be rather inefficient.

However, with these computational methods, only the solid phase and the energy changes occurring in that phase were taken into account. In the physical situation there is also an energy change taking place due to the phase transformation itself and the energy change associated with this process could be different for K_2ZrF_6 and K_2HfF_6. This energy change

will also play a role in the degree to which solid solutions can form and also the amount of simultaneous crystallization that can take place and therefore also influence the separation efficiency. Therefore for the process illustrated in Equation (3.18) the separation efficiency will improve the larger the difference in the energy change (ΔH_{cr}) between K_2ZrF_6 and K_2HfF_6.

$$2K^+(aq) + Zr(Hf)F_6^{2-}(aq) \xrightarrow{\Delta H_{cr}} K_2Zr(Hf)F_6\ (s) \qquad (3.18)$$

Note that in the reaction scheme illustrated above it is assumed that the fluorine complexes of the two metals behave in the same manner and that the complexes are stable in solution. Therefore, the speciation of the compounds is currently ignored to reduce the complexity of the system. The energy change taking place during crystallization is the crystallization enthalpy and is approximately equal to the negative of the dissolution enthalpy (i.e. the energy change for the reverse of crystallization). This energy change was also calculated by molecular modelling using DMol^3. As mentioned in Section 3.2.2.2, DMol^3 was used with the COSMO model whereby the effects of solvation (in water in this case) for molecular systems can be taken into account. The same computational parameters were used as for the modelling of the solid solutions with DMol^3 as described in detail in Section 3.2.2.2. The method used to calculate the energy changes during crystallization of K_2ZrF_6 and K_2HfF_6 are illustrated in Fig. 3.19, where K_2ZrF_6 is used as an example: Firstly, the energy of the pure crystal (CASTEP optimized structure) is calculated using DMol^3 (of which the data from the solid solution simulations were used), and then the energy increase associated with the dissociation (ΔE_{dis}) of the crystal into the individual ions is determined by calculating the energy of the ions in vacuum. The energy change of solvation (ΔH_{sol}) of the ions is then calculated using the COSMO model to calculate the energy of the solvated ions. Therefore, the total energy change for the process illustrated in Equation (3.18) corresponds with the energy change ΔH_{cr}, the negative of which is equal to the dissolution enthalpy. For the energy calculations of the solvated and unsolvated ions, the optimized geometry of the MF_6^{2-}-ions were used.

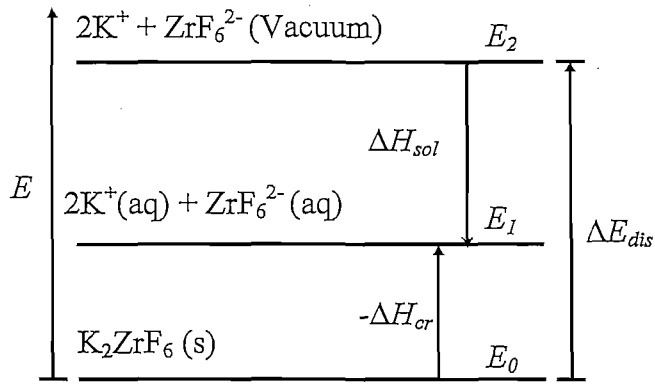

Figure 3.19: Schematic representation of computational method used to determine ΔH_{cr}.

The energy change ΔE_{dis} can therefore be calculated with Equation (3.19):

$$\Delta E_{dis} = E_2 - E_0 = E(2K^+ + ZrF_6^{2-}\ (\text{vacuum})) - E(K_2ZrF_6(s)) \qquad (3.19)$$

Accordingly, the energy change ΔH_{sol} can be calculated using the following equation:

$$\Delta H_{sol} = E_1 - E_2 = E(2K^+ + ZrF_6^{2-}\ (aq)) - E(2K^+ + ZrF_6^{2-}\ (\text{vacuum})) \qquad (3.20)$$

The crystallization enthalpy, ΔH_{cr}, can then be calculated according to:

$$\Delta H_{cr} = E_0 - E_1 = E(K_2ZrF_6(s)) - E(2K^+ + ZrF_6^{2-}\ (aq)) = -\Delta H_{sol} - \Delta E_{dis} \qquad (3.21)$$

The results from the calculations of both K_2ZrF_6 and K_2HfF_6 (Table 3.15) show that there is a larger energy decrease (ΔH_{sol}) for the solvation of the K_2ZrF_6-ions with respect to the K_2HfF_6-ions. This means that K_2ZrF_6 is more stable in solution (in its dissolved state) than K_2HfF_6. Also, the crystallization enthalpy (ΔH_{cr}) for K_2HfF_6 is higher than that of K_2ZrF_6 (absolute value), in other words more energy is released upon the crystallization of K_2HfF_6 in comparison with K_2ZrF_6. Therefore, the dissolution enthalpy (the negative of the crystallization enthalpy, ΔH_{cr}) of K_2HfF_6 is higher than that of K_2ZrF_6. Thus, K_2HfF_6 requires more energy to be dissolved in water than K_2ZrF_6, which corresponds with a lower solubility

in comparison with K_2ZrF_6. This correlates with the higher stability of K_2ZrF_6 in solution as predicted by the ΔH_{sol}-values.

Therefore, these results predict that K_2HfF_6 will be the first to crystallize from solution as more energy is released in comparison with the crystallization of K_2ZrF_6. However, because the concentration of Zr in $K_2Zr(Hf)F_6$, obtained from chemical processing of Zircon, is much higher with respect to that of Hf (Chapter 4), Zr will have a tendency to crystallize first when an unsaturated solution reaches a state of metastability, despite the fact that the thermodynamics suggests otherwise. The lower solubility of K_2HfF_6 however is contradictory with literature [1], but the difference between the crystallization enthalpies of K_2ZrF_6 and K_2HfF_6 is relatively low (~10 kJ.mol^{-1}) as indicated in the last column of the table, in view of the large dissolution enthalpies. The difference between the crystallization enthalpies of the two compounds is less than 10% of the crystallization enthalpies of the individual salts. Furthermore, the dissolution enthalpies of both salts are relatively high, for example the experimental heats of dissolution of appreciably soluble salts (for example NaCl) are in the range of 4 – 10 kJ.mol^{-1} [29]. Therefore the high dissolution enthalpies of K_2ZrF_6 and K_2HfF_6 predict low solubility for both salts.

Table 3.15: Energy calculations according to equations (3.19) – (3.21) using results of the DND basis set. M^{4+} = Zr/Hf.

ΔE (kJ.mol^{-1} M^{4+})	K_2ZrF_6	K_2HfF_6	ΔZr/Hf
ΔH_{cr}	-154.6	-164.9	10.2
ΔE_{dis}	1565.4	1571.0	5.6
ΔH_{sol}	-1410.8	-1406.2	4.7

Note that the difference between the dissociation energy of K_2ZrF_6 and K_2HfF_6, namely 5.6 kJ.mol^{-1} corresponds with a 0.4 % difference. Considering that these values are already the difference between large electronic energies (the calculated energies are given in Hartrees which is a very large unit as depicted in the conversion factors table at the beginning of this dissertation), it becomes apparent that the modelling calculations have to be exceptionally accurate to deal with the Zr/Hf system. Therefore, accurate basis sets are required to treat systems such as these, which are so similar, with confidence.

The lower solubility of K_2HfF_6 as predicted by the calculations might therefore be due to the modelling parameters (basis sets) that were used. For this reason, another basis set was tested using the same procedure as described above. As discussed in Section 3.2.2.2, the use of the alternative DNP basis set was investigated for the determination of the crystallization enthalpies. For the DNP basis set test, the same accuracy, functional and other parameters were used as for modelling with the DND basis set (full computational details are given in Section 3.2.2.2).

Modelling of all the ions in vacuum and in the solvated state with the DNP basis set resulted in identical energy values as with the DND basis set. Only, the energies of the crystals were about 30 kJ.mol^{-1} M^{4+} (M^{4+} = Zr/Hf) lower than with the DND basis set. As shown in Table 3.16, this resulted in the dissociation energy and crystallization enthalpy (absolute values) increasing by 30 kJ.mol^{-1}. These results however still show that the solubility of K_2HfF_6 will be lower than that of K_2ZrF_6.

Table 3.16: Energy calculations according to equations (3.19) – (3.21) using results of the DNP basis set. M^{4+} = Zr/Hf.

ΔE (kJ.mol^{-1} M^{4+})	K_2ZrF_6	K_2HfF_6	ΔZr/Hf
ΔH_{cr}	-186.1	-194.6	8.5
ΔE_{dis}	1597.0	1600.8	3.8
ΔH_{sol}	-1410.8	-1406.2	4.7

The difference between the crystallization enthalpy values (last column of Table 3.16) remained in the order of 10 kJ.mol^{-1}, decreasing only by 1.8 kJ.mol^{-1} in comparison with the DND basis set (Table 3.15). Furthermore, the solvation energy of the ions remained unchanged for the DNP basis set because the energy levels E_1 and E_2 (refer to Fig. 3.19) were the same for the DNP basis set as for the DND basis set and only the calculated energies of the crystals changed (E_0). This small discrepancy between the results of the two basis sets might be due to the interactions between the K^+- and MF_6^{2-}- ions in the crystal that differs for the two basis sets. The higher solubility predicted for K_2ZrF_6 by both basis sets could be due to the molecular model used which might not accurately describe the physical situation. Thus, simple dissociation and solvation of the ions might actually not occur because the fluorine-ion complexes might not be stable in solution but instead hydrolyse. This can result in the

formation of different hydroxyl-species which causes the Hf-complexes to be more stable than the corresponding Zr-complexes at equilibrium conditions leading to a higher experimentally observed solubility of K_2HfF_6. Therefore, the speciation of the compounds in aqueous solution might have significant influence on the stabilization of the species in solution, which in turn can influence their separation. Other factors such as entropy can also influence the solubility. For example, NH_4NO_3 is known to be soluble in water and yet its dissolution process is endothermic, thus $-\Delta H_{cr}$ is positive. On the other hand, NaOH is also soluble but upon dissolution produces a large amount of heat and the process is therefore exothermic, corresponding with a negative $-\Delta H_{cr}$. Therefore, the dissolution can be driven by various processes including the thermodynamic energy change. However, the difference between the results of the basis sets also puts the accuracy of the modelling itself under the spotlight. It could be that the basis sets for Zr and Hf are not yet sufficiently accurately defined leading to inaccurate results as discussed above in light of the small differences in energy between K_2ZrF_6 and K_2HfF_6 in comparison with the large electronic energies. This observation then also applies to the CASTEP results.

Nevertheless, in conclusion it would seem that a relatively low solubility was predicted for both K_2ZrF_6 and K_2HfF_6 due to the high dissolution enthalpies calculated by molecular modelling. The difference between the values of K_2ZrF_6 and K_2HfF_6 is less than 10 % of the dissolution enthalpies and is therefore a relatively small difference which means that there would not be an appreciable difference in the energy changes of the two compounds during crystallization. However, a difference in the energy changes of the two compounds during crystallization might be sufficient to improve the separation efficiency beyond that which is predicted by the solid state thermodynamics. Thus, if accurate results were obtained from the modelling of solid solutions (Section 3.3.1.5) then the predicted selectivity could be improved slightly due to solvent effects. However, it seems that according to the modelling results, that crystallization as a method of separating Zr and Hf might not be very efficient and furthermore, might not be technically feasible to achieve the desired purity of Zr (< 100 ppm Hf). Further investigation of this method by experimental methods is discussed in Chapter 4.

3.4. Conclusions

In conclusion, the separation efficiency of K_2ZrF_6 and K_2HfF_6 by crystallization was assessed using results from the DFT simulations of theoretical solid solutions of both compounds. Two different methods were used for the description of the electronic wave functions which resulted in different possible explanations of the physical situation. With the pseudopotential plane-wave method using CASTEP, the results obtained from the Ultrasoft A pseudopotential computational scheme together with a thermodynamic model predicted quite poor separation efficiency, in view of the relative ease with which the Hf-impurity can be incorporated into the crystal structure of the desired Zr-salt due to the small thermodynamic barrier that has to be overcome for solid solution formation. The results obtained from the alternative Ultrasoft B pseudopotential for Zr, which in turn affects the behaviour of the plane-wave functions used to approximate the electronic wave functions, predicted even lower separation efficiency. This is due to the fact that even lower energy requirements are predicted by this dataset for solid solution formation. This decrease in the energy changes is such that solid solutions with low Hf-concentrations (in the region of pure K_2ZrF_6) were predicted to be thermodynamically slightly favourable. However, this small thermodynamic driving force would not be sufficient to effectively separate impure mixed crystals from the resulting mother liquor, which is only barely enriched with Zr. Therefore, the formation of solid solutions from the pure constituent species during crystallization, as predicted by the modelling results in these two cases, greatly restricts the separation efficiency. Furthermore, based on these results, the desired purity of a Hf-concentration smaller than 100 ppm with respect to Zr would be technically difficult.

The results of both the Ultrasoft A and Ultrasoft B computational schemes showed good correlation with the experimental crystal structure data of K_2ZrF_6. Furthermore, results obtained with the Be(Zn)O and Al-TM alloy test systems agreed well with published data. However, it was shown that the calculated formation enthalpies of both the $K_2Zr_{(1-z)}Hf_zF_6$ solid solutions and, ZrF_4 and HfF_4 were in disagreement with the available experimental data of the tetrafluorides. Therefore, the accuracy of the calculated mixing enthalpy and the predicted separation efficiency seems to be questionable. Since the results of the Ultrasoft B pseudopotential scheme indicated a smaller difference in the thermodynamic stability of the pure potassium salts than the Ultrasoft A scheme, according to the ΔH_{form}-results, lower separation efficiency was consequently predicted. The decrease in thermodynamic stability of solid solutions with increasing Hf-content, as predicted by the results of both datasets, was

also confirmed by the mixing enthalpy results. It was shown that with decreasing purity, more energy is needed for the formation of the solid solutions via the substitution of the Hf-impurity into the crystal structure of the desired Zr-salt. However, these energy changes are only marginally positive, and at low Hf-concentrations marginally negative according to the Ultrasoft B pseudopotential scheme results. The small mixing enthalpies, however, do not correlate with the large difference in the thermodynamic stability of the pure crystals that were predicted by the formation enthalpy results, which might also be a point of concern.

The observed discrepancies between the calculated and experimental data could be due to different factors. These include the fact that all calculations were performed at 0 K, which is easily manageable in terms of computational time, but it is possible that the observed trends may change when temperature effects are taken into account. Calculations may be performed at finite temperatures whereby the thermodynamic quantities can be evaluated as a function of temperature. However, this would require analysis of the vibrational spectra of the lattices which would be very time intensive. As already mentioned, the accuracy of the modelling calculations may also be influenced by the pseudopotential plane-wave basis functions that are used for the description of the electronic wave functions; which are required for electron density calculations on which the entire DFT method relies. Therefore, if the interactions of the electrons with each other are not accurately described, this would result in inaccurate physical properties. This is not to say that the functions used in this study are incorrect, but that the basis functions for Zr and Hf which are not very common, might not be as rigorously parameterized as those of more common elements such as Al and Si for example. Thus, it seems that there exists room for improvement in this regard. It should further be kept in mind that the electron count of Zr and Hf, which is also coupled with the pseudopotential method, might create artifacts which are not fully removed by the numerical calculation method used for the determination of the formation enthalpies. Recall that the electronic energies were referenced to the corresponding electronic energies of the constituent elements for the formation enthalpy calculations. This may therefore also lead to the large formation enthalpy differences that were observed. On the other hand, the method used for the mixing enthalpy calculations in which the electronic energy of a solid solution with specific composition was referenced to the compositional average of the pure compounds, could lead to the cancellation of the systematic errors associated with the DFT method. Thus, this could have lead to the small enthalpy changes that were predicted during mixing of the two compounds which is in accordance with the small structural differences between the compounds of Zr and Hf.

Therefore, not only does the accuracy of the separate basis functions of Zr and Hf play a role in the accuracy of the results, but also their behaviour with respect to each other in terms of the calculated total electronic energies.

Because of these difficulties, the numerical basis functions of DMol^3 were used to perform the same thermodynamic calculations. It was shown that the difference in thermodynamic stability between both K_2ZrF_6 and K_2HfF_6 and the corresponding tetrafluorides were more accurately predicted by the DMol^3-data in terms of the experimental data. Moreover, according to the formation enthalpy results, the thermodynamic stability of $K_2Zr_{(1-z)}Hf_zF_6$ solid solutions increases with increasing Hf-content. The greater thermodynamic stability of the solid solutions therefore resulted in negative mixing enthalpy changes for the formation of solid solutions via the incorporation of Hf in the crystal structure of K_2ZrF_6.

Therefore, the DMol^3 results predicted that Hf can be favourably incorporated into the crystalline product during crystallization. Classical separation of crystals enriched with the desired product from an impure mother liquor should therefore not occur according to these results. Instead, impure, mixed crystals could possibly be removed from the resulting mother liquor that has been deprived of the impurity. However, because the absolute mixing enthalpy values were in the same range as those predicted by the CASTEP results, this process was also predicted to be rather inefficient, thus, not enough Hf will be incorporated in the product crystals in a single step due to the low thermodynamic driving force for solid solution formation (small negative enthalpy changes and assuming that the entropy change is negligible). The CASTEP results, on the other hand, predicted a small thermodynamic barrier that prevents the formation of solid solutions and therefore also leads to low separation efficiency especially at low Hf-concentrations. Consequently, the separation efficiency decreases with increasing purity. This might be the reason why it has been observed in the past that a large amount of recrystallizations are needed to obtain a high purity Zr-product, which also means that the product yield would be low, if no attempt is made to recover the Zr remaining in the impure fraction. It has not yet been reported that the reverse separation process that was predicted by the DMol^3 results has been observed experimentally. However, the fact remains that solid solution formation of the two salts may be a dominant factor that restricts the separation of Zr and Hf via crystallization and causes the method to be less effective when compared to other crystallization processes.

It was shown by the modelling of the solvated ions that the 0 K enthalpy changes of the pure K_2ZrF_6 and K_2HfF_6 during crystallization from an aqueous solution do not differ significantly. Some discrepancies between the predicted and experimentally observed solubilities of K_2ZrF_6 and K_2Hf_6 were however noted. It was concluded that this could have been caused by the accuracy of the numerical basis sets, or the validity of the molecular model used. In this regard, a better understanding of the speciation of the compounds in solution could shed light on the stability of the solvated fluorine complexes. Speciation might therefore influence the experimentally observed stability, or solubility, of the fluorine complexes of the two metals. Nevertheless, the relatively small difference in the calculated energy changes of K_2ZrF_6 and K_2HfF_6 during crystallization suggests that the predicted separation efficiency, obtained by only considering the solid phase, should not be largely influenced by solvent effects.

In spite of all the misgivings, this study has shown that molecular modelling can be advantageously applied to study different aspects of crystallization. In this case, the poor separation that was predicted at low Hf-fractions (in the concentration region of interest), gives a possible explanation of why a large number of recrystallizations are needed experimentally to sufficiently purify the Zr-salt by crystallization [2]. The separation seems to be hampered by the relative ease of solid solution formation especially at low Hf-concentrations which is due to the small enthalpy changes associated with solid solution formation. These small enthalpy changes are the result of the difference between electronic energy values that are orders of magnitude larger than the calculated difference. As illustrated for the DMol[3] calculations, this implies that the modelling calculations, and therefore the basis functions and parameters used, have to be exceptionally accurate to measure the small differences between compounds such as the Zr- and Hf-salts that are so similar correctly.

The basis functions (modelling parameters) of Zr and Hf could therefore definitely be improved. This is not to say that modelling of Zr- and Hf-compounds cannot be used to quantify differences between these and other metal-compounds. In fact, the modelling of Al_3Zr and Al_3Hf intermetallics with CASTEP have shown that results can be obtained that are in accordance with experimental and published data. Instead, the level of development of the modelling parameters of Zr and Hf, for which accurate thermodynamic data is also needed, must be of the same quality to accurately measure the small differences between the two species. It can be expected that accurate thermodynamic data might be lacking for exotic elements such as Hf, which can lead to the development of basis functions of inadequate

accuracy. Therefore, analogous to a moving pendulum that oscillates about the potential energy well as it approaches its state of rest, the calculated enthalpy changes associated with solid solution formation can oscillate about the zero-point when a small change is made in the accuracy of the modelling calculations. This causes slightly positive or slightly negative enthalpy values as predicted by the 450 eV Ultrasoft A data, or the 330 eV Ultrasoft B- and DMol^3-datasets respectively which indicates that the compounds will not be easily separated regardless of the absolute correct values. It should still be noted however that the vibrational entropy change that was assumed to be negligible in comparison with the enthalpy change (Equation 3.12) may also have an influence on the degree of separation, especially if the enthalpy change is relatively small as is the case here. It is shown in Chapter 5 how the possible contribution of the vibrational entropy to the degree of solid solution formation can be approximated.

As a final remark, the advances in the field of molecular simulations and technological innovations will contribute to improve the accuracy of this and other methods that can be applied to accurately study different aspects of various systems. Furthermore, molecular modelling can be used as an effective tool to study chemical and physical phenomena that are not easily accessible experimentally. Molecular modelling can hence be applied to increase workflow or to identify promising routes to follow for further research.

3.5. References

1. von Hevesy, G. The discovery and properties of hafnium. *Chem. Rev.* **2** (1) (1925) 1 – 41.

2. Vinarov, I.V. Modern methods for separating zirconium and hafnium. *Russ. Chem. Rev.* **36** (7) (1967) 522 – 536.

3. Sajin, N.P. & Pepelyaeva, E.A. Separation of hafnium from zirconium and production of pure zirconium dioxide. In Proceedings of the Second united Nations International Conference on the Peaceful uses of Atomic Energy, Geneva, 1958. Vol. 8, Paper P/634, pp 559–562.

4. Givand, J.C., Teja, A.S. and Rousseau, R.W. Effect of relative solubility on amino acid crystal purity. *A.I.Ch.E J.* **47** (12) (2001) 2705 – 2712.

5. Nie, Q., Wang, J. and Yin, Q. Effect of solution thermodynamics on the purification of two isomorphic steroids by solution crystallization. *Chem. Eng. Sci.* **61** (2006) 5962 – 5968.

6. Bode, H. and Teufer, G. Die kristalstruktur des kaliumhexafluorozirkonats und kalium hexafluorohafnats. *Acta. Cryst.* **9** (1956) 929 – 933.

7. Givand, J., Chang, B-K. Teja, A.S. and Rousseua, R.W. Distribution of isomorphic amino acids between a crystal phase and an aqueous solution. *Ind. Eng. Chem. Res.* **41** (2002) 1873 – 1876.

8. Rosenberger, F. and Riveros, H.G. Segregation in alkali halide crystallization from aqueous solutions. *J. Chem. Phys.* **60** (2) (1974) 668 – 673.

9. Meenman, P.A., Anderson, S.R. & Klug. D.L. 2002. The influence of impurities and solvents on crystallization. In Myerson, A.S., ed. Handbook of industrial crystallization. 2nd ed. Boston: Butterworth-Heinemann. p. 67 - 100.

10. Geertman, R.M. *Crystallization of organic compounds: Studies on crystal morphology and purity.* Ph.D-thesis, Katholiek Universiteit, Nijmegen, 1993.

11. Diepen, P.J. Cooling crystallization of organic compounds: processes, purity and permeability. Ph.D-thesis, Technische Universiteit, Delft, 1998.

12. Segall, M.D., Lindan, P.J.D., Probert, M.J., Pickard, C.J., Hasnip, P.J., Clark, S.J. and Payne, M.C. First-principles simulation: ideas, illustrations and the CASTEP code. *J. Phys.: Condens. Matter.* **14** (2002) 2717 – 2744.

13. Accelrys Software Inc.,Materials Studio Modelling Environment, Version 4.0 and 4.2, San Diego: Accelrys Software Inc., 2007.

14. Monkhorst, H.J. and Pack, J.D. Special points for Brillouin-zone integrations. *Phys. Rev. (B).* **13** (12) (1976) 5188 - 5192.

15. Perdew, J.P., Burke, K. and Ernzerhof, M. Generalized gradient approximation made simple. *Phys. Rev. Lett.* **77** (18) (1996) 3865 – 3868.

16. Vanderbilt, D. Soft self-consistent pseudopotentials in a generalized eigenvalue formalism. *Phys. Rev. (B).* **41** (11) (1990) 7892 – 7895.

17. Berghout, A., Zaoui, A., Hugel, J. and Ferhat, M. First-principles study of the energy-gap composition dependence of $Zn_{1-x}Be_xSe$ ternary alloys. *Phys. Rev. (B).* **75** (2007) 205122-1 – 205122-9.

18. Ding, S.F., Fan, G.H., Li, S.T., Chen, K. and Xiao, B. Theoretical study of $Be_xZn_{1-x}O$ alloys. *Phys. B.* **394** (2007) 127 – 131.

19. Løvvik, O.M. and Opalka, S.M. Density functional calculations of Ti-enhanced $NaAlH_4$. *Phys. Rev. (B).* **71** (2005) 054103-1 – 054103-10.

20. Ghosh, G. and Asta, M. First-principles calculation of structural energetics of Al-TM (TM = Ti, Zr, Hf) intermetallics. *Acta Mater.* **53** (2005) 3225 – 3253.

21. Papiernik, P. R., Mercurio, D. and Frit, B. Structure du Tétrafluorure de zirconium, ZrF_4 α. *Acta Crystallogr., Sect. B.* **38** (1982) 2347-2353.

22. Amrani, B., Ahmed, R. and El Haj Hassan, F. Structural, electronic and thermodynamic properties of wide band gap $Mg_xZn_{1-x}O$ alloy. *Comp. Mater. Sci.* **40** (2007) 66 – 72.

23. El Haj Hassan, F. and Akbarzadeh, H. First-principles investigation of BN_xP_{1-x}, BN_xAs_{1-x} and BP_xAs_{1-x} ternary alloys. *Mater. Sci. Eng. B.* **121** (2005) 170 – 177.

24. Amrani, B., El Haj Hassan, F. and Zoaeter, M. First-principles study of rock-salt $AgCl_xBr_{1-x}$ alloys. *Phys. B.* **396** (2007) 192 – 198.

25. Klamt, A. and Schüürman, G. COSMO: A new approach to dielectric screening in solvents with explicit expressions for the screening energy and its gradient. *J. Chem. Soc. Perkin Trans.* **2** (1993) 799-805.

26. Tomasi, J. and Persico, M. Molecular interactions in solution: An overview of methods based on continuous distributions of the solvent. *Chem. Rev.* **94** (1994) 2027 – 2094.

27. Klamt, A. Prediction of the mutual solubilities of hydrocarbons and water with COSMO-RS. *Fluid Phase Equilibr.* **206** (2003) 233 – 235.

28. Bradley, D.C. and Thornton, P. 1973. Zirconium and Hafnium. In: C. Bailar, H.J. Emeleus, R Nyholm and A.F. Trotman-Dickenson, eds. Comprehensive Inorganic Chemistry. Pergamon Press, Oxford, p.419-490.

29. Perry, R.H. and Green, D.W. 1997. Perry's chemical engineering handbook. 7th ed. New York: McGraw-Hill. p. 2-120 – 2-124.

CHAPTER 4

Cooling Crystallization of $K_2Zr(Hf)F_6$

4.1. Introduction

The use of fractional crystallization of $K_2Zr(Hf)F_6$ to separate Zr and Hf, which is based on the premise that the solubility of K_2HfF_6 is larger than that of K_2ZrF_6, was first presented by Coster and von Hevesy [1, 2], who also discovered element 72, i.e Hf [3]. Although relatively little information of the method was given in their original patent, it was stated that fractional crystallization from a 10 % HF and 5 % KF solution could be used where separation was achieved through repeated crystallization.

As mentioned in Section 2.1.5.2, the method was also investigated by Sajin et al. [4, 5] who used only deionised water in their crystallization studies. Although they were able to separate Zr and Hf on a laboratory scale, the process was characterized by a relatively low separation efficiency [5], hence 16 – 18 recrystallizations were necessary to purify the Zr-salt. Also, due to the nature of the recrystallization process, the total yield of the purified K_2ZrF_6 was very low, i.e. in the order of 10 %. Using an elaborate scheme in which the mother liquor of the previous crystallization was used as solvent for the next crystallization, they were able to increase the yield of the purified product to 80 %. The mother liquors obtained from the first two steps were removed from the cycle, and deionised water was again used as the solvent in the final stage. Whether or not this process was ever commercialized is uncertain.

Since K_2ZrF_6 and K_2HfF_6 have isomorphic crystal structures, it is possible that the efficiency of separation during crystallization from solution is lowered by the formation of solid solutions [6, 7], i.e. by incorporation of Hf directly into the crystal structure of K_2ZrF_6. In the previous chapter, it was shown that according to molecular modelling, where the calculated mixing enthalpies of solid solution formation were applied to a simplified form of the thermodynamic model [8] presented in Equation (4.1), relatively poor separation efficiency seemed likely.

$$\beta_0 = \frac{\gamma'_{Hf(l)}}{\gamma^{sat}_{Hf(l)}} \frac{x^{sat}_{Zr}}{x^{sat}_{Hf}} exp\left(\frac{-\Delta H^{dis}_{Hf} + T\Delta S^{vib}_{Hf}}{RT}\right) \quad (4.1)$$

Although different calculation methods were used that led to somewhat different results, the poor separation efficiency predicted could in general be ascribed to a small thermodynamic barrier that has to be overcome for the formation of solid solutions. The small thermodynamic barrier is characterized by the marginally positive or negative (depending on the calculation method) values of ΔH_{mix}, which were calculated from the modelling results. Thus, solid solution formation might well be the cause of the low separation efficiency, which would implicate the use of numerous crystallization stages to achieve the desired purity. Moreover, modelling of the solvated ions showed that there might not be a large difference in the solubility of hexafluoride salts in aqueous media, which, according to Equation (4.1) could also contribute to the predicted low separation efficiency.

Different studies have been done on the crystallization of various isomorphic compounds from solution [6, 7, 9, 10]. In these studies isomorphic amino acid compounds were mostly used, where the influence of different solvents and co-solvents on the crystal purity was investigated, with respect to the amount of incorporation of the isomorphic impurity in the crystalline product [7, 9, 10]. Consequently, the purity of the crystallized product was related to the relative distribution coefficient. This approach was therefore also used in this study (Section 3.3.1.5, Section 2.2.4.2), according to Equation (4.2).

$$\beta_{Hf,Zr} = \frac{z_{Hf}/x_{Hf}}{z_{Zr}/x_{Zr}} = \frac{K_{Hf}}{K_{Zr}} \quad (4.2)$$

An explanation of the different symbols is given in Section 2.2.4.2. The results of the abovementioned studies showed a definite relationship between the relative solubility ratio of the two pure isomeric compounds and the purity of the final crystalline product exists. More specifically, when the solubility of the impurity with respect to the desired compound in a solution with a specific composition increased, improved purity of the crystalline product could be obtained. Therefore, the influence of the relative solubility ratio on the separation efficiency according to the thermodynamic model of Rossenberger and Riveros, i.e. Equation (4.1) were validated by these results, at least for these isomeric systems. In fact, in the study of Nie et al. [9], it was shown that by neglecting the vibrational entropy contribution of

Equation (4.1), as well as the activity coefficient ratio (Chapter 3) for their isomeric steroid system, a linear relationship was obtained between the solubility ratio and the relative distribution coefficient. Accordingly, the value of the relative distribution coefficient increased as the solubility ratio increased, i.e. as the solubility of the impurity increased with respect to the desired compound. In all of these studies it was concluded that the solubility ratio is influenced by the solvent composition, where different solvent mixtures could effect a favourable change in the solubility ratio that in turn could be used to enhance the purity of the crystallized product, thus improving the separation efficiency of crystallization.

In light of the aqueous KF and HF mixture that was used by Coster and von Hevesy for fractional crystallization, crystallization of $K_2Zr(Hf)F_6$ from aqueous KF solutions with varying concentration with and without the presence of HF with a constant concentration was further investigated in this study. The influence of the solvent composition on the separation efficiency was studied by measuring the relative distribution coefficient as expressed in Equation (4.2). It is shown that by varying the solvent composition, the degree of crystallization can be influenced which in turn can also affect the separation efficiency. Furthermore, with the help of SEM and XRD analysis, the influence of the solvent composition on crystal structure and morphology was also evaluated, which was used to qualitatively explain the change in the separation efficiency when the solvent composition was varied.

4.2. Experimental Methods

4.2.1. Materials

Potassium hexafluorozirconate, K_2ZrF_6 [16923-95-8] which contained approximately 1 - 2 % K_2HfF_6 by mass, was purchased from Sigma-Aldrich, South Africa and was used for all crystallization experiments and solubility studies without further purification. The Hf content was determined via ICP-OES analysis, which will be detailed in Section 4.2.4.1.A. Accordingly, the K_2ZrF_6 purity was determined as approximately 90 – 92 % by mass. Potassium fluoride, KF [7789-23-3], with a minimum purity of 98.5 %, purchased from Merck; and aqueous hydrofluoric acid (48 % by mass), HF [7664-39-3], purchased from Fluka was used to prepare the aqueous solvent mixtures of different compositions that were used in the crystallization of $K_2Zr(Hf)F_6$. Absolute ethanol, [64-17-5] (Merck) was used to

wash the crystalline products for SEM analysis, as well as the containers to remove any adhering salt. Sulphuric acid, H_2SO_4, (98 %) [7664-93-9] from Saarchem was used to lower the HF concentration of HF-containing mother solutions to be suitable for ICP analysis as is described in Section 4.2.4.1.B.

$ZrOCl_2$ and $HfOCl_2$ standard solutions with concentrations of 1000 mg/L M(IV) (M = Zr/Hf) each (CertiPUR), purchased from Merck, were used as supplied to prepare standard solutions by dilution for ICP-OES calibration. Both $ZrOCl_2$ and $HfOCl_2$ solutions are certified to contain less than 0.1 mg/L Hf and 0.1 mg/L Zr respectively. Hydrochloric acid, HCl (32 %) [7647-01-0], Saarchem, was used to adjust the HCl concentration of the calibration standards to a constant value of 0.2 mol/L. Potassium calibration standards, also for ICP-OES purposes, were prepared from potassium dichromate, $K_2Cr_2O_7$ [7778-50-9], with a minimum purity of 99.5 % (Sigma-Aldrich). Nitric acid, HNO_3 [7697-37-2] (55 %), from Saarchem, was used for the preparation of these standard solutions. Whatman no. 542 ashless filter paper was used for filtration. Deionised water with a resistivity of 18 MΩ.cm was used in the preparation of all aqueous solutions.

4.2.2. Solubility Studies of $K_2Zr(Hf)F_6$

In an attempt to quantify the changing salt solubility during crystallization from aqueous solutions of KF, and KF and HF mixtures with varying KF concentration (see Section 4.2.3.3), the solubility of the unpurified salt was determined. This implies that the total solubility, including the Hf-impurity and other possible contaminants, was determined. The solubility was determined in pure H_2O and aqueous solutions of varying KF concentration with and without the presence of a constant HF concentration of 2.5 mol/L as a function of temperature. Note that an Adam PW series 4-decimal balance was used for all gravimetric determinations.

4.2.2.1. Open Circulation System

Initially, the solubility of $K_2Zr(Hf)F_6$ in pure H_2O was determined using an open water bath system to regulate the temperature of the solutions that were housed in polyethylene containers. The experimental setup is shown in Fig. 4.1. Temperature regulation was provided by a Julabo FP50-ME thermostat bath that circulated the bath fluid (water) to the external

water bath. The thermostat bath has a reported temperature stability of ± 0.01°C. The solubility was determined at discrete temperatures of 35 °C to 65 °C at intervals of 10 °C. An excess of $K_2Zr(Hf)F_6$ was weighed in four separate polyethylene bottles, and the same weight of salt was used for each bottle. One hundred millilitres of deionised H_2O was measured using volumetric flasks and added to each of the four bottles. A magnetic stirrer bar was added to each mixture and the containers were sealed tightly using screw-caps. The bottles were then immersed in the water bath that was used to keep the temperature constant for 24 hours at the desired temperature setting.

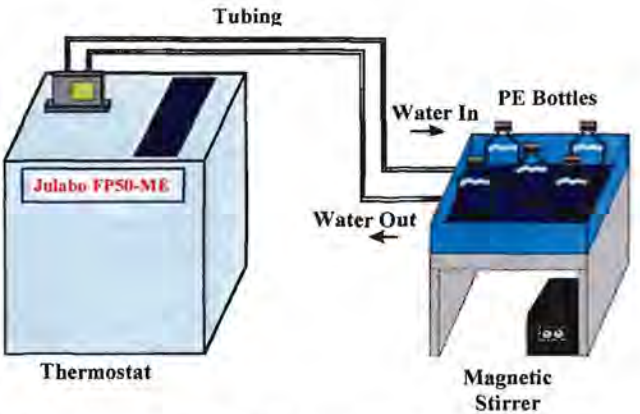

Figure 4.1: Experimental setup used to determine the total solubility of $K_2Zr(Hf)F_6$ in H_2O at different temperatures.

The water bath was placed on top of a multiple magnetic stirrer assembly whereby the mixtures in each bottle could be kept well-mixed. One hour was allowed after the bottles were placed in the water bath to allow the mixture to also achieve thermal equilibrium; thereafter the 24 hour period was commenced. Using this method the solubility was thus determined four times at each temperature.

Just before the 24 hour period was completed, the mass of 4 different filter papers were determined. After the mixtures were held at a constant temperature for 24 hours, the mixtures were filtered as quickly as possible using a Büchner funnel, and ethanol was used to wash the remainder of the undissolved salt from the inside of the containers. The filtered products and

filter papers from each of the four cases were dried overnight in an oven at 50 °C. The mass of the dried product and filter papers were determined, whereby the mass of the undissolved salt could be calculated from which the mass of the dissolved product was determined. The data from the four measurements were then used to determine the average solubility as well as the standard deviation.

4.2.2.2. Closed Circulation System

The use of the open circulation system proved to be practically difficult though, especially at high temperatures where evaporation of the bath fluid (water) led to the thermostat switching off automatically when the fluid level dropped below a certain minimum. Since the temperature needed to stay constant for 24 hours, the same jacketed vessels used for the crystallization experiments (Section 4.2.3), were used for the determination of the solubility in KF, and KF and HF solutions. This experimental setup greatly restricted the loss of the bath fluid by evaporation. While the solution volume had to be doubled (and therefore also the weight of salt that was used) to ensure effective stirring with the overhead stirrers, no other change was made in the experimental method used to determine the solubility. The measured solubility is reported in g salt per 100 mL solvent for both methods.

For this experimental design, the setup is illustrated in Fig. 4.2. To be able to repeat the same experiment in a single run, another vessel was used in parallel to the one shown in Fig. 4.2. The second vessel had the same basic construction and the same type of impeller was used in both vessels to ensure repeatable results. The jacketed vessels were constructed of a glass outer shell with Teflon inner vessels with a thickness of about 0.5 mm. The Teflon vessels (see Fig. 4.3) were constructed using glass moulds that were coated on the inside with a thin layer of Teflon, whereby versatile containers could be produced that are resistant against HF. The Teflon vessels were fitted with a rubber seal and secured in place with screws as shown in the photographs of Fig. 4.3. The solubility of $K_2Zr(Hf)F_6$ in aqueous solutions of KF with varying concentrations of 0.1 mol/L to 0.5 mol/L with and without the presence of a constant HF concentration of 2.5 mol/L was determined using this setup.

As mentioned earlier, the same basic method was used as for the determination of the solubility in H_2O (Section 4.2.2.1). The solubility was determined at discrete temperatures of 35 °C to 65 °C at intervals of 10 °C. An excess of $K_2Zr(Hf)F_6$ was weighed for each of the

equilibrium vessels, and the same weight of salt was used for each vessel. Two mol/L KF stock solutions were prepared by weighing approximately 117.4 g of KF which was then dissolved in H_2O to a final volume of 1000 mL.

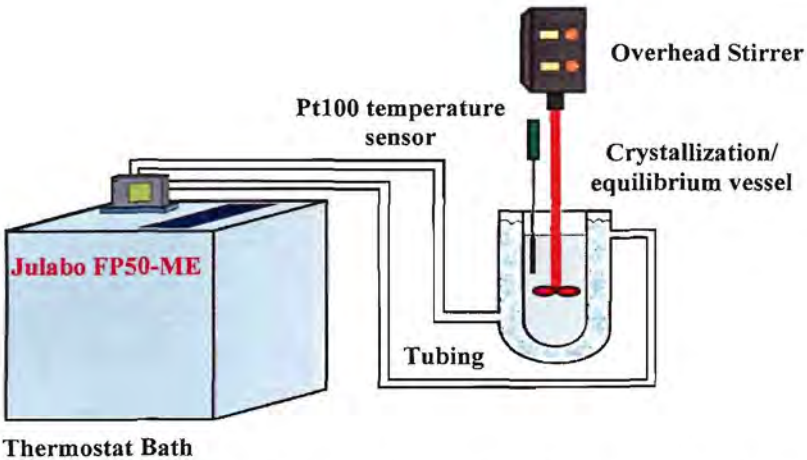

Figure 4.2: Experimental setup used for solubility studies as well as crystallization experiments. To conserve space, the extra vessel that was used in parallel is not shown.

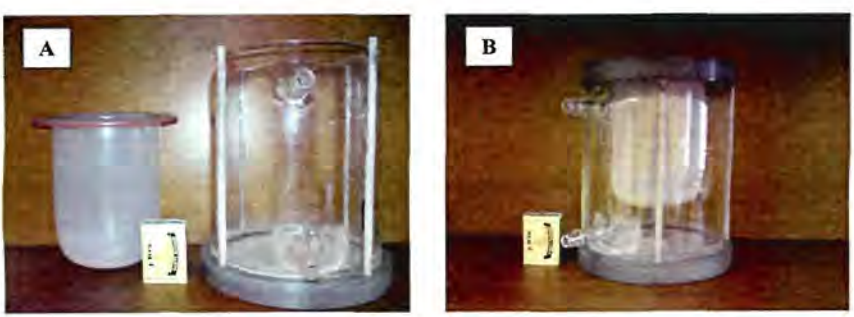

Figure 4.3: Photographs of one of the jacketed Teflon vessels used for crystallization experiments and solubility studies. Figure A shows the Teflon vessel and outer shell, and Figure B shows the whole assembly.

One set of stock solution was used for each of the KF, and KF and HF experiments respectively. Two hundred millilitres solutions with the desired KF concentration with and without 2.5 mol/L HF were prepared from the stock solutions and the 48 % HF solution by dilution. A-grade glassware was used for the preparation of the KF solutions. The KF + 2.5 mol/L HF solutions on the other hand, were prepared by measuring the desired volume of the KF stock solution and HF solution using A-grade glass pipettes and micropipettes (only micropipettes with plastic tips were used to transfer the HF solution) which was then added to polyethylene bottles. The mixtures were then diluted to 200 mL by adding the required amount of H_2O using A-grade pipettes and micropipettes.

A 50 mL volumetric flask was used to test whether a change in the volume occurred when KF, and KF and HF is mixed with H_2O. This was done by adding a certain volume of concentrated KF, and KF and HF to the volumetric flask which was then filled to the mark with H_2O with as little disturbance of the bottom layer as possible. The flask was then shaken so that the contents were well mixed. The solutions were then left to settle for a few seconds. Since the liquid level remained unchanged, it was assumed that the correct volume will be obtained with the solution preparation method described in the previous paragraph.

The prepared solutions of KF, and KF and HF were transferred to each vessel with an excess amount of salt. The containers were sealed tightly using laboratory film (Parafilm "M") and the mechanical stirrers (PTFE-coated shaft and PTFE blades) were fitted with a rubber seal and vacuum grease to the lids of the vessels. An external temperature sensor was used to regulate the temperature of the external vessels. This sensor was tightly fitted to the lid of one of the vessels using PTFE tape. A stirring speed of 200 rpm was used for each vessel, and the temperature of the circulating water was kept constant at the desired setting for approximately 24 hours. One hour was allowed after the circulation was started to allow the mixture to achieve thermal equilibrium; thereafter the 24 hour period was initiated.

After the 24 equilibrium period was completed, the same method was used as described for the Open circulation system (Section 4.2.2.1) with regard to the determination of the weight of the undissolved salt and filter papers, from which the solubility was determined gravimetrically. The data from the two measurements from the two Teflon vessels were then used to determine the average solubility as well as the standard deviation for each measurement.

4.2.3. Cooling Crystallization

4.2.3.1. Experimental Setup: Testing and Optimization

4.2.3.1.A. Temperature Regulation

The experimental setup shown in Figs. 4.2 and 4.3 was also used for the cooling crystallization experiments. Because of the Teflon construction of the crystallization vessels, and the fact that Teflon has relatively poor heat conduction properties, the temperature regulation of the external system was first tested to determine how the system will behave under conditions of heating and cooling, as a relatively quick and effective temperature change is necessary for cooling crystallization.

To determine the difference in the rate of temperature change of the thermostat bath itself and the external vessels, different temperature profiles of heating and cooling were run using pure H_2O in the vessels. As mentioned in Section 4.2.2.2., a temperature sensor, fitted to one of the vessels was used to regulate the temperature of both external vessels. The temperature sensor (Julabo) was supplied Teflon-coated to be resistant against corrosive solutions, e.g. HF solutions. The temperature in the second vessel was measured using a thermometer for the regulation tests.

At a heating and cooling rate of 0.6 °C/min, the there was an initial temperature lag of 5 °C with respect to the temperature of the external vessels. At a heating and cooling rate of 0.3 °C/min, i.e. two-fold lower, the difference decreased to about 3 °C. In all cases the difference between the two vessels was smaller than 1 °C. A rate of 0.3 °/min is comparable to the cooling rate used for crystallization, and it was therefore concluded that the temperature can be effectively controlled using this experimental setup.

4.2.3.1.B. Reproducibility Tests and Optimization

The deviation in the attributes of the crystallized products between the two crystallization vessels was first tested to be able to conduct single experiments in duplicate at the same time, similar to the solubility studies. The procedure was as follows: First, equal amounts of $K_2Zr(Hf)F_6$ (between 25.000 g and 25.001 g) were dissolved at elevated temperatures in equal amounts of pure water (500 mL). The clear solutions were filtered and transferred to the two jacketed Teflon vessels (crystallization vessels) as shown in Figs. 4.2 and 4.3. The solutions

were cooled to 15 °C to achieve supersaturation, where the solution temperature was then kept constant. Subsequently, the mother liquors and crystals were sampled, and a small portion of the crystals was washed with ethanol for analysis using SEM, while the rest was washed with deionised water and dried overnight in an oven at 50 °C. The dried product was redissolved in deionised water, and the redissolved products and mother liquors were analyzed using ICP-OES. Thereby, the separation efficiency could be determined for the crystallization in each vessel. The detailed method followed for crystallization is discussed in Section 4.2.3.2.

Initially, a run was performed (Run A) in which a stirring rate of 150 rpm was used for both vessels. Only one vessel (Vessel 1) was equipped with an external temperature sensor that allows the temperature inside the vessel to be controlled instead of the internal bath temperature. This also gave adequate temperature control for the second vessel (Vessel 2) connected in parallel (Sections 4.2.3.1 A. and 4.3.2.1.A). A second run (Run B) was then performed in which the same procedure was followed but the stirring rate was lowered to 100 rpm. The thermocouple arrangement remained the same as for Run A. In the case of Vessel 2, the formed crystals were not clearly defined when inspected visually, and had an almost powdery appearance. Therefore, only the product of Vessel 1 was filtered, but because the presence of the temperature sensor, which seemingly acts as a baffle, clearly influenced the flow pattern of the liquid and thereby the formation of the crystals, the temperature profile was restarted for Vessel 2. The temperature sensor was then placed in Vessel 2 and the stirring rate was again increased to 150 rpm. After the temperature profile was completed, the crystals (which could be clearly distinguished this time) and mother liquor were sampled as was done for Run A.

4.2.3.2. Crystallization with a Constant Salt Concentration

The experimental method used in this study was based on the basic method described by Nie et al. [9] and Givand et al. [10] in their respective studies on the crystallization of isomorphic compounds.

Crystallization of $K_2Zr(Hf)F_6$ from aqueous solutions of varying KF concentration without and with HF (at a constant concentration of 2.5 mol/L) was studied. Crystallization was first performed using a constant salt concentration by dissolving between 20.0000 g and 20.0009 g of $K_2Zr(Hf)F_6$ in 500 mL of the prepared solutions of KF and KF + HF at elevated

temperatures in polyethylene containers. The solutions were prepared in the same way as with the solubility studies, i.e. 2 mol/L KF stock solutions were prepared by dissolving about 117.4 g KF in H_2O so that the solution had a final volume of 1000 mL. The KF, and KF and HF solutions were prepared from the 2 mol/L KF and 48 % HF stock solutions. The KF concentration was varied between 0.05 mol/L and 0.5 mol/L at intervals of 0.05 mol/L without and with a constant HF concentration of 2.5 mol/L, as well as crystallization from pure H_2O. After approximately one hour, to allow dissolution of the salt, the clear solutions were filtered and transferred to the jacketed Teflon vessels (crystallization vessels as illustrated in Figs.4.2 and 4.3).

The optimized experimental setup (Sections 4.2.3.1.B. and 4.3.2.1.A) was used for all crystallization experiments. The temperature of the solutions was held constant at 70 °C for 1 hour before it was cooled to 15 °C at a cooling rate of approximately 0.18 °C/min to achieve supersaturation. The temperature of the solutions was then kept constant at 15 °C for 5 hours to allow for equilibrium to be achieved. Subsequently, the mother liquors were sampled and filtered, and the crystals were collected by filtration. Before the mother liquors were sampled however, a portion of the liquid from each experiment was filtered through the filter papers so that the filter papers were saturated with the solution. This was done to prevent the Hf concentration (relatively small in comparison with that of Zr) to change due to absorption on the dry filter papers. A small portion of the crystalline products was taken and washed with ethanol for analysis using SEM, and the rest was washed with deionised water and dried overnight in an oven at 50 °C. The dried products were redissolved in deionised water, and both the redissolved products and mother liquors were analyzed by ICP-OES, to determine the separation efficiency.

Each experiment was conducted in duplicate to assure reliable results using the two jacketed Teflon vessels connected in parallel (see solubility studies, Section 4.2.2.2). The stirring rate was increased from 150 rpm to a maximum of 205 rpm with increasing KF concentration. This was necessary to ensure that crystals remained in suspension throughout the crystallization process, which seems to be related to the number of nuclei formed, which depends on the solution composition. A second non-functional temperature sensor of the same basic design as the primary sensor was used in the second crystallization vessel to duplicate the physical conditions of the first crystallization vessel as accurately as possible (Sections 4.2.3.1.B. and 4.3.2.1.A).

4.2.3.3. Crystallization with a Controlled Salt Concentration

As shown in Section 4.3.1, the total solubility of $K_2Zr(Hf)F_6$ decreased as the KF concentration increased, whereas the addition of HF resulted in a slight increase in the solubility. Therefore, during crystallization from KF, and KF and HF solutions with increasing KF concentration, wherein a constant concentration of $K_2Zr(Hf)F_6$ was used, the supersaturation conditions were different for the different experiments. This can lead to changes in the growth and nucleation rates [11 - 14], which can have an influence on the crystal morphology [15] and purity [11]. The decrease in solubility caused by the modification of the solvent compositions is commonly known as salting-out [12]. KF, has the K^+-ion in common with $K_2Zr(Hf)F_6$ and therefore exhibits both a common ion effect as well as a slight salting-out effect which explains the decrease in solubility with increasing KF concentration.

To compensate for the decreasing solubility of $K_2Zr(Hf)F_6$ for crystallization from KF and KF plus HF solutions with increasing KF concentration, additional experiments were performed wherein the relative excess amount of $K_2Zr(Hf)F_6$ dissolved at $T = 70$ °C with respect to the solubility at $T = 15$ °C in each solvent, were kept constant. Thereby, the effects of KF, and KF with HF on the separation efficiency during crystallization could be isolated. The initial $K_2Zr(Hf)F_6$ concentration at $T = 70$ °C was adjusted using the solubility data (Sections 4.2.2 and 4.3.1) so that the same relative surplus amount of $K_2Zr(Hf)F_6$ would be dissolved at $T =$ 70 °C with respect to the equilibrium solubility at 15 °C for each solvent composition.

Analogous to the concept of the relative supersaturation ratio (Equation (4.3)) [13, 16], the required amount of $K_2Zr(Hf)F_6$ that needed to be dissolved at a specific KF concentration with and without HF (2.5 mol/L) was calculated using Equation (4.4).

$$\sigma = \frac{c_i - x_i^{sat}}{x_i^{sat}} \tag{4.3}$$

In Equation (4.3), c_i is the solute concentration (g/100 mL solvent) at temperature T (K), and x_i^{sat} is the equilibrium concentration (g/100 mL solvent), or solubility at temperature T. The relative supersaturation ratio therefore relates the degree of supersaturation to the relative excess amount of solute dissolved at temperature T divided by the solubility at temperature T. Using this idea, it is postulated that the total excess amount of dissolved solute at temperature

T_2 (70 °C), with respect to the solubility at temperature, T_1 (15 °C), divided by the solubility at T_1, should give a quantitative measure of the total amount of dissolved solute. This can be expressed according to:

$$\Sigma = \frac{c_{tot}(T_2) - x_{tot}^{sat}(T_1)}{x_{tot}^{sat}(T_1)} \tag{4.4}$$

where $c_{tot}(T_2)$ is the concentration of the dissolved salt ($K_2Zr(Hf)F_6$, hence the subscript) at temperature T_2, while $x_{tot}^{sat}(T_1)$ is the total solubility of the salt at temperature T_1. The concentrations ($c_{tot}(T_2)$ and $x_{tot}^{sat}(T_1)$) are measured here in grams per volume solvent (mL), which as for the crystallizations with a constant salt concentration, was g/500 mL solvent in this study. By rearranging Equation (4.4), the amount of $K_2Zr(Hf)F_6$ ($c_{tot}(T_2)$) that needed to be dissolved at temperature T_2 to yield a predetermined value for Σ could be calculated. Thus, the relative excess amount of salt dissolved at temperature T_2 with respect to temperature T_1 could be kept constant for the changing solvent compositions. When the relative excess amount of dissolved salt is increased, the value of Σ increases and a larger mass of crystals will be produced. The parameter Σ can therefore be used to characterise the degree of crystallization.

Two sets of experiments were performed for each of the KF, and KF plus HF series of crystallizations, i.e. with values of Σ = 2.5, and Σ = 5. For these experiments however, crystallization was only performed from solutions with KF concentrations of 0.1 mol/L, 0.3 mol/L, and 0.5 mol/L with and without the presence of a constant HF concentrations of 2.5 mol/L, together with crystallization from pure H_2O with the same values of Σ. The solutions were prepared using the same method as described in Section 4.2.3.2, where 2 mol/L KF stock solutions were prepared for use in each of the KF, and KF plus HF crystallizations. The basic experimental procedure, as used for the crystallization with a constant salt concentration (Section 4.2.3.2), was used for these experiments, where every experiment was conducted in duplicate.

4.2.3.4. Staged Crystallizations

The efficiency of separation and the change in purity of the crystalline product resulting from a mini cascade-type crystallization process was also studied, to determine the efficiency of crystallization as a function of crystallization stage.

For these stage-wise crystallizations, a simple cascade method [17], illustrated in Fig. 4.4, was used where the mother liquor from each stage is discarded. The notation y_{Zr} represents the composition of the feed in terms of the Zr-content. z_n ($n = 1, 2, 3$) represents the composition of the crystalline products from each crystallization stage, and x_n the composition of the mother liquor. For these experiments the mother liquors were sampled according to the method described in Section 4.2.4.1.B, to determine the separation efficiency of each stage.

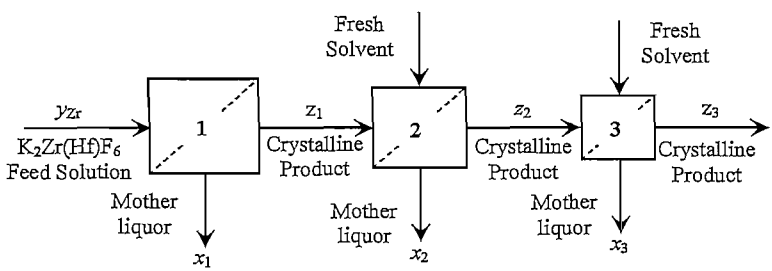

Figure 4.4: Schematic illustration of the method used for staged crystallization experiments.

Three batch crystallizations were performed in series using the same experimental setup as used for the other crystallization experiments (Sections 4.2.3.2 and 4.2.3.3). Two sets of experiments were performed; firstly, where the crystallization was conducted from a 0.5 mol/L KF solution, and secondly, where crystallization was conducted from a 0.45 mol/L KF with 2.5 mol/L HF solution. In both cases the same concentration of $K_2Zr(Hf)F_6$ (20 g/500 mL solvent) was used for each stage. For the first crystallization in each set, the amount of solvent and mass of $K_2Zr(Hf)F_6$ used was doubled (40 g/1000 mL); in other words the crystallization volume was doubled. For the second crystallization in each set, the crystallization volume was halved, where half the amount of salt (using the crystals produced in the first stage) and half the amount of solvent (which was freshly prepared) was used (20 g/500 mL). This sequence was continued to the third stage, where the volume was again half that of the second stage (10 g/250 mL). Since the total yield during crystallization from KF, and KF and HF solutions was more than 50 %, enough crystals could be produced during one

crystallization stage (which was first dried overnight at 50 °C before it was used in the next stage), so that half of the starting mass of the previous crystallization could be used with half of the amount of solvent in the next stage. Therefore, the ratio of the mass of salt to the volume of solvent was kept constant during the cascade, with fresh solvent being used in each stage.

The same basic experimental method, used for the other crystallization experiments, was employed (Section 4.2.3.2), and each experiment was conducted in duplicate. A 2 mol/L KF stock solution was prepared for each series of experiments according to the method previously described (4.2.3.2). Because of the volume change however, the stirring rate used in each vessel for both sets of experiments was set at 200 rpm for the first two stages, and then lowered to 170 rpm for the third crystallization stage. A small amount (about 0.625 g) of the dried crystals from each stage was redissolved in H_2O for ICP analysis. Together with the analysis of each mother solution, the separation efficiency could be determined for each crystallization stage for both sets of experiments.

4.2.3.5. Mass Balance

To determine whether mass balance conditions were satisfied when Zr and Hf is distributed in different ratios between the solid and liquid phases after crystallization, two experiments were performed. In one experiment, crystallization was performed from a pure H_2O solution, and in the other crystallization was conducted from a 0.25 mol/L KF solution.

Since the mass of the crystalline products had to be accurately measured, crystallization experiments were scaled down to a more manageable volume. Accordingly, the solvent volume was decreased to 100 mL, and the weight of salt used for the crystallization was also reduced. Experiments were conducted in duplicate by weighing between 4.0000 g and 4.0009 g $K_2Zr(Hf)F_6$ that was added to two separate polyethylene bottles. One hundred millilitres of the solvent, either H_2O or 0.25 mol/L KF solution, was measured using volumetric flasks and added to the containers with magnetic stirrer bars. The 0.25 mol/L KF solutions were prepared from a 2 mol/L KF stock solution. The polyethylene containers were sealed tightly using screw caps and PTFE tape. The salt was then dissolved in the respective H_2O and 0.25 mol/L KF solutions at ~ 90 °C using a water bath – stirrer hotplate configuration for at least one hour.

Thereafter, the magnetic stirrers were removed using a magnetic retriever after which the containers were resealed. The temperature was kept constant at ~ 90 °C for another 30 min to allow the system to reach thermal equilibrium. After this period, the heating was switched off and the solutions were left to cool naturally to ambient temperature in the water bath overnight for at least ten hours.

Filter papers were weighed and the mother liquors were filtered and sampled for ICP analysis (Section 4.2.4.1.B) using the same method as for the other crystallization experiments (Section 4.2.3.2). The rest of the solutions were filtered using a Büchner funnel, and the polyethylene bottles were washed with copious amounts of ethanol to remove the remaining crystals adhering to the containers' walls. No water was used in the washing stage as this can lead to partial dissolution of the crystals, and therefore a change in the total mass. The filtered crystals were dried overnight with the filter papers in an oven at 50 °C. After cooling for a couple of hours, the dried products together with the dried filter papers were weighed. Using this weight and the weight of the clean filter papers, the weight of crystals, i.e. the weight of $K_2Zr(Hf)F_6$ remaining in the mother liquor, could be determined gravimetrically. For this purpose, it was assumed that the volume of the solutions did not change significantly during the course of the experiments.

The dried crystals were also sampled and redissolved in H_2O for ICP analysis (Section 4.2.4.1.B). A $K_2Zr(Hf)F_6$ sample solution was prepared using the method described in Section 4.2.4.1.B, which was divided into four equal volumes for repeated ICP analysis to determine the Zr and Hf concentrations in the starting solutions.

4.2.4. Analytical Methods

4.2.4.1. Inductively Coupled Plasma: ICP-OES

4.2.4.1. A. Analytical Method

ICP-OES was used in this study to determine the Zr, Hf, and K concentrations for which a Thermo-Scientific *i*CAP 6000 Series ICP-OES, with the *i*TEVA software, was employed.

Zirconium and Hafnium

Calibration standards for both Zr and Hf were prepared from 1000 mg/L M(IV) standard solutions by serial dilution. First, 100 mg/L solutions of each Zr and Hf were prepared from the standard solutions by diluting with H_2O, which resulted in an HCl concentration of 0.2 mol/L (the supplied standard solutions contained HCl with a concentration of approximately 2 mol/L). 50 mg/L and 10 mg/L solutions were then prepared by diluting the 100 mg/L solution with a 0.2 mol/L HCl solution that was prepared beforehand, whereby the HCl concentration remained constant for all the solutions. Thus, standard solutions for both Zr and Hf with concentrations of 0 mg/L (blank solution), 10 mg/L, 50 mg/L, and 100 mg/L, in an aqueous matrix of 0.2 mol/L HCl were used for calibration. Quality control solutions were prepared from the 1000 mg/L stock solutions of Zr and Hf to validate the accuracy of the concentration measurement via ICP-OES at predefined intervals with each analytical run. These solutions consisted of a mixture of Zr and Hf with a concentration of 50 mg/L each. The solutions were prepared by 10-fold dilution with H_2O of an equivolume mixture of the Zr and Hf stock solutions to yield a solution with an HCl concentration of 0.2 mol/L. The Zr and Hf concentrations were thus effectively diluted 20-fold in the process to yield concentrations of 50 mg/L for each species. A-grade glassware was used in the preparation of all these solutions. The maximum allowable error in the concentration measurement via ICP-OES was set at 10 %, which for the 50 mg/L quality control solutions, corresponded with a variation of $\pm$ 5 mg/L.

The initial calibration was done at two spectral emission wavelengths for both Zr and Hf that according to the *i*TEVA software gave the highest sensitivity for each Zr and Hf and the least amount of interference between them (Table 4.1). The calibration for each of the emission lines resulted in calibration curves for both Zr and Hf with correlation coefficients above $R^2 = 0.999$ (see Appendix A.1). Using the calibrations for the emission lines of Zr and Hf, the calibration standards were analyzed again to test the accuracy of the concentration determination of each emission line for both Zr and Hf. From the results (Appendix A.2) it was concluded that the emission lines of 343.8 nm for Zr and 263.8 nm for Hf gave the most accurate results which were subsequently used for further analyses.

Table 4.1: Relative intensity of selected emission lines of Zr and Hf. The percentage interference represents the amount of interference that can occur with Zr/Hf for a specific emission line.

Emission Line (nm)	Relative Intensity	% Interference of Zr/Hf
Zr (339.1)	3500000	0.77
Zr (343.8)	2500000	0.6
Hf (263.9)	1000000	8
Hf (339.9)	600000	8.33

Crystallization was performed in the absence of HCl, while the calibration standards consisted of 0.2 mol/L HCl solutions with different Zr- and Hf concentrations. Therefore, a test run was done to determine whether the metal concentrations in the crystallization samples could be accurately determined without the addition of HCl to the sample solutions. The test was performed using the samples obtained from the setup optimization runs (Section 4.2.3.1.B.), where one set of test solutions was prepared according to the sample preparation method used for all crystallization samples (Section 4.2.4.1.B). A second set of test solutions was prepared from the same "raw" sets of samples with the addition of HCl so that all of these samples would have the same metal concentrations as that of Set A, but with a constant HCl concentration of 0.2 mol/L. Both sets of samples were analyzed in a single run.

Additional test runs were performed by analyzing solutions with the same Zr and Hf concentrations that were prepared in a matrix of H_2SO_4 with increasing concentration. This was performed to test the influence of the H_2SO_4 concentration on the analytical method as H_2SO_4 was used in the sample preparation of the HF-containing mother liquors (Section 4.2.4.1.B.). The results are shown in Appendix B.1. Sequential analysis of a single solution that was divided into twenty portions was also performed to test the consistency of the analytic apparatus. The test solution (a 50:50 mixture of Zr and Hf by volume) also contained 0.2 mol/L HCl. The results of this test are shown in Appendix B.2.

Potassium

Calibration standards with concentrations ranging between 0 mg/L and 500 mg/L, based on the Cr(VI)-concentration, were prepared by serial dilution of a 1000 mg/L Cr(VI)-solution. This solution was prepared by dissolving 1.4216 g $K_2Cr_2O_7$ in a 0.1 mol/L HNO_3 solution to yield a final volume of 500 mL (Appendix C.1). Concentrated HNO_3 was added to each solution to keep the HNO_3 concentration constant at 0.1 mol/L.

Calibration was performed according to the corresponding K^+-concentrations of each solution, again for two different emission wavelengths of K, namely the 766.4 nm and 769.8 nm emission lines. Calibration curves with correlation coefficients above $R^2 = 0.999$ were obtained using both wavelengths (Appendix C.2). Using these calibrations, 50 mg/L and 100 mg/L (Cr(VI)-concentration) solutions were analyzed to determine the accuracy of the calibrations. According to the results (Appendix C.3), the 766.4 nm emission line was the most accurate and was therefore used for further potassium analysis. The potassium concentrations of different crystallization samples (the exact same samples used for the determination of Zr and Hf concentrations), were determined using this method. This was done to quantitatively determine the K/Zr ratios of the redissolved crystalline products for comparison with XRD results (Section 4.3.2.3.B).

4.2.4.1.B. Sample Preparation

The oven-dried crystals from each experiment were weighed, of which between 0.6250 g and 0.6259 g of the crystals (measured using an Adam PW series 4-decimal balance) were dissolved in H_2O at room temperature for approximately one hour using magnetic stirrers to yield a total volume of 250 mL. The solutions were then diluted 10-fold while the mother liquors produced from the 0 – 0.5 mol/L KF crystallizations were diluted 40-fold for ICP-OES analysis.

In the case of HF-containing mother liquors, the HF-content was first reduced via evaporation to avoid damage to the glass instrumentation of the ICP analytical apparatus. The method was as follows: Equal amounts of the HF-containing mother liquor and concentrated sulphuric acid were poured into a Teflon beaker which was then heated to between 200 °C and 210 °C in a sand-bath inside a fume hood. Magnetic stirrers were used to provide gentle agitation. A

glass cover slip was used to determine whether HF had evaporated from the solutions, since the glass cover slip is etched in the presence of HF-vapours. After approximately ten hours, no more visible etching of a clear cover slip occurred and it was assumed that most of the HF had been removed from the solutions. After 10 hours the volume of the solutions in the Teflon beakers had decreased by almost half the original volume. The warm solutions were allowed to cool, and were diluted 40-fold with H_2O to obtain an aqueous solution which was suitable for ICP analysis, i.e. having a H_2SO_4 concentration in the order of 0.5 mol/L. During the evaporation process, no precipitation of the dissolved compounds was noted. This method should also not influence the relative concentrations of Zr and Hf as separation had already been completed during the crystallization stage and the resulting mother liquors were stable for long periods of time (no further crystallization occurred during storage). Also, only the more volatile HF was removed while any other non-volatile compounds should remain in solution.

The dilution of the samples as described in the above two paragraphs produced sample solutions with Zr concentrations lower than 100 mg/L, and Hf concentrations lower than 10 mg/L. The dilution further meant that the additives such as KF, and H_2SO_4 in the case of the prepared samples of HF-containing mother liquors, should not have had a profound influence on the concentration determination of Zr and Hf (consult Appendix B.1).

Multiple $K_2Zr(Hf)F_6$ solutions were prepared using the commercial $K_2Zr(Hf)F_6$ (Sigma-Aldrich reagent before recrystallization). These solutions were also analyzed by ICP-OES to serve as reference for the purity of the crystallized products. The solutions were prepared by weighing between 0.6250 g and 0.6259 g $K_2Zr(Hf)F_6$ which was then dissolved in H_2O to yield a final volume of 250 mL which was then diluted 10-fold (just as for the recrystallized products).

4.2.4.2. Scanning Electron Microscopy (SEM)

Crystal morphology was examined using scanning electron microscopy (SEM). Air-dried crystal samples were washed with ethanol and then coated with a thin film of Au/Pd (80/20). Images were generated under vacuum using a FEI Quanta 200 ESEM electron microscope. Depending on the crystal size and homogeneity of the sample, the voltage used was varied between 10 kV and 15 kV to prevent overexposure to larger crystals.

4.2.4.3. X-Ray Diffraction (XRD)

XRD analysis was used to identify the crystalline products obtained during crystallization from the different solvent mixtures used in this study. H_2O-washed, and oven dried crystals were ground to a fine powder using a mortar and pestle. A PW1770/10 powder sample preparation kit was used for sample preparation whereby the powdered samples were heaped into the sample holder ring (PW 1811/16). The powders were pressed down firmly by hand using a powder press block, and a knife was used to scrape the excess powder from the sample holder ring. This was repeated until a densely packed powder specimen was obtained. XRD spectra were collected using a Röntgen PW3040/60 X'Pert Pro diffractometer system. A Cu PW – 3373/10 tube was used at 40 kV and 45 mA as the radiation source. Spectra were interpreted using the 2007 Relational Database (International Centre for Diffraction Data).

4.3. Results and Discussion

4.3.1. Solubility of $K_2Zr(Hf)F_6$

The solubility of $K_2Zr(Hf)F_6$ as a function of temperature in aqueous mixtures containing varying concentration of KF are shown in Fig. 4.5.

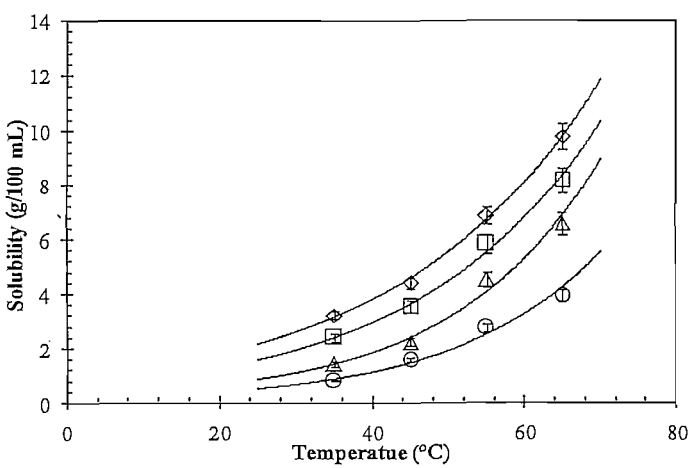

Figure 4.5: Total solubility of $K_2Zr(Hf)F_6$ in aqueous solutions with varying KF concentration as a function of temperature (T = 35 °C – 65 °C). ◊ – Pure H_2O, □ – 0.1 mol/L KF, Δ – 0.3 mol/L KF, ○ – 0.5 mol/L KF.

The results indicate a relatively low solubility which increases with temperature. The relative standard deviation for each of the measured data points did not exceed 6.2 %. The exponential fits are according to the empirical observation and not attributed to any chemical model and were used to extrapolate the solubility to 15 °C for use in Equation (4.4) (Section 4.3.2.3). The correlation coefficients for each of the fits were between $R^2 = 0.98$ and $R^2 = 0.9999$.

The results of the solubility measurements in KF mixtures with the same concentrations, in the presence of a constant HF-concentration of 2.5 mol/L are shown in Fig. 4.6, in which the solubility of K_2ZrF_6 in pure H_2O is also included. The relative standard deviation of each of the data points did not exceed 4.7 %. The decrease in solubility with increasing KF concentration may be attributed to a combination of the common ion effect, and a slight salting-out effect.

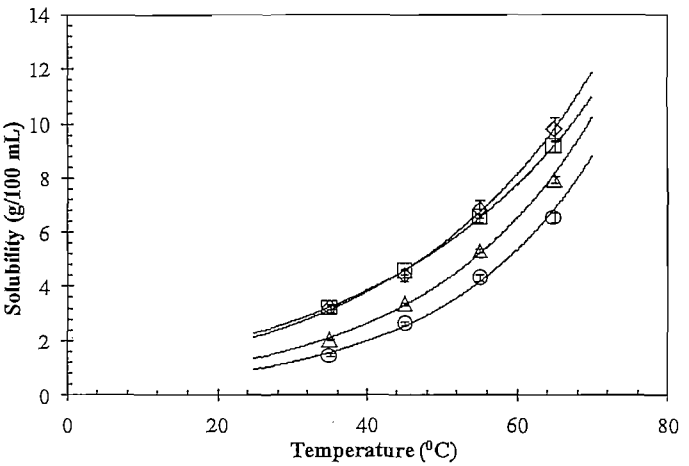

Figure 4.6: Total solubility of $K_2Zr(Hf)F_6$ in aqueous solutions of 2.5 mol/L HF and KF with varying concentration, as a function of temperature (T = 35 °C – 65 °C). ◊ - Pure H_2O, □ – 0.1 mol/L KF, Δ – 0.3 mol/L KF, ○ – 0.5 mol/L KF.

When comparing Figs. 4.5 and 4.6, it is clear that the addition of HF leads to an increase in the solubility of $K_2Zr(Hf)F_6$. This increase in solubility, in the presence of HF, may be caused by the speciation of the ions in solutions. In acidic HF-media, the formation of large

polynuclear hydroxo-bridged species [18] might be inhibited in which case solvation of the complex M(IV) ions can take place more easily. Speciation studies are needed however to confirm this speculation.

4.3.2. Cooling Crystallization

4.3.2.1. Experimental Setup: Testing and Optimization

The temperature regulation of the external Teflon vessels were deemed sufficient as explained in Section 4.2.3.1.A, and therefore the results will not be discussed in any further detail in this section. Only the results from the reproducibility tests (Section 4.2.3.1.B) will be highlighted to illustrate the accuracy of the experimental method used for crystallization.

4.3.2.1.A. Reproducibility Tests and Optimization

It was observed during the crystallization of Run A that the crystals remained in suspension for Vessel 1 whereas encrustation of the crystals occurred on the walls of the Teflon vessel in Vessel 2. SEM images taken of the crystals, shown in Fig. 4.7, indicate that the crystals of Vessel 1 (Fig. 4.7 A) exhibit more homogeneous growth than that of the encrusted crystals of Vessel 2 (Fig. 4.7 B). From the images we can also see that although a more homogeneous crystal size distribution (CSD) is obtained by growth of the crystals in suspension in comparison with the crystals grown on the wall of the crystallizer, a relatively wide CSD is still obtained for the crystals grown in Vessel 1. It is also apparent that a certain amount of agglomeration still occurred during suspension-growth, which can influence the purity of the product due to inclusion formation. However, in both cases crystals with a needle-shaped morphology were produced as shown in Fig. 4.7 C and D.

During Run B, crystallization in Vessel 1 (100 rpm stirring rate) produced crystals with a large degree of agglomeration and encrustation as shown in Fig. 4.8 A. As mentioned in Section 4.2.3.1.B, crystallization in Vessel 2 produced poorly defined crystals and therefore the product was not filtered. However, because the experiment in Vessel 1 was completed (the mixture was filtered and the crystals and mother liquor were sampled), the temperature profile was restarted for Vessel 2, for which the temperature sensor was placed in Vessel 2 and the stirring speed was increased to 150 rpm. This time, the crystals also remained in suspension during crystallization, similar to the crystallization in Vessel 1, Run A.

When comparing Figs. 4.7 A and 4.8 B it is clear that crystallization in both cases produced crystals with similar characteristics, i.e. with respect to the crystal size distribution (qualitatively speaking) and morphology of the crystals.

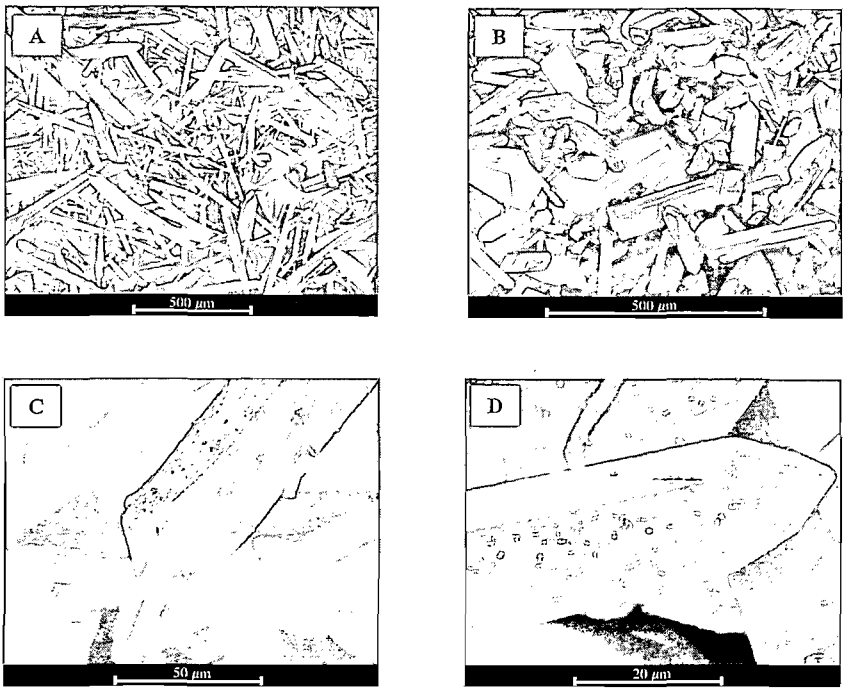

Figure 4.7: SEM micrographs of crystals crystallized in Vessel 1 (A and C) and Vessel 2 (B and D) during Run A.

The observed crystal roughness of the crystals obtained from Vessel 2 (Fig. 4.8 D) can be attributed to the onset of dissolution of the crystals, as it was accidentally washed with H_2O instead of ethanol. Nonetheless, this is an example of how the crystalline products that were washed with water and dried for ICP-OES analysis looked like. By, partially dissolving crystals used in the preparation of sample solutions for ICP-OES analysis, any adhered mother liquor, which will lower the purity of the product, was minimized. The samples obtained from each experiment were analyzed using the ICP-OES (Section 4.2.4.1) to determine the Zr and Hf concentrations. These results were then used to calculate the relative distribution

coefficient according to Equation (4.2). The concentrations obtained from ICP-OES analyses were used to calculate the relative mole fractions of Zr and Hf (designated z_i for the solid phase, and x_i for the liquid phase) on a solvent-free basis by neglecting the concentrations of any impurities. The relative distribution coefficients were then determined using this calculation method.

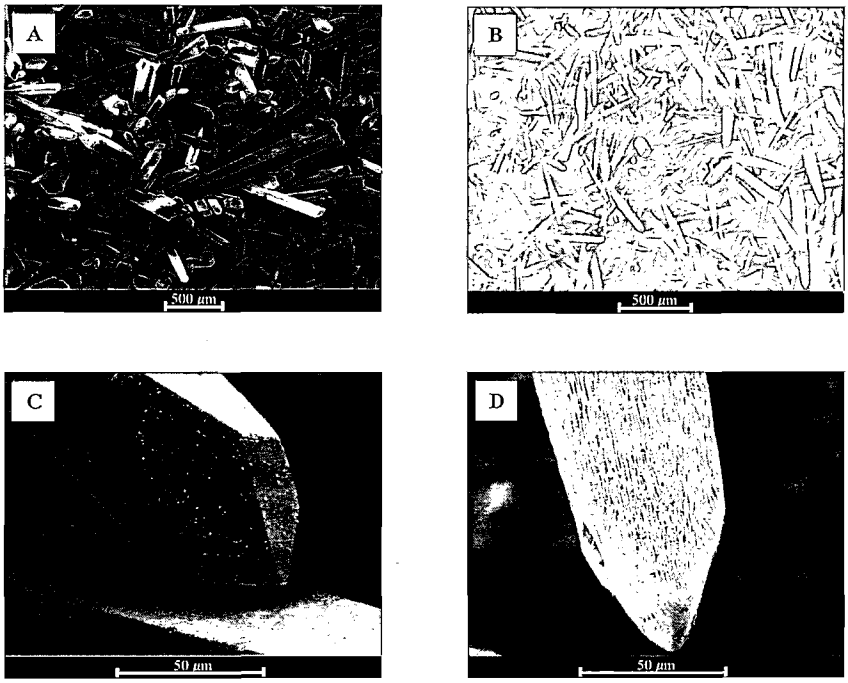

Figure 4.8: SEM micrographs of crystals crystallized in Vessel 1 (A and C) and Vessel 2 (B and D) during Run B.

The results for these experiments are shown in Fig. 4.9 which indicates that the separation efficiency decreased slightly for Vessel 2 (the lower the value of $\beta_{Hf,Zr}$, the better the efficiency) due to the encrustation of the crystals, when comparing the results of the two vessels for Run A. This is also reflected by the results of Run B when compared with that of Run A for Vessel 1, where the lower stirring rate prevented the crystals from being suspended in the mother solution.

It seems that the flow conditions within the crystallization vessels affect the behaviour of the particles which can indirectly influence the separation efficiency. Moreover, as the result from Vessel 2, Run B (where the conditions were more closely matched with that of Vessel 1, Run A) also shows, the calculated separation efficiency agrees better with that of Vessel 1, Run A. However, these fluctuations may also be due to unrelated experimental errors, because the relative standard deviation between all the measurements was 7.1 %. Nevertheless, for all the other crystallization experiments, a second, non-functional temperature sensor with the same construction as that used in Vessel 1 was used for Vessel 2 (Section 4.2.3.2). This was done to duplicate the conditions of Vessel 1 as closely as possible in Vessel 2, to ensure reliable and reproducible results. However, with regard to the 7.1 % variation in the measured distribution coefficient, encrustation vs. suspended-growth does not have a profound influence on the separation efficiency. Encrustation seems to be caused by a low agitation speed and the absence of a baffle in the form of the temperature sensor.

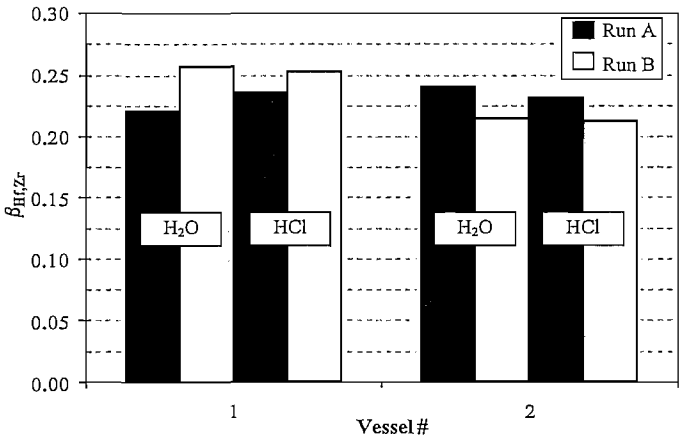

Figure 4.9: Relative distribution coefficient for crystallizations from Runs A and B. Results from ICP-OES analysis using pure H_2O- and 0.2 mol/L HCl matrix for sample solutions are shown.

The results of the relative distribution coefficient as calculated using the concentrations determined using ICP analysis of the same samples, which were prepared in HCl solutions of 0.2 mol/L (Section 4.2.4.1.A) are also shown in Fig. 4.9. The results show that there is not a significant difference in the results of the "HCl-samples" and the "H_2O-samples". These

results were also factored into the calculated variation of 7.1 % and are comparable with the fluctuation of the analytical apparatus (Appendix B.2). Therefore, provided that the samples are well diluted, the analyses are not influenced by the absence of HCl in the sample solutions and for this reason the sample preparation method discussed in Section 4.2.4.1.B was used.

To conclude this section, it was illustrated that reliable and reproducible results could be obtained using the experimental setup. The second vessel used in parallel was only fitted with a temperature sensor, which acts as a kind of baffle, to ensure that the experimental conditions of the two vessels were matched as closely as possible for the purpose of conducting experiments in duplicate. Furthermore, the small HCl concentration of 0.2 mol/L, as used in the calibration standards, did not seem to influence the analysis for Zr and Hf in the sample solutions, and therefore the solutions were prepared without the inclusion of HCl in the matrices according to the method presented in Section 4.2.4.1.B.

4.3.2.2. Crystallization with a Constant Salt Concentration

4.3.2.2.A. Crystallization from KF Solutions

The results of crystallization from aqueous solutions of varying KF concentration at a constant $K_2Zr(Hf)F_6$ concentration are shown in Fig. 4.10.

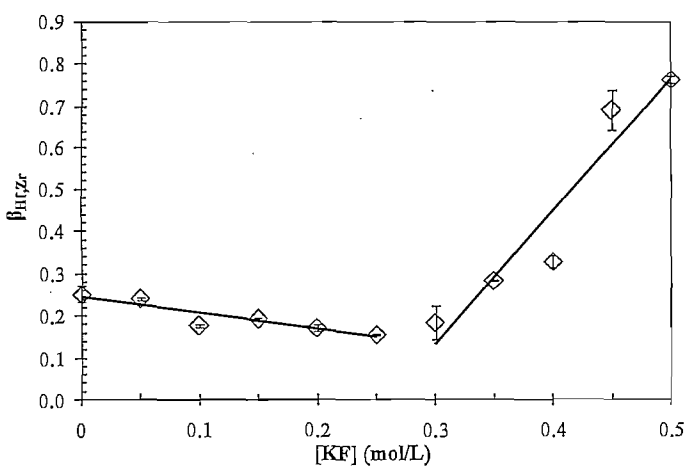

Figure 4.10: Measured distribution coefficient during crystallization of $K_2Zr(Hf)F_6$ from aqueous solutions of varying KF concentration, at a constant $K_2Zr(Hf)F_6$ concentration.

According to the results, $\beta_{Hf,Zr}$ decreased and therefore the selectivity increased slightly with increasing KF concentration up to 0.25 mol/L KF. With further increase in the KF concentration however, the relative distribution coefficient increased, resulting in a rapid decrease in the selectivity. For example, at a KF concentration of 0.5 mol/L, the distribution coefficient was 0.76 which corresponds to a separation factor (β^{-1}) of 1.31, indicating poor selectivity. However, since $\beta_{Hf,Zr}$ had a value smaller than unity for all the crystallizations means that the crystalline product is enriched with Zr during crystallization. Therefore, according to the definition of $\beta_{Hf,Zr}$ (Equation (4.2)) the relative Hf concentration in the mother liquor is higher than that in the crystalline product, i.e. $x_{Hf} > z_{Hf}$.

Fig. 4.11 shows the calculated Zr:Hf mole fraction ratios at equilibrium for both the solid (z_{Zr}/z_{Hf}), and liquid phases (x_{Zr}/x_{Hf}). The error bars shown for each value represent the average relative standard deviation for the solid and liquid phases respectively. The Zr:Hf ratio in $K_2Zr(Hf)F_6$ before recrystallization (i.e. the Sigma-Aldrich sample) is also shown for comparison. From the figure, it is evident that with increasing KF concentration, the ratio z_{Zr}/z_{Hf} (i.e. for the solid phase) decreased, therefore the relative concentration of Hf in the crystalline product increased. The question is then, why does the separation efficiency increase with an increase in the KF concentration up to 0.25 mol/L when the product purity decreases?

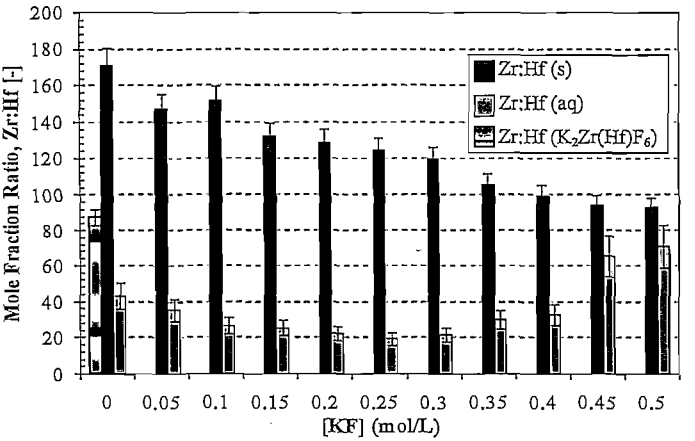

Figure 4.11: Mole fraction ratios of Zr:Hf in both the solid (s) and liquid phases (aq) at equilibrium during crystallization of $K_2Zr(Hf)F_6$ from aqueous solutions of varying KF concentration.

It is evident from Fig 4.11 that the Zr:Hf ratio in the liquid phase (x_{Zr}/x_{Hf}) simultaneously decreased slightly up to a KF concentration of 0.25 mol/L. Therefore, the concentration of Hf relative to Zr in the liquid phase (x_{Hf}) also increased, or in other words, at higher KF concentration more Hf remained in solution with respect to Zr which led to better separation of the two species with respect to the two phases. The simultaneous increase of z_{Hf} and x_{Hf} seems to be erroneous; therefore additional experiments were performed to determine whether mass balance conditions were satisfied. The results are discussed in Section 4.3.2.5 where the simultaneous decrease of both mole fraction ratios z_{Zr}/z_{Hf} (solid phase) and x_{Zr}/x_{Hf} (liquid phase) are justified and it is shown that the purity is also influenced by the product yields.

Before elaborating further on Fig. 4.11, it might be useful to take a closer look at the separation factor. Notice that by rearrangement of Equation (4.2), the relative distribution coefficient can be written in the form:

$$\beta_{Hf,Zr} = \frac{x_{Zr}/x_{Hf}}{z_{Zr}/z_{Hf}} \tag{4.5}$$

Therefore, the relative distribution coefficient also equals Zr:Hf (aq)/ Zr:Hf (s) as represented in Fig. 4.11. The inverse of the relative distribution coefficient equals the separation factor as shown in Equation (4.6) [17]:

$$\beta^{-1} = \alpha_{Zr,Hf} = \frac{z_{Zr}/z_{Hf}}{x_{Zr}/x_{Hf}} \tag{4.6}$$

The relative distribution coefficient and the separation factor are both measurements of the separation efficiency. Where the relative distribution coefficient relates the separation efficiency in terms of the relative amount of the impurity that is incorporated into the product (Equation (4.2)), the separation factor relates the separation efficiency in terms of the degree of enrichment of the product with the desired component.

During separation processes, the enriched product produced from a single separation stage is known as the *heads* stream, and the depleted waste stream (depleted of the desired component) is known as the *tails* stream [17]. Therefore, in analogy to the crystallization

experiments presented here, the crystalline product can be termed the heads stream and the impure mother liquor the tails stream even though we are dealing with batch processes. Using these concepts, the separation efficiency can also be defined in terms of the heads and tails streams. For a given feed composition, i.e. the composition of the unsaturated solution at T = 70 °C before crystallization, the heads separation factor is defined as the relative increase in the purity of the heads stream (crystalline product) with respect to the feed composition [17]:

$$\delta_{Zr,Hf} = \frac{z_{Zr}/z_{Hf}}{y_{Zr}/y_{Hf}} \tag{4.7}$$

where the feed composition is represented by y_i. The tails separation factor on the other hand is defined as the relative increase in the impurity concentration of the tails stream (mother liquor) with respect to the feed composition [17]:

$$\gamma_{Zr,Hf} = \frac{y_{Zr}/y_{Hf}}{x_{Zr}/x_{Hf}} \tag{4.8}$$

Notice that the overall separation factor, $\alpha_{Zr,Hf}$ can then be written as:

$$\alpha_{Zr,Hf} = \delta.\gamma = \frac{z_{Zr}/z_{Hf}}{x_{Zr}/x_{Hf}} \tag{4.9}$$

Therefore, when x_{Hf} increased, and the ratio x_{Zr}/x_{Hf} therefore decreased with increasing KF concentration up to 0.25 mol/L as shown in Fig. 4.11, the tails separation factor, γ, increased. The increase in the tails separation factor is more effective than the decrease in the heads separation factor (the ratio z_{Zr}/z_{Hf} decreases), resulting in an increase in α (Equation 4.9) even though the crystal product purity decreased slightly. This seems to explain why the separation efficiency increased (i.e. β decreased and α increased) even though the product purity did not increase.

Returning to Fig. 4.11; with further increase in the KF concentration, i.e. beyond 0.25 mol/L KF, the ratio z_{Zr}/z_{Hf} continued to decrease while the ratio x_{Zr}/x_{Hf} increased (Fig. 4.11). Therefore, x_{Hf} decreased with respect to x_{Zr}, and z_{Hf} increases with respect to z_{Zr} thus, more

and more Hf is transferred to the solid phase, be it by solid solution formation or co-crystallization. Therefore, the selectivity (and therefore α) decreased, because both δ and γ decreased, and at a KF concentration of 0.5 mol/L, the mole fraction ratios x_{Zr}/x_{Hf} and z_{Zr}/z_{Hf} were nearly equal leading to the value for $\beta_{Hf,Zr}$ of 0.76, or α = 1.31. Therefore, with increasing KF concentration, crystal growth became less selective due to the increased incorporation of Hf in the crystalline product relative to that of Zr. However, up to a KF concentration of 0.25 mol/L, the relative amount of Hf with respect to Zr remaining in the mother solution also increased, leading to improved separation in terms of the tails separation factor. With a further increase in the KF concentration, crystal growth became increasingly less selective and the Hf-concentration in the mother liquor decreased with respect to that of Zr. Accordingly, the Hf-concentration in the solid phase increased with respect that of Zr leading to the poor separation observed.

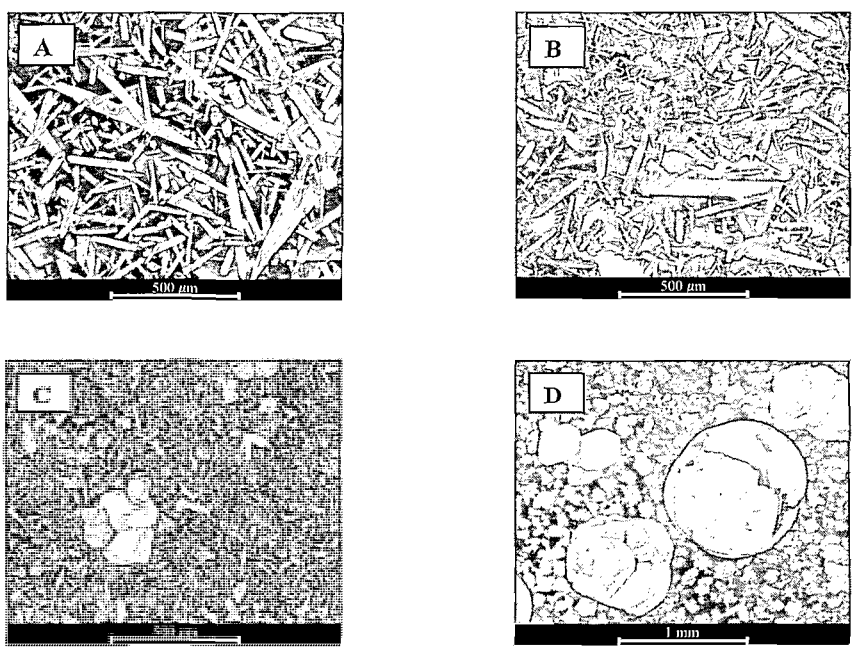

Figure 4.12: SEM micrographs of the crystalline products obtained by crystallization from aqueous KF solutions with concentrations of 0.25 mol/L (A), 0.3 mol/L (B), 0.35 mol/L (C), and 0.5 mol/L (D) at low magnification.

SEM images of the crystals obtained by crystallization from solutions with different KF concentrations are shown in Figs. 4.12 and 4.13. According to the images, at a KF concentration up to 0.25 mol/L, where better separation was obtained, needle-shaped crystals were formed. With increasing KF concentration, i.e. where the selectivity decreased, the crystal size decreased significantly as shown in Fig. 4.12 (B) and (C) and Fig. 4.13 (B) and (C). The crystal morphology also seems to change, i.e. from thin needles to a more spherical shape which led to the formation of large agglomerates, shown in Figs. 4.12 (D) and 4.13 (D). The decrease in the crystal size with increasing KF concentration (above 0.25 mol/L) may be the result of an increased nucleation rate [12] whereby the amount of growth per crystal decreased, thereby relieving the supersaturation.

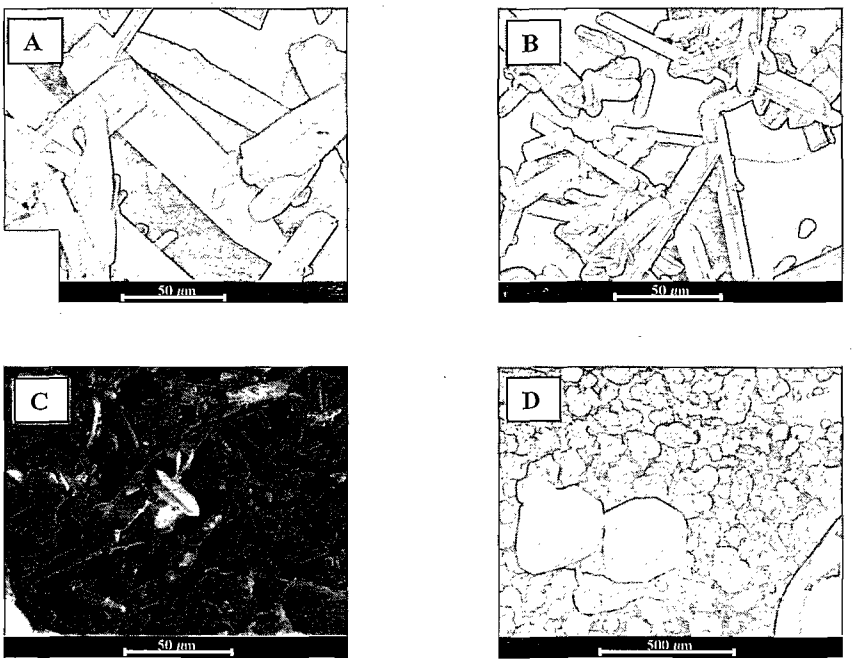

Figure 4.13: SEM micrographs of the crystalline products obtained by crystallization from KF solutions with concentrations of 0.25 mol/L (A), 0.3 mol/L (B), 0.35 mol/L (C), and 0.5 mol/L (D) at higher magnification.

It has been shown that adsorption of the additive on the growing crystal surface can affect the growth process [15] which can then also lead to a decrease in the crystal size. If we assume that the decrease in size is due to increased nucleation, i.e. more nuclei are formed per unit volume per unit time, then the "speed" of crystallization increased.

This increase in the nucleation rate can cause the crystallization process to be less selective in comparison with controlled crystallization where the growth units have more time to be preferentially incorporated into the crystal structure. Thus, with more spontaneous formation of nuclei, the crystallization equilibrium with respect to the transport of growth units to and from the crystal surface-solution interface is disturbed leading to more chaotic deposition of growth units onto the growing crystal surface. This might explain the decrease in the crystal purity (Fig. 4.11) and separation efficiency (Fig. 4.10) above the 0.25 mol/L KF threshold.

Representative results of XRD analyses of the product crystals, with the most probable identifications, are shown in Fig. 4.14 (A) and (B). The results show that in addition to the orthorhombic crystal structure used to model solid solutions of $K_2Zr_{(1-z)}Hf_zF_6$ (Chapter 3), the occurrence of the monoclinic structures are also possible (Fig. 4.14 (A)). With increasing KF concentration the cubic heptafluorides were also observed (Fig. 4.14 (B)), which might be the reason for the significant change in the appearance of the crystals shown in Figs. 4.12 (D) and 4.13 (D). Therefore, instead of a simple morphological change, it is possible that the crystal structure changes to that of the heptafluorides ($K_3Zr(Hf)F_7$) during crystallization from solutions with high KF concentrations. This possibility was investigated by ICP-OES analysis (Section 4.2.4.1.A) and the results thereof are discussed in Section 4.3.2.3.

In summary, it was shown from the SEM and XRD results that the following three factors influence the separation efficiency during crystallization of $K_2Zr(Hf)F_6$ from solution:

- crystallization kinetics,
- crystallization equilibria as a result of changes in the crystallization kinetics, and
- crystal structure (i.e. hexafluoride vs. heptafluoride).

It was shown that the decrease in crystal size, which occurred during crystallization from KF solutions with concentrations larger than 0.25 mol/L, was accompanied by a decrease in the crystal purity. The efficiency of separation therefore decreased with a decrease in the crystal size which was attributed to an increased nucleation rate. At high KF concentrations, the

formation of the heptafluorides could occur according to the XRD results. The heptafluoride (K_3ZrF_7) has a different structure than the hexafluoride (K_2ZrF_6) and therefore a different morphology, which might explain the large particles seen in Figs. 4.12 (D) and 4.13 (D). The heptafluoride might be less selective towards rejection of the Hf-impurity which could help explain the poor selectivity obtained at high KF concentrations.

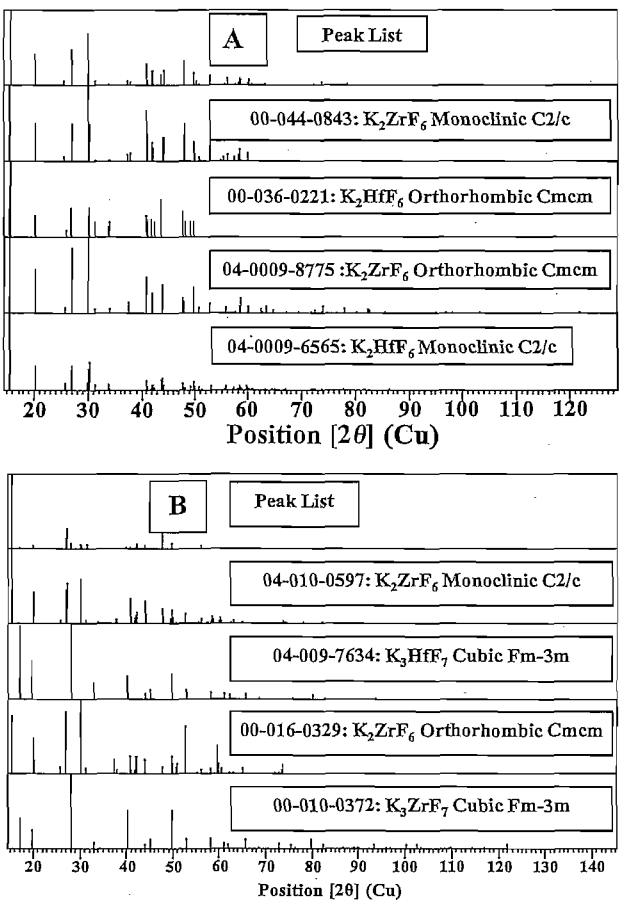

Figure 4.14: Results of XRD analyses of the crystalline products obtained by crystallization from a 0.2 mol/L KF solution (A), and a 0.4 mol/L KF solution (B).

4.3.2.2.B. Crystallization from KF Solutions with HF Added

The results of crystallization from aqueous solutions with varying KF concentration with a constant HF concentration of 2.5 mol/L are shown in Fig. 4.15. In comparison with the crystallization from pure H_2O solution, the distribution coefficient decreased (separation efficiency increases) with increasing KF concentration when HF was present. With respect to the crystallization from only KF solutions, improved separation efficiency was therefore obtained, with an optimum separation efficiency of $\beta = 0.13$ at a KF concentration of 0.45 mol/L. It seems that the negative effect of the high KF concentration is suppressed by HF.

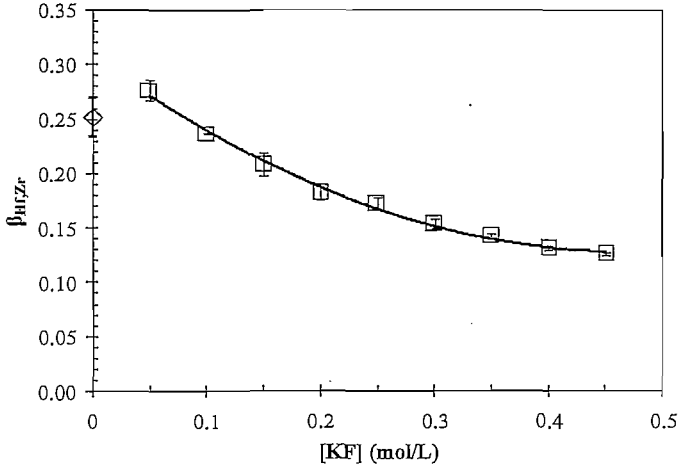

Figure 4.15: Measured distribution coefficient during crystallization of $K_2Zr(Hf)F_6$ from aqueous solutions of KF with varying concentration with a constant HF concentration of 2.5 mol/L. ◊ - Crystallization from pure H_2O solution.

The corresponding mole fraction ratios are shown in Fig. 4.16. Again, the errors associated with each value represent the average relative standard deviation for the solid and liquid phases respectively. The results show that the ratio x_{Zr}/x_{Hf} decreased with increasing KF concentration. Therefore, the Hf-concentration increased relative to the Zr-concentration in the liquid phase, i.e. x_{Hf} increased. Thus, the Hf-impurity is concentrated more effectively in the liquid phase with increasing KF concentration when HF is added. While the ratio z_{Zr}/z_{Hf} also decreased with increasing KF concentration for the "KF-crystallizations", there was now

an initial decrease with respect to the "H_2O-crystallization", while the ratio remained more or less constant with increased KF concentration. Thus, with HF as additive (together with KF) less of the Hf-impurity is incorporated into the solid phase while it's concentration in the liquid phase increased with respect to the Zr-concentration as the KF concentration increased.

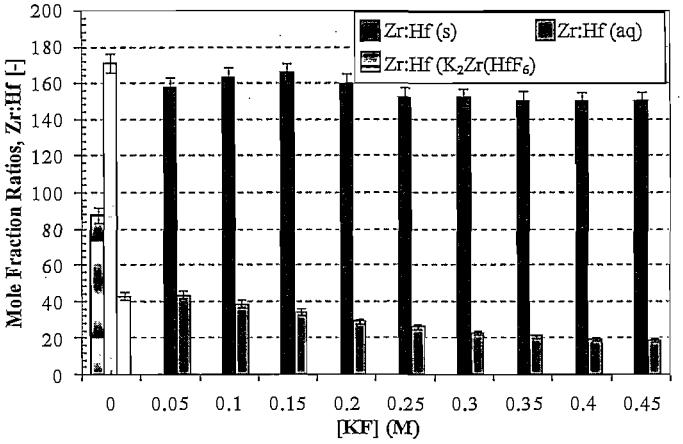

Figure 4.16: Mole fraction ratio of Zr:Hf in both the solid (s) and liquid phases (aq) at equilibrium during crystallization of $K_2Zr(Hf)F_6$ from aqueous solutions of varying KF concentration with a constant HF concentration of 2.5mol/L. □,□ – Crystallization from pure H_2O.

In comparison with crystallization from KF solutions, the addition of HF causes the crystallization process to be more selective towards the desired compound (ZrF_6^{2-}) whereby the Hf-impurity is concentrated more effectively in the liquid phase as the KF concentration increased leading to improved separation efficiency.

With regard to the heads and tails separation factors, the decrease of the ratio x_{Zr}/x_{Hf}, due to the increase in x_{Hf}, resulted in a steadily increase in the tails separation factor, γ with increasing KF concentration when HF was present. There was little change in the ratio z_{Zr}/z_{Hf}, implying that z_{Hf} also changed very little. This resulted in a small change in the heads separation factor, δ. Therefore, with the addition of HF, the heads separation factor (amount of enrichment of the solid phase with Zr) remained more or less constant when the KF concentration was increased beyond 0.25 mol/L while the tails separation factor increased

which was not observed for crystallization in the absence of HF. The constant enrichment of the solid phase, coupled with increasing efficiency with regard to the tails stream (mother liquor) therefore led to improved separation efficiency.

SEM images of the crystals (Figs. 4.17 and 4.18) indicate that there was no drastic change in crystal structure or morphology during crystallization with increasing KF concentration in the presence of HF, contrary to the results obtained for crystallization in the absence of HF. The crystal size did however decrease slightly with increasing KF concentration, but not to the same extent as was observed for crystallization without HF (Figs. 4.12 and 4.13).

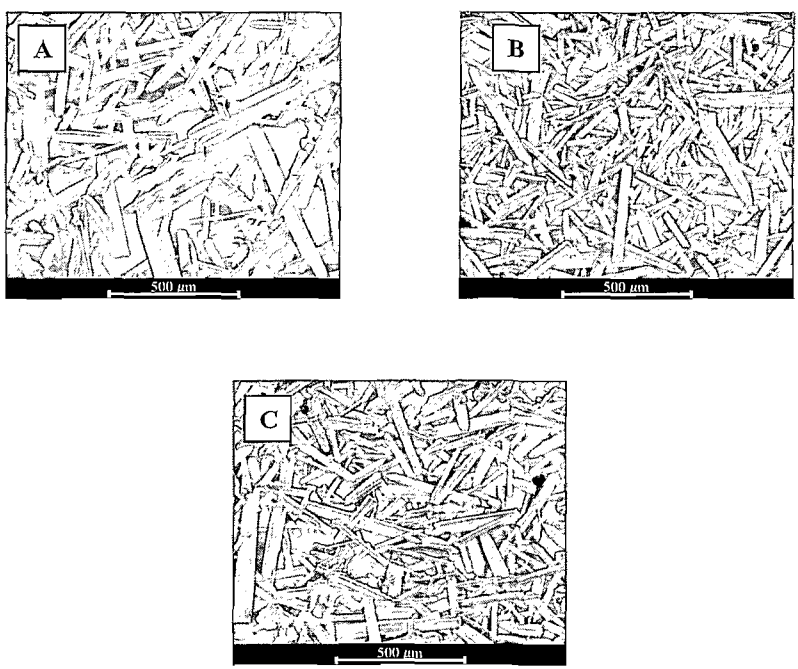

Figure 4.17: SEM micrographs of the crystalline products obtained by crystallization from HF solutions (2.5 mol/L) with KF concentrations of 0.2 mol/L (A), 0.4 mol/L (B), and 0.45 mol/L (C) at low magnification.

HF therefore seems to suppress the formation of small crystallites and spherical agglomerates at high KF concentrations which seems to correlate with the improved separation efficiency, supporting the previous notion that the separation efficiency is influenced by the crystallization kinetics with respect to an increased nucleation rate.

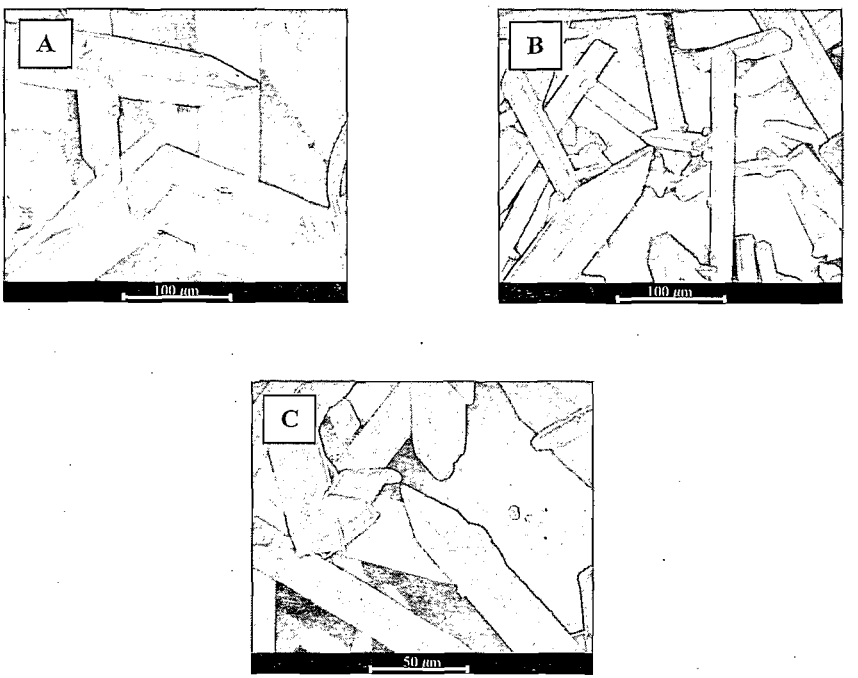

Figure 4.18: SEM micrographs of the crystalline products obtained by crystallization from HF solutions (2.5 M) with KF concentrations of 0.2 mol/L (A), 0.4 mol/L (B), and 0.45 mol/L (C) at higher magnification.

Where the rate of nucleation seemed to increase due to the visible decrease in crystal size as the KF concentration was increased for crystallization without HF as additive, the rate of crystallization (with respect to the nucleation and growth rates) appears to be comparable with increasing KF concentration in the presence of HF. This also results in comparable purity of the crystalline products produced by crystallization with increasing KF concentration with a constant concentration of HF as indicated by Fig. 4.16. It seems that the addition of HF

created more favourable conditions for crystallization whereby the crystallization kinetics were modified to promote more controlled crystallization. Therefore, selectivity of the growth process is not only controlled by the thermodynamics (Chapter 3), but perhaps also the transport equilibria.

Results of XRD analyses of the crystalline product obtained by crystallization from a 2.5 mol/L HF solution with a KF concentration of 0.2 mol/L are shown in Fig. 4.19, which serves as representative data for the crystallization of $K_2Zr(Hf)F_6$ from 2.5 mol/L HF solutions with increasing KF concentration. Image (A) shows the collected spectra of the sample, while image (B) shows the interpretation according to the system's database. The cubic $K_3Zr(Hf)F_7$ were not detected with XRD analysis, although different modifications of both the monoclinic and orthorhombic structures of K_2ZrF_6 as well as K_2HfF_6 were again observed. The different monoclinic and orthorhombic possibilities are only small differences in the structures contained within the structural database which are then matched to the acquired spectra by the system's software.

The fact that the cubic heptafluorides were not detected by XRD, even in the crystalline products obtained by crystallization from solutions with high KF concentrations, seems to confirm the SEM results. From the SEM and XRD results it therefore seems that the formation of $K_3Zr(Hf)F_7$ is suppressed during crystallization from solutions of high KF concentration when HF is present in a sufficient amount. When HF is omitted, the formation of $K_3Zr(Hf)F_7$ is more likely, with a simultaneous decrease in the separation efficiency. The hypothesis, that the formation of the heptafluoride can lower the separation efficiency, as noted in the previous section, might therefore be correct.

Thus, it seems that there is some correlation between crystal size and separation efficiency, and therefore the growth kinetics. The growth kinetics are in some way related to the KF concentration, where optimum growth conditions can be achieved with the addition of HF, which also appears to prevent the formation of $K_3Zr(Hf)F_7$. The formation of $K_3Zr(Hf)F_7$ seemed to be related to lower separation efficiency during crystallization which was prevented by the addition of HF to an unsaturated solution of $K_2Zr(Hf)F_6$ with KF a concentration of roughly 0.5 mol/L. This phenomenon might be attributed to speciation, although this is only speculative. The solution thermodynamics, in terms of the solubility ratios and the relative activity of the Hf-impurity in solution as the concentration of the additives changes, could also

play a role as implied by the thermodynamic model of Equation (4.1) (Section 4.1). The effects of KF and HF on the separation efficiency are discussed in more detail in the next section.

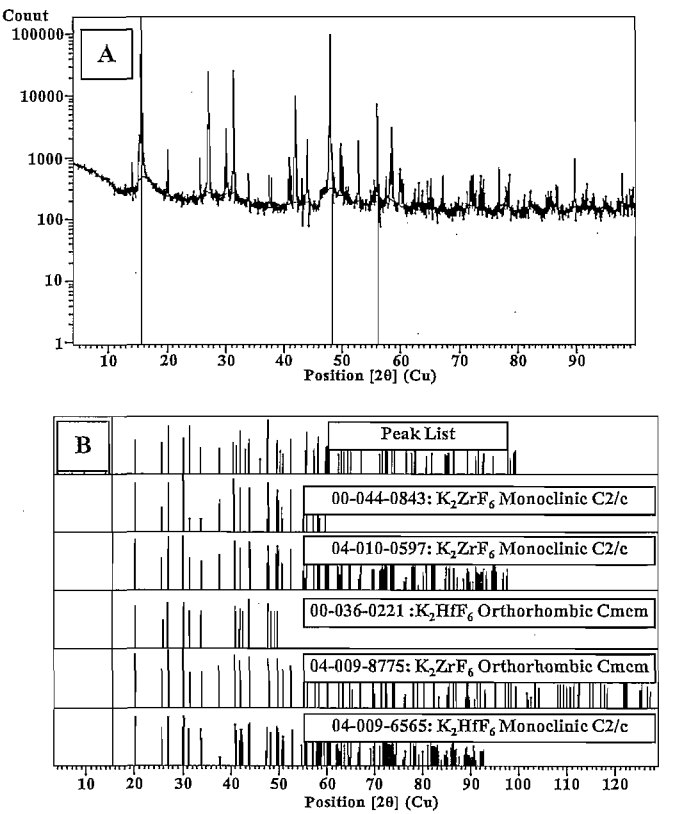

Figure 4.19: Results of XRD analyses of the crystalline product obtained by crystallization from a 2.5 mol/L HF solution with a KF concentration of 0.2 mol/L. (A) – XRD spectra of sample, (B) – Interpretation. For these particular results, the graphs were modified to illustrate the peaks of lower intensity.

4.3.2.3. Crystallization with a Controlled Salt Concentration

As explained in Section 4.2.3.3, crystallization was performed using the conditions of $\Sigma = 2.5$ and $\Sigma = 5$ calculated according to Equation (4.4). These values were chosen based on the conditions that corresponded with the most efficient separation of the KF, and KF and HF series of crystallizations. For example, for crystallization from KF solutions with varying concentration without HF (Section 4.3.2.2.A), optimum separation efficiency was obtained at a KF concentration of 0.25 mol/L. The solubility data presented in Section 4.3.1 was used to extrapolate the solubility of $K_2Zr(Hf)F_6$ at 15 °C in KF solutions with concentrations of 0 mol/L to 0.5 mol/L, which is shown in Fig. 4.20.

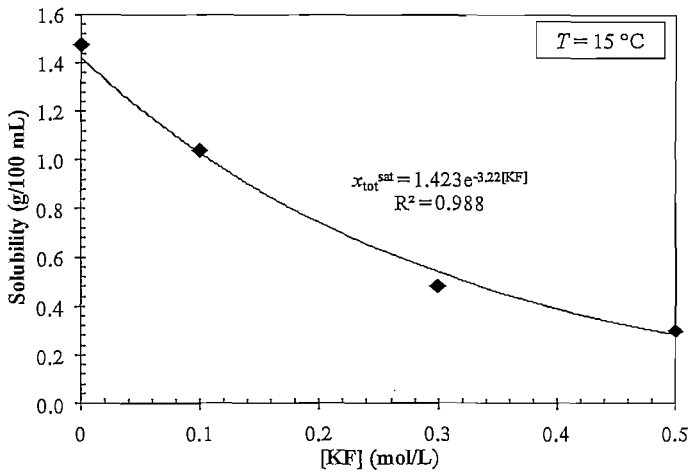

Figure 4.20: Solubility of $K_2Zr(Hf)F_6$ in aqueous solutions of KF as a function of the KF concentration at 15 °C.

Using this data it was possible to calculate the solubility of $K_2Zr(Hf)F_6$ in a 0.25 mol/L KF solution at 15 °C, which is 0.64 g/100 mL or 3.18 g/500 mL. Since $c_{tot}(T_2)$ is known, the value for $x_{tot}^{sat}(T_1)$ can be substituted into Equation (4.4), giving a value for Σ of 5.29. Using the same method, a value for Σ of 5.52 is obtained for the crystallization from a 0.45 mol/L KF with 2.5 mol/L HF solution, which is where the most efficient separation was obtained for the crystallization from HF solutions of 2.5 mol/L with varying KF concentration. Therefore, it seems that the most efficient separation was obtained for $\Sigma \approx 5$, and for the crystallization of

$K_2Zr(Hf)F_6$ from H_2O; $\Sigma \approx 2$. This is the reason why $\Sigma = 2.5$ and $\Sigma = 5$ was chosen for further experiments where the effect of the solvent composition and the relative degree of crystallization was evaluated in more detail.

4.3.2.3.A. Crystallization from KF Solutions

The results for crystallization from KF solutions with increasing KF concentration are shown in Fig. 4.21 for $\Sigma = 2.5$ and $\Sigma = 5$ (which are abbreviated by $\Sigma_{2.5}$ and Σ_5). With crystallization from solutions of low KF concentration, i.e. below 0.3 mol/L, it can be seen from the figure that the KF concentration has a relatively small influence on the separation efficiency.

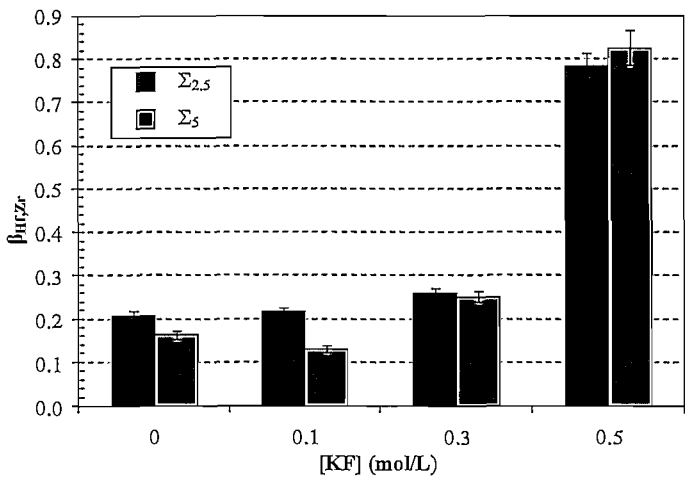

Figure 4.21: Relative distribution coefficient for the crystallization of $K_2Zr(Hf)F_6$ from aqueous KF solutions with varying concentration at conditions of $\Sigma = 2.5$ and $\Sigma = 5$.

With an increased relative excess of the salt (Σ_5) however, there seems to be an improvement in the separation efficiency as characterized by the decrease in the value of $\beta_{Hf,Zr}$. With crystallization from KF solutions of higher concentration, i.e. above 0.3 mol/L KF, the effect of Σ appears to be negligible and the KF concentration is evidently the determining factor. Therefore, for crystallization from KF solutions with increasing concentration for which a constant $K_2Zr(Hf)F_6$ concentration was used (Section 4.3.2.2.A), the separation efficiency did not decline because of an increased degree of crystallization, but as these results show was

caused by the increased KF concentration. Furthermore, during the crystallization from the 0.5 mol/L KF solution poor separation efficiency was obtained at both $\Sigma_{2.5}$ and Σ_5 which is comparable to the results obtained with the crystallization using a constant $K_2Zr(Hf)F_6$ concentration.

Therefore, according to these results, the separation efficiency is partially controlled by the degree of crystallization, as characterized by the value of Σ. During crystallization from solutions with increased KF concentration, this effect is overshadowed by the high KF concentration which leads to poor separation efficiency.

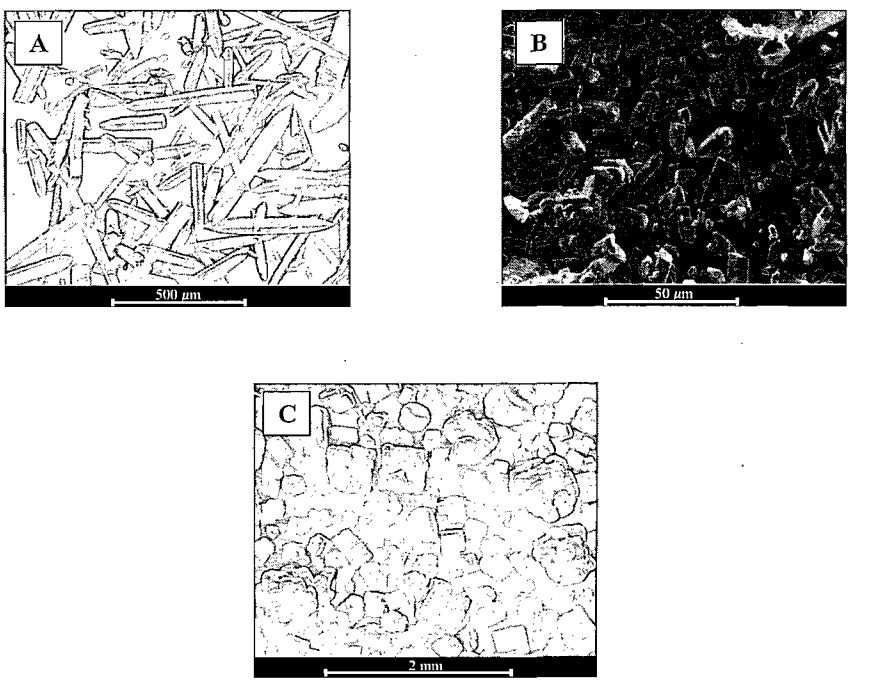

Figure 4.22: SEM micrographs of the crystalline products obtained by crystallization from (A) H_2O, (B) 0.3 mol/L KF, and (C) 0.5 mol/L KF solutions with $\Sigma = 2.5$.

SEM micrographs of the crystals obtained from both the $\Sigma_{2.5}$ and Σ_5 experiments (Figs. 4.22 and 4.23 respectively) indicate that the same transition in the appearance of the crystals

occurred in both cases, as was observed for crystallization with a constant salt concentration (Section 4.3.2.2.A). This is namely that needle-shaped crystals are produced by crystallization from KF solutions of low concentration (Figs. 4.22 (A) and 4.23 (A)) where the crystal size decreases as the KF concentration increases (i.e. Figs. 4.22 (B) and 4.23 (B)). With further increase in the KF concentration, the crystal morphology changes as shown by Figs. 4.22 (C) and 4.23 (C). Therefore, the change in crystal size and morphology/structure is independent of the relative excess amount of solute, Σ, but is rather caused by the increased KF concentration of the solution. The decrease in crystal size as depicted in Figs. 4.22 (B) and 4.23 (B), which is due to an increased nucleation rate, is therefore induced by the additive which affects the crystallization kinetics indirectly.

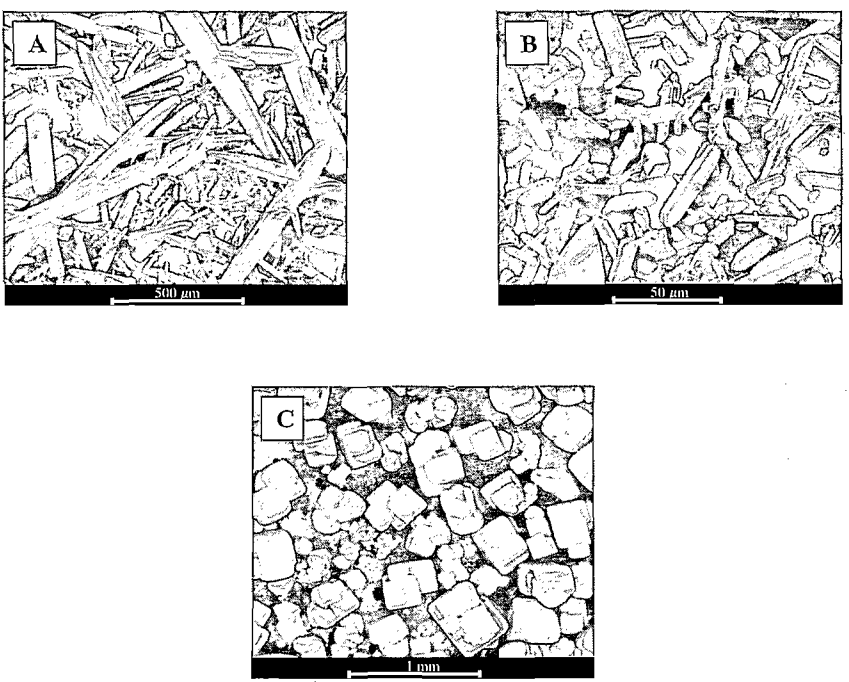

Figure 4.23: SEM micrographs of the crystalline products obtained by crystallization from (A) 0.1 mol/L KF, (B) 0.3 mol/L KF, and (C) 0.5 mol/L KF solutions with $\Sigma = 5$.

This induced effect of the additive seems to be prominent at higher KF concentrations, i.e. above 0.3 mol/L, where the effect of Σ is negligible, explaining the decrease in the separation efficiency with increasing KF concentration (above 0.25 mol/L).

XRD results, of which representative data is shown in Fig. 4.24, indicate the formation of $K_3Zr(Hf)F_7$ is probable for both $\Sigma_{2.5}$ and Σ_5 when the KF concentration is 0.5 mol/L. Again, the formation of the heptafluorides is not determined by the relative excess amount of solute, but rather is caused by the high KF concentration. The cubic crystal structure of the heptafluorides correlates with the cubic morphology of the crystals produced by crystallization from 0.5 mol/L KF solutions for both $\Sigma_{2.5}$ and Σ_5 (Figs. 4.22 (C) and 4.23 (C)). Note that the morphology of the heptafluoride crystals differs from that obtained for crystallization using a constant salt concentration (Figs. 4.12 (D) and 4.13 (D)), where the rounded, agglomerated particles were also identified as $K_3Zr(Hf)F_7$. This could be because of the lower salt concentration that was used for the $\Sigma_{2.5}$ and Σ_5 experiments in comparison with that experiment which may cause slower crystallization for the heptafluorides which would then result in better defined crystals with less agglomeration.

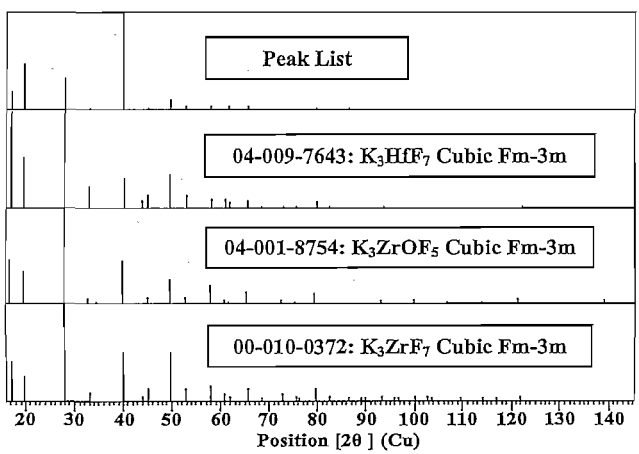

Figure 4.24: Results of XRD analyses of the crystalline product obtained by crystallization from a 0.5 mol/L KF solution with $\Sigma = 2.5$.

The XRD results also indicate that the formation of an oxyfluoride is possible during crystallization from 0.5 mol/L KF solutions which also has a cubic crystal structure, although this result is inconclusive.

It is evident however that poor separation efficiency is obtained when crystallization of $K_3Zr(Hf)F_7$ occurs. The identification of the heptafluorides in the crystalline products obtained by crystallization from KF solutions with high concentrations by XRD are supported by ICP-OES analysis which is discussed in the next section. This leads one to believe that the heptafluoride crystal structure is less selective towards rejection of the Hf-impurity.

4.3.2.3.B. Crystallization from KF Solutions with HF Added

The results of crystallization from KF solutions with increasing concentration with a constant HF concentration (2.5 mol/L), shown in Fig. 4.25, indicate that, in comparison with the crystallization from H_2O, the separation efficiency improved slightly. The KF concentration appears to have a negligible influence on the separation efficiency as the value of $\beta_{Hf/Zr}$ remained constant while the KF concentration was increased (Fig. 4.25).

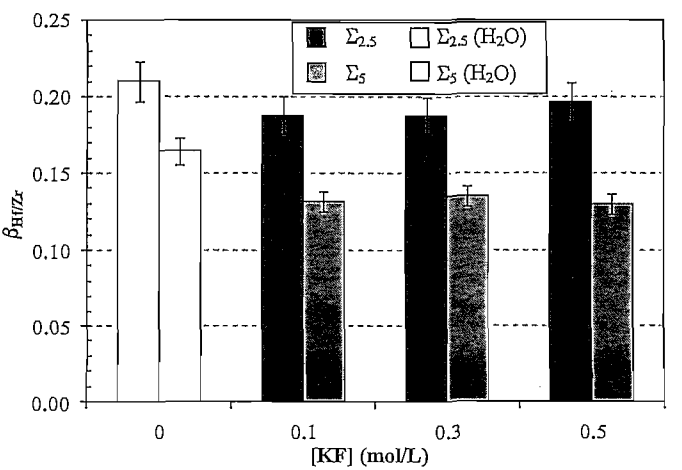

Figure 4.25: Relative distribution coefficient for the crystallization of $K_2Zr(Hf)F_6$ from aqueous KF solutions with varying concentration with a constant HF concentration of 2.5 mol/L, at conditions of $\Sigma = 2.5$ and $\Sigma = 5$.

The relative excess amount of solute however has a significant influence on the separation efficiency, where the efficiency improved noticeably with a two-fold increase in Σ. In light of the crystallization from only KF solutions, it is evident that the addition of HF regulates the effects of the KF concentration. Thus, when HF is added, the separation efficiency is controlled mainly by the degree of crystallization, as characterised by the value of Σ and not by the KF concentration. When crystallization was performed from 2.5 mol/L HF solutions with increasing KF concentration using a constant $K_2Zr(Hf)F_6$ concentration (Section 4.3.2.2.B), Σ increased because of the decrease in the solubility of $K_2Zr(Hf)F_6$ with increasing KF concentration. Thus, the separation efficiency improved for crystallization from 2.5 mol/L HF solutions with increasing KF concentration.

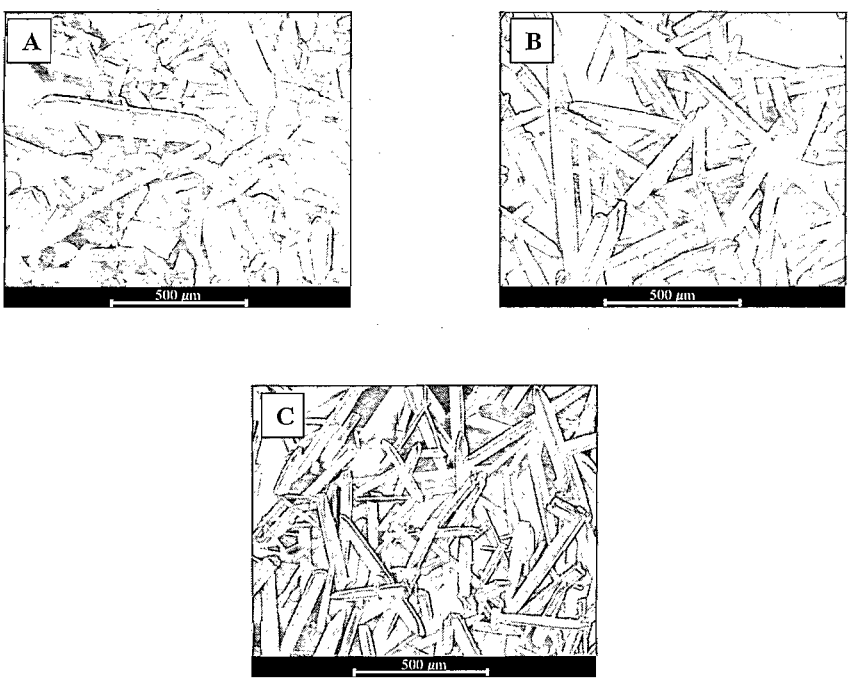

Figure 4.26: SEM micrographs of the crystalline products obtained by crystallization from 2.5 mol/L HF solutions with KF concentrations of (A) 0.1 mol/L, (B) 0.3 mol/L, and (C) 0.5 mol/L for Σ = 2.5.

The regulation of the effect of increasing KF concentration on the crystallization process becomes apparent when studying the SEM and XRD results. Firstly, SEM micrographs of the crystals obtained from both the $\Sigma_{2.5}$ and Σ_5 experiments, which are shown in Figs. 4.26 and 4.27 respectively, indicate that none of the cubic crystals were formed at high KF concentration, and that the morphology remained unchanged with increasing KF concentration for both $\Sigma_{2.5}$ and Σ_5. Although, the agglomeration of the crystals formed by crystallization from a 2.5 mol/L HF solution with a KF concentration of 0.1 mol/L at Σ_5 (Fig. 4.27 (A)), does present an anomaly, which could be attributed to polycrystalline growth.

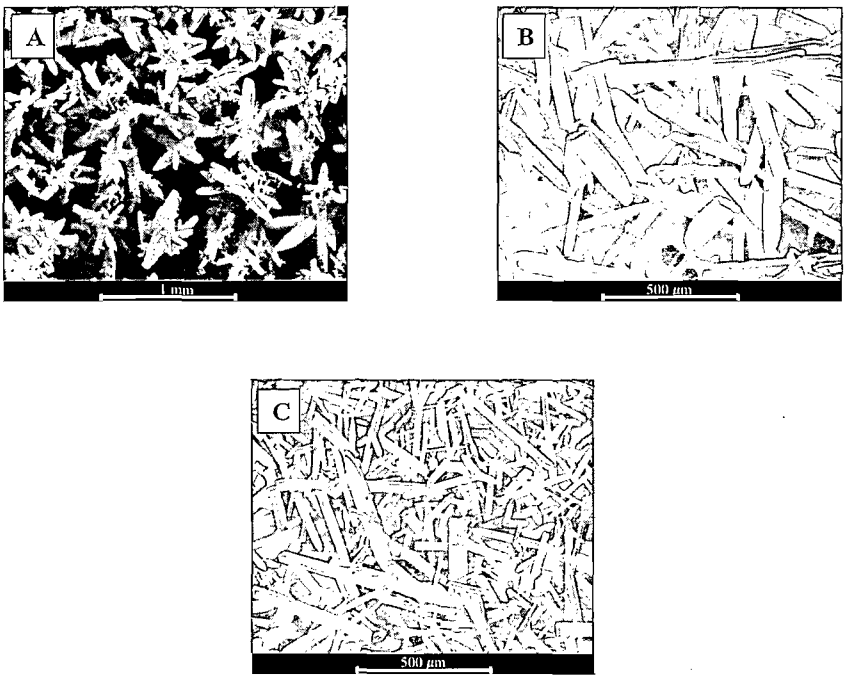

Figure 4.27: SEM micrographs of the crystalline products obtained by crystallization from 2.5 *mol/L HF solutions with KF concentrations of* (A) 0.1 *mol/L*, (B) 0.3 *mol/L*, and (C) 0.5 *mol/L* for $\Sigma = 5$.

Nonetheless, the fact that crystals with comparable shape and size are produced by crystallization from aqueous solvent mixtures of KF (with varying concentration) and HF

(with a constant concentration) shows that the addition of HF creates conditions where crystallization can proceed with comparable crystallization kinetics whereby the indirect effects of KF on the crystallization kinetics are negated.

Secondly, the XRD results, of which representative data are shown in Fig. 4.28, correlates with the SEM results in the sense that none of the heptafluorides were detected, even for the crystals produced by crystallization from a solution of 0.5 mol/L KF with 2.5 mol/L HF. However, different modifications of the orthorhombic and monoclinic structures for both the Zr and Hf hexafluorides were also found (also see Fig. 4.19).

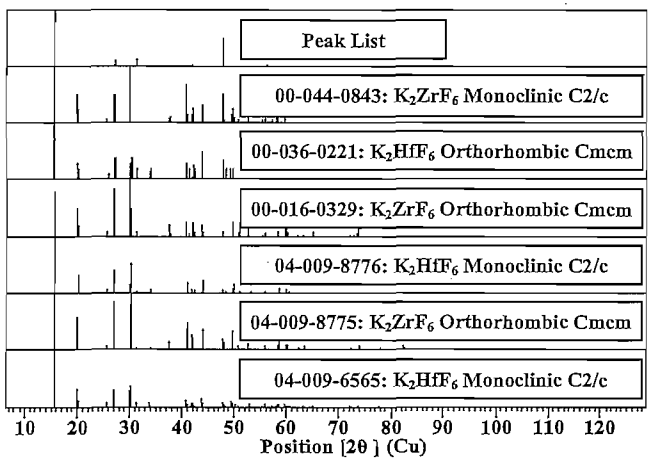

Figure 4.28: Results of XRD analyses of the crystalline product obtained by crystallization from a 0.5 mol/L KF solution with an HF concentration of 2.5 mol/L, for $\Sigma = 5$.

ICP-OES analyses were used to determine the potassium concentrations in the crystalline products (Section 4.2.4.1.A) of the varying salt concentration experiments. From this data the K/Zr concentration ratios ($mg.L^{-1}/mg.L^{-1}$) were calculated and compared to the XRD results. The results for crystallization from KF solutions with increasing concentration at $\Sigma_{2.5}$, and crystallization from 2.5 mol/L HF solutions with increasing KF concentration at Σ_5 are shown in Fig. 4.29 (A) and (B) respectively.

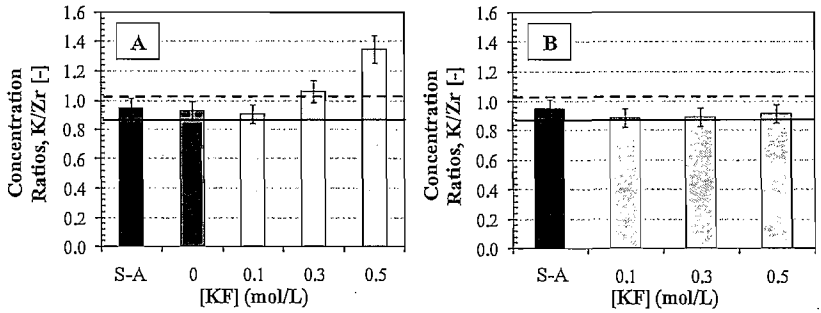

Figure 4.29: K/Zr concentration ratios as determined by ICP-OES analyses of product solutions obtained by crystallization from KF solutions with increasing concentration at $\Sigma_{2.5}$ (A), and crystallization from 2.5 mol/L HF solutions with increasing KF concentration at Σ_5. (B). ■ - Pre-crystallized $K_2Zr(Hf)F_6$ (Sigma-Aldrich), ▣ - Crystallization from H_2O solution, ▣ - Crystallization from solutions with increasing KF concentration with and without HF with a concentration of 2.5 mol/L.

The solid and dashed lines represent the theoretical K/Zr ratios (mass ratios) for K_2ZrF_6 and K_3ZrF_7 respectively, which were calculated using the molecular weights of the two elements. The results show that the formation of the heptafluoride is possible for the crystallization from KF solutions with concentrations equal to and larger than 0.3 mol/L (Fig. 4.29 (A)). In the presence of HF however, the formation of the heptafluorides are less likely, irrespective of the KF concentration, since the concentration ratios remained below the threshold which corresponds to the heptafluorides. It should however be kept in mind that only the K/Zr ratios were measured, and therefore any potassium attributed to K_2HfF_6 is also factored into the results which can results in values of K/Zr that are slightly higher than the theoretical ratio of K_2ZrF_6. Nevertheless, these results support the XRD results with respect to the inhibition of the formation of the heptafluorides by HF during crystallization from aqueous solutions of high KF concentrations.

The inhibiting effect of HF towards the formation of $K_3Zr(Hf)F_7$ during crystallization from KF solutions of high concentration, prevents the negative effects that the crystallization of $K_3Zr(Hf)F_7$ has on the separation efficiency. Furthermore, during crystallization of $K_2Zr(Hf)F_6$ from KF solutions (wherein a constant salt concentration was used despite the increase in the KF concentration), the addition of HF caused a gradual increase in the relative excess amount of solute with increasing KF concentration. In light of the results presented in this section and Section 4.3.2.3.A, the increased relative excess amount of solute resulted in

improved separation efficiency. Therefore in accordance with the results presented in Section 4.3.2.3.A, the relative distribution coefficient, and therefore the separation efficiency is dependent on the degree of crystallization, as characterized by the value of Σ. It should be noted that the relative distribution coefficient measured in this study (Equation 4.2), is an effective, or average, distribution coefficient, because the composition in the solution changes during the course of crystallization, and only the ratio of the compositions in the solution and crystals at the end of the crystallization was measured. Therefore, the value of $\beta_{Hf,Zr}$ (effective distribution coefficient) is influenced by the degree of crystallization, which is almost certainly the reason for the dependence of the separation efficiency on Σ. The use of HF as additive, together with KF, therefore creates optimum conditions for crystallization of $K_2Zr(Hf)F_6$ with respect to the extent to which crystallization proceeds before equilibrium is achieved, as well as the crystallization kinetics, which to a certain degree, contributes to improved separation efficiency.

4.3.2.4. Staged Crystallizations

As mentioned in Section 4.2.3.4, serial crystallization was done from 0.5 mol/L KF solutions without HF, and 0.45 mol/L KF solutions with added HF (2.5 mol/L). These conditions were chosen as crystallization from a 0.5 mol/L KF solution resulted in the worst separation efficiency, and crystallization from 0.45 mol/L KF with 2.5 mol/L HF in the best separation efficiency. Using these conditions, the separation efficiency and the degree of purification as a function of separation stage was studied.

The results of the measured relative distribution coefficient as a function of crystallization stage are shown in Fig. 4.30 for crystallization from 0.5 mol/L KF solutions. The separation efficiency improved slightly with each crystallization stage, although the change in efficiency was not very significant. Accordingly, the purity of the crystalline product did not change appreciable with each recrystallization, as depicted in Fig. 4.31. The solid-phase ratio z_{Zr}/z_{Hf} changed only slightly with each recrystallization and therefore with respect to the feed composition of the first stage little enrichment in the purity of the final crystalline product was achieved during the whole process. The poor separation efficiency resulting from this mini cascade process is therefore characterized by a poor heads separation factor, δ.

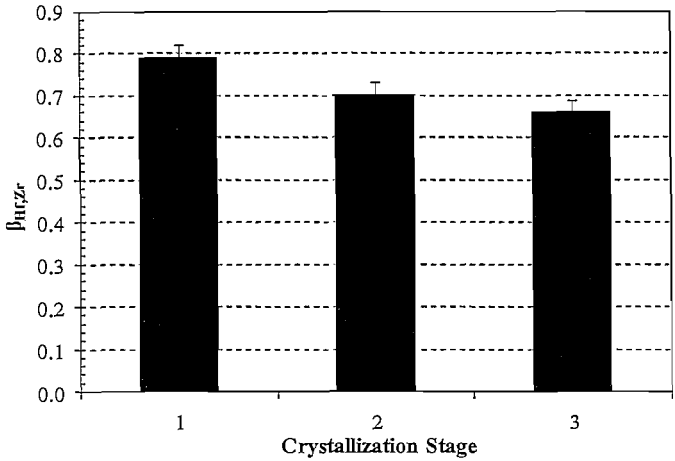

Figure 4.30: Relative distribution coefficient as a function of crystallization stage for crystallization from 0.5 mol/L KF solutions.

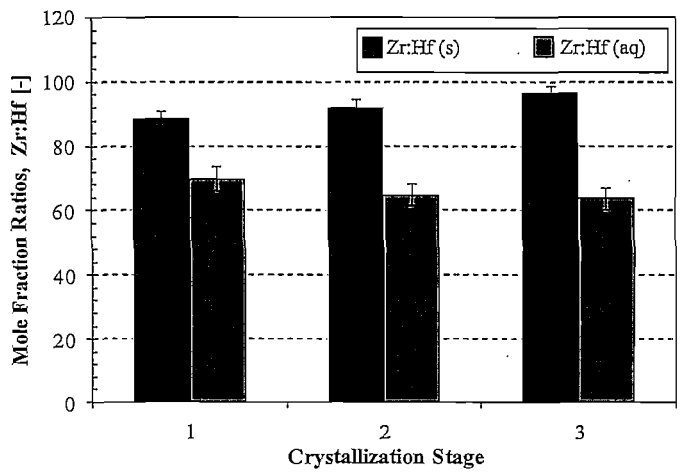

Figure 4.31: Mole fraction ratios of Zr:Hf in both the solid (s) and liquid phases (aq) at equilibrium during crystallization of $K_2Zr(Hf)F_6$ from aqueous KF solutions with concentrations of 0.5 mol/L.

However, due to the relatively large values of the liquid-phase ratios, x_{Zr}/x_{Hf}, in comparison with the solid-phase ratios z_{Zr}/z_{Hf}, the poor separation efficiency of the process is therefore

also characterized by a poor tails separation factor ,γ, as defined by Equation (4.8); also refer to Section 4.3.2.2.A. Hence, the average values of δ and γ for the process were calculated as 1.04 and 1.35 respectively, and because the separation efficiency did not change significantly for each recrystallization, the average values of δ and γ varied by 1.6 % and 7.2 % respectively.

The results of the measured relative distribution coefficient as a function of crystallization stage for the crystallization from 0.45 mol/L KF solutions with 2.5 mol/L HF are shown in Fig. 4.32. Here, the separation efficiency as characterized by the value of $\beta_{Hf,Zr}$ remained constant within the uncertainty of experimental error. In accordance with the results presented in Section 4.3.2.2.B, superior separation efficiency was obtained in comparison with crystallization from 0.5 mol/L KF solutions.

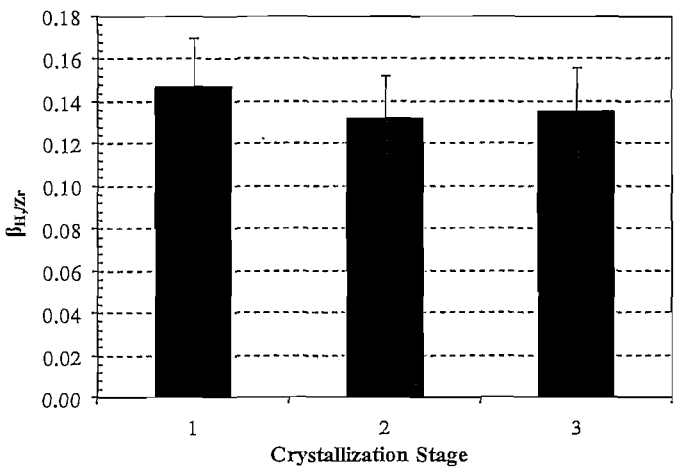

Figure 4.32: Relative distribution coefficient as a function of crystallization stage for crystallization from 0.45 mol/L KF solutions with HF concentrations of 2.5 mol/L.

The corresponding mole fractions ratios, i.e. z_{Zr}/z_{Hf} and x_{Zr}/x_{Hf} are shown in Fig. 4.33 from which it is apparent that an appreciable degree of purification was obtained due to the increase in the ratio of z_{Zr}/z_{Hf} (Zr:Hf (s)) with each recrystallization. The enhanced separation efficiency is also noticeable from the increased rate at which the purity of the crystalline product increased with each recrystallization. The ratio of the purified salt that would be

suitable for nuclear applications (<100 ppm Hf) corresponds to 10000. Thus, the purity of the salt produced from this mini cascade process ($z_{Zr}/z_{Hf} \approx 310$), although significantly improved, is still insufficient and would therefore have to be subjected to more crystallization stages. This aspect is discussed in more detail in Chapter 5.

Nonetheless, with respect to the serial crystallization from 0.5 mol/L KF solutions, the improved separation efficiency is characterized by an increase in the average value of δ of approximately 47 %, and most notably, an increase in the average value of γ of approximately 250 %. The average values of δ and γ were calculated in this case as 1.53 and 4.74 respectively, with a variation of respectively 3.8 % and 7.3 %, and can therefore also be taken as being constant for all practical purposes. Thus, the superior separation efficiency can largely be attributed to the increase in the tails separation factor, γ, whereas the heads separation factor contributed much less to the improved separation efficiency.

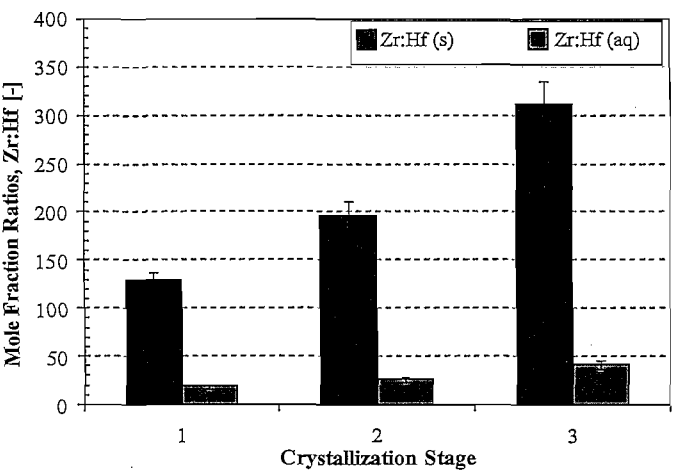

Figure 4.33: Mole fraction ratios of Zr:Hf in both the solid (s) and liquid phases (aq) at equilibrium during crystallization of $K_2Zr(Hf)F_6$ from aqueous KF solutions with concentrations of 0.5 mol/L with HF concentrations of 2.5 mol/L.

Recall that it was noted in Section 4.3.2.2 that enhanced separation efficiency was obtained by crystallization from a 0.25 mol/L KF solution with respect to crystallization from only H_2O

and even better separation efficiency for crystallization from a 0.45 mol/L KF solution with an HF concentration of 2.5 mol/L. With respect to crystallization from H_2O, the improved separation efficiency obtained by crystallization from a 0.25 mol/L KF solution was attributed to the increase in the tails separation factor, although the heads separation factor decreased (Fig. 4.11). On the other hand, the superior separation efficiency obtained by crystallization from a 0.45 mol/L KF solution with an HF concentration of 2.5 mol/L could be attributed to an even better tails separation factor although the heads separation factor also decreased slightly with respect to crystallization from H_2O (Fig. 4.16). The decreased product purity, or decreased heads separation factor seemed to contradict the enhanced separation efficiency. However, in light of the results presented in Figs. 4.31 and 4.33, it was shown that an increase in the tails separation factor, γ, (more effective concentration of the Hf-impurity in the mother liquor) can indeed cause the overall separation to be more effective in terms of the rate at which the purity of the crystalline product increases for a stage-wise process. Note that it is assumed here that the increase in γ, which for this case was five times greater than the increase in δ, is the determining factor and that the increase in δ can be neglected for these two cascade-type crystallizations. Furthermore, it could be possible that the poor heads separation factor is the result of solid solution formation, which seems to be supported by the molecular modelling results (Chapter 3).

It is somewhat surprising though that the separation efficiency remained constant with each crystallization stage, as it was predicted by molecular modelling that the separation efficiency should decrease as the purity of the salt increased. Although, this experimental result is favourable, supporting the use of fractional crystallization of $K_2Zr(Hf)F_6$ as a separation method. On the other hand, as shown in Fig. 4.33, the Hf-concentration relative to the Zr concentration in the liquid phase did begin to decrease noticeably for the final crystallization stage as indicated by the increase in x_{Zr}/x_{Hf}. Therefore, coupled with the fact that the Hf-concentration is still relatively high, it is possible that the separation efficiency might decrease if the number of stages are increased.

4.3.2.5. Mass Balance Tests

The mass balance tests were performed using crystallization of $K_2Zr(Hf)F_6$ from pure H_2O solutions and 0.25 mol/L KF solutions as described in Section 4.2.3.5. These two conditions were used to determine whether it is possible for both the ratios z_{Zr}/z_{Hf} and x_{Zr}/x_{Hf} (i.e.

Zr:Hf (s) and Zr:Hf (aq)) to decrease while the separation efficiency increases when the KF concentration is increased (Section 4.3.2.2.A). The relevant results obtained from these experiments are summarized in Table 4.1.

Note that the values of $\beta_{Hf,Zr}$ are higher than that obtained using the larger crystallization setup (for example 0.324 vs. 0.251 for crystallization from H_2O). This could be due to the absence of stirring in these experiments which led to the formation of larger crystals. Nevertheless, the same trends were observed as was the case with the results presented in Section 4.3.2.2.A. These are namely that in comparison with the crystallization from H_2O solution, crystallization from a 0.25 mol/L KF solution resulted in improved separation efficiency, due to the lower value of $\beta_{Hf,Zr}$ (see Fig. 4.10). Simultaneously, both the ratios z_{Zr}/z_{Hf}, and x_{Zr}/x_{Hf} decreased with increasing KF concentration compared to the crystallization from only H_2O solutions (see Fig. 4.11).

Table 4.1: Summary of results obtained for the mass balance experiments.

Crystallization Solution	**H_2O**		**0.25 mol/L KF**	
Statistics	**Average**	**% RSD**	**Average**	**% RSD**
Product Yield (g)	2.2756	0.22	3.1902	0.19
$\beta_{Hf,Zr}$	0.324	1.00	0.267	0.41
z_{Zr}/z_{Hf}	156.70	0.46	128.06	2.12
x_{Zr}/x_{Hf}	50.70	1.46	34.19	2.53

Using the total product yield measured for the two sets of experiments, the mass of $K_2Zr(Hf)F_6$ remaining in solution after crystallization was calculated according to Equation (4.10), which corresponds to total mass balance:

$$M_F = M_C + M_M \tag{4.10}$$

M_F is the total mass of $K_2Zr(Hf)F_6$ used for the crystallization (feed), M_C is the mass of the crystalline product (crystals), and M_M is the mass remaining in the solution (mother liquor) after crystallization, with all the masses expressed in grams (g). Two calculation methods were used to test the mass balance conditions, which are designated Method A and Method B.

Method A

Using the results for each of the experiments together with the Zr-concentrations of the feed, solid products, and mother solutions that were determined by ICP-OES analysis, the fractional mass balance for Zr was tested. According to Equation (4.11):

$$M_F^{Zr} = M_C^{Zr} + M_M^{Zr} \tag{4.11}$$

where M_i^{Zr} is the fractional mass of elemental Zr, which can be calculated according to:

$$M_i^j = M_i \cdot f_i^j \tag{4.12}$$

where M_i is the total mass of salt in stream i (i = F, C, M) with j = Zr or Hf, and f_i^j is the total mass fraction of elemental Zr (or Hf) in the salt of each stream (in other words the mass percentage of Zr in the salt of each stream). Using the concentrations as determined from ICP-OES analysis, the total mass fractions of Zr were calculated together with the fractional mass of Zr in each stream. The fractional mass balance for Zr could then be tested, of which the results of both the crystallizations from H_2O and 0.25 mol/L KF solutions are shown in Table 4.2. Note that the fractional mass balance for Hf was not tested as its contribution to the total mass is negligible in comparison with that of Zr, although it is used in calculation Method B.

Table 4.2: Results of fractional mass balance calculated using Equations (4.10) – (4.12) for Zr, for crystallization from both H_2O- and 0.25 mol/L KF solutions. Values represent the average values of each series.

Crystallization Solution	M_F^{Zr} (g)	M_C^{Zr} (g)	M_M^{Zr} (g)	$M_F^{Zr} = M_C^{Zr} + M_M^{Zr}$ (g)	Δ (mg)
H_2O	1.1614	0.6256	0.4564	1.0820	79.4
0.25 mol/L KF	1.1614	0.8670	0.1796	1.0466	114.8

The results show that there is a loss of mass in both experiments in the order of 100 mg, which corresponds with a percentage difference of 8.6 % with regard to the value of M_F^{Zr} calculated according to Equation (4.12). This is comparable to the variation observed in the

analytical measurement of the concentrations via ICP-OES (Appendix B.2). The unaccounted mass can therefore also be attributed in part to the error associated with the analytical method used to measure the Zr-concentrations. If viewed from this perspective, the 8.6 % difference is acceptable. To incorporate the effect of Hf, calculation method B was used.

Method B

In this method, an equation is derived that was used to predict the mole fraction ratio of the solid-phase (crystalline product) and the liquid-phase (mother liquor), in terms of the fractional masses calculated using Equation (4.12) and the mole faction ratios of the other two streams.

Only metallic Zr and Hf are treated in this method with respect to each stream. Analogous to Equation (4.10), the total mole balance (with respect to the total mole of only Zr and Hf) can be expressed according to Equation (4.13):

$$n_F = n_C + n_M \tag{4.13}$$

The number of moles of Zr, and of Hf in each stream is therefore:

$$n_i^j = n_i . r_i^j \tag{4.14}$$

Again, n_i is the total number of moles with respect to Zr and Hf in stream i (i = F, C, M) with j = Zr or Hf, and r_i^j is the relative mole fraction of Zr or Hf in the salt of each stream. Therefore, the total mole balance for Hf can be written as:

$$n_F . y_{Hf} = n_C . z_{Hf} + n_M . x_{Hf} \tag{4.15}$$

where y_{Hf} represents the relative mole fraction of Hf in the feed stream, z_{Hf} the relative mole fraction of Hf in the crystalline product, and x_{Hf} the relative mole fraction of Hf in the mother liquor. This notation then also applies to Zr. Because the concentration of Zr is much larger than that of Hf in the whole system, i.e. $r_i^{Zr} >> r_i^{Hf}$, it is assumed that $r_i^{Zr} = 1$. Therefore:

$$\frac{r_i^{Hf}}{r_i^{Zr}} \approx r_i^{Hf} \tag{4.16}$$

whereby Equation (4.15) can be written as:

$$n_F \cdot \frac{y_{Hf}}{y_{Zr}} = n_C \cdot \frac{z_{Hf}}{z_{Zr}} + n_M \cdot \frac{x_{Hf}}{x_{Zr}} \tag{4.17}$$

Furthermore, the total number of moles in each stream (with respect to Zr and Hf) can be calculated using Equation (4.18):

$$n_i = \frac{M_i^{Zr}}{M_W^{Zr}} + \frac{M_i^{Hf}}{M_W^{Hf}} \tag{4.18}$$

in which M_W^j is the molecular weight of Zr or Hf, and M_i^j can be calculated using Equation (4.12). Equation (4.17) can thus be written as:

$$\frac{y_{Hf}}{y_{Zr}}\left(\frac{M_F^{Zr}}{M_W^{Zr}} + \frac{M_F^{Hf}}{M_W^{Hf}}\right) = \frac{z_{Hf}}{z_{Zr}}\left(\frac{M_C^{Zr}}{M_W^{Zr}} + \frac{M_C^{Hf}}{M_W^{Hf}}\right) + \frac{x_{Hf}}{x_{Zr}}\left(\frac{M_M^{Zr}}{M_W^{Zr}} + \frac{M_M^{Hf}}{M_W^{Hf}}\right) \tag{4.19}$$

where the following relation holds:

$$\frac{r_i^{Hf}}{r_i^{Zr}} = \left(\frac{r_i^{Zr}}{r_i^{Hf}}\right)^{-1} \tag{4.20}$$

By rearrangement of Equation (4.19) and using it together with Equations (4.12) and (4.20), the expected mole fraction ratios z_{Zr}/z_{Hf} and x_{Zr}/x_{Hf} were calculated for both the crystallization from the H_2O and 0.25 mol/L KF solutions. For example, in calculating the mole fraction ratio of one particular stream, the mole fraction ratios of the other two streams, as calculated from the ICP-OES analysis results, were used in Equation (4.19) together with the masses calculated using Equation (4.12). The calculated results are shown in Table 4.3 which is compared with the measured results (from ICP-OES analyses).

From Table 4.3, it is clear that the calculated results correlate with the measured results, in that both the mole fraction ratios z_{Zr}/z_{Hf} and x_{Zr}/x_{Hf} decreased when the KF concentration of the crystallization solution was increased. The measured ratios are also predicted quite accurately, especially for crystallization from H_2O. Thus, the simultaneous decrease of both z_{Zr}/z_{Hf} and x_{Zr}/x_{Hf} are validated by these results.

Table 4.3: Comparison between the measured and expected mole fraction ratios, calculated using Equation (4.19), of the solid and liquid phases for crystallization from both H_2O and 0.25 mol/L KF solutions.

Crystallization Solution	H_2O		0.25 mol/L KF	
Mole Fraction Ratios	Measured	Calculated	Measured	Calculated
z_{Zr}/z_{Hf}	156.70	155.51	128.06	111.71
x_{Zr}/x_{Hf}	50.70	50.53	34.19	28.86

Also, as shown in Table 4.1 the product yield of crystallization from 0.25 mol/L KF solutions is higher than that for crystallization from H_2O. Therefore, crystallization from the 0.25 mol/L KF solutions continued for a longer period of time before equilibrium was reached whereby it is possible that more of the impurity can be incorporated into the solid product. This correlates with the decreased purity of the crystalline product characterized by the decrease in z_{Zr}/z_{Hf} with respect to crystallization from only H_2O solutions. Thus the relative concentration of Zr in the liquid phase, x_{Zr} would then decrease as the crystallization proceeds further. This can also contribute to more efficient separation as the separation of Zr and Hf between the two phases becomes more efficient because the value of the tails separation factor increases.

Therefore, as also mentioned in Section 4.3.2.3.B, the product purity and thus separation efficiency can be influenced by regulating the degree of crystallization. The degree of crystallization, which is dependent on the relative excess amount of solute, as characterized by the value of Σ, can therefore be yet another factor that in turn is influenced by the use of different additives such as KF and HF. This may therefore explain the increased separation efficiency when a larger relative excess amount of solute was used for the crystallization of $K_2Zr(Hf)F_6$ from aqueous solutions of KF, and KF plus HF (Sections 4.3.2.3.A and 4.3.2.3.B).

4.4. Conclusions

In this chapter it was shown experimentally that the crystalline product obtained from cooling crystallization of $K_2Zr(Hf)F_6$ from solution can be enriched with Zr and that the efficiency of separation is influenced by various factors that in turn are affected by the solution composition.

Crystallization of $K_2Zr(Hf)F_6$ from KF solutions of varying concentration with and without HF with a concentration of 2.5 mol/L have shown that the overall separation efficiency was improved by enhancement of the tails separation efficiency (i.e. with regard to the mother liquor), as characterized by the tails separation factor, γ. The tails separation factor can in turn be controlled by adjusting the KF concentration. The enrichment of the crystalline products, as is characterized by the heads separation factor, δ, was relatively poor in all cases, although an improvement was observed for crystallization from KF solutions when a constant amount of HF was added. Furthermore, the use of HF as an additive together with KF resulted in improved tails separation efficiency which contributed to an overall improvement of the separation efficiency.

SEM results have shown that crystallization from KF solutions of high concentrations resulted in a decrease in the crystal size and a change in the crystal shape and appearance (i.e. formation of large rounded particles), which also correlated with a decrease in the separation efficiency. However, with the addition of HF (2.5 mol/L), the change in crystal size and appearance at high KF concentrations was inhibited which also resulted in improved separation efficiency in comparison with crystallization from solutions of high KF concentrations without HF. Using XRD analysis, it was shown that the change in the crystal shape and appearance for crystallization from KF solutions of high concentration could be caused by the crystallization of the heptafluorides, instead of the hexafluorides, i.e. $K_3Zr(Hf)F_7$ instead of $K_2Zr(Hf)F_6$. However, in accordance with the SEM results, XRD analyses have also shown that the formation of the heptafluoride crystal structure during crystallization from KF solutions with high concentrations was avoided by the addition of HF.

In addition, by controlling the relative excess amount of solute, as characterized by the value of Σ, for crystallization of $K_2Zr(Hf)F_6$ from KF solutions of varying concentration with and without HF (2.5 mol/L), it was shown that improved separation efficiency could be obtained

when using a higher relative excess amount of solute. Moreover, for crystallization from KF solutions, it was shown by SEM and XRD results that the change in crystal size and appearance could be attributed to the increased KF concentrations and not the relative excess amount of solute (and therefore the supersaturation). The decrease in the crystal size with increasing KF concentration therefore seems to have been caused by an increased nucleation rate which suggests that KF can influence the characteristics of the crystallization kinetics on an indirect manner. The increased nucleation rate, which causes the growth rate per crystal to decrease, can contribute to a decreased purity of the crystalline product (Section 4.3.2.2.A), whereby the increased KF concentration can cause the separation efficiency to decrease.

However, with crystallization of $K_2Zr(Hf)F_6$ from KF solutions with increasing concentration with added HF, at the same relative excess amount of solute, it was confirmed that the adverse effects of KF, across the whole concentration range tested, could be suppressed by the addition of HF. More specifically, the influence that KF solutions of high concentration have on the crystallization kinetics is suppressed by the addition of a sufficient amount of HF to the solution. This is supported by SEM results which indicated that the crystals produced by crystallization from the KF and HF mixtures had a comparable size and morphology, even for crystallization from 0.5 mol/L KF solutions. Furthermore, the fact that the formation of the heptafluoride crystal structure can be avoided by the addition of HF to KF solutions was also confirmed by these experiments. This was supported by both XRD results as well as the results of ICP-OES analyses of the potassium concentrations of the product crystals, whereby the K/Zr concentration ratios were calculated; wherein an increase in the K/Zr ratio therefore indicated a higher probability for the formation of the heptafluorides. Using HF as an additive together with KF, the only effect that an increasing KF concentration had on the crystallization process was that it caused a gradual increase in the relative excess amount of solute, due to the decrease in solubility, whereby enhanced separation efficiency was affected (Section 4.3.2.3.B).

Based on these results, although only qualitative evidence exists, it can therefore be concluded that the separation efficiency with respect to Zr and Hf during cooling crystallization of $K_2Zr(Hf)F_6$ is influenced in part by the kinetics of crystallization. More specifically, an increased nucleation rate, which can be effected indirectly by the addition of KF with a high concentration to the crystallization solution, lowers the separation efficiency. Furthermore, when an increasingly high KF concentration is used, the crystal structure of the crystallizing

compound changes from the hexafluoride to the heptafluoride which also results in inferior separation efficiency. Both of these factors can be controlled by the addition of a sufficient amount of HF to the crystallization solution.

However, maybe the most notably, is that by using KF together with HF as additives, the degree of crystallization can be adjusted by an increase in the relative excess amount of solute, represented by the value of Σ, wherein improved separation efficiency could be obtained when Σ was increased. As explained earlier, the degree of crystallization increases as relative excess amount of solute in solution is increased. Thus, as concluded from the mass balance results (Section 4.3.2.5), the separation efficiency can also be influenced by the degree (extent) of the crystallization, whereby the tails separation factor, γ, can be improved when the crystallization medium is exhausted of nutrients to a larger extent. Therefore, this may be the reason for the improved separation efficiency at an increased relative excess amount of solute, which is directly related to the extent of crystallization.

With respect to a cascade-type crystallization process, it was shown that increased tails separation efficiency, can contribute to improved efficiency of the process as a whole, even though the heads separation efficiency (separation efficiency with respect to the enrichment of the crystalline product) is relatively poor. Solid solution formation may contribute to the relatively low heads separation efficiency, proof of which can be found in the molecular modeling results (Chapter 3).

The relationship between the experimental and molecular modelling results are discussed further in Chapter 5, together with the evaluation of cooling crystallization of $K_2Zr(Hf)F_6$ as applied to a cascade process.

4.5. References

1. von Hevesy, G. The discovery and properties of hafnium. *Chem. Rev.* **2** (1) (1925) 1 – 41.

2. Coster, D. and von Hevesy, G. Process of separating zirconium and Hafnium. U.S. Pat. 1,618,960 (1927).

3. Blumenthal, W.B. 1958. The chemical behaviour of zirconium. D. van Nostrand Company Inc., New York. p. 1 – 45.

4. Sajin, N.P. & Pepelyaeva, E.A. Separation of hafnium from zirconium and production of pure zirconium dioxide. In Proceedings of the Second united Nations International Conference on the Peaceful uses of Atomic Energy, Geneva, 1958. Vol. 8, Paper P/634, pp 559–562.

5. Vinarov, I.V. Modern methods for separating zirconium and hafnium. *Russ. Chem. Rev.* **36** (7) (1967) 522 – 536.

6. Teja, A.S., Givand, J.C. and Rousseau, R.W. Correlation and prediction of crystal solubility and purity. *A.I.Ch.E J.* **48** (11) (2002) 2629 – 2634.

7. Givand, J.C., Teja, A.S. and Rousseau, R.W. Effect of relative solubility on amino acid crystal purity. *A.I.Ch.E J.* **47** (12) (2001) 2705 – 2712.

8. Rosenberger, F. and Riveros, H.G. Segregation in alkali halide crystallization from aqueous solutions. *J. Chem. Phys.* **60** (2) (1974) 668 – 673.

9. Nie, Q., Wang, J. & Yin, Q. Effect of solution thermodynamics on the purification of two isomorphic steroids by solution crystallization. *Chem. Eng. Sci.* **61** (2006) 5962 – 5968.

10. Givand, J., Chang, B-K. Teja, A.S. & Rousseua, R.W. Distribution of isomorphic amino acids between a crystal phase and an aqueous solution. *Ind. Eng. Chem. Res.* **41** (2002) 1873 – 1876.

11. Ulrich, J. & Strege, C. Some aspects of the importance of metastable zone width and nucleation in industrial crystallizers. *J. Cryst. Growth* **237 – 239** (2002) 2130 – 2135.

12. Nývlt, J., Söhnel, O., Matuchová, M. & Broul, M. 1985. The kinetics of industrial crystallization. Amsterdam: Elsevier science publishers. 350 p.

13. Schwartz, A.M. & Myerson, A.S. 2002. Solutions and solution properties. In Myerson, A.S., ed. Handbook of industrial crystallization. 2nd ed. Boston: Butterworth-Heinemann. p. 1 – 31.

14. Mersman, A., Eble, A. & Heyer, C. 2001. Crystal growth. In Mersman, A., ed. Crystallization technology handbook. 2nd ed. New York: Marcel Dekker. p. 81 - 143.

15. Lu, J.J. & Ulrich, J. An improved prediction model of morphological modifications of organic crystals induced by additives. *Cryst. Res. Technol.* **38** (1) (2003) p. 63 – 73.

16. Mullin, J.W. 2001. Crystallization. 4th ed. Boston : Butterworth-Heinemann. 594 p.

17. Benedict, M., Pigford, T.H. and Levi, H.W. 1981. Nuclear chemical engineering. 2nd ed. McGraw-Hill.

18. Poriel, L., Chitry, F., Pellet-Rostaing, S., Lemaire, M. and Favre-Réguillon, A. Zirconium and hafnium separation part 3. Ligand-enhanced separation of zirconium and hafnium from aqueous solution using nanofiltration. *Sep. Sci. Technol.* **41** (2006) 2883 - 2893.

CHAPTER 5

Evaluation

5.1. Molecular Modelling of $K_2Zr_{(1-z)}Hf_zF_6$ Solid Solutions

In an attempt to theoretically evaluate the separation efficiency of Zr and Hf via fractional crystallization of $K_2Zr(Hf)F_6$, the thermodynamic properties of $K_2Zr_{(1-z)}Hf_zF_6$ solid solution formation was studied using Density-Functional Theory simulations. Some discrepancies were observed when comparing the calculated formation enthalpies (although, strictly speaking; the zero-temperature formation energies) of $K_2Zr_{(1-z)}HfF_6$, and $Zr(Hf)F_4$, with the available experimental data of $Zr(Hf)F_4$ (Sections 3.3.1.4 and 3.3.2.1.A). However, literature data of $Be_xZn_{1-x}O$ and Al-Zr(Hf) alloys was satisfactorily reproduced (Section 3.3.1.2) using the pseudopotential plane-wave method of CASTEP in conjunction with the computational parameters employed in this study. Therefore, the methodology that was used in this study appears to be sound, where the disagreement between the calculated and experimental data seems to be related to the level of accuracy of the basis functions used for Zr and Hf, i.e. the pseudopotentials in the case of CASTEP and the numerical basis sets of DMol^3.

Consequently, the use of (i) different pseudopotentials, as applied to the plane-wave method of CASTEP and (ii) numerical basis functions, employed in the numerical method of DMol^3, produced varying results with regard to the thermodynamic properties of mixing. This was evident from the fluctuation in the calculated mixing enthalpies that accompanied the variation in the computational parameters. While the 450 eV Ultrasoft A data (Section 3.3.1.5) predicted that solid solution formation would be slightly thermodynamically unstable, the 330 eV Ultrasoft B data (Section 3.3.1.5) and DMol^3 data (Section 3.3.2.1.B), predicted that solid solution formation would be marginally thermodynamically favoured. By implementing the calculated mixing enthalpies in a simplified thermodynamic model (Sections 3.3.1.5 and 3.3.2.1.B), relatively poor separation efficiency was predicted in all cases. As a result, it was predicted that purification beyond a Hf fraction of 0.05 would be impractical due to the very poor separation efficiency which was calculated for the region of very low Hf-concentration.

This is because the formation of $K_2Zr_{(1-z)}Hf_zF_6$ solid solutions was predicted to occur with relative ease (only more so according to the 330 eV Ultrasoft B- and Dmol^3 results than according to the 450 eV Ultrasoft A results), due the small mixing enthalpy changes (in the order of -5 kJ.mol^{-1} to 5 kJ.mol^{-1}) associated with the incorporation of Hf in the crystal lattice of K_2ZrF_6.

These small mixing enthalpies are in agreement with the small change in the structural properties of $K_2Zr_{(1-z)}Hf_zF_6$ solid solutions with changing composition, z (Section 3.3.1.3). Therefore, although there were some disagreements between the calculated and experimental data (Sections 3.3.1.4 and 3.3.2.1.A), a relatively limited interaction of the impurity with the host crystal structure (desired crystal structure of K_2ZrF_6) could be detected. Thus, it was concluded that the efficient separation of Zr and Hf by fractional crystallization of $K_2Zr(Hf)F_6$ could indeed be hampered by lattice substitution of the Hf-impurity into the crystal structure of K_2ZrF_6, or in other words, solid solution formation. As explained in Section 3.4, the small ΔH_{mix}-values imply that the modelling calculations have to be exceptionally accurate to correctly determine the absolute degree of impurity-host interaction. This implies that the basis functions of Zr and Hf (i.e. pseudopotentials in the case of CASTEP, and numerical basis sets of DMol^3) needs to be more rigorously defined. Therefore, it can be concluded that the current Zr- and Hf basis functions should be improved to enable one to more accurately measure the small differences between the two analogous elements.

5.2. Cooling Crystallization of $K_2Zr(Hf)F_6$

By studying the crystallization of $K_2Zr(Hf)F_6$ using cooling crystallization from aqueous solutions, has shown that the separation efficiency was influenced by the addition of KF and/or HF. By adjusting the solvent composition, it was shown that both enhancement and reduction of the separation efficiency with respect to Zr and Hf could be effected.

With the aid of SEM and XRD analysis, a qualitative correlation was observed between the crystallization kinetics, crystal structure and separation efficiency, which seemed to be controlled by the KF concentration. For example, at moderate KF concentrations, a noteworthy decrease in crystal size was observed (Section 4.3.2.2.A), that was confirmed by the controlled salt concentration experiments (Section 4.3.2.3.A), which led to a decreased separation efficiency. This phenomenon was attributed to an increased nucleation rate which

therefore appeared to be indirectly caused by the increased KF concentration (i.e. by disturbing the crystallization equilibria). At higher KF concentrations, XRD results showed that the crystal structure of the crystalline product probably changed from the hexafluoride to the heptafluoride (Sections 4.3.2.2.A and 4.3.2.3.A), which in effect also contributed to inferior separation efficiency. It was found however, that the effect that KF has on the kinetics and crystal structure could be favourably regulated (suppressed) by the addition of HF with a concentration of 2.5 mol/L (Sections 4.3.2.2.B 4.3.2.3.B), whereby enhanced separation efficiency could be obtained. It was shown that the relative amount of dissolved $K_2Zr(Hf)F_6$ (with respect to the solubility) used, influenced the degree of crystallization, which seemed to be the determining factor with regard to enhancement of the separation efficiency. It was found that the inhibiting effect of HF towards the negative influence of high KF concentrations during crystallization from aqueous solutions could be used to control the degree of crystallization (Sections 4.3.2.2.B and 4.3.2.3.B), and therefore also the separation efficiency.

The degree of crystallization corresponds with the extent to which the mother solution is depleted of nutrients (i.e. $K_2Zr(Hf)F_6$) (Sections 4.3.2.5 and 4.4). Therefore, the tails separation efficiency (characterized by the tails separation factor, $\gamma_{Zr,Hf}$) could be improved, using an aqueous solvent with a high KF concentration in the presence of HF, which also contributed to an improved separation efficiency.

The enrichment of the crystalline phase was characterized by a relatively poor heads separation efficiency (represented by a relatively small value of the heads separation factor, $\delta_{Zr,Hf}$), which however did not improve with an increased tails separation efficiency. It therefore seems that the separation efficiency was largely controlled by the tails separation factor, $\gamma_{Zr,Hf}$, where solid solution formation could contribute to the comparatively poor degree of enrichment of the crystalline phase, which is supported by the molecular modelling results. It was shown that a superior tails separation efficiency (which causes improvement in the overall separation efficiency, $\alpha_{Zr,Hf}$) can contribute to an increased rate of enrichment of the crystalline phase with regard to the sequential crystallization steps in a cascade process (Section 4.3.2.4).

Based on these results, it was therefore concluded that the solution properties can play an important role in facilitating improved separation efficiency during fractional crystallization

of $K_2Zr(Hf)F_6$. These solution properties may include changes in the solubility ratio of pure K_2ZrF_6 and K_2HfF_6 which might be influenced when using KF and HF as additives. According to the thermodynamic model of Rosenberger et al. [1] (Equations (2.43) and (3.14)), this can contribute to enhanced separation efficiency, which was confirmed for other isomorphic systems [2, 3]. Speciation effects may also play an important role, where the stability of the Zr- and Hf complexes in solution would determine the total thermodynamic energy changes of the compounds during crystallization. Any significant differences in thermodynamic stability between the corresponding Zr- and Hf-compounds in solution could therefore be exploited to afford further enhancement of the separation efficiency. Knowledge of the aqueous chemistry of $K_2Zr(Hf)F_6$ is deficient at present, and although an investigation into the speciation of the Zr(IV)/Hf(IV) system fell beyond the scope of this study, further studies in this direction would be beneficial.

In summary, an attempt was made in this study to understand the specific influence of the solution properties on the separation efficiency, where the degree of crystallization, as was characterized by Σ (Equation 4.4), was found to be one of the determining factors. In addition, the effect of KF on the crystallization kinetics and crystal structure (i.e. formation of K_3ZrF_7 instead of K_2ZrF_6), which could be regulated by adding HF to the crystallization solutions, was also found to be important with regard to its effect on the separation efficiency.

5.3. Separation Efficiency: Modelling vs. Crystallization

As mentioned in Section 5.1, according to the evaluation of the solid state thermodynamics of the $K_2Zr(Hf)F_6$ system, as determined by using molecular modelling, relatively poor separation efficiency was predicted since solid solution formation appeared to be possible. Consequently, unfeasible separation efficiency was predicted beyond a Hf-content of $z_{Hf} = 0.05$, i.e. purification beyond a Zr-fraction of 0.95. A Hf-fraction of $z_{Hf} = 0.05$ corresponds to $z_{Zr}/z_{Hf} \approx 20$. Experimentally however, superior separation efficiency was obtained which was even further enhanced by the use of KF and HF as additives. For example in only one crystallization step, a ratio of z_{Zr}/z_{Hf} in the order of 150 was obtained.

Therefore, it is clear that the separation efficiency is greatly underestimated by the molecular modelling results. The poor correlation between the modelling and experimental results might be attributed to the following factors:

(i) Inadequacy of the pseudopotential and numerical basis functions used for the modelling of $K_2Zr_{(1-z)}Hf_zF_6$ solid solutions via the CASTEP- and DMol^3 methods respectively, in terms of accurately describing the small differences between the Zr and Hf compounds.

(ii) The fact that simulations were performed at 0 K. It might be inaccurate to compare results obtained from the theoretical simulations, at 0 K, with the physical process, which occurs at finite temperatures.

(iii) The fact that only the solid state thermodynamics were considered. As was illustrated in Chapter 4, (see also Section 5.2), the solution thermodynamics with respect to the change in the solubility ratios, which could be caused by the additives, is a possible shortcoming of the thermodynamic model used to predict the separation efficiency.

(iv) The thermodynamics of the whole crystallization process. The total energy changes of Zr(IV) and Hf(IV), in being transferred from the liquid phase (solution) to the solid phase, that includes the formation of mixed crystals, also dictates the purity of the crystalline product. While this aspect is only important during slow (equilibrium) crystallization, it can still be a contributing factor, which was neglected for the theoretical predictions of the separation efficiency. Molecular modelling of the $Zr(Hf)F_6^{2-}$ compounds in solution was simulated (Section 3.3.2.2), however, these results were inconclusive.

(v) Crystallization kinetics. It was shown that the characteristics of the crystals, i.e. size and morphology/structure, obtained by crystallization from aqueous solutions mixtures of KF and HF, also influence the separation efficiency. This aspect could not be accounted for in the theoretical evaluation and would even further reduce the observed separation efficiency.

(vi) Polymorphic crystal structures. In addition to the formation of K_3ZrF_7, during crystallization from solutions with high KF concentrations without added HF, the XRD results (Sections 4.3.2.2 and 4.3.2.3) have indicated that crystallization of $K_2Zr(Hf)F_6$ in both the monoclinic and orthorhombic crystal structures are possible. However, only the orthorhombic structure was used for the modelling of $K_2Zr_{(1-z)}Hf_zF_6$ solid solutions. It is possible that the energetics of solid solution formation (as well as the selectivity of crystal growth) could be different for different polymorphs.

(vii) In addition to the factors described above, that could not be incorporated into the thermodynamic model used to evaluate the separation efficiency, the change in the vibrational entropy (according to Equations (2.43) and (3.14)) during solid solution formation was also assumed to be negligible. However, due to the discrepancy between

the modelled and experimental separation efficiency, this assumption was re-evaluated as discussed in the next section.

5.3.1. The Influence of the Vibrational Entropy

Recall that the calculated mixing enthalpy change was relatively small and comparable to the ideal mixing entropy, in $T\Delta S_{mix}$, calculated using Equation (3.11). If the vibrational entropy change is in the same order of magnitude, it could contribute to the thermodynamic stability of solid solutions. Therefore, by including the vibrational entropy term according to Equations (2.43) and (3.14), and using Equation (5.1) instead of (3.15) for predicting the separation efficiency, a more accurate result might be obtained if the entropy has a significant influence.

$$\beta_0 = exp\left(\frac{-\Delta H_{mix} + T\,\Delta S_{vib}}{RT}\right) \tag{5.1}$$

The vibrational entropy cannot easily be evaluated through molecular modelling, because of the computational intensive nature of the simulations, for a full vibrational analysis. To obtain a quantitative idea of the possible contribution of the vibrational entropy, the problem was therefore addressed using the Debye model of solid vibrations [4 - 6]; a statistical thermodynamic model, to approximate the vibrational entropy.

According to this model, each atom in a solid is treated as an identical three-dimensional harmonic oscillator with energy, ε:

$$\varepsilon = h\nu \tag{5.2}$$

where h is Planck's constant (J.s), and ν is the vibration frequency (s^{-1}). Different modes of oscillation can occur that are equally spaced. These equally spaced vibrational modes, or energy levels, are termed phonons, and the allowed energy levels are quantified in terms of the ground-state vibrational mode according to:

$$\varepsilon_i = h\nu(v_i + \tfrac{1}{2}) \tag{5.3}$$

where v_i is the quantum number of the i'th energy level. The total vibrational energy of a solid is then the sum of the energies of the allowed energy levels. According to the Debye model there is an upper limit to the phonon energy; this upper limit corresponds with the vibrational energy of the energy level with a maximum vibration frequency, ν_D, or lowest wavelength. In other words, the maximum allowed frequency of the atomic vibrations that does not cause the solid to dissociate. This can be expressed conveniently in dimensionless form, at temperature T, according to:

$$y = \frac{h.\nu_D}{k.T} = \frac{\Theta_D}{T}$$
$$\text{and} \quad \Theta_D = \frac{h.\nu_D}{k} \tag{5.4}$$

where k is the Boltzmann constant ($J.K^{-1}$), T is the temperature of interest (K) and Θ_D is the characteristic Debye temperature. Therefore, the Debye temperature is a quantitative measure of the vibrational energy of the highest vibrational mode of the solid, and can be viewed as a measure of the rigidity of a lattice. For example, the Debye temperature of diamond, which is stiff and hard, will be high in comparison with that of lead which is soft and more elastic. According to the Debye model the entropy due to the atomic vibrations (S_{vib}) can then be expressed as [4]:

$$S_{vib} = R\left[-3\ln\left(1-e^{-y}\right)+4D(y)\right] \tag{5.5}$$

The function, $D(y)$ is known as the Debye function and is defined as [4 - 6]:

$$D(y) = 3\left(\frac{T}{\Theta_D}\right)^3 \int_0^{\Theta_D/T} \frac{y^3}{e^y-1}\,dy \tag{5.6}$$

and increases from 0 in the low temperature limit to 1 in the high temperature limit [6]. It can be shown that the entropy change during the transfer of an impurity, from its own lattice to the lattice of the desired compound, with application to the K_2ZrF_6/K_2HfF_6 system, can be calculated according to Equation (5.7) [1]:

$$\Delta S_{vib} = S_{Zr} - S_{Hf} = 3R.ln\left[\frac{\left(1-e^{-y_{Hf}}\right)}{\left(1-e^{-y_{Zr}}\right)}\right] + 4R\left[D\left(y_{Zr}\right) - D\left(y_{Hf}\right)\right] \qquad (5.7)$$

Intuitively, the vibrational entropy is a measure of the vibrational energy change of the lattice when Hf is substituted for Zr in the crystal structure of K_2ZrF_6; thus whether the lattice vibrations become more energetic or less energetic, when the impurity is incorporated into the host lattice. Equation (5.7) gives the maximum difference in the vibrational entropy between the two pure crystal structures, or in other words the maximum change that can occur when the impurity (Hf) is incorporated into the lattice of K_2ZrF_6.

Kittel [7] gives the Debye temperatures of elemental Zr and Hf as 292 K and 252 K respectively. Although these are the values for the metals, the potassium salts should have the same ratio, as the vibrations of both the K- and F-ions in K_2ZrF_6 and K_2HfF_6 should be identical. The only difference is the vibration frequency of the metal centres of which the mass differs. It is this difference that is of interest to us. Using these Debye temperatures, ΔS_{vib}, was calculated at a temperature of 288 K, which corresponds with the experimental crystallization temperature. The first term in Equation (5.7) can easily be calculated using the known Debye temperatures. The Debye functions of Zr and Hf were calculated numerically using the mathematical software *Polymath* at the chosen temperature of T = 288 K. This calculation results in a vibrational entropy of ΔS_{vib} = -3.51 $J.K^{-1}.mol^{-1}$, which is not insignificant when compared to the value of the universal gas constant, i.e. R = 8.314 $J.K^{-1}.mol^{-1}$. Moreover, when multiplied by the temperature (according to Equation (5.1)), this corresponds to a value of -1.01 $kJ.mol^{-1}$.

Since the predicted separation efficiency resulting from the use of the 450 ev Ultrasoft A simulation data correlated best with the experimental results, i.e. the enrichment of the solid phase was both predicted and observed experimentally, the vibrational entropy analysis presented here will therefore be applied to this data set. When comparing the calculated vibrational entropy to the ΔH_{mix} data as illustrated in Fig. 5.1, it becomes clear that the two terms are indeed in the same order of magnitude.

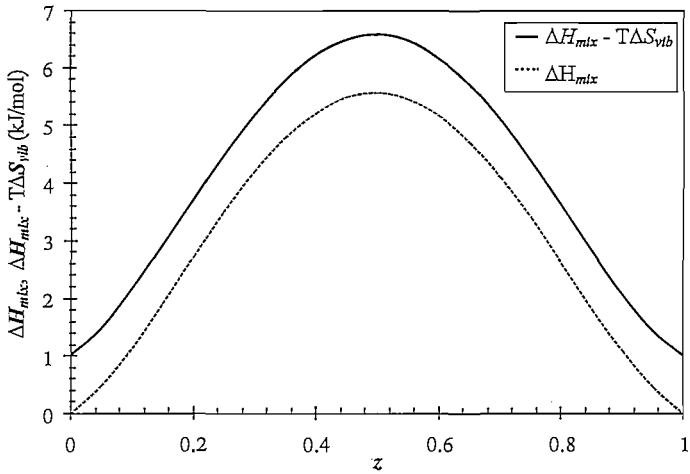

Figure 5.1: Contribution of the calculated vibrational entropy to the thermodynamic stability of $K_2Zr_{(1-z)}Hf_zF_6$ solid solutions.

Thus, the vibrational entropy contribution might not be as insignificant as first anticipated. Using the $\Delta H_{mix} - T\Delta S_{vib}$ term, (see Fig. 5.1), β_0 was calculated following the same method used in Sections 3.3.1.5 and 3.3.2.1.B together with Equation (5.1), the "entropy-corrected" distribution curve of Hf was calculated, which is presented in Fig. 5.2. In comparison with the results shown in Fig. 3.13 (no entropy correction), improved separation efficiency is predicted especially at low Hf-concentrations, i.e. separation is theoretically possible at $z_{Hf} < 0.05$. Furthermore, as shown in the insert of Fig. 5.2, the purification of K_2ZrF_6 up to a Hf-fraction of 0.0001, indicated by the vertical line, still seems possible; where a tolerable separation efficiency of $\beta = 0.7$ is predicted.

It can therefore be concluded that for systems such as K_2ZrF_6 and K_2HfF_6, in which the mixing enthalpy changes are relatively small, i.e. in the order of 1 – 10 kJ.mol^{-1}, the vibrational entropy can still play an important role in terms of the separation during crystallization. Thus, in addition to the other factors that were shown to have an influence on the separation efficiency (Section 5.3), it was illustrated here that the poor correlation between the modelling and experimental results observed initially, might in part be due to the

neglected vibrational entropy when the role of the solid-state thermodynamics were initially evaluated.

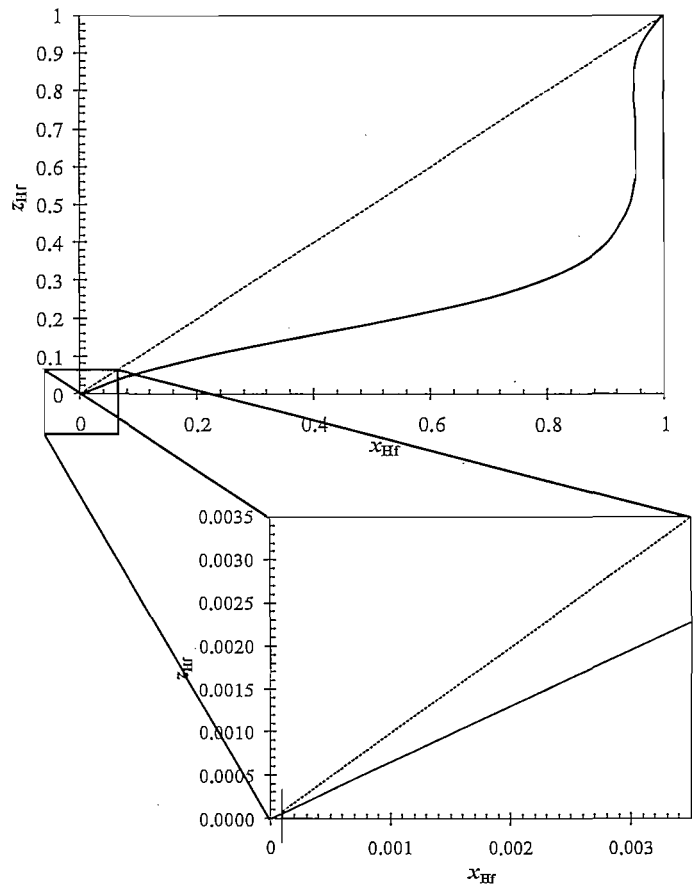

Figure 5.2: ΔS_{vib}-corrected distribution curve of Hf using the 450 eV Ultrasoft A CASTEP-data. The effect of ΔS_{vib} can be seen by comparison of the figure with Fig. 3.13.

5.4. Qualitative Process Evaluation

In this section, before the final remarks and recommendations are discussed, the separation efficiency of Zr and Hf separation by fractional crystallization of $K_2Zr(Hf)F_6$, is evaluated using a mathematical model to determine the number of stages that would be required to

effect the desired purification. A recycle-type cascade process is proposed to afford an appreciable recovery of Zr(IV), in which some design possibilities are also outlined that may form part of further studies on this subject.

For the staged crystallization experiments presented in Sections 4.2.3.4 and 4.3.2.4, a simple cascade method was used wherein the mother liquor from each stage was discarded. The product stream, i.e. the feed stream to the next stage, then simply consisted of the product stream (i.e. heads stream) of the previous stage. Note that although these experiments were conducted in a batch-wise process and not continuously, this can still be used to illustrate the underlying principle. Using this method, Zr(IV), remaining in the impure mother liquors is therefore also discarded, which results in an insufficient yield of Zr(IV)-enriched crystals, with respect to the crude starting material, just as was observed by Sajin et al. [8] (Section 4.1).

To increase the product yield, the mother liquors from each crystallization stage must therefore be reprocessed to recover the remaining Zr(IV). This may be done using a recycle type cascade [9], which is illustrated in Fig. 5.3, and which should be interpreted as a continuous process. In this type of cascade, the feed for one stage (for example stage i), consists of the heads stream from the previous stage (Stage $i-1$) and the tails stream from the next stage (Stage $i+1$). Thus, this cascade process is analogous to a countercurrent-type distillation process. Two different areas can be distinguished in this recycle-type cascade, namely the enriching section and the stripping section. After the feed stream has been separated into the heads and tails stream at the feed stage, the heads stream is sent to the enriching section where further purification proceeds. The tails stream resulting from the feed stage, however, is sent to the stripping section where the remaining fraction of the desired compound is recovered. As a result, there exists an upward flow (towards the product end of the cascade) of the desired compound of which the fraction increases with each stage. Consequently, the undesired compound(s) move downward in the cascade, causing the tails stream of each stage to be increasingly depleted of the desired compound. Thus, with regard to fractional crystallization of $K_2Zr(Hf)F_6$, there is an upward flow with respect to the crystalline products, and a downward flow with respect to the mother liquors. The feed stage depends on the composition of the feed and the degree of purification that is desired.

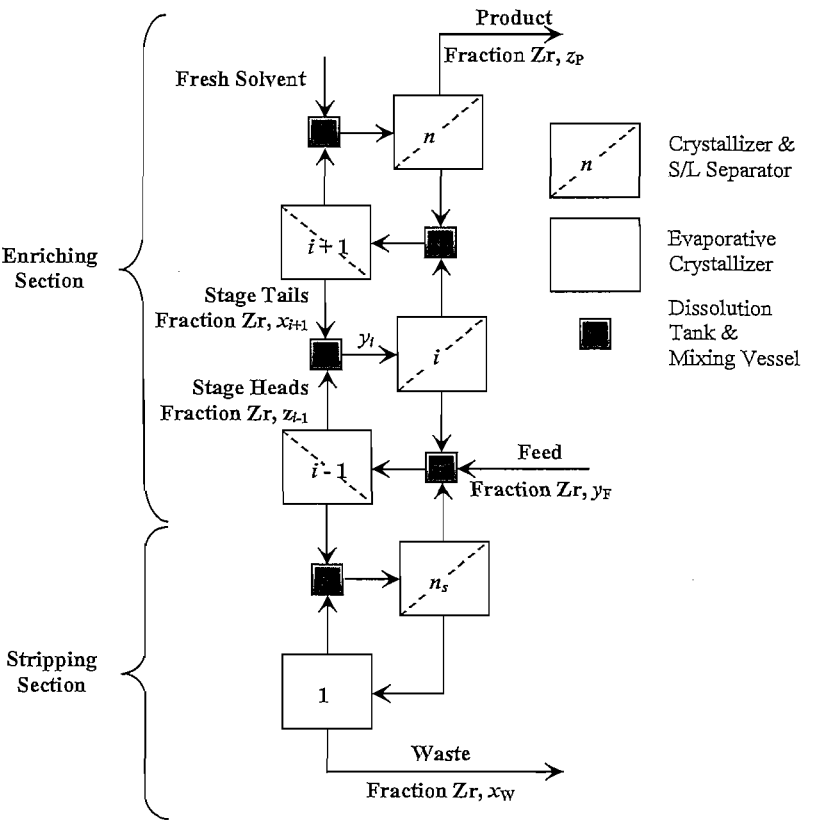

Figure 5.3: Schematic illustration of a recycle-type cascade as applied to the fractional crystallization of $K_2Zr(Hf)F_6$. Adapted from Ref. [9].

With specific application to fractional (cooling) crystallization of $K_2Zr(Hf)F_6$, a qualitative explanation of the process follows hereafter. Adopting the conditions identified experimentally that yielded the most efficient separation (Chapter 4), i.e. crystallization from a 0.45 mol/L KF solution with an HF concentration of 2.5 mol/L, and assuming that the solvent composition remains constant, the proposed cascade would proceed as follows. First, solid $K_2Zr(Hf)F_6$ is fed to a mixing tank where it is mixed with the mother liquor from Stage i and the solid product from Stage n_s, which is heated to dissolve the crystals. The feed stream is then separated into the heads and tails streams, where the crystalline product, i.e. heads

stream, is further enriched with Zr in the enriching section, whereas the remaining Zr-fraction is recovered in the stripping section. During the final enriching stage, fresh solvent must be added to the last dissolution tank to dissolve the crystalline product produced in the preceding stage, which also serves as the source of the solvent for the entire cascade. By carefully controlling the flow rate of solvent added to the final dissolution tank, the flow rate ratio of the crystals and mother liquor streams fed to each dissolution/mixing tank can be regulated, thus keeping the salt concentration of the solution fed to each crystallizer constant. Thereby the conditions in each crystallizer would be the same. This is important as it was shown in Chapter 4 that the initial salt concentration of the unsaturated solution also influences the separation efficiency. However, the stream entering the first stage in the cascade, i.e. Stage 1 in Fig. 5.3, consists only of the cold unsaturated mother solution that is enriched with Hf. Therefore, the salt concentration would be insufficient to allow cooling crystallization in this stage, because no additional solid is added to this stage. To produce a crystalline product to be fed to the next higher stage, evaporative crystallization may be used, where water vapor together with a Hf-enriched mother liquor is removed from the cascade. Note that the solute concentration in the feed also depends on the ratio of the total amount of crystals fed from the stripping and the total mother liquor volume fed from the enrichment section. Thus, depending on this ratio, the feed (crude $K_2Zr(Hf)F_6$) must be added either as a solid or as a solution to ensure a sufficient solute concentration. If the feed stream is added in solution form, the amount of solvent added to the solid $K_2Zr(Hf)F_6$ would be the same as that added to the top dissolution tank, because the same solute concentration is desired at each stage. However, this would mean that the solvent load in the stripping section is doubled, causing the solute concentration to be halved, thus leading to an increase in the required cooling capacity. In addition, the mixtures in each mixing/dissolution tank will also have to be reheated to produce an unsaturated solution for the next crystallization stage, and if the solvent volume is doubled in the stripping section, as explained above, the energy requirements will increase. This can have negative effects on the economical efficiency of the process, and careful consideration should therefore be given to this aspect.

While a full evaluation of the process with regard to the solute and solvent flow rates, and mass balances is beyond the scope of this study, the number of stages required to produce K_2ZrF_6 with the desired purity, were estimated using the Ideal cascade model. The complete theory of the Ideal cascade was described by Benedict et al. [9] and only some of the most important aspects will be highlighted here with a minor change in notation.

An Ideal cascade is one in which the following conditions are satisfied:

- The heads separation factor, δ_i, remains constant throughout the cascade, and
- The heads and tails streams fed to each stage have the same composition, i.e:

$$x_{i+1} = z_{i-1} = y_i \quad (i = 2, 3, ..., n\text{-}1) \tag{5.8}$$

It can then be shown that the following relationship exists between the heads separation factor (δ_i as defined in Equation (4.7)), the separation factor (α_i as defined in Equation (4.6)), and the tails separation factor (γ_i as defined in Equation (4.8)) attributed to each stage of the cascade:

$$\delta_i = \sqrt{\alpha_i} = \gamma_i \tag{5.9}$$

This is an important property of the Ideal cascade, because only when the heads and tails separation factors are equal, and constant (thus α is also constant), can the condition of Equation (5.8) be reached, which ensures that the purity of the feed to each stage is at a maximum, whereby optimum efficiency can be obtained. When the composition of the heads and tails streams fed to each individual stage are not equal, for example $x_{i+1} < z_{i-1}$, the degree of enrichment obtained in the previous stage would be compromised due to the mixing of the enriched stream with the tails stream which contains a lower concentration of the desired compound.

It was however shown in Chapter 4 and Section 5.2 that the tails separation factor, γ, contributed more to the separation efficiency, i.e. increase in α, than the heads separation factor, δ. It was thus observed experimentally that the heads and tails separation factors were not equal (Equation (5.9)) for the cooling crystallization of $K_2Zr(Hf)F_6$.

By calculating the heads separation factor using Equation (5.9), for crystallization of $K_2Zr(Hf)F_6$ from a solution of 0.45 mol/L KF with 2.5 mol/l HF, would therefore yield an average value for δ and γ. Assuming the Ideal cascade model can be applied to cooling crystallization of $K_2Zr(Hf)F_6$ using the said solvent composition of KF and HF, the number of stages required to separate the feed, with a Zr-fraction of y_F into a product stream with a Zr-fraction of z_P, and a waste stream with a Zr-fraction of x_W can then be calculated according to Equation (5.10) [9]:

$$n = 2\frac{ln\left[y_P(1-x_W)/(1-y_P)x_W\right]}{ln\,\alpha} - 1 \qquad (5.10)$$

The number of stages required for the stripping section (n_S) may be obtained by:

$$n_S = \frac{ln\left[z_F(1-x_W)/(1-z_F)x_W\right]}{ln\,\delta} - 1 \qquad (5.11)$$

where the number of stages in the enriching section (n_E) can be calculated by:

$$n_E = n - n_S \qquad (5.12)$$

Two possible scenarios was identified for the purification of $K_2Zr(Hf)F_6$, namely (i) an appreciable recovery of Zr(IV), i.e. "complete" separation of Zr and Hf by using a large stripping section, or (ii) the production of nuclear grade K_2ZrF_6 without an appreciable recovery of Zr(IV), i.e. using a small stripping section. Using the Ideal cascade model equations, i.e. Equations (5.9) – (5.12), these two scenarios are treated theoretically, of which the results are presented in Table 5.1.

Table 5.1: Cascade parameters for cooling crystallization of $K_2Zr(Hf)F_6$ from 0.45 mol/L KF and 2.5 mol/L HF solutions (α = 7.7), for the production of $K_2Zr(Hf)F_6$ with a concentration of z_P = 0.99995 (100 ppm Hf).

Cascade Parameters	High Recovery	Low Recovery
x_W	0.01	0.5
n	13	9
n_E	5	6
n_S	8	3
Feed stage	9	4

From the results shown in Table 5.1, it is evident that the number of stages do not only increase with increasing purity of the product stream, but also increase as the degree of recovery of the desired compound increased.

The composition of the streams leaving each separation stage may be calculated using Equation (5.13), for the enriching section, in which the index i is used to indicate the stage number:

$$z_i = y_{i+1} = x_{i+2} = \frac{\delta^i . z_p}{\delta^i . z_p + \delta^n . (1 - z_p)} \tag{5.13}$$

For the stripping section, the relation between the composition and stage number is given by Equation (5.14), where the index j is used to indicate the stage number:

$$x_j = y_{j-1} = z_{j-2} = \frac{\delta^{j-1} x_W}{\delta^{j-1} x_W + (1 - x_W)} \tag{5.14}$$

Subsequently, the experimental results obtained from the mini-cascade crystallization of $K_2Zr(Hf)F_6$ from a 0.45 mol/L KF solution with an HF concentration of 2.5 mol/L (Section 4.3.2.4), were compared with those obtained using the Ideal cascade model. Recall that the mother solutions (tails) were not reprocessed for these experiments, and therefore only enrichment of the crystalline product was attained using three consecutive stages. Therefore, the experimental results with respect to the heads composition, i.e. purity of the product leaving each stage, were compared with the calculated composition of the heads streams of the first three enriching stages in the Ideal cascade.

The modeled results for the case of high Zr(IV) recovery is used for illustration purposes, where the feed stage, i.e. stage 9 (see Table 5.1) corresponds with the first enriching stage in the recycle cascade. The results of the following two enriching stages, i.e. stages 10 and 11, were then used for comparison with the experimental results (Section 4.3.2.4), as shown in Fig. 5.4. Note that for the purpose of comparing the modeled and experimental data, it is assumed that the crystallization kinetics of the batch experiments and the (hypothetical) continuous process is comparable and therefore has no influence on the separation efficiency. However to accomplish this, would require pilot scale studies to optimize the flow rates. Nevertheless, according to the results (Fig. 5.4) a larger degree of purification was predicted by the Ideal cascade model in comparison with the experimental results. This is probably due to the more efficient heads separation, i.e. because of the larger value of δ calculated by

Equation (5.9) in comparison with the experimentally obtained value. Therefore, in practice more stages might be required to obtain the desired purity, than was predicted by the Ideal cascade model. It was further assumed for this analysis that the separation efficiency remains constant throughout the cascade, which did seem to be the case according to the experimental results (Section 4.3.2.4). However, as shown by the molecular modeling results (Section 3.3.1.5), the separation efficiency might deteriorate significantly with increasing purity, which would mean that larger enriching section might be required.

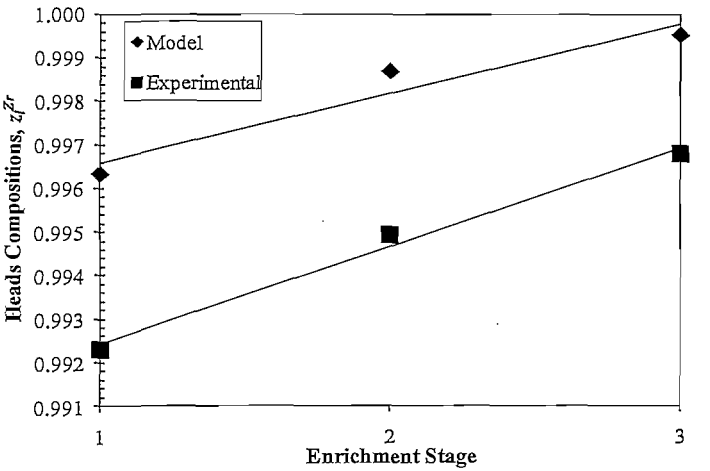

Figure 5.4: Comparison between the amount of enrichment of $K_2Zr(Hf)F_6$ in the first three enriching stages of a recycle cascade, calculated according to the Ideal cascade model, and experimental results obtained by recrystallization of $K_2Zr(Hf)F_6$. Linear fits are to serve as a visual guide.

In light of the results shown in Table 5.1, a full techno-economical evaluation should be conducted to identify the best strategy for the purification of $K_2Zr(Hf)F_6$ by fractional crystallization. In other words, the economic viability of different strategies should be evaluated for which further studies are required. For example, it was shown that a high degree of Zr(IV) recovery would require a large stripping section (Table 5.1), and therefore more stages which would result in an increase in process costs in comparison with a lower degree of recovery. The advantage of a process design to obtain a high Zr(IV) recovery however is that $K_2Zr(Hf)F_6$, which is of sufficient purity for use in the production of nuclear grade Zr is

obtained together with a high purity $K_2Hf(Zr)F_6$-waste stream, which may counteract the high process cost. It is possible to use a smaller number of stages for a lower Zr(IV) recovery, wherein a smaller stripping section would suffice. Thereby, the process cost would be lowered, however Zr(IV) production would decrease and a low-value waste stream would be produced.

Based on the vibrational entropy-corrected molecular modeling results that predicted viable separation in the region of low Hf-content, i.e. 100 ppm, and the results predicted by the Ideal cascade model, the purification of $K_2Zr(Hf)F_6$ by fractional crystallization for nuclear applications might be possible, although other aspects must also be given consideration. While it was shown that sufficient enrichment would require approximately five crystallization stages (according to the Ideal cascade model), a higher number of stages would be required for a recycle cascade if appreciable recovery of Zr(IV) is desired, due to the large stripping section (approximately 8 stripping stages) that would be needed for this purpose. The large number of stripping stages required to effect a high Zr(IV) recovery might be attributed to the relatively poor efficiency of the fractional crystallization process to separate Zr(IV) and Hf(IV) (Sections 4.3.2.2 and 4.3.2.3). In practice however, the total number of stages required might be higher than that predicted by the Ideal cascade model, as it was shown that this model overestimates the efficiency in comparison with the experimental results of the batch experiments (Fig. 5.4).

5.5. Final Remarks and Recommendations

This study has therefore shown that the use of KF and HF as additives, as was first done by Coster and von Hevesy [10], influences the separation efficiency of fractional crystallization of $K_2Zr(Hf)F_6$, which could be attributed to factors such as the degree of crystallization and crystal morphology and structure that is affected by these additives. Also, with specific concentrations of KF and HF the separation efficiency could be noticeably improved (Sections 4.3.2.2 and 4.3.2.3), seemingly because of improvement of the tails separation efficiency, although enhancement of the heads separation efficiency is ultimately desired for further improvement of the efficiency of a cascade process. The molecular modelling results provided some insight into the solid-state thermodynamics, where the predicted relative ease of solid solution formation might give an explanation for the comparatively poor enrichment

of the crystalline product that is achieved during fractional crystallization, i.e. as characterized by the low heads separation efficiency.

Therefore, based on the results obtained in this study, it is recommended that future studies on fractional crystallization of $K_2Zr(HF)F_6$ should be directed towards the following aspects.

Molecular Modelling

Studying the solid-state thermodynamics of the $K_2Zr(Hf)F_6$ system using molecular modeling techniques provides valuable insight into the effects of solid-solution formation on the separation efficiency as shown in this study. However, to improve the accuracy of the predictions, investigation of the following aspects will be useful:

(i) Improvement of the accuracy of the basis functions of Zr and Hf, i.e. the pseudopotentials utilized in CASTEP and the numerical basis functions that were used for DMol^3, within the DFT framework. This requires accurate thermodynamic data of both Zr and Hf, which is currently limited.

(ii) Modelling of the different polymorphic structures of $K_2Zr(Hf)F_6$. While the experimental results have shown that $K_2Zr(Hf)F_6$ can also crystallize in the monoclinic structure, the solid solution simulations were done using only the orthorhombic structures. Modelling of $K_2Zr_{(1-z)}Hf_zF_6$ solid solutions using the monoclinic structure could clarify whether any significant difference between the two polymorphs exists.

(iii) Modelling of $K_3Zr(Hf)F_7$ to determine whether there is a significant difference between the hexafluoride and heptafluoride structures with respect to the thermodynamics of Hf-incorporation into the crystal structures. The results could then possibly confirm the poor selectivity of the heptafluoride structure observed experimentally.

(iv) Improvement of the methodology used for solid solution simulations. By including vibrational analysis in the computational method, the finite-temperature thermodynamic quantities such as enthalpies, entropies, and subsequently Gibbs free energies may also be calculated which would probably lead to a higher degree of accuracy for the separation efficiency predictions.

Experimental

As mentioned previously, cooling crystallization of $K_2Zr(Hf)F_6$ has shown that the separation efficiency is influenced by varying the solvent composition using additives such as KF and HF. Different factors that influence the separation efficiency, due to the use of the additives, were identified in this study, although, no clear classification could be made as to what the underlying factors are that caused the change in the separation efficiency. Additional insight may be gained by studying the following:

(i) Continued solubility studies of pure K_2ZrF_6 and K_2HfF_6; to determine whether additives, such as KF and HF, cause a change in the solubility ratio, which according to the thermodynamic model presented in Equations (2.43) and (3.14), could influence the separation efficiency. Combining this data together with molecular modelling results could help with the development of a more accurate model to predict the separation efficiency of Zr and Hf via fractional crystallization.

(ii) Quantitatively determining the influence of the additives on the crystallization kinetics. Hereby the effect of the additives on the growth and nucleation rates, and its relation to the resulting separation efficiency, can be elucidated.

(iii) Studying the phase equilibria for fractional crystallization of $K_2Zr(Hf)F_6$ from aqueous solutions, by which phase diagrams may be constructed, can aid in the design of a fractional crystallization process [11, 12]. Although it has been shown in this study, through molecular modeling, that the $K_2Zr(Hf)F_6$ system is prone to solid solution formation during crystallization, knowledge of the phase equilibria could be used to optimize the process, thus further improving the separation efficiency.

(iv) Speciation studies of $K_2Zr(Hf)F_6$ in aqueous media can provide valuable insight into the solution chemistry of the system, which can be used as follows to improve the efficiency of cooling crystallization.

   a. By studying the speciation of both compounds in solution one might be able to identify differences in the stability of certain complexes that form at specific conditions. Ideally, the separation efficiency of crystallization would be enhanced by a greater stability of the Hf-complex in solution, which might however change the composition of the crystal product.

   b. Using the knowledge of the aqueous chemistry of the complex salts, ligands might be identified that selectively stabilizes Hf(IV) in solution, which could be used to prevent (or restrict) Hf(IV) from entering the solid phase. The separation

efficiency could hereby be significantly improved with respect to the heads separation factor.

c. Another possibility might be the use of an extractive crystallization process. The process then consist of an additional phase where an organic extractant is used that selectively extracts Hf(IV) from the aqueous solution, thereby lowering the amount of Hf-incorporation in the solid phase.

(v) Validation of the molecular modeling results with respect to solid solution formation may be undertaken using a technique called zone melting. The thermodynamics of mixing for K_2ZrF_6 and K_2HfF_6 may then be studied experimentally by cooling molten salt mixtures using a zone refiner [13], whereby the validity of the molecular modeling predictions could be evaluated.

Staged Crystallization using a Recycle Cascade Setup

The efficiency of the cascade (Section 5.4) could be improved by enhancing the separation efficiency as discussed above. Nevertheless, the following challenges should be considered in further studies if the process is to be optimized with respect to production cost and production rate.

(i) $K_2Zr(Hf)F_6$ has a relatively low solubility in the aqueous solutions studied in this research. Since the throughput of purified $K_2Zr(Hf)F_6$ is directly dependent on the solubility of the salt, other solvent mixtures may be tested to increase the solubility of $K_2Zr(Hf)F_6$. HF with different concentrations may be investigated considering the effect HF had on the solubility of $K_2Zr(Hf)F_6$ in this study.

(ii) Optimization of solvent volume. The solvent volume is also related to the solubility, where a larger volume of solvent would be needed with decreasing solubility of the salt. The volume of solvent needed is important, as more energy would be needed to transport the solutions from one stage to the next the higher the volume of solvent.

(iii) The cooling capacity is also related to the solubility, as a higher solubility would lead to the use of a smaller volume of solvent to achieve a certain production. The solvent volume (as discussed in (ii)) then also influences the amount of energy used for cooling. In this study, cooling to a temperature of 15 °C was used experimentally, which is difficult and expensive to achieve on a large scale. This problem may be overcome by applying cooling-tower water which typically has a temperature of 25 °C. However, the

mass of salt produced will then be lower compared to solutions which have been cooled to 15°C, and the separation efficiency may change slightly because the separation efficiency appears to be related to the extent of crystallization (Section 5.2).

(iv) The volume of solvent required also influences the energy requirements for heating, as the cooled solutions needs to be re-heated after mixing with the crystalline product in each dissolution tank.

(v) Conducting a full techno-economical evaluation. This will have to be undertaken to identify the most economically feasible route for the implementation of fractional crystallization on a large scale, with respect to the degree of Zr(IV) recovery as noted in Section 5.4.

(vi) Optimization of interstage flow rates to effect desirable crystallization kinetics for continuous crystallization with regard to optimized separation efficiency. Therefore, to optimize volumetric production (by also considering of the abovementioned aspects) and still ensuring optimum separation efficiency.

5.6. References

1. Rosenberger, F. and Riveros, H.G. Segregation in alkali halide crystallization from aqueous solutions. *J. Chem. Phys.* 60 (2) (1974) 668 – 673.

2. Nie, Q., Wang, J. & Yin, Q. Effect of solution thermodynamics on the purification of two isomorphic steroids by solution crystallization. *Chem. Eng. Sci.* 61 (2006) 5962 – 5968.

3. Givand, J., Chang, B-K. Teja, A.S. & Rousseua, R.W. Distribution of isomorphic amino acids between a crystal phase and an aqueous solution. *Ind. Eng. Chem. Res.* 41 (2002) 1873 – 1876.

4. Morse, P.M. 1969. Thermal physics 2nd ed. New York: W.A. Benjamin. 431 p.

5. Schroeder, D.V. 2000. An introduction to thermal physics. Addison Wesley Longman. 422 p.

6. Stowe, K. 2007. An Introduction to thermodynamics and statistical mechanics 2nd ed. Cambridge: Cambridge University Press. 556 p.

7. Kittel, C. 1966. Introduction to solid state physics. 3rd ed. New York: John Wiley and Sons. 648 p.

8. Sajin, N.P. & Pepelyaeva, E.A. Separation of hafnium from zirconium and production of pure zirconium dioxide. In Proceedings of the Second united Nations International Conference on the Peaceful uses of Atomic Energy, Geneva, 1958. Vol. 8, Paper P/634, pp 559–562.

9. Benedict, M., Pigford, T.H. and Levi, H.W. 1981. Nuclear chemical engineering. 2nd ed. McGraw-Hill.

10. Coster, D. and von Hevesy, G. Process of separating zirconium and Hafnium. U.S. Pat. 1,618,960 (1927).

11. Dye, S.R. & Ng, K.M. Fractional crystallization: Design alternatives and tradeoffs. *AIChE J.* **41** (11) (1995) p. 2427 - 2438.

12. Mersman, A. 2001. Design of crystallizers. In Mersman, A., ed. Crystallization technology handbook. 2nd ed. New York: Marcel Dekker. p. 323 - 392.

13. Diepen, P.J. Cooling crystallization of organic compounds: processes, purity and permeability. Ph.D-thesis, Technische Universiteit, Delft, 1998.

APPENDIX A

ICP-OES Method for Zr and Hf Analyses

A.1. Representative Calibration Curves

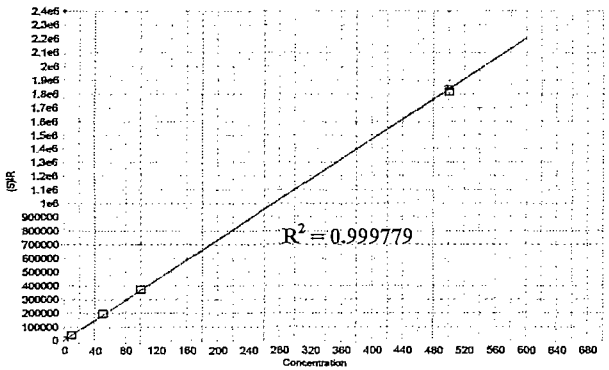

Figure A.1: Representative calibration curve of Zr using the 343.8 nm emission line.

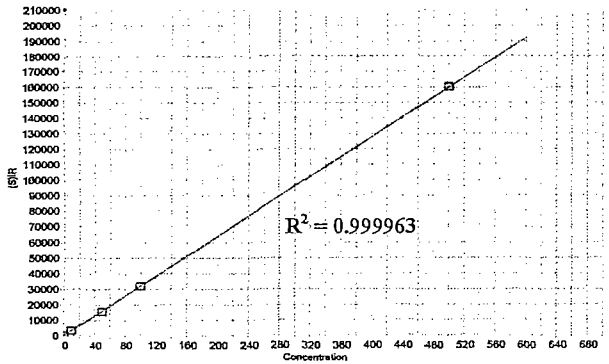

Figure A.2: Representative calibration curve of Hf using the 263.8 nm emission line.

A.2. Quality Tests

Table A.1: Accuracy tests for calibrated emission lines of Zr and Hf. Values in brackets are in nm.

M(IV)	Concentration (mg/L)	Determined Concentrations (mg/L)			
		Zr(339.1)	Zr(343.8)	Hf(263.8)	Hf(339.9)
Zr+Hf	Blank	-0.512	-0.457	0.703	2.353
Zr	10	10.320	10.360	0.676	2.290
Zr	50	53.740	53.460	0.701	2.336
Zr	100	104.400	104.900	0.712	2.624
Zr	500	495.300	502.700	0.832	3.690
Hf	1.0	-0.458	-0.468	1.207	2.998
Hf	10	0.275	0.316	10.860	13.930
Hf	50	-0.459	-0.316	52.010	60.700
Hf	100	-0.278	-0.033	100.400	114.300
Hf	500	-0.101	0.112	494.700	557.600

Based on these results, the emission lines of 343.8 nm for Zr and 263.8 nm for Hf were used in all ICP-OES analyses.

APPENDIX B

ICP-OES Reliability Tests for Zr and Hf Analyses

B.1. Influence of H_2SO_4 Concentration on Accuracy

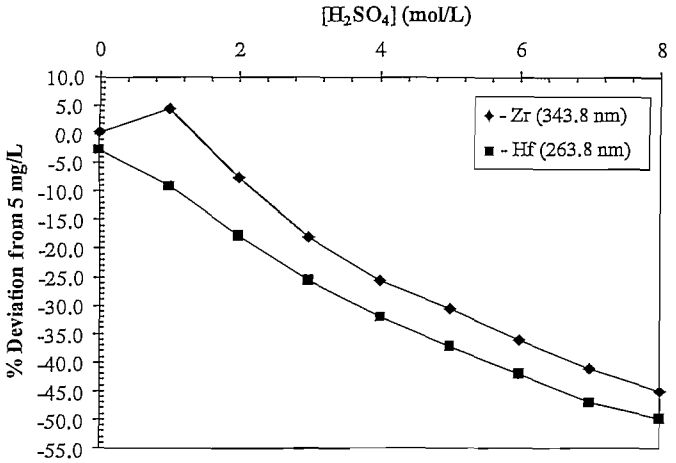

Figure B.1: Influence of H_2SO_4 concentration on the determination of Zr(IV) and Hf(IV) *concentrations via the ICP-OES method used in this study.*

Above 2 mol/L H_2SO_4 the determination of the Zr(IV) and Hf(IV) concentrations were significantly compromised with the method used in this study. During sample preparation, the H_2SO_4 concentration, if present, was well below this limit ensuring reliable results.

B.2. Reproducibility Test

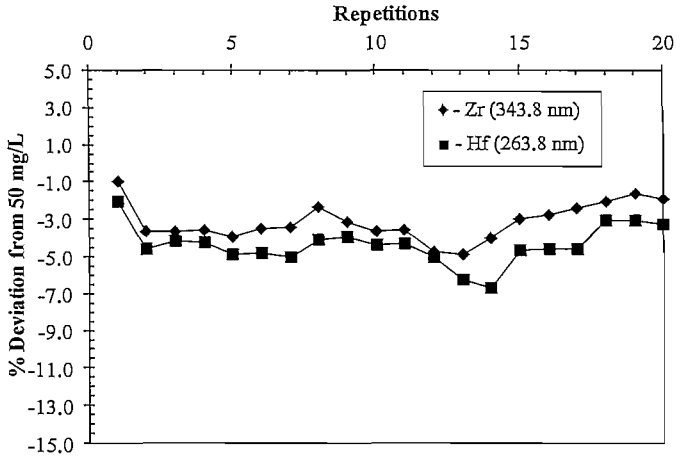

Figure B.2: Results of reproducibility tests performed by sequential analysis of a single aqueous solution mixture of Zr(IV) and Hf(IV) with concentrations of 50 mg/L each.

APPENDIX C

ICP-OES Analyses Method for Potassium

C.1. Preparation of Calibration Standards

Using $K_2Cr_2O_7$, the amount of solid required to yield a concentration of 1000 mg/L Cr(VI) was calculated as follows:

On a 1 L basis:

1000 mg = 1g/51.9961 g/mol = 0.0192 mole.

But, mole Cr(VI) : mole $K_2Cr_2O_7$ = 2 : 1.

Thus, 0.0096 mole $K_2Cr_2O_7$ is required.

Therefore, the mass of solid required: $M_{K2Cr2O7}$ = 0.0096 mol x 294.1846 g/mol

= 2.8289 g (for 100% purity).

The purity of the salt used is 99.5 %, thus 2.8431 g of the 99.5 % pure salt is required.

To prepare a 500 mL solution, 1.4216 g $K_2Cr_2O_7$ (99.5% pure) can thus be dissolved in a 0.1 mol/L HNO_3 solution, for which a volumetric flask was used to adjust the total volume to 500 mL.

The resulting solution therefore has a potassium concentration of 755.7 mg/L. Calibration standards with concentrations of 0 mg/L, 7.557 mg/L, 37.79 mg/L, 75.57 mg/L, and 377.9 mg/L were prepared from this solution by serial dilution. A calculated amount of concentrated HNO_3 was added to each solution to keep the concentration constant at 0.1 mol/L:

C.2. Representative Calibration Curves

Initially, two emission lines of K, i.e. with wavelengths of 766.4 nm and 769.8 nm, were used for calibration, representative results of which are shown in Figures C.1 and C.2.

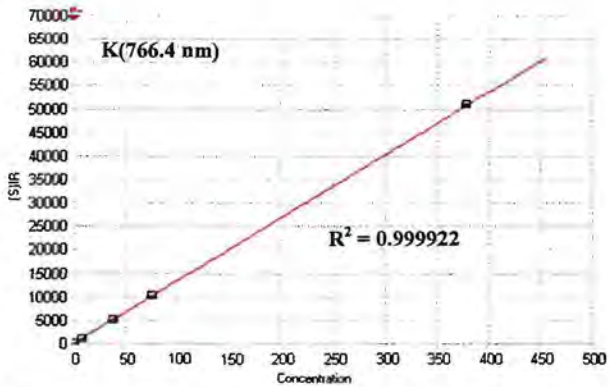

Figure C.1: Representative calibration curve of K using the 766.4 nm emission line.

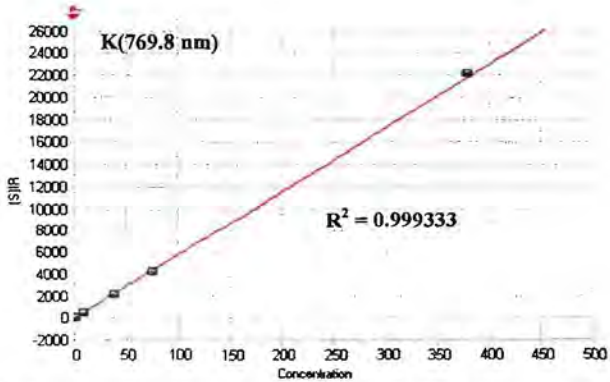

Figure C.2: Representative calibration curve of K using the 769.8 nm emission line.

C.3. Quality Tests

Table C.1: Accuracy test for calibrated emission lines of K.

Concentration	37.79 mg/L		75.57 mg/L	
Wavelength	766.4 nm	769.8 nm	766.4 nm	769.8 nm
Concentration (mg/L)	37.25	34.68	75.63	72.2
Standard Deviation	0.11	0.15	0.39	0.38
%RSD	0.2953	0.4368	0.52	0.5287

Based on these results, the 766.4 nm emission line of K were used in all ICP-OES analyses.